Aalborg Universitet

# Modeling of Reverberation Effects for Radio Localization and Communications

Steinböck, Gerhard

*Publication date:*
2013

*Document Version*
Accepted author manuscript, peer reviewed version

Link to publication from Aalborg University

*Citation for published version (APA):*
Steinböck, G. (2013). *Modeling of Reverberation Effects for Radio Localization and Communications*.

**General rights**
Copyright and moral rights for the publications made accessible in the public portal are retained by the authors and/or other copyright owners and it is a condition of accessing publications that users recognise and abide by the legal requirements associated with these rights.

- Users may download and print one copy of any publication from the public portal for the purpose of private study or research.
- You may not further distribute the material or use it for any profit-making activity or commercial gain
- You may freely distribute the URL identifying the publication in the public portal -

**Take down policy**
If you believe that this document breaches copyright please contact us at vbn@aub.aau.dk providing details, and we will remove access to the work immediately and investigate your claim.

Downloaded from vbn.aau.dk on: April 20, 2024

# *Modeling of Reverberation Effects for Radio Localization and Communications*

BREAKING NEW GROUND
AALBORG UNIVERSITY

# *Modeling of Reverberation Effects for Radio Localization and Communications*

Gerhard Steinböck
Ph.D. Thesis

September 2013

Department of Electronic Systems
Aalborg University
Fredrik Bajers Vej 7
9220 Aalborg East, Denmark

Steinböck, Gerhard.
Modeling of Reverberation Effects for Radio Localization and Communications

Copyright ©2013 Gerhard Steinböck, except where otherwise stated.
All rights reserved.

**ISBN 978-87-7152-024-8**

Department of Electronic Systems
Aalborg University
Fredrik Bajers Vej 7
DK-9220 Aalborg East
Denmark

This Ph.D. thesis was defended November 8, 2013, at Aalborg University.

Assessment committee:

Associate Professor Ph.D. Davide Dardari, University of Bologna at Cesena.
Associate Professor Ph.D. Christopher L. Holloway, National Institute of Standards and Technology.
Associate Professor Ph.D. Troels Bundgaard Sørensen, Aalborg University (Chairman).

Supervisor:

Professor Dr. Sc. Techn. Bernard H. Fleury and Associate Professor Ph.D. Troels Pedersen, Aalborg University.

Typeset by the author using LaTeX.
Main font: MinionPro by Adobe.
Printed by Uniprint, Aalborg, Denmark.

# Abstract

For decades the terrestrial radio channel has been characterized and modeled for communication purpose only, e.g. to design wireless systems and/or to assess their performance by means of Monte Carlo simulations. The recent emergence of localization capabilities in terrestrial wireless systems demand for novel channel models that, in addition, accurately emulate the location-dependent features of real channels.

In this thesis we address and provide answers to the central questions of the cause, the effect and the modeling of the diffuse component observed in delay power spectra measured in indoor environments. We show that this component carries a significant portion of the total received power. Thus, the accurate modeling of it is of prime importance for both communication and positioning.

To clarify the cause of the diffuse component we first experimentally investigate the spread in delay and direction of multipath components in an indoor environment. The results indicate small per-path-component spreads. This finding suggests that the diffuse component is contributed by a multitude of (weak) specular multipath components. Others have also experimentally confirmed this conclusion using an ultra-wideband (UWB) set-up: measured UWB delay power spectra exhibit a transition from early specular components to a diffuse component. We name this transition the "avalanche effect". We propose a propagation graph that mimics propagation conditions in an environment: transmitters, receivers, and scatterers are represented as vertices and propagation conditions between these vertices as (labeled) edges. Due to its recursive structure, the graph model is capable of reproducing the avalanche effect and the diffuse component, even though propagation along the edges is assumed specular.

Experimental evidence also shows that the diffuse component of delay power spectra measured in the same room decays exponentially with nearly the same decay rate and magnitude regardless of the transmitter-receiver distance. Only its onset varies with distance. We incorporate these empirical features into a distance dependent model of the delay power spectrum, which we then validate experimentally. From this model we derive secondary models that predict the received power, the mean delay, the rms delay spread and the kurtosis versus distance.

The behavior of the diffuse component versus distance in indoor environment is linked to reverberation effects analog to reverberation effects observed in room acoustics and electromagnetic reverberation chambers. Reverberation models of room acoustics relate the decay rate of the diffuse component to the room geometry and an average absorption coefficient. Following a

recently proposed approach, we transcribe these models to electromagnetics and validate them experimentally following a systematic procedure. These transcribed models provide accurate predictions of the delay power spectrum in a typical office environment. Furthermore, they can predict changes in the diffuse power due to opening windows, the presence of people or by changing the size of the room.

As an example of the benefits of modeling the diffuse component in indoor environments we present a study of the performance of a positioning estimator that jointly utilizes the secondary models of received power and mean delay versus distance. The results indicate that the mean delay carries relevant location-dependent information that can be exploited to enhance the localization accuracy.

# Dansk resumé

I flere årtier har man modelleret og karakteriseret de terrestriske trådløse kanaler udelukkende til kommunikationsformål. Sådanne kanalmodeller bruges eksempelvis til at designe og teste mobile kommunikationssystemer. For nylig er man begyndt at bruge terrestriske trådløse kommunikationssystemer i forbindelse med positionering, dvs. til at finde de geografiske positioner af afsender og/eller modtager. Dette positioneringsformål kræver nye kanalmodeller, som reflekterer positionsafhængige egenskaber.

Denne ph.d.-afhandling tager udgangspunkt i spørgsmål om hvilke årsager og effekter, der giver anledning til diffuse komponenter i trådløse indendørskanaler. Dette leder naturligt til spørgsmål om, hvordan man på passende vis kan modellere sådanne diffuse komponenter. Vi viser, at tilstedeværelsen af en diffus komponent påvirker bland andet den modtagede signalstyrke. Kommunikations- og positioneringssystemer er i stor udstrækning signalstyrkebaseret, og derfor spiller modelleringen af de diffuse komponenter en afgørende rolle.

Indendørs måleeksperimenter er blevet udført og årsagen til forekomsten af diffuse komponenter undersøgt. Først undersøges udspredningen af separate komponenter i tidsforsinkelse (delay) og retning. Resultaterne indikerer en meget lille udspredning af de enkelte komponenter, og disse simulerers derfor som spekulere komponenter i praksis. Den begrænsede udspredning understøtter vores formodning om, at enhver diffus komponent udgøres af mange men svage spekulere komponenter. Andre forskningseksperimenter, med målinger af meget højt båndbredde (ultra wideband), indikerer en række spekulere komponenter med lav tidsforsinkelse, efterfulgt af en overgang til en samlet diffus komponent med større tidsforsinkelse. Denne overgangstendens omtaler vi som "lavine"-effekten. Vi har forslået en såkaldt "udbredelsesgrafmodel" til simulering af lavineeffekten. I modellen svarer afsender, modtager og punktreflektorer til knudepunkter i grafen. Grafens kanter modellerer udbredelsesegenskaber af radiobølger mellem knudepunkterne. Den rekursive struktur af grafen genskaber lavineeffekten og den diffuse komponent, selvom modellen kun er baseret på spekulere tidsforsinkelser mellem knudepunkterne.

Eksperimenter påviser, at den diffuse komponent målt i et individuelt rum har det samme eksponentielle henfald og styrke, uanset positionerne af afsender og modtager. Kun begyndelsestidspunktet af det eksponentielle henfald ændres med afstanden mellem afsender og modtager. Disse eksperimentelle observationer antyder en afstandsafhængig model af det såkaldte "delay power spectrum". Baseret på en sådan afstandsafhængig model udleder vi så afstandsafhængige sekundære modeller af modtaget signalstyrke, middel delay, delay spredning og kurtosis.

Den diffuse komponents egenskaber, set i forhold til de fysiske afstande i et givet indendørs rum, sammenlignes med efterklangseffekten, som vi kender den fra rumakustik og elektromagnetiske efterklangsrum. Efterklangsmodeller fra akustik relaterer graden af det eksponentielle henfald, kaldet efterklangstiden, til rummets fysiske størrelse og rummets gennemsnitlige absorptionskoefficient. Vi anvender en tidligere benyttet fremgangsmåde til at oversætte modeller fra akustisk til elektromagnetisme. Vi tester deres gyldighed med et specialdesignet eksperiment. Vores eksperiment viser, at de oversatte modeller er i stand til at forudsige ændringerne i efterklangstiden, når rummets egenskaber ændres. Rummets egenskaber kan eksempelvis ændres ved at åbne vinduer eller ved tilstedeværelsen af flere eller færre personer i rummet. Individuelle rum med forskellige størrelser kan også benyttes.

Gennem eksempler illustrerer vi fordelene ved modellerne, som er blevet forslået til beskrivelse af den diffuse komponent. Vi diskuterer et detaljeret eksempel, som benytter de sekundære modeller af modtaget signalstyrke og middel delay til at afgøre afsenderens position. Resultaterne viser, at middel delay afspejler gode afstandsinformationer, og brugen af middel delay forbedrer derfor præcisionen af afsenderens estimerede position.

# *Preface*

This thesis is submitted to the Doctoral School of Engineering and Science at Aalborg University, Denmark, in partial fulfillment of the requirements for the degree of doctor of philosophy. Chapters 1 – 6 provide an introduction and a brief description of the contributions of the thesis. The main body consists of seven papers referred to as Paper A – Paper G published in peer-reviewed conferences and journals listed at pp. 69–213. The work has been carried out during the period September 2008 – August 2013 at the Department of Electronic Systems, Aalborg University. It has been supported in part by the Faculty of Engineering and Science with PhD Stipend J.No. 562/06-FS-28045 and in part by the European projects ICT-217033 Wireless Hybrid Enhanced Mobile Radio Estimators (WHERE) and ICT-248894 Wireless Hybrid Enhanced Mobile Radio Estimators – Phase 2 (WHERE2). Parts of the work have been performed within the Network of Excellence in Wireless COMmunication NEWCOM$^{++}$ (ICT-216715 FP7) and NEWCOM$^{\sharp}$ (Grant agreement no. 318306) and the European Co-operation in the field of Scientific and Technical Research Action 2100 (COST 2100) and IC1004 (COST IC1004). I would like to thank Wei Wang and Ronald Raulefs from DLR (German Aerospace Center) for their collaboration with the measurement campaign used extensively within this thesis.

I would like to thank my former colleagues from Austrian Institute of Technology (AIT) and Forschungszentrum Telekommunikation Wien (FTW) who have inspired my early curiosity in radio communications and supported me when I decided to enroll in the Master programm at Aalborg University after years of collaboration. I wish to express my sincere gratitude and thanks to my supervisors Professor, Dr. sc. techn. Bernard H. Fleury and Associate Professor Troels Pedersen. Both of them provided supervision, when ever necessary, and guided me through my Master program and finally my PhD studies. Many thanks to everybody who helped with the recommendation letters and reviewing my application for my PhD Stipend.

I'm grateful for the past years here in Aalborg and I would like to acknowledge my present and former colleagues and fellow PhD students at Aalborg University for many pleasant and inspiring discussions. I would like to thank our secretary Nina and her colleagues for their help and assistance throughout the years. I thank my friends, both back home in Austria, whom I still can count on everyday, and the new ones I gained here in Aalborg.

Zum Abschluss möchte ich mich noch bei meinen Eltern und meiner Schwester herzlichst bedanken für deren Unterstützung.

Gerhard Steinböck
Aalborg, September 2013

# Contents

*Abstract* . . . . . . . . . . . . . . . . . . . . . . . . . . . . . . . . . . *v*

*Dansk resumé* . . . . . . . . . . . . . . . . . . . . . . . . . . . . . . *vii*

*Preface* . . . . . . . . . . . . . . . . . . . . . . . . . . . . . . . . . . . *ix*

*Thesis Details* . . . . . . . . . . . . . . . . . . . . . . . . . . . . . . *xiii*

*1 Introduction to and Motivation for Channel Modeling in Communications and Localization* . . . . . . . . . . . . . . . . . . *1*
- 1.1 Motivation and Purpose of Channel Modeling for Communications 2
- 1.2 Motivation and Purpose of Radio Channel Models in Localization 4
- 1.3 Focus of the Thesis 6
- 1.4 Structure of the Thesis 7

*2 Preliminaries in Radio Channel Modeling* . . . . . . . . . . . . . . *9*
- 2.1 Path Loss or Path Gain Models 11
- 2.2 Shadow Fading 12
- 2.3 Narrowband and Wideband Channel Characterization 12

*3 The Reverberant Channel* . . . . . . . . . . . . . . . . . . . . . . . . . *17*
- 3.1 Observations Related to the Diffuse Component 17
- 3.2 Interpretations of the Diffuse Component 19
- 3.3 White-box Models for Reverberant Channels 21
- 3.4 Black-box Models for Reverberant Channels 29

*4 Research Questions, Methodology and Applications Considered in this Thesis* . . . . . . . . . . . . . . . . . . . . . . . . . . . . . *35*
- 4.1 Research Questions on Reverberant Channel Modeling 35
- 4.2 Research Methodology 36
- 4.3 The Research Methods Adopted in this Thesis 39
- 4.4 Applications of the Reverberation Models and the Model of the Delay Power Spectrum 42

*5 Contributions to Reverberant Channel Modeling* . . . . . . . . . . . *45*
- 5.1 Results on the Per-Path Component Spreads 45
- 5.2 Impulse Response Modeling with Propagation Graphs 46
- 5.3 Predict the Delay Power Spectrum for Specific Environments Using Reverberation Models 47
- 5.4 The DPS Model and its Secondary Models 49

5.5 Application of the DPS Model in Localization 52

*6 Conclusions and Outlook . . . . . . . . . . . . . . . . . . . . . . . 55*
6.1 Conclusions 55
6.2 Outlook 57

*References . . . . . . . . . . . . . . . . . . . . . . . . . . . . . . 61*

*A Experimental Characteristics of Indoor Wideband MIMO Radio Channels and their Impact on Stochastic Modeling . . . . . . . . . . . 69*
A.1 Introduction 71
A.2 Signal Model 73
A.3 Dispersive Path Parameter Estimators 73
A.4 Numerical and Experimental Results 76
A.5 Discussion and Conclusion 82
References 83

*B Modeling of Reverberant Radio Channels Using Propagation Graphs 85*
B.1 Introduction 87
B.2 Representing Radio Channels as Graphs 89
B.3 Transfer Matrix of a Propagation Graph 93
B.4 Example: Stochastic Model for In-Room Channel 103
B.5 Conclusions 108
B.I Appendix 109
References 110

*C Experimental Validation of the Reverberation Effect in Room Electromagnetics . . . . . . . . . . . . . . . . . . . . . . . . . . 115*
C.1 Introduction 117
C.2 Reverberation Models 119
C.3 Model Validation 125
C.4 Measurements and Results 129
C.5 Discussion 136
C.6 Applications 138
C.7 Conclusion 143
References 144

*D Model for the Path Loss of In-room Reverberant Channels . . . . . . 147*
D.1 Introduction 149
D.2 Delay Power Spectrum Model 150
D.3 Predictions of the Delay Power Spectrum Model 152
D.4 Measurement Data 153
D.5 Results 156
D.6 Discussion 159
D.7 Conclusions 160

References 160

E *Distance Dependent Model for the Delay Power Spectrum of In-room Radio Channels* . . . . . . . . . . . . . . . . . . . . . . . . . *163*

E.1 Introduction 165
E.2 Model of the Delay Power Spectrum 167
E.3 Measurement Data 177
E.4 Validation of the Proposed Model 181
E.5 Examples of Applications 186
E.6 Conclusions 190
E.I Impulse Response Model Relations 191
E.II Derivation of Normalized Centered Moment Generating Function and Kurtosis 192
E.III Further Properties of $K(d)$ 192
E.IV Estimation of $K(d)$ and $K_\mathrm{p}$ 193
References 193

F *Channel Measurements and Characteristics for Cooperative Positioning Applications* . . . . . . . . . . . . . . . . . . . . . . . . *197*

F.1 Introduction 199
F.2 Multi-link Model for Positioning 200
F.3 Channel Measurement Campaign 201
F.4 Data Processing 203
F.5 Results 206
F.6 Conclusion and Outlook 208
References 210

G *Wireless Indoor Positioning Relying on Observations of Received Power and Mean Delay* . . . . . . . . . . . . . . . . . . . . . . . . . *213*

G.1 Introduction 215
G.2 Signal Model 216
G.3 Position Estimation 218
G.4 Measurement Data 220
G.5 Results 221
G.6 Conclusion 224
References 225

# Thesis Details

**Thesis Title:** Modeling of Reverberation Effects for Radio Localization and Communication

**PhD Student:** Gerhard Steinböck

**Supervisors:** Prof. Dr. Sc. Techn. Bernard H. Fleury, Aalborg University
Associate Prof. Ph.D. Troels Pedersen, Aalborg University

The main body of this PhD thesis consists of the following seven papers:

*Paper A* G. Steinböck, X. Yin, T. Pedersen, and B. Fleury, "Experimental Characteristics of Indoor Wideband MIMO Radio Channels and their Impact on Stochastic Modelling," in *Proc. 13th IEEE Digital Signal Processing Workshop and 5th IEEE Signal Processing Education Workshop, 2009. DSP/SPE 2009.*, Jan. 2009, pp. 302–307.

*Paper B* T. Pedersen, G. Steinböck, and B. Fleury, "Modeling of Reverberant Radio Channels Using Propagation Graphs," *IEEE Trans. Antennas Propagat.*, vol. 60, no. 12, pp. 5978–5988, Dec. 2012.

*Paper C* G. Steinböck, T. Pedersen, B. Fleury, W. Wang, and R. Raulefs, "Experimental Validation of the Reverberation Effect in Room Electromagnetics," *IEEE Trans. Antennas Propagat.*, IN PREPARATION.

*Paper D* G. Steinböck, T. Pedersen, B. Fleury, W. Wang, T. Jost and R. Raulefs, "Model for the Path Loss of In-room Reverberant Channels," in *Vehicular Technology Conference (VTC 2011-Spring), 2011 IEEE 73rd*, May 2011, pp. 1–5.

*Paper E* G. Steinböck, T. Pedersen, B. Fleury, W. Wang, and R. Raulefs, "Distance Dependent Model for the Delay Power Spectrum of In-room Reverberant Channels," *IEEE Trans. Antennas Propagat.*, accepted, 2013.

*Paper F* W. Wang, G. Steinböck, T. Jost, T. Pedersen, R. Raulefs, and B. Fleury, "Channel Measurements and Characteristics for Cooperative Positioning Applications," in *International Conference on Localization and GNSS (ICL-GNSS)*, Jun. 2012.

*Paper G* S. Begusic, D. Nygaard Urup, J. Kolonic, H. Holbæk Pedersen, W. Wang, R. Raulefs, M. Jakobsen, G. Steinböck, and T. Pedersen, "Wireless Indoor Positioning Relying on Observations of Received Power and

Mean Delay," in *IEEE ICC 2013 Workshop on Advances in Network Localization and Navigation (ANLN)*, Jun. 2013.

Additionally, the following papers were authored and co-authored by Gerhard Steinböck during his PhD studies:

*Paper 1* G. Steinböck, T. Pedersen, and B. Fleury, "Calibration of the Propagation Graph Model in Reverberant Rooms," in *URSI Commission F Triennial Open Symposium on Radiowave Propagation and Remote Sensing*, May 2013.

*Paper 2* B. Denis, R. Raulefs, B. Fleury, B. Uguen, N. Amiot, L. de Celis, J. Dominguez, M. Koldsgaard, M. Laaraiedh, H. Noureddine, E. Staudinger, and G. Steinböck, "Cooperative and Heterogeneous Indoor Localization Experiments," in *IEEE ICC 2013 Workshop on Advances in Network Localization and Navigation (ANLN)*, Jun. 2013.

*Paper 3* G. E. Kirkelund, G. Steinböck, X. Yin, and B. H. Fleury, "Tracking of the Temporal Behaviour of Path Components in the Radio Channel - A Comparison between Methods," in *Proceedings of Annual IEEE Student Paper Conference (AISPC'08)*, Aalborg, Denmark, February 15th 2008.

*Paper 4* X. Yin, T. Pedersen, G. Steinböck, G. E. Kirkelund, P. Blattnig, A. Jaquier, and B. H. Fleury, "Tracking Multi-Dimensional Time-Variant Parameters of Radio Propagation Paths using Particle Filtering," in *Proceedings of 2008 IEEE Radar Conference*, Rome, Italy, May 16-30 2008.

*Paper 5* X. Yin, G. Steinböck, G. E. Kirkelund, T. Pedersen, P. Blattnig, A. Jaquier, and B. H. Fleury, "Tracking of Time-Variant Radio Propagation Paths using Particle Filtering," in *Proceedings of IEEE 2008 International Communications Conference*, Beijing, China, May 19-23 2008.

This thesis has been submitted for assessment in partial fulfillment of the PhD degree. The thesis is based on the submitted or published scientific papers which are listed above. Parts of the papers are used directly or indirectly in the extended summary of the thesis. As part of the assessment, co-author statements have been made available to the assessment committee and are also available at the Faculty. The thesis is not in its present form acceptable for open publication but only in limited and closed circulation as copyright may not be ensured.

Chapter 1

# Introduction to and Motivation for Channel Modeling in Communications and Localization

This work considers radio channel modeling for wireless communications and localization[1] systems. In order to define the meaning of radio channel modeling we assume for simplicity that both communication and localization[2] systems consist of a single transmitter and receiver. The antenna of the transmitter radiates an electromagnetic wave which contains information of some form. The wave propagates through and interacts with the physical environment until it is finally sensed at the antenna of the receiver. The receiver attempts to extract the transmitted information from the sensed signal. Extraction of information is possible only if the sensed signal fulfills certain quality criteria. One such criterion is for instance that the sensed signal is sufficiently stronger in magnitude than the ambient noise and thermal noise in the receiver. Radio channel models characterize some aspects of the transformation performed by the channel on the signal at the transmit antenna input – we denote it as $x(t)$ – to produce the signal, say $y(t)$, at the output of the sensing antenna. In the sequel we refer to $x(t)$ and $y(t)$ as the transmitted and the received signals, respectively. Thus radio channel models are of paramount importance to radio engineers in designing and testing wireless systems for communication and localization.

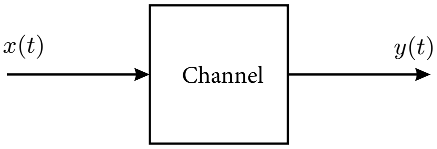

*Fig. 1.1: Sketch of the transformation performed by the channel on the transmitted signal $x(t)$ to produce the received signal $y(t)$.*

---

[1] Note that in the open literature the terms localization and positioning are often used interchangeably. Within Chapters 1 to 6 we use the term localization.

[2] Note that typically multiple transmitters and/or receivers are necessary for ambiguity free localization. However, to ease the introduction to channel modeling we consider only one transmitter and receiver.

We concretize the above description of the communication or localization system as shown in Fig. 1.1 with a transmit signal $x(t)$, the radio channel as a box, and the received signal $y(t)$. The mathematical description of radio channel models can be based on theoretical results from physics, e.g. electromagnetics, or on empirical observations. In general the transmitter and receiver may move or the environment may change. Thus, the radio channel is time-variant. For simplicity we consider the time-invariant case in this thesis. We characterize the propagation mechanisms of the radio waves between the transmit antenna and the receive antenna using the theory of linear time-invariant (LTI) systems for fixed positions of the antennas and a static environment. The output signal $y(t)$ of such a linear time-invariant system is the convolution of the input signal $x(t)$ with the system's impulse response $h(t)$:

$$\begin{aligned} y(t) &= x(t) * h(t), && (1.1) \\ &= \int_{-\infty}^{\infty} x(\tau)\, h(t-\tau)\mathrm{d}\tau. && (1.2) \end{aligned}$$

An alternative to the time domain representation with the impulse response is the representation of the LTI system in the frequency domain by its transfer function. The transfer function is the Fourier transform of the impulse response. The received signal in the frequency domain reads

$$Y(f) = X(f)\, H(f), \tag{1.3}$$

where $H(f)$ the channel transfer function and $X(f)$ and $Y(f)$ are the Fourier transforms of $x(t)$ and $y(t)$, respectively. Thus in radio channel modeling we may use either the channel impulse response or the channel transfer function to characterize the radio channel.

## 1.1 Motivation and Purpose of Channel Modeling for Communications

Now that we have established the concept of radio channel models, we focus on their purpose. In this section we discuss the purpose of channel models for wireless communications and in Section 1.2 for localization.

In general the research in communication systems and radio channel models is motivated by an ever increasing demand for capacity in the wireless communication networks and for lowering the power consumption of devices. Increasing the capacity is done under the constraint of a limited bandwidth. We may visualize the demand for more capacity by considering the number of mobile communication users (subscribers). The number of subscribers has risen from approximately 2 to 6.8 billion over the past eight years [1]. Thus there are almost as many subscribers as people living on the planet [1], although a single person often has multiple subscriptions specially in the developed countries. The increase of subscribers is slowing down, however, with the use of mobile internet the generated data traffic per user is steadily increasing. Furthermore, fixed broadband links are more often substituted by wireless connections and thus create an additional demand for capacity increase in wireless networks. As an example the mobile-broadband subscriptions have risen from 268 million in 2007 to 2.1 billion in 2013 [1].

The demand for more capacity has lead to an increase of the complexity of the transmission systems over the past years. The extraction of the information contained in the transmitted signal $x(t)$ from the received signal $y(t)$, under the inherent limitations of the radio channel, is essential for increasing the performance of the communication systems. Knowledge of these limitations is exploited in the design of the communication systems, especially to optimize the system's performance. When designing different units in a given communication system we often utilize radio channel models with different purpose. We distinguish often between large scale and small scale models. The former include for instance path loss and shadowing effects. These effects characterize the received signal strength versus distance and are important for link budget analysis, the transmit power, cell sizes and the choice of antenna elements [2, 3]. The small scale models, detailed in Section 2.3, are used to characterize the channel dispersion in delay, Doppler frequency, direction, etc. The dispersive behavior of the channel is important for the choice of modulation techniques, diversity schemes, equalizers, antenna array structures, error correction codes, etc., [2]. In the receiver we use models of the radio channel to retrieve the information embedded in the signal $x(t)$ from $y(t)$. For this purpose the signal $x(t)$ is usually partially known to the receiver. This knowledge is exploited in the receiver to estimate the parameters of an assumed underlying channel model. With these estimates, the receiver removes distortions created by the radio channel in the received signal prior to demodulation and decoding.

Radio channel models are often devised only for one specific part or purpose in a communication system. This allows to model only the necessary effects of the radio channel in order to keep the model complexity, e.g. the number of required model parameters, at a minimum. For instance in network planning, the coverage analysis is done with path loss models or ray tracing models. These models provide the average received signal strength versus distance or location. The analysis of the bit error rate performance of the receiver algorithms requires a large number of realizations of the radio channel. Stochastic impulse response models are ideal for this purpose [2]. Typically these models are normalized in power and delay. Normalization in delay means shifting the onset of the impulse response to the origin under the assumption of perfect synchronization. Normalization in power is done because typical communication systems include a transmit power control and an automatic gain control at the receiver. The automatic gain control ensures the full signal range at the input of the analog to digital converters. The power control and gain control act similar to a normalization of the impulse responses. Accordingly, bit error rate simulations consider a signal to noise ratio rather than an average received signal strength versus distance obtained from path loss models.

## 1.2 Motivation and Purpose of Radio Channel Models in Localization

Research activities on location based services aim at increasing the capacity in future networks. This increase in capacity is achieved by optimizing the infrastructure by physical layer enhancements, cross layer optimization (phy/mac) and relaying and cooperative communications based on location information. Physical layer enhancements use the location information in receiver algorithms. Examples of such enhancements are an improved synchronization in the receiver [4] or predictive channel estimation with the use of movement information [5]. Selection of specific multiple input multiple output techniques based on the users' location are proposed in [4] and the coordination of intercell interference based on location information is proposed in [6]. Network operators benefit from the cross layer optimization by using strategies in radio resource management which include location information. Thus users separated in space can use the same resources even within the same cells [7, 8]. These examples clearly indicate how the location information can be used to increase the capacity in future networks.

The user has access to location based services, like emergency and security, navigation and tracking, information and advertising, games and leisure services. The early research on localization using communication systems was initiated by the emergency call regulations for E-911 and E-112 in US and Europe, respectively. Network operators must provide the location information of distress calls within an accuracy of 100 $\mathrm{m}$ for 67% of all calls (300 $\mathrm{m}$ for 95%) [9, 10]. This is required to send rescue units to the right location as an increasing amount of distress calls originate from mobile phones and the callers often do not know their location. The increased usage of the mobile internet contributes to the popularity of information services based on the users' location. These services provide information such as the nearest pharmacy, restaurant, and other points of interest including a certain rating or ranking by other users. "Ingress" is one very popular example of games using location based services. This game is an augmented-reality massive-multiplayer online game where virtual portals at real world locations need to be captured.

The above few examples of location based services stress the importance of these services for network operators and users. However, one question remains: How do we obtain the location for these services? Nowadays, so-called smart and feature phones have in-built receivers for global navigation satellite systems (GNSSs). These systems can be used outdoors with clear view to the sky (satellites). However, they fail in dense city centers with high-rise buildings or indoors. In addition, localization should be possible with unsophisticated devices, e.g. wireless sensors, and not only with smart phones.

Terrestrial wireless communication systems are considered to assist GNSSs outdoors or complement them in indoor environments. Radio localization techniques which rely on terrestrial communication systems utilize location dependent features of the radio channel. The location dependent features are extracted from the received signal $y(t)$ by knowing partly or entirely the transmitted signal $x(t)$ and utilizing an appropriate radio channel model. Thus the radio channel model is used to infer the location of either transmitter or receiver units. The location is inferred typically from models that are analytically simple and often empirically obtained, e.g. the one-slope path loss model [11].

Radio channel models are used to evaluate the performance of location estimation algorithms too. The evaluation of the localization algorithms requires often the simulation of very specific scenarios and environments. For this purpose radio channel models should accurately reflect the scenarios and environments. Ray-tracing channel models allow for accurate descriptions of the environments, the placement of transmitters and receivers, the movement of people or objects. With these descriptions, location dependent features are simulated with a ray-tracing model. This makes ray-tracing models very suitable for evaluation of localization algorithms.

### *Radio Localization Methods and Location Dependent Parameters*

Radio localization methods use location dependent features/parameters such as estimates of the arrival/departure angles [11] (triangulation) or distance based location dependent features such as time of arrival [12, 13] or received signal strength [14, 15] (trilateration) to infer the location. Time of arrival localization requires a very accurate synchronization between the transmitters and the receivers. To circumvent the synchronization one may use time difference of arrival methods [11]. Details on different localization methods can be found for instance in [11, 13, 16]. The directional and time of arrival/time difference of arrival methods rely on a proper detection of the line of sight component within the impulse response of the channel. Different methods are proposed to realize this detection [11, 13], but it is, however, a difficult task and the solutions are error prone.

Alternative localization techniques are for instance fingerprinting methods. These methods are based on pattern matching techniques of fingerprints. Fingerprints are location based parameters [11, 17] sampled at a specific grid in the considered environment and stored thereafter. This is done in an "off-line" phase prior to any active localization. In the "on-line" phase, fingerprints obtained from an active user are matched to the ones in the database in order to obtain an estimate of the location. The fingerprinting technique potentially does not suffer from non-line of sight conditions. However, difficulties occur when the environment changes (replacing or moving furniture), the devices used in the off-line phase and on-line phase differ, or when the devices are differently operated, i.e. differently held, rotated or shadowed by the human body.

### *Models of Location Dependent Features of the Radio Channel*

Radio channel models developed for communication purpose can often be used for localization too. However, their original purpose is different and they need to be carefully selected or modified for localization. As already mentioned path loss models developed for communication purpose can be directly reused for localization purpose. Typically the path loss models are used to infer the distance between transmitter and receiver from received signal strength observations [11]. Impulse response models from communications may be used in both the development and testing phases of localization algorithms. However, in communications the power of the impulse responses is normalized and the reference delay (origin) is selected to coincide with the onset delay of the impulse response. These transformations remove the distance information potentially exploitable for localization. Thus in order to use impulse response models from communications all distance dependent information needs to be re-inserted.

## *1.3 Focus of the Thesis*

This thesis focuses on indoor channel modeling. More specifically, we consider in-room radio channels for radio communications and localization. The single room scenario is considered as a basic element for modeling entire buildings. It was experimentally observed that in-room channels include diffuse components [18–23] which affect characteristics of the channel, e.g. the received signal strength, the dispersion in delay, the capacity, etc., important for communications and localization. For in-room scenarios it is conjectured that the diffuse component is caused by reverberation effects.

We use theoretical results from electromagnetic fields in cavities and reverberation models from room acoustics to explain empirical observations of the diffuse component, its relation to the room geometry and conduct an experimental validation of these theoretical models. Furthermore, we propose a distance dependent characterization of the reverberant channel with focus on the delay dispersion. Such a characterization is crucial for radio communications and localization.

## *1.4 Structure of the Thesis*

In this chapter we present a general introduction to radio channel modeling and its purposes in communication and localization. We motivate our focus on modeling the reverberant radio channel.

The remainder of the thesis is organized as follows:

*Chapter 2* provides an introduction to radio channel models. We introduce the terminology and the notation used in radio channel modeling.

*Chapter 3* provides an overview of experimental observations and empirical evidence on the diffuse component to stress its importance. We present interpretations of the effects leading to the diffuse component and the state of the art in reverberant channel modeling.

*Chapter 4* introduces research questions to be answered in Chapter 5 and in Papers A-G. Furthermore this Chapter discusses and presents our research methods applied in Papers A-G and outlines some applications of the proposed reverberant channel models in Papers A-G.

*Chapter 5* summarizes, discusses, and presents the main results of the proposed models in Papers A-G.

*Chapter 6* presents our conclusions and gives an outlook for future investigations.

*Papers A-G* contains the contributions consisting of peer-reviewed conference and journal articles. The articles are reformatted in the style of the thesis. The wording and notation was kept as in the original published versions.

Chapter 2

# Preliminaries in Radio Channel Modeling

In this Chapter we aim to familiarize the reader with some of the radio channel modeling terminology, concepts and basic models. We detail our previous definition of radio channel modeling in Chapter 1 as a LTI system. As already stated a LTI system is entirely characterized by its impulse response or equivalently by its frequency response, see Fig. 2.2. Note that we obtain the system's impulse response as the system output $y(t)$ upon setting $x(t)$ equal a Dirac delta function. In experimental investigations this can be done by sending a Dirac delta like pulse. Practical systems are bandlimited and thus a pulse with a finite width will be transmitted. Alternatively one may consider to measure the frequency response and apply the inverse Fourier transform to obtain the impulse response.

As illustrated in Fig. 2.1, the transmitted signal typically reaches the receiver via multiple propagation paths. This is denoted also as multipath propagation. By linearity we obtain at the receiver multiple copies of the transmitted signal time shifted by the propagation time $\tau_n$ and weighted with a complex gain $a_n$

$$y(t) = x(t) * h(t) = \sum_{n=1}^{N} a_n x(t - \tau_n). \tag{2.1}$$

Setting the input signal $x(t)$ equal the Dirac delta function $\delta(\,\cdot\,)$, we obtain

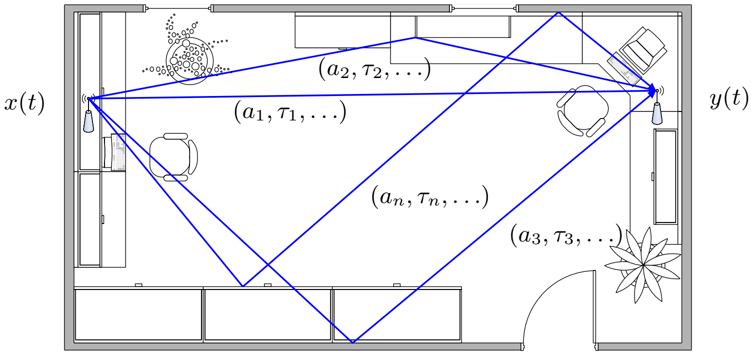

*Fig. 2.1: Sketch of multipath propagation of radio waves in an office.*

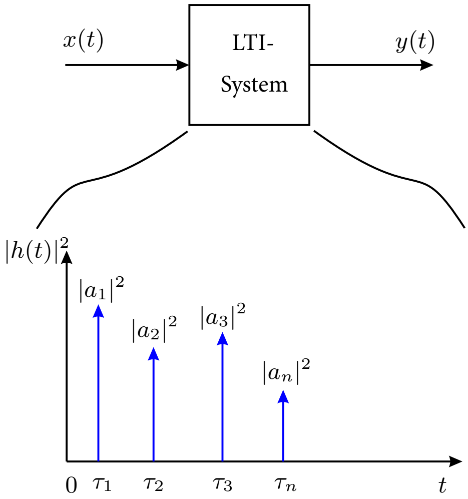

*Fig. 2.2: Sketch of the channel as a linear time-invariant system with the squared magnitude of the system's impulse response.*

the impulse response as

$$h(t) = \sum_{n=1}^{N} a_n \delta(t - \tau_n). \tag{2.2}$$

The number $N$ of path components may be large, possibly infinite. A graphical representation of the impulse response is shown in Fig. 2.2.

So far we used the LTI system to characterize the channel for a static environment. If we consider for a moment the environment sketched in Fig. 2.1, we see that the delay, of one of the sketched propagation paths, depends on the distance from transmitter to receiver via an interaction point. Thus the delay is location dependent. The magnitude of the complex gain exhibits typically only small variations with location; however the phase, depending on the wavelength, changes rapidly with location. Thus the channel impulse response of the radio channel is location dependent.

A time dependent characterization of the impulse response can be obtained by considering a certain movement model. Depending on the used carrier frequency, the moving velocity and the chosen modeling approach we need to extend the time-invariant model of the impulse response to include additional phase rotations of the complex gains due to the Doppler effect. We refer the interested reader to [2, 3, 24–26] for details on time dependent models and the inclusion of the Doppler effect.

## 2.1 Path Loss or Path Gain Models

Path loss models are used to characterize the average received signal strength with respect to distance $d$ between the transmitter and the receiver. The inverse of the path loss is the path gain. The free space path loss model is one of the most well-known models. In this model the transmit and receive antennas are considered in free space without surrounding objects. In this case the received power in the far field of the transmit antenna decays with distance $d$ as (Friis equation) [27]:

$$P_R(d) = P_T\, G_T\, G_R \left(\frac{\lambda}{4\,\pi\, d}\right)^2, \tag{2.3}$$

where $P_T$ and $P_R$ are the transmit and receive power, respectively. The transmit and receive antenna gains are $G_T$ and $G_R$ and the wavelength is obtained as $\lambda = c/f$ where $c$ is the speed of light and $f$ the considered frequency. For such a free space situation the impulse response consists only of a single component with delay $\tau_1 = d/c$ and the weight satisfying $|a_1|^2 = (\frac{\lambda}{4\,\pi\, d})^2$. In channel modeling it is common to exclude the antenna gains from the parameters of the channel. The characteristics of the antennas are considered as design parameters of the communication systems.

In the following we describe indoor path loss models in more realistic indoor scenarios, see Fig. 2.1, where objects such as walls, furniture, etc., surround the transmit and receive antennas. We remark that, the path loss is given as $L(d) = P_T\, G_T\, G_R/P_R(d)$. The indoor path loss models take into account the interactions of the electromagnetic waves with the environment and are typically obtained from empirical observations. The one-slope model [28] describes the average path loss versus distance in dB as

$$L(d) = L_0 + 10\, n\, \log(d), \tag{2.4}$$

where $L_0$ is the path loss in dB at the reference distance of $1\,\mathrm{m}$ and $n$ is the path loss exponent. The one-slope model and Friis equation without the antenna gains are equal for $n = 2$ and $L_0 = 20\, \log(\frac{4\,\pi}{\lambda})$. Pathloss exponents $n < 2$ have been observed in environments with wave guiding effects such as tunnels. Empirical observations show that wall penetrations lead to path loss exponents $n > 2$ when considering entire buildings or floors. Other investigations extend the one-slope model by taking into account wall and floor penetrations. Such models are for instance the Motley-Keenan model [29, 30], the partition loss models reported in [31] or the multiwall model [28]. These empirical models are similar to (2.4) except that they include additional terms. As an example the multiwall model [28] reads

$$L(d) = L_0 + 10\, n\, \log(d) + \sum_{i=1}^{I} k_{\mathrm{w},i}\, L_{\mathrm{w},i} + k_{\mathrm{f}}^{\frac{k_{\mathrm{f}}+2}{k_{\mathrm{f}}+1} - b}\, L_{\mathrm{F}}. \tag{2.5}$$

The additional terms in (2.5) take into account the penetration of $k_{\mathrm{w},i}$ walls of type $i$ and with respective wall attenuation $L_{\mathrm{w},i}$. The last term considers the nonlinear attenuation by penetration of floors with attenuation $L_{\mathrm{F}}$, the number $k_{\mathrm{f}}$ of floors and the empirical parameter $b$. Empirical values for different wall and floor attenuations can be found for instance in [28, 31].

Ray-tracing [2, 3, 32, 33] provides an alternative to the above empirical models to predict the path loss. However, these models typically need a very detailed description of the environment, including wall materials, furniture placement and so forth. Thus a large number of parameters need to be specified which makes the ray-tracing models laborious. We refer the reader to [2, 3] and references therein for details on ray-tracing models.

## 2.2 Shadow Fading

If the transmitter or receiver moves over several meters, for instance moves outside of a room or turns a corner in a hallway, the propagation conditions may change drastically. New propagation paths may occur or some may disappear. This appearance/disappearence of paths causes fluctuations of the received signal strength. This effect is called large scale or shadow fading. A typical empirical model for the shadow fading is a log-normal random process characterized by a certain (distance) correlation function. For details on these models we refer the reader to [2, 3, 24, 28, 31].

## 2.3 Narrowband and Wideband Channel Characterization

For the purpose of radio channel modeling we may distinguish between a characterization of the radio channel with narrowband or wideband sounding signals. The definition of narrow- or wideband sounding signals is related to the delay dispersion of the radio channel. A narrowband sounding signal has in the time domain a “large” pulse width in relation to the maximum excess delay of the channel. The maximum excess delay is the delay difference between the latest and earliest components in the channel impulse response. Considering the signal model (2.1) in the narrowband case, a weighted pulse possibly slightly widened will be obtained. This widening is negligible with respect to the pulse width. As a result $y(t)$ is a weighted and delayed version of $x(t)$. For a wideband sounding signal the pulse width is small and in the range of or even below the maximum excess delay. Referring to the signal model (2.1) the received signal will consist of multiple copies of differently weighted and time shifted pulses.

The delay dispersion of the radio channel is crucial in a wideband communication system. The delayed versions of the transmit signal are strongly shifted relative to each other and their superposition leads to strong distor-

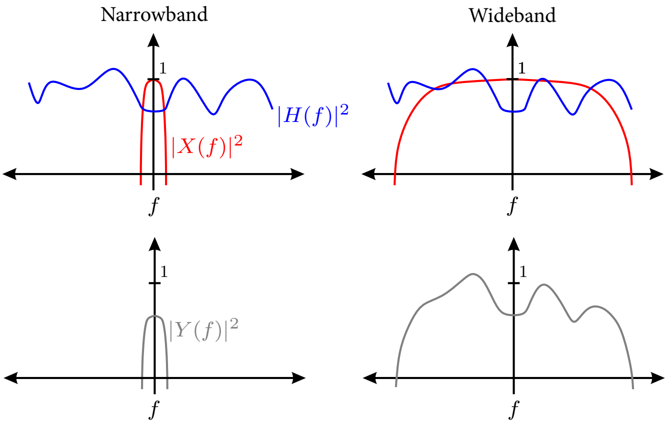

*Fig. 2.3: Effect of the radio channel on narrowband and wideband communication signals. For a narrowband system, the received signal is merely a scaled version of the transmitted signal. For a wideband system, the channel transfer function affects selectively the spectral components of the transmitted signal.*

tions in the received signal. This effect is called inter-symbol interference (ISI) in communications. For wideband communication systems the delay dispersion of the radio channel needs to be modeled appropriately. The effect of the radio channel on narrowband and wideband communication systems is depicted in Fig. 2.3 in the frequency domain. In the narrowband case, the received signal $Y(f)$ is only a scaled version of the transmitted signal $X(f)$. Contrary, in the wideband case the channel has a frequency selective affect on the transmitted signal $X(f)$.

### *Narrowband Fading*

For a narrowband system the delay dispersion is negligible. Following the principle of parsimony[1], we may simplify the channel impulse response to a single component with its weight obtained as the sum of the complex weights of all components. The received signal for this case reads

$$y(t) = x(t-\tau)\sum_{n=1}^{N} a_n. \tag{2.6}$$

The sum of the weights $a_n$ adds up constructively or destructively depending on their respective arguments. In the literature this effect is often called small scale fading, short term fading or even fast fading [24]. This fading process may create a variation of the received power up to 40 dB. Typical fading models of the magnitude of the complex sum in (2.6) are Rayleigh and Rician fading [2, 3, 24]. Rician fading is proposed for impulse responses with one strong dominat component. This component is often associated with the contribution from the directly propagating path. We call this a radio channel in line of sight (LOS) condition. For a channel in LOS condition the fading is typically not so severe. The Rician fading is characterized with the K-factor. The K-factor is defined as the power ratio of the dominating component and all remaining components.

---

[1] The principle of parsimony is also known as Occam's razor [34].

If the channel is in non-line of sight condition, meaning there is no dominating pulse, Rayleigh fading applies. Many other fading models with different fading statistics have been proposed, see for instance [2, 3, 24].

### *Delay Dispersion of the Radio Channel*

The delay dispersion is important in wideband communication systems as it determines the severity of inter-symbol interference. We characterize the delay dispersion with the delay power spectrum, which is obtained as the expectation of the squared magnitude of the impulse response:

$$G(\tau) = \mathrm{E}[|h(\tau)|^2]. \tag{2.7}$$

The expectation operator represents the mathematical abstraction of an averaging procedure to suppress variations due to small and possibly large scale fading. The delay power spectra are obtained empirically by averaging the squared magnitude of impulse responses measured at different transmitter and receiver locations. The delay power spectrum can be used in stochastic impulse response models to characterize the second order moment of path weights conditioned on delay and some appropriate arrival rate of components [35]. One of the most important parameters in radio communications that characterizes the delay dispersion is the second order moment of the delay power spectrum. This moment is also known as the root mean squared (rms) delay spread $\sigma_\mathcal{T}$. To obtain the rms delay spread we first derive the average path gain and mean delay (first order moment)

$$G = \int G(\tau)\,\mathrm{d}\tau, \tag{2.8}$$

$$\mu_\mathcal{T} = \frac{1}{G}\int \tau\, G(\tau)\,\mathrm{d}\tau, \tag{2.9}$$

respectively. Therefrom we obtain the rms delay spread as

$$\sigma_\mathcal{T} = \sqrt{\frac{1}{G}\int \tau^2\, G(\tau)\,\mathrm{d}\tau - \mu_\mathcal{T}^2}. \tag{2.10}$$

Similarly, higher order centered moments of $n$th order are obtained as

$$\sigma_\tau^n = \frac{1}{G} \int \tau^n \, G(\tau) \, \mathrm{d}\tau - \mu_\tau^n. \tag{2.11}$$

The rms delay spread is related to the coherence bandwidth [36]. The coherence bandwidth is an important design parameter affecting the design of communication systems, e.g. for systems using orthogonal frequency-division multiplexing (OFDM). OFDM systems encode the data on multiple carrier frequencies. Details on OFDM communication systems can be found for instance in [2, 3]. The coherence bandwidth is the least frequency difference for which the frequency correlation function, estimated from the channel transfer function, is below some defined threshold. A typical threshold is 0.5. For this setting the relationship between coherence bandwidth and rms delay spread is [36] given by

$$B_\mathrm{c} \gtrsim \frac{1}{2\,\pi\,\sigma_\tau}. \tag{2.12}$$

So far we discussed the dispersion in the delay domain. However, as illustrated in Fig. 2.1, signals arrive from different directions too. The characterization of the dispersion in the directional domain is important for multi antenna systems. Similarly, we can define the angular power spectrum and its respective moments. Other dispersion domains and their respective spectra exist, for instance the Doppler power spectrum. Joint power spectra, for instance the angle-delay power spectrum, are common too. For details on the characterization of dispersion in these domains we refer the interested reader to [2, 3, 24–26, 31].

Chapter 3

# The Reverberant Channel

In this Chapter we provide an overview of observations of the diffuse component in form of measurements and empirical evidence. The aim of this overview of observations is to stress the importance of modeling the diffuse component. Furthermore, we present interpretations of the effects leading to a diffuse component. These interpretations aim at providing an intuition of what is the diffuse component and how it is connected to reverberation. Thereafter, we present a summary of the state of the art on modeling of the reverberant channel. In the state of the art we distinguish between white-box and black-box models. White-box models rely on a priori information on the propagation mechanisms from physics, which are used to describe the mathematical functions of the model. White-box models are therefore able to make site-specific simulations and predictions. The black-box models are derived from experimental observations and replicate typically only the statistical properties of the observations. The functional description is built upon the data of observations. Although the observations may have physical interpretations, these interpretations are not considered in the formulation of the model. Simulations of the black-box models are conducted for a range of so-called "typical" environments. The simulations follow the statistics of previous observation in such typical environments. Note that practically all models are somewhere between these white- and black-box definitions. In the state of the art we, however, chose to group the models into these two extreme categories.

## 3.1 Observations Related to the Diffuse Component

It was observed by comparison of e.g. out- and indoor ray-tracing simulations with experimental data, that specular reflections and diffraction upon buildings, walls and other objects are not sufficient to entirely characterize the dispersion of the radio channel [37–42]. There could be numerous explanations for the cause of these observations. Diffuse reflection (scattering), caused by rough surfaces or within the material structure, is proposed to improve the modeling of the dispersion in ray-tracing [37–42]. Please note that we do not consider a single diffuse reflection as a diffuse component. However, there may be a large number of components originating from diffuse reflections which together represent one or multiple diffuse components.

Experimental delay power spectra reported for an in-room scenario in [18] are obtained from ultra wideband radio channel measurements. The delay power spectra obtained from local spatial averages exhibit a transition in delay from early specular and well separated components towards a diffuse tail. We term this observed diffusion process the avalanche effect. A simulated example of the avalanche effect can be seen in Fig. 3.1b. In the range up to 30 $\mathrm{ns}$, well separated components are visible. With increasing delay the intensity of occurrence of the components increases and they become non-separable.

Other observations from experimental data indicate that high-resolution path parameter estimation algorithms are not able to represent the radio channel fully when relying on a specular component model like (2.2). A vast amount of specular parameters need to be extracted to capture a sufficient amount of power. For instance in [43] parameters of 3000 specular components were estimated from data collected in a small macrocell. These components capture approximately 70% of the total power. It is unclear if these components are all estimates of true propagation paths or if they are artifacts caused by calibration and estimation errors. Using the specular components estimated with high resolution algorithms to reconstruct the radio channel and compare the reconstruction with the original measured channel indicates that important parameters, such as total received power, rms delay spread, capacity, etc., are not appropriately modeled/reconstructed [19–23]. The characteristics of received power, delay spread and capacity are of great importance for radio communications and localization. An alternative modeling approach for high-resolution parameter estimation considers not only specular components but diffuse components [44, 45] too. The diffuse components are dispersive in delay and angular domain.

In indoor radio channel modeling, more precisely in-room scenarios, it is conjectured that reverberation causes the diffuse component(s). The impact of reverberation on the performance of wireless local area networks in large conference rooms is investigated in [46–49]. The authors discuss the effect of reverberation on coverage problems, power consumption and data throughput for these networks in single and multi antenna scenarios. Similarly, localization with communication systems is influenced by reverberation [50, 51]. So, modeling the reverberation effects is of importance.

In short, the reported observations indicate that a specular channel representation with just a few specular components is not sufficient. A diffuse component is present in the channel and its characterization is of importance.

## 3.2 Interpretations of the Diffuse Component

One interpretation for the diffuse components may be as follows [44]: The equipment used to communicate over the radio channel has limited resolution in delay and direction, due to the considered bandwidth, the used antenna arrays, etc. If multiple specular components are within this resolution they cannot be separated. This leads to what is often considered as diffuse components in radio communications [44]. Although this interpretation is practical it, however, does not provide any physical explanation on how and why components are closely spaced. Neither does it provide functional descriptions for the delay and/or angular dispersion.

We visualize this interpretation by means of simulations in Fig. 3.1. The simulation considers specular wall reflections in 2D in Fig. 3.1a for transmitter positions along a certain track. A bandwidth of 4.8 GHz allows to trace all signal components up to the first 75 ns of the impulse response. If the simulation is extended to the 3D case, meaning that specular reflections from the ceiling and the floor are included, components are becoming denser in delay, see Fig. 3.1b. Up to the first 30 ns we can separate the components. In the later part only a mixture of components is visible. Knowing traces from Fig. 3.1a we may still see patterns of these traces in Fig. 3.1b for delays above 30 ns. For a smaller bandwidth of only 120 MHz we cannot separate components or see traces of them, see Fig. 3.1d. If we apply a high resolution algorithm on such data to estimate specular components, the algorithm will return specular components, however these are just a fit to the response and are most likely not related to specific single components of the simulations. We remark that, by using models which include the directional dependency at transmitter and receiver we may separate more components due to the additional degrees of freedom.

In in-room environments the observed diffuse component is associated with reverberation. Theoretical models which consider reverberation exist in acoustics [52–54] and in electromagnetics for special rooms such as reverberation chambers [55, 56]. The models originate from wave theory in acoustics or electromagnetics, respectively. Both models from acoustics and electromagnetics predict the diffuse component and allow to characterize it in the delay domain based on the room geometry. In the following we call the diffuse component as well the reverberant component. Further details on these models can be found in Section 3.3. Although these models exist investigations are needed to

- validate that these theoretical models apply as well for electromagnetics in typical home and office environments and
- find out how to make use of these models for communication and localization.

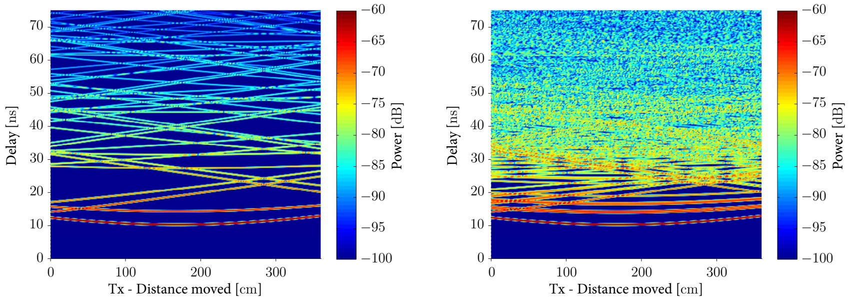

(a) 2D simulation with 4.8 GHz bandwidth (b) 3D simulation with 4.8 GHz bandwidth

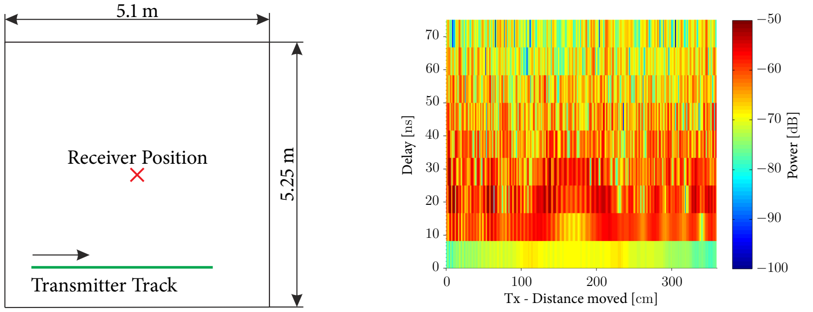

(c) (d) 3D simulation with 120 MHz bandwidth

*Fig. 3.1: Simulation of the impulse response versus transmitter displacement in the scenario shown in (c) with room height* 2.78 m. *The responses are generated with a ray-tracing model using the mirror source method. The simulations are conducted for a center frequency of 5.2* GHz *and bandwidth of 4.8* GHz *in (a) and (b) and 120* MHz *in (d). The results for 2D simulations are shown in (a) and for 3D in (b) and (d). The reflection coefficient upon a wall interaction was set to* $\approx \sqrt{0.6}$ *for all simulations. For practical reasons we added an additional delay offset of 3.86* ns *to the impulse responses onset to make the simulations comparable to our measurements. The channel transfer functions are filtered with a Hann window to suppress sidelobes in the time domain.*

## 3.3 White-box Models for Reverberant Channels

White-box models replicate the physical propagation mechanisms. Models of electromagnetic fields in cavities and reverberation models in acoustics are based on the same assumption. They assume that only a single source located inside the room generates the electromagnetic or acoustic field. The white-box models allow to characterize the reverberant component of the delay power spectrum $G_{\mathrm{rev}}(d, \tau)$, see Fig. 3.2. More specifically, a functional description of the power decay versus delay and the decay rate is derived by using results from theory of electromagnetic (or acoustic) fields. This is done in an average sense for an entire room. Ray-tracing and radiosity models allow to simulate delay power spectra for specific room geometries and wall materials. Thereby, they characterize the avalanche effect, the diffuse component and the early part in the delay power spectrum according to the specific room geometry.

### Electromagnetic Fields in Cavities

The theory of electromagnetic fields in cavities originates from electromagnetic capability (EMC) testing. Electromagnetic capability tests are done for instance in so-called reverberation chambers. Reverberation chambers reproduce the reverberation effect to generate with low input powers high electromagnetic field strengths. The diffuse electromagnetic fields, generated in the reverberation chambers, allows for susceptibility/vulnerability tests of devices without the need of rotating the devices under test.

A well established theory of electromagnetic fields in reverberation chambers is available [55, 56]. The theory builds upon Maxwell's equations to derive the electromagnetic field in the empty chamber. We may consider the reverberation chamber as a cavity resonator. In this cavity resonator, standing waves occur with eigenfrequencies depending on the room dimensions. For these eigenfrequencies we can obtain the respective transversal electric and magnetic eigenmodes. Rectangular room shapes allow for the derivation of closed form expressions of the eigenmodes and their respective eigenfrequencies. Reverberation chambers are characterized by their quality factor $Q$. The quality factor of an eigenmode is defined as the product of the eigenfrequency and the ratio of the eigenmode's total stored energy in the chamber and the absorbed power on the walls. The absorbed power depends on the wall materials. To obtain large $Q$ factors typically the walls are made of highly conductive materials, such as copper, etc. For a multimode excitation of the reverberation chamber and an arbitrary room shape an approximation of $Q$ is [55]

$$Q \approx \frac{3\,V}{2\,\delta\,S}, \tag{3.1}$$

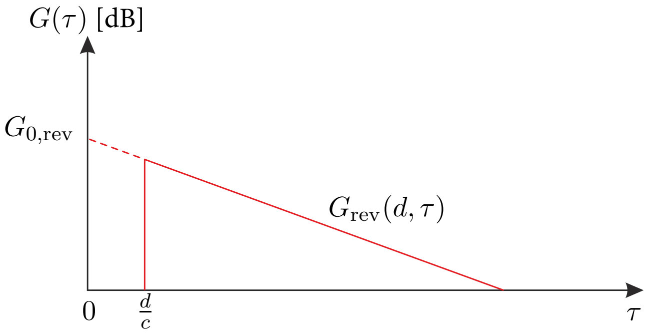

*Fig. 3.2: The reverberant component of the delay power spectrum.*

where $\delta$ is the skin depth of the conducting wall material, $V$ and $S$ are the volume and surface of the room, respectively. An excitation of the chamber leads to an inhomogeneous field distribution due to the standing waves. In order to create a homogenous field throughout the chamber a mode "stirrer" is inserted in the chamber. By stepping or continuous movement of the stirrer a part of the chamber changes leading to varying eigenmodes in the chamber and thus creates a diffuse field in the chamber.

For the purpose of radio channel modeling we would like to obtain an expression for the delay power spectrum observed in a reverberation chamber. For the derivation of the delay power spectrum we consider the decay of the energy in the chamber upon stopping the excitation of the chamber. When the excitation is stopped, the energy in the chamber will decay due to the wall losses. It can be shown that the energy in the chamber decays exponentially with a chamber decay time given as [55]

$$T_{\mathrm{RC}} = \frac{Q}{2\,\pi\,f}. \tag{3.2}$$

Similar to the energy, the delay power spectrum decays exponentially with the chamber decay time $T_{\mathrm{RC}}$ and reads

$$G_{\mathrm{rev}}(d,\tau) = \begin{cases} G_{0,\mathrm{rev}}\, e^{\frac{-\tau}{T_{\mathrm{RC}}}} & \tau > d/c, \\ 0 & \text{elsewhere.} \end{cases} \tag{3.3}$$

We remark that, the reference gain $G_{0,\mathrm{rev}}$ depends on the antenna gains and $Q$. However, $G_{0,\mathrm{rev}}$ does not depend on the transmitter-receiver distance $d$. This means that regardless of transmitter and receiver positions in the reverberation chamber we observe for various $d$:

- delay power spectra with an exponential decay and the same decay time,

- for all $d$ the delay power spectra coincide, and
- only the onset of the delay power spectrum depends on $d$, as described in (3.3).

For details on $G_{0,\mathrm{rev}}$, we refer to [55]. Note that inserting (3.3) into (2.10) leads to $\sigma_\tau = T_{\mathrm{RC}}$ [57].

Recently, reverberation chambers have been utilized also to emulate radio channels for over-the-air device testing [57–60]. For radio channel emulation, [57] establishes the relation between various parameters relevant to radio communication to parameters specific to reverberation chambers. For instance, the radio communication parameters rms delay spread and coherence bandwidth are related to decay time and quality of the reverberation chamber. Of particular importance is the behavior of the delay power spectrum versus delay, when the chamber is “loaded” with absorbers. The absorbers are used to reduce $Q$ and thus $T_{\mathrm{RC}}$ for emulating radio channels in over-the-air device testing. The behavior of the delay power spectrum is modeled as a double exponential model. One exponential accounts for the early delay behavior and the other for the late tail caused by reverberation.

The theory of reverberation chambers is applied in radio channel modeling for communications to model propagation effects in cars [61–63] and airplanes [64, 65]. Ships and pre-engineered buildings [65] were investigated for EMC testing capabilities. These environments may be classified as “moderately” reverberant [65] and resemble in their characteristics well the metal clad reverberation chambers with the exception of the missing stirrer. The investigated pre-engineered building in [65] has aluminium walls and a steel structure. Storage shelves were distributed in one half of the building. The experimental observations in [65] indicate the presence of reverberation in the building. The experimental delay power spectra, observed at different carrier frequencies, showed clearly exponentially decaying tails, except at one specific carrier frequency. At the carrier frequency of approximately 400 MHz was the tail non-exponential. This phenomenon could not be explained in [65]. A possible explanation may be found in [66], where it is shown that at low frequencies the antenna losses can not be neglected. The author in [65] reports that the observed field was non-isotropic in direction, which differs from the “ideal” reverberation chambers. So far it is unclear how well the theory of reverberation chambers works for “typical” buildings with small values of $Q$.

### *Acoustic Reverberation Models*

The research on the acoustical reverberation phenomenon was pioneered by the work of Sabine [52] in the early 20th century. This work focused on the perception of sound in concert halls and auditoria. One objective was to understand why in some auditoria the spoken word was not recognizable. Sabine concluded that reverberation, namely the persistence of sound in the room, was responsible for the perception of the voice and music. The reverberation was characterized by the reverberation time, i.e. the decay rate of the delay power spectrum. Thus research in acoustics was devoted to models characterizing the delay power spectrum based on the room geometry and the absorbtion coefficients of walls, furniture, audience, etc.

Acoustic reverberation has been developed before electromagnetic reverberation. The later has been inspired by the former. Rooms can be analyzed with wave theory [54] leading to a similar discussion of eigenmodes as previously for electromagnetic fields in cavities. The decoration, interior, audience, etc., in concert halls act similarly as the stirrer in the electromagnetic reverberation chambers to obtain an acoustic reverberant field. As in the theory of electromagnetic fields in cavities, after stopping the acoustical excitation of the room, the energy of the diffuse field decays exponentially due to the losses on walls, interior, etc. We obtain from this exponential energy decay a distance dependent model of the delay power spectrum as in (3.3). The model exhibits a tail which decays exponentially versus delay. The tail of the delay power spectrum coincides for different transmitter-receiver distances. Only the onset of the tail depends on the transmitter-receiver distance. In acoustics the exponential decay rate is called reverberation time $T$ [52, 54].

Over the past century several models of the reverberation time [52–54] have been proposed. These models use simple relations between the average absorption coefficient, the surface and the volume of the considered room to predict the reverberation time and thus the decay rate of the exponentially decaying tail of the delay power spectrum. Two well-known models have been proposed, one by Sabine [52] and one by Eyring [53] :

$$T = \begin{cases} \frac{4\,V}{c\,S\,\bar{a}}, & \text{Sabine,} \\ \frac{-4\,V}{c\,S\,\ln(1-\bar{a})}, & \text{Eyring.} \end{cases} \tag{3.4}$$

The average wall absorption coefficient is denoted $\bar{a}$ and $c$ is the speed of sound in acoustics and the speed of light in electromagnetics. Sabine's model is derived based on the assumptions of a diffuse field inside the room and power absorbtion occurs on the room surfaces. Eyring developed his model based on the mirror theory and did not a priori assume a diffuse field. For more details on Sabine's and Eyring's models we refer to [52–54] or the short review in Paper C.

If we use, as did Eyring, the mirror theory model we can simulate delay power spectra. The simulated spectra obtained from local spatial averages exhibit the avalanche effect[1]. The avalanche effect was empirically observed for instance in ultra wideband radio channel measurements in typical indoor environments [18]. The previously mentioned double exponential model of the delay power spectrum in reverberation chambers [57] is related to the avalanche effect.

---

[1] The avalanche effect is the afore mentioned transition from early specular components to a late reverberant tail.

Sabine's and Eyring's models were transcribed from acoustics to electromagnetics for the characterization of the delay power spectrum [55, 67–71] of reverberant in-room channels. The transcribed models fit well the experimental observations. However, it is not apparent that the analogy between acoustics and electromagnetics is valid. The wall absorption coefficients for radio waves are different and the waves propagate more easily through walls in comparison to the acoustic waves. Radio waves may even reenter the room, thus the assumption of a single source exciting the the room is void. As such it is not clear if the reverberation is determined by a single room or by the outer structure of the building. As an example, [69, 70] report average absorption coefficients. These coefficients are estimated from observations of the reverberation times using Sabine's model. Thus the reported absorption coefficients depend on what the authors believed to be the "right" surface area and volume. A validation of the choice of surface area and volume, e.g. from the single room or entire building, is required for Sabine's and Eyring's models.

### *Ray-tracing Models*

Sofar the presented white-box models of electromagnetic fields in cavities and room acoustics allow to characterize the delay power spectrum in an average sense for an entire room. Ray-tracing and radiosity models are applicable for a location specific characterization. These models simulate the avalanche effect according to the characteristics of the environment.

Delay power spectra which depend on the environment and the transmitter and receiver locations can be simulated with ray-tracing models. In ray-tracing the response of the radio channel is assumed to be comprised of a sum of specular components as in (2.2). These specular components originate from direct propagation, specular and diffuse reflections (scattering on rough surfaces), diffraction, etc. To obtain components that originate from specular reflections, see Fig. 3.3a, the mirror source method [32] can be applied. For a rectangular room, this method allows, with a moderate computational effort, to find the incidence and departure angles on the wall surfaces, the correct distances, and the outgoing and incoming angles at the transmitter and receiver, respectively. The reflection and transmission coefficients upon wall interactions can be found from the dielectric properties of the material and Snell's law [2, 3]. The mirror source method is sketched for a two dimensional case in Fig. 3.3c for four first and four second order reflections. The positions of the mirror sources, corresponding to these reflections, are indicated with

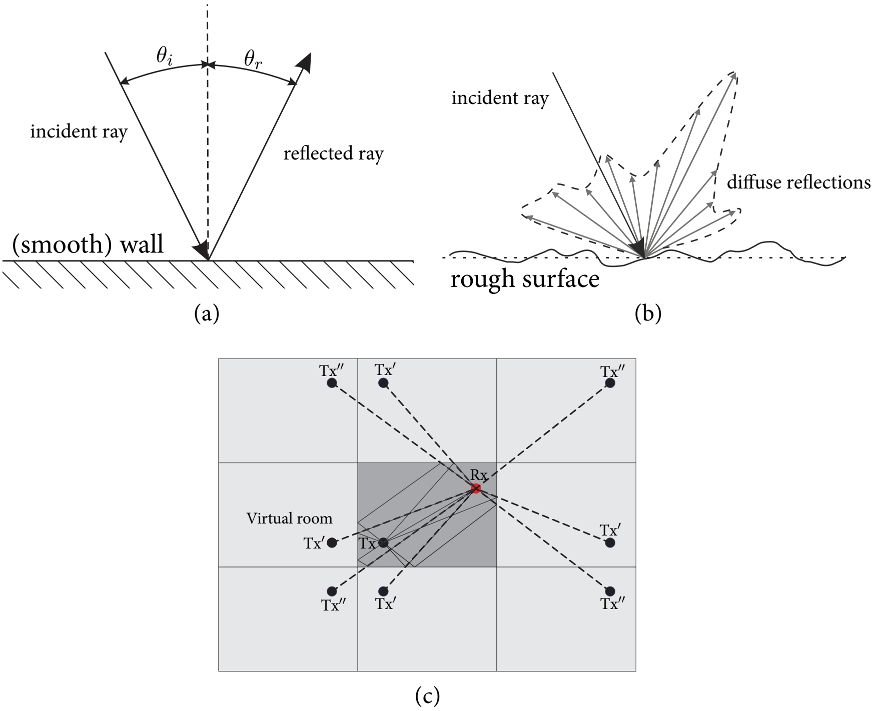

*Fig. 3.3: A specular reflection is shown in (a), while (b) sketches diffuse reflections. (c) illustrates an application of the mirror source method in the 2 dimensional case for a rectangular room. The prime and double prime symbols indicate the positions of virtual transmitters associated with first order and second order reflections, respectively. Note that not all second order reflections are included.*

the prime and double prime symbols. A functional description with a cubic increase, of the approximate number of sources (received components) up to delay $\tau$, is derived [54] for the three dimensional case. The approximate number of components is shown in Fig. 3.4 together with results obtained from the mirror source method with two different receiver positions. For the considered room dimensions, we observe that roughly up to 40 $\mathrm{ns}$ the number of components depends on the position. Above 40 $\mathrm{ns}$ the results are close to the theoretical approximation. At 200 $\mathrm{ns}$ for the dimensions of this office roughly 12000 specular reflected components are generated. Thus the computational complexity of a ray-tracing model is high, e.g. for the purpose of bit error rate simulations.

In [37] indoor measurements of ultra wideband channels indicate that a component originated from a specular reflection is usually accompanied by other specular components. According to Janson [37], these additional specular components originate from diffuse reflections close to the interaction

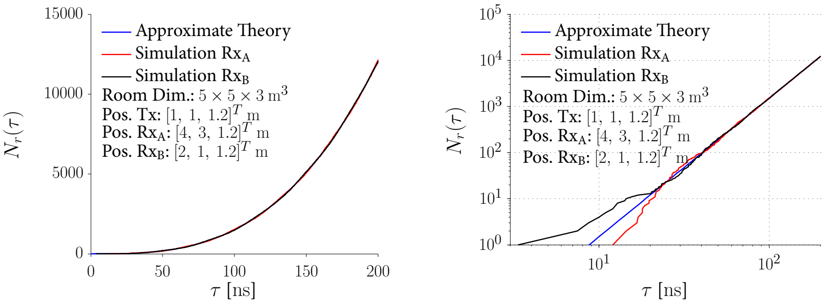

(a) (b)

*Fig. 3.4: The number of components $N_r(\tau)$ up to delay $\tau$ computed with the mirror source method are shown in (a) and (b) as a log-log plot. In (b) we see that for small delays the approximation fails and that the number of arrivals depends on the positions of transmitter and receiver. Roughly above 40* ns *the approximation provides good results for these room dimensions.*

point where the specular reflection takes place. These diffuse reflections are traced back to inhomogeneity, e.g. in the structures of/inside walls or due to cupboards filled with different objects [37]. A graphical representation of a specular reflection and the accompanying specular components from diffuse reflections is shown in Fig. 3.5. Janson proposes to extend the ray-tracing model by placing randomly point scatterers, as shown in Fig. 3.5, around the reflection point of the specular reflection. The propagation paths through each of the point scatterers need to be simulated, which drastically increases the computational effort.

Other proposals considering diffuse reflections in the ray-tracing models split the surface area of walls and objects in the considered environment into patches of a certain size. Components are generated from the center of these patches. The complex weight of these components is calculated based on an effective roughness model [38–42]. As an alternative to discrete patches, [72] proposes a continuous model to describe the distribution of the received power from diffuse reflection on a wall.

Clearly, by including diffuse reflections in ray-tracing models an even larger number of specular components is obtained as in comparison to the mirror source method. As a result, the approximate number of specular components increases even faster than cubic. Diffuse reflections in comparison to specular reflections are weaker in amplitude. However, a large number of these components typically reach the receiver and thus contribute to the delay power spectrum, the total received power, the rms delay spread and capacity of the radio channel. The potentially vast number of components leads to simulations which are computationally very intensive. Thus often the number

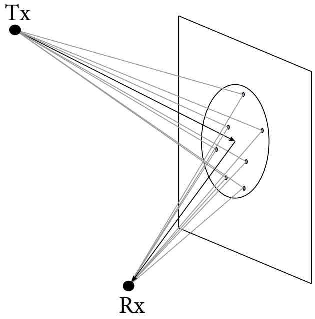

*Fig. 3.5: Geometric interpretation of a dispersive component modeled as a group of specular components. Redrawn from [37].*

of components is limited for instance up to a certain number of wall interactions or only components above a certain threshold are considered. Often the components originating from diffuse reflections are considered weak in comparison to specular reflections. Therefore, components originating from diffuse reflections with higher order interactions are often neglected. This limitation of the number of components, however, influences the simulation results of the delay power spectrum.

### *Radiosity Models*

Radiosity models are an alternative approach to ray-tracing. Radiosity models include higher order diffuse reflections. These models originate from light simulations in computer graphics and are applied in acoustics and in radio propagation simulations, e.g. [73, 74]. Radiosity is well suited for diffuse reflection simulations [73]. Surfaces are split into smaller facets between which a power transfer occurs according to some power density functions. The method is well suited to simulate the avalanche effect of the delay power spectrum. A disadvantage of the method is that it only considers the power transfer and thus no phase nor polarization information is included. However, one main advantage over ray-tracing is the independency of the receiver antenna position. In ray-tracing all rays depend on this position and need to be recalculated for a new position. In radiosity, however, the power transfer between facets can be calculated independently of the receiver position. Thus this method is computationally more efficient when the power distribution over the entire room is of interest, e.g. in coverage analysis [73].

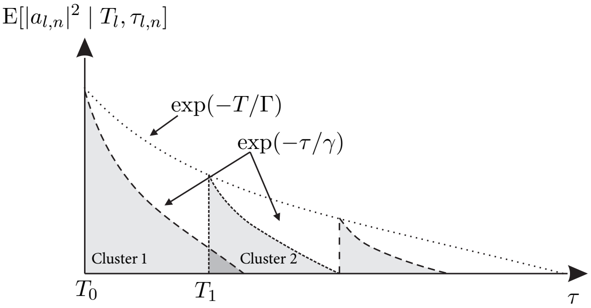

*Fig. 3.6: Conceptual overview of the Saleh and Valenzuela model. The weights of specular components within a cluster decay exponentially with rate $\gamma$. The clusters are weighted exponentially with decay rate $\Gamma$.*

## 3.4 Black-box Models for Reverberant Channels

The black-box models are based on empirical observations only. Parametric functions describing the effect rendered by the observations are postulated for the model. The parameters of these functions are estimated by fitting these functions to measurement data. These parameters are often collected and tabulated for so-called “typical” environments, like office, home, or industrial environments. Black-box models do not allow to make predictions when the characteristics of the environment significantly deviate from those of the environments for which the model was calibrated.

We review only a small selection of models. Our focus is on models which allow to model the avalanche effect or include the diffuse component in some way. Black-box models are of interest in combination with white-box models. We may use white-box models to predict parameters for the black-box models. For instance we predict the decay rate of the delay power spectrum for a certain room geometry and this predicted value is used in a black-box model.

### Stochastic Impulse Response Models for the Avalanche Effect

The well-known Saleh and Valenzuela model [75] originates from measurements of an entire floor. The observations of Saleh and Valenzuela indicate delay power spectra with typically one and occasionally multiple exponentially decaying cluster(s). The additional clusters are associated with late reflections caused by the buildings “hyper” structure, such as for instance a metallic door at the end of a corridor in [75]. The impulse response of the Saleh and Valenzuela model reads

$$h(t) = \sum_{l=0}^{\infty} \sum_{n=0}^{\infty} |a_{l,n}| \exp(j\theta_{l,n}) \cdot \delta(t - T_l - \tau_{l,n}), \tag{3.5}$$

where $|a_{l,n}|$ is the gain of the $n$th path in the $l$th cluster, $\theta_{l,n}$ is its phase. The onset of the $l$th cluster is defined as $T_l$ and the relative delay of the $n$th propagation path within the $l$th cluster is denoted as $\tau_{l,n}$. The first cluster onset $T_0$ corresponds to the direct path from the transmitter to the receiver. The cluster onsets $\{T_1, T_2, \ldots\}$ form a homogenous Poisson process on $[T_0, \infty)$ with arrival rate $\Lambda$. For cluster $l$, the (relative) delays $\{\tau_{l,1}, \tau_{l,2}, \ldots\}$ form another homogenous Poisson process on $[T_l, \infty)$ with arrival rate $\lambda$. The mean squared gain of the first component in cluster $l$ decays exponentially according to $\exp(-T_l/\Gamma)$ with the cluster independent power-decay constant $\Gamma$. The mean squared gain of a multipath component within cluster $l$ decays relatively to the first component according to a second exponential function $\exp(-\tau_{l,n}/\gamma)$ with cluster independent power-decay constant $\gamma$. A graphical representation of the mean squared gains conditioned on $\tau_{l,n}$ and $T_l$ can be seen in Fig. 3.6.

For the proposed parameter settings in the original paper [75] and for typical dynamic ranges in communication systems often only a single cluster with the homogenous path intensity $\lambda$ is generated within the considered delay range. This does not recreate the avalanche effect as predicted by the white-box models in Section 3.3 and observed in ultra wideband measurements [18]. For an example of simulated impulse responses with such a transition see Fig. 3.1b. However, when considering the specular components of all clusters we see that the intensity of the specular components is linearly increasing [76]. Thus this model can simulate impulse responses which exhibit an avalanche effect by adjusting the intensities $\Lambda$ and $\lambda$ of clusters and components and the decay rates $\Gamma$ and $\gamma$ for the weights of clusters and component.

As an alternative to the rather complicated multiple-cluster construction one may apply the model by Turin, et al. in [77] with a non-homogenous Poisson point process for the delays of the multipath components. This was already indicated by Turin in his original work. Thus, Turin's single cluster model could create a specular to diffuse transition.

An alternative approach to model the avalanche effect in ultra wideband channels is proposed in [78]. Specular components up to a certain number of wall interactions are generated with the mirror source model. Clusters are then attached to a selection of these specular components. Thus, the cluster onsets $\{T_1, T_2, \ldots\}$ are generated according to the room geometry using the mirror source method instead of a homogenous Poisson point process as done in the Saleh and Valenzuela model. Another difference is that specular components in a cluster are not created with a point process. Instead, they are equally spaced in delay according to a certain sample grid. We remark that, a large number of stochastic impulse response models exist. For an overview of these models, we refer the reader to [26].

### *Models for Path Parameter Estimation Under the Constraint of Diffuse Components*

The estimation of multipath parameters with high resolution algorithms requires a model of the impulse response which appropriately includes diffuse components. As already mentioned in Section 2 the radio channel sounders have a limited resolution and not all multipath components in the impulse response can be separated. Thus, Richter [44] proposes to model the impulse response as a combination of few well resolvable specular components and one diffuse component corresponding to the many non-resolvable components. Considering only the delay domain, the received signal with such an impulse response model reads:

$$y(t) = \underbrace{\sum_{\ell=1}^{L} a_\ell x(t-\tau_\ell)}_{L \text{ specular components}} + \underbrace{\int_{-\infty}^{\infty} x(\tau')\xi(t-\tau')\mathrm{d}\tau'}_{\text{diffuse component}} + \underbrace{n(t)}_{\text{AWGN}} \,. \tag{3.6}$$

The impulse response has $L$ specular components with weight $a_\ell$ and delay $\tau_\ell$ and a diffuse component $\xi(t)$. For an illustration of the impulse response see Fig. 3.7. The model is considered of the specular components in delay, direction of departure, direction of arrival, Doppler, and polarization domains. For simplicity and clarity we omit this here. In the original work by Richter [44] the power of the diffuse component is assumed to be exponentially decaying versus delay and uniform versus direction. Note that this assumption is in accordance with the definition of the reverberant component obtained from the theoretical results of electromagnetic fields in cavities and room acoustics, see Section 3.3. Later work includes a directional dependency of the diffuse component [45, 79].

Yin proposes in [80] a method for path parameter estimation of diffuse components that considers non-specular components. Wideband experimental investigations [80–84] indicate that non-specular components are dispersive in the delay and directional domains. These non-specular components are modeled with a bi-directional delay power spectral density [80, 85–87]. The space-alternating generalized expectation-maximization (SAGE) algorithm is used to estimate the first and second order moments of these power spectral densities. These moments are required for modeling purposes. For instance Yin's method would allow to estimate the first and second order moments of the bi-directional delay spread of diffuse components similar to the ones proposed in Janson's ray-tracing model [37], see Fig. 3.5.

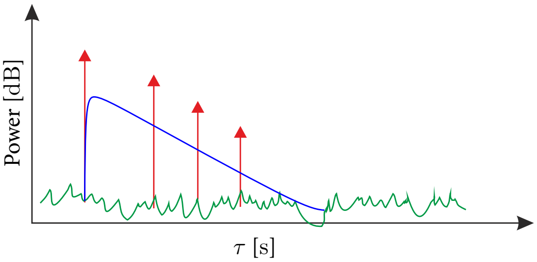

*Fig. 3.7: Illustration of the specular and the diffuse components in the radio channel model by [44].*

### *Geometric Stochastic Channel Models with Diffuse Components*

Geometric stochastic channel models (GSCM) are parameterized with estimation results of high resolution algorithms [88–90]. Thus it is natural that these models are extended to include diffuse components too. Well resolvable specular components with similar delays and angles of departure and arrival are grouped. These groups are sometimes called clusters[2]. We name the clusters containing the well resolvable components specular clusters.

The simulation procedure in GSCMs is as follows: Clusters and point scatterers in the clusters have a spatial interpretation. Clusters are placed randomly according to some "typical" distribution for the considered scenario, e.g. an office indoors or typical urban outdoors. The size of specular clusters is determined by experimental values of bi-directional and delay spreads. Point scatterers are placed randomly in the cluster. Each point scatterer generates a specular component in the channel response. By using ray-tracing we obtain the propagation delays, direction of arrival, etc. of the specular components from the geometry. The gain coefficients of the specular components are adjusted to fit some bi-directional delay power spectrum. A geometric representation of the clusters and point scatterers can be seen in Fig. 3.8.

Several methods have been proposed to include the diffuse components in the GSCMs. One method proposed in [91] models the diffuse components by defining a diffuse cluster around the specular clusters. Point scatterers are placed randomly in the diffuse cluster. Each point scatterer generates a specular component in the impulse response. The specular components originating from the diffuse cluster are treated differently than the ones originating from the specular clusters. In [91], ray-tracing is used only to obtain the angles of the specular components in the diffuse cluster. The delays are generated by a Poisson point process over $[\tau_{l,0}, \infty)$, where $\tau_{l,0}$ corresponds

---

[2] There exist many different interpretations of the meaning of a cluster in radio channel modeling. For instance Saleh and Valenzuela [75] has a different interpretation of clusters.

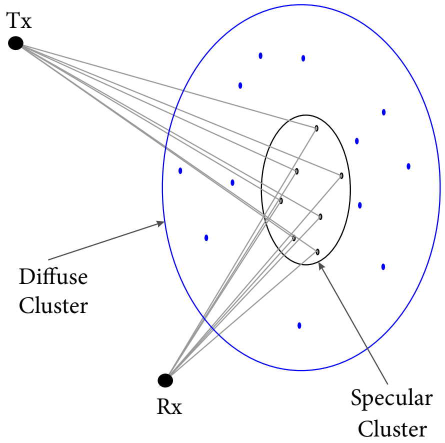

*Fig. 3.8: Geometric interpretation of the diffuse components in the geometric stochastic channel models. A diffuse cluster centered around a specular cluster models the diffuse component. Each cluster is comprised of its own group of specular components.*

to the propagation delay from the transmitter to the receiver via the center of the $l$th diffuse cluster.

In [21, 92], it is proposed to use a stochastic model for the diffuse component. There is no geometrical representation in the sense of (spatial) diffuse clusters and point scatterers as in [91]. However, the parameter values of this stochastic model are related to the specular clusters. For details we refer to [21, 92].

Chapter 4

# Research Questions, Methodology and Applications Considered in this Thesis

This Chapter is organized in three main parts. Each part is related to the following three questions on modeling, validation, and application aspects.

1. How to model the phenomenon of reverberation and its characteristics for localization and communications?
2. How to validate a proposed candidate model?
3. The original purpose of these investigations was to propose reverberation models for localization and communication. The proposed models allow for large variety of applications within localization and communications, which are these?

We detail Question 1 on modeling of the diffuse component and its characteristics in Section 4.1 and provide answers to it in Chapter 5. To answer Question 2 on model validation, we present in Section 4.2 a more general discussion on validation and detail our methods in Section 4.3. We review the applications considered in this thesis in Section 4.4 and present results of these applications in Chapter 5.

## 4.1 Research Questions on Reverberant Channel Modeling

The question with respect to modeling of the reverberation phenomenon is detailed in the following sub-questions.

- *Which physical propagation mechanisms govern the diffuse component?*

  This question is partly answered in the state of the art of the white-box models of acoustics and electromagnetic fields in cavities given in Section 3.3. However, these white-box models have not been thoroughly validated for "typical" in-room environments. Such a validation is done in Section 5.3.

- *Can we characterize the delay dispersion of the radio channel versus distance, e.g. the delay power spectrum, by means of physical propagation mechanisms?*

  The observed diffuse component corresponds to the tail in the delay power spectrum. The white-box models in Section 3.3 characterize the diffuse component with respect to transmitter and receiver distance and room geometry. Thus, we have a possible solution for the tail of the delay power spectrum. Further answers to this question, for instance on the early part of the delay power spectrum, can be found in Section 5.3.

- *Can we employ only specular components in the impulse response to adequately model the avalanche effect and the diffuse tail?*

  From a modeling perspective and with respect to the principle of parsimony specular components are preferable to dispersive components. Dispersive components follow certain distributions in the different dispersion domains. The type of distributions is unknown and usually based on assumptions. The distributions have multiple parameters. Specular component have only a single parameter in each considered domain.

- *How to model the reverberant channel for localization purpose such that geometric properties of the room and distance dependency are included?*

  This question is partly answered together with the previous questions.

- *How to model the reverberant channel for localization purpose such that we obtain location dependent parameters which are easily measured in practice, e.g. received power, mean delay, and rms delay spread?*

  The aim is on finding location dependent parameters that are easily measurable and have analytically simple models to infer the location.

## *4.2 Research Methodology*

In the following, we outline methods on validation of models and estimators for the model parameters. Furthermore, we discuss a potential problem upon combining models.

We start by defining our terminology used in the following discussion of the research methodology. We remark, that there may be other definitions in the open literature.

*Verification* is an examination with the purpose of checking whether a model or estimator fulfills its specifications.

*Fitting* of a model is the process of estimating the model parameters from experimental data.

*Evaluation* of a model is the examination of how well a model, with fitted or predicted parameters, describes the experimental data by means of purposefully chosen metrics, e.g. the root mean squared error, etc.

*Prediction* with a model is the generation of outcomes using selected values of the model parameters.

*Validation* of a model is the process of designing and conducting an experiment which allows the evaluation of the model prediction.

Note that model validation does not include model fitting.

### *On Model Validation*

We assume that a proposed model, which should be validated, was verified and has passed general plausibility checks. The proposed model follows the principle of parsimony [34]. If this is not fulfilled there is basically no need to validate the model.

The validation of proposed models is of great importance as we can not rely on a model that was proposed from, fitted to and evaluated with a single set of experimental data. In such a case the model does not give more information or insights than we already could obtain directly from the experimental data. Even worse, one may end up in circular reasoning for the applicability of the proposed model. To circumvent circular reasoning, the model should be evaluated by testing its prediction capabilities. To this end, one should consider two disjoint sets of data. One set is used for model fitting and the other is used for the evaluation of the model prediction. Often an available set of data is split into these two parts. How to split the data is not obvious and we need to make specific choices. If the data sets are small a cross-validation [93] procedure can be applied.

Ideally, we would like to apply a validation procedure which uses a specifically designed validation experiment. The experiment should be designed such that values of most of the model parameters can be appropriately adjusted for the validation data. We remark that, such a validation is stronger in comparison to a validation where only few or no model parameter change compared to their values obtained in the fitting experiment. To illustrate this more clearly, we consider the following two examples of a validation procedure:

1. We fit a model to experimental data of room A and use data from room B for validation. We remark that, room B is different, e.g. in size, shape, etc. Therefore, we need to adjust the values of the model parameters for room B in order to predict the experimental data collected in room B and evaluate these predictions.
2. We split the experimental data of room A into a fitting set and validation set. We fit the model to one half of the data. We use the parameters obtained from fitting in the validation with the other half of the experimental data.

We consider the validation in Example 1 as stronger in comparison to Example 2. We can easily compare the metrics obtained from evaluation of the fitted and predicted data in Example 2. For Example 1, we may fit the model to room B, evaluate the fit and compare the metrics, obtained from prediction and fitting, against each other.

### *Combining Models*

In radio channel modeling we focus typically on one particular phenomenon which we would like to model for a specific purpose. We may consider as an example the characterization of the received signal strength of a narrow-band system. There exist path loss models which characterize the average received signal strength versus distance. We may combine the path loss model with models for shadow fading and small scale fading in order to model the received signal strength at a certain distance. A variety of models exists in the open literature which can be potentially combined in this way in a composite model. In this case, one needs to be careful not to overlook possible dependencies between the component models.

Generally speaking, whenever we combine models we should be aware that there might be dependencies between the models due to a common phenomenon. Following Occam's razor [34], we should model the common phenomenon and obtain one set of model parameters instead of having a composite model which consists of multiple independently obtained models. Each of these independent models has its individual and possibly independent set of parameters. Note that the individual sets of parameters will often be larger than one common set and the combined models may be inconsistent. As a simple toy example, we may consider independently derived models for the first and second moment of a random process. If for some reason we would need to characterize the variance (centered second moment) of this random process, we could use the two independent models of the first and second moments. However, for some choices of independent parameter settings of the two models we may obtain negative variances. This, obviously, does not make sense. The two independent models are inconsistent with respect to their respective parameters and the resulting variance. We remark that, a check for consistency should be included in the validation procedure.

### *On Testing Estimators of Model Parameters*

Another topic related to modeling methodology is the estimation of model parameters. An estimator of certain model parameters is derived typically from the model itself. In a basic step, we verify that the estimator works appropriately. This can be done by estimating the parameters for a few toy examples. The verification of toy examples is followed by extensive Monte Carlo simulations. In the Monte Carlo simulations the estimator is applied on randomly generated data and its performance is compared against some appropriate bound, e.g. Cramér-Rao Bound.

However, often the model or the estimator includes free parameters, which cannot be estimated, when applied on experimental data. In the evaluation with simulation data one is tempted to choose the free parameters in an optimal way, unconsciously. As an example, we may consider the channel model in (2.2). In simulations we set the parameter $N$, which defines how many components to be simulated. One is tempted to select the same number in the estimation algorithm to find the parameters $a_n$ and $\tau_n$ for $n \in \{1, 2, \ldots, N\}$. However, in experimental data $N$ is unknown. Often, the free parameters are chosen heuristically when the estimator is applied on experimental data. The heuristic choice makes it more difficult to evaluate and compare results obtained from such estimators. It is required to evaluate the influence of the free parameters on the estimation results. This could be done by simulations. In addition, we propose to compare different estimators. These different estimators should be chosen such that they differ in their underlying models or if possible one of them is a model free estimator. Preferably, the estimators should differ in their free parameters too. A comparison of different estimators would allow to validate the estimators and the obtained results, at least to some degree.

## 4.3 The Research Methods Adopted in this Thesis

In this section we outline the research methods adopted in this thesis. We aim specifically at investigations on modeling the reverberation effect and validating the models with experimental data.

### Investigations of the Per-Path Component Spread

One of our research questions in Section 4.1 is related to modeling of the avalanche effect and the diffuse tail. Results from ultra-wideband measurements indicate that early components appear to be specular [18], however, the tail is diffuse. Other observations from wideband measurements [80–84] indicate that components are dispersive in delay and directional domains. We denote these components as dispersive path components. Dispersive path components are often represented as clusters, as done in stochastic [84, 94, 95] and geometric stochastic channel models [81–83]. We may ask a question like how to model the avalanche effect with the specular components and the diffuse tail, e.g. by a very large number of specular components or few dispersive path components. Thus, it is of interest to investigate experimentally the per-path component spread.

For the investigation of the per-path component spread we follow the approach addressed in the previous discussion on parameter estimators in Section 4.2. Two per-path component spread estimation methods are compared: a heuristic method [81–84, 95] and the density-based approach introduced in [80, 85–87]. We first apply both methods on synthetic data and compare the estimated per-path component spreads. Here, we focus on the evaluation with respect to the free parameters of the heuristic method, e.g. the pruning threshold for grouping specular components into one dispersive component. We then select and apply the more "robust" method on experimental data to estimate the per-path component spreads. We compare visually the results of the selected method and those of a model free estimator. Furthermore, we compare our findings with reported values from open literature. A summary of the findings is presented in Section 5.1 and details are included in Paper A.

### *Validation of Reverberation Models from Acoustics When Applied to Electromagnetics*

Reverberation models from room acoustics have been used in electromagnetics to predict the decay rate in the diffuse component. As already mentioned in Section 3.3, it is not immediately clear that the models from room acoustics, e.g. Sabine's or Eyring's, apply as well for electromagnetics due to the different considered frequency ranges and consequently different properties of wall materials. The absorption coefficients used in the reverberation models for electromagnetics may be largely different from acoustics. The used volume and surface areas considered in the reverberation models may be questioned as the electromagnetic waves propagate trough walls more easily. Thus a validation of the reverberation models, when applied to electromagnetics, is required, according to our discussion in Section 4.2.

The proposed validation procedure is inspired by Sabine's original work to characterize reverberation in room acoustics. In this thesis, we present a validation procedure where the average absorbtion coefficient is modified by opening windows, similar to Sabine's [52] approach. We use Sabine's and Eyring's reverberation models to predict for the modified absorption coefficients the reverberant component. The predicted reverberant component is compared with the respective observations. Furthermore, we predict the reverberant component for a room different in size and compare it to measurements. We investigate the influence of human absorption on the reverberant component. This is of importance to assess the performance of communication systems deployed in large conference rooms, where a large audience may create unforeseen changes in the propagation conditions. A summary of the results of these investigations can be found in Section 5.3 and details are presented in Paper C.

### *Validation of a Delay Power Spectrum Model*

We propose a distance dependent model for the delay power spectrum (DPS) with a “primary” and a “reverberant” component. We remark that, the proposed model is based on empirical observations from the open literature [67, 69]. The primary component is assumed to represent the superposition of the line of sight and first order reflection components. The reverberant component corresponds to the tail of the DPS. It is constituted of the contributions from a multitude of higher order reflections. The distance dependent DPS model allows to derive secondary models of the path loss, the mean delay and the rms delay spread as a function of transmitter-receiver distance. Additionally, distance dependent higher order moments and the kurtosis of the proposed DPS model are derived. Thus the DPS model represents a hierarchically higher model with respect to these secondary models. As discussed in Section 4.2 consistent secondary models with one single set of parameters can be derived from this hierarchically higher model. Details on the proposed DPS model and its secondary models can be found in Section 5.4 and Papers D and E.

Note that the empirical observations in [67, 69], that inspired our model of the reverberant component of the DPS, behave similarly to the theoretical results on reverberation described in Section 3.3 by the models of electromagnetic fields in cavities and room acoustics. However, for the validity of the proposed DPS model it is not required that the theoretical reverberation models of room acoustics or electromagnetic fields in cavities are valid too. Only the primary and the reverberant components of the DPS model need to be in accordance with the behavior in experimental data.

In the following we outline the validation procedure of the DPS model. First we investigate if the locally averaged delay power spectra, obtained from our experimental data, show a distance dependent behavior as described by the model for the primary and the reverberant component. Then we split the measurement data into two sets, one for model fitting and one for validation, according to our discussion in Section 4.2. We fit the model by estimating the decay rate of the reverberant component in the experimental delay power spectra. The remaining model parameters are obtained by fitting the secondary model of the path gain to estimated path gains computed from the fitting data set. The secondary model of the path gain is validated with the estimated path gains computed from the validation set. The mean delay, rms delay spread and kurtosis values are not used in the model fitting procedure. Thus they can be used for the validation with both the fitting and validation sets. We check the consistency of the secondary models with respect to transmitter-receiver distance.

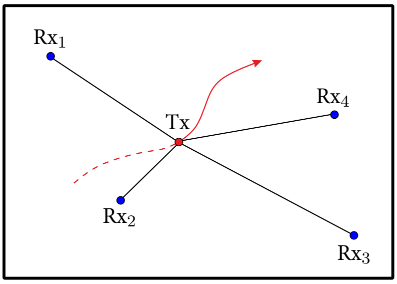

*Fig. 4.1: Localization scenario with four receivers and one transmitter moving through the room along the indicated trajectory. Location dependent parameters of the radio channels of the communication links are used to estimate the location of the transmitter.*

## 4.4 Applications of the Reverberation Models and the Model of the Delay Power Spectrum

In this section we deal with the question of "What can we use the reverberation models for?". We present a selection of applications which follow the initially considered purpose of proposing reverberation models for communications and localization. We remark that, the reverberation models are very versatile and many more applications are possible.

After validating the theoretical reverberation models from acoustics for electromagnetics, i.e. Sabine's and Eyring's models, these models can be used to characterize the reverberant component of the DPS model. Sabine's and Eyring's models predict the decay rate and reference gain of the reverberant component for rooms with different sizes and shapes. We combine the prediction capability of Sabine's and Eyring's models with the distance dependent DPS model. This combination allows to predict parameters such as path gain, mean delay, and rms delay spread for rooms with different size and shape. Such an application, of combining Sabine's or Eyring's model with the DPS model, is considered in Paper C and results are summarized in Section 5.3.

The DPS model allows for the characterization of the Rice factor versus distance under certain assumptions. The Rice factor is an important parameter in communications. It characterizes the severity of fading. The severity of fading of the radio channel [2, 3] affects the achievable bit error rate and the capacity of a communication system. We outline this model briefly in Section 5.4 and present some results. More details can be found in Paper E.

The DPS model allows for a distance dependent description of a tapped delay line model for the channel impulse responses. The proposed tapped delay line model includes the distance dependent behavior of the Rice factor. As such the tapped delay line model is useful for testing of receivers in mobile communication and time of arrival estimation in localization. Details on the tapped delay line model can be found in Paper E.

Finally, we utilize the secondary models of the DPS model in a localization example. For this purpose, we consider a transmitter and several receivers located in the same room as depicted in Fig. 4.1. We like to localize the moving transmitter from observations of location dependent parameters of the channel. The secondary models allow to characterize the path gain, mean delay, and rms delay spread for all communication links in the room. The most promising parameters for localization are the path gain and the mean delay due to their specific behavior with distance. Results on the application of the secondary models can be found in Section 5.5 and in more details in Paper G.

Chapter 5

# Contributions to Reverberant Channel Modeling

The contributions of this thesis are detailed in Papers A to G and summarized in this Chapter.

## 5.1 Results on the Per-Path Component Spreads

We investigate in Paper A the per-path component spread of dispersive components. This investigation should answer the question, posed in Section 4.1, if components are specular or if they can be assumed specular. We investigate the delay and angle domains. For this purpose, we compare two estimation methods, namely the grouping/clustering approach [81, 83, 84] and the density approach [85–87]. The grouping approach applies pruning when selecting and grouping estimated specular components into a dispersive component. Simulations show that the results of this widely used approach strongly depend on a heuristically chosen threshold in the pruning process. An overestimation of the per-path component spreads is easily possible as there is no indication on how to chose the threshold. The estimated per-path component spreads from the density approach are close to the simulated values and this method is more robust.

The estimates of the per-path component spreads, obtained from the density approach, are observed to be small. Particularly in the delay domain. Actually, these values are so small that the component can be considered specular. The estimated specular-like components are all early in delay, i.e. within the first 30 ns after the line of sight component. This is in accordance with ultra wideband investigations in [18], where the early components in the channel impulse response appear to be specular too. The finding that components are specular-like is beneficial for modeling purposes. Specular components are easier to model. The number of parameters to describe a specular component is lower in comparison to the number of parameters needed to characterize a dispersive component. We utilize the observation that components appear to be specular in the propagation graph model in Section 5.2.

Finally, we have two suggestions for future investigations:

- The directional behavior of the reverberant component, the late part of the impulse response, should be investigated.

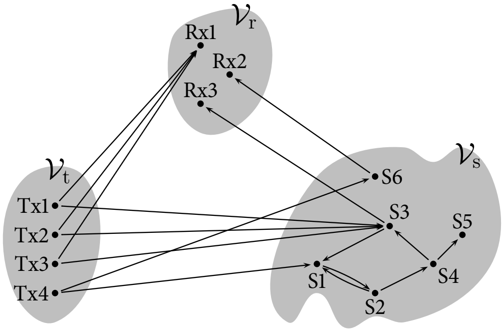

*Fig. 5.1: Representation of the propagation graph. The transmitter, receiver and scatterer vertices are the elements of the sets $\mathcal{V}_\mathrm{t}$,$\mathcal{V}_\mathrm{r}$ and $\mathcal{V}_\mathrm{s}$, respectively.*

- Further investigations should be conducted with ultra wideband measurement data. Limited by the resolution of our measurement equipment, the obtained per-path component spreads can encompass the diffuse components of Janson's hybrid ray-tracing model [37]. Janson's model is proposed for ultra wideband.

## 5.2 Impulse Response Modeling with Propagation Graphs

In Paper B, we present a model for impulse responses that includes the avalanche effect and the diffuse component but considers only specular components. The assumption of considering specular components only is supported by the investigations on per-path component spreads in Section 5.1 and the observations in [18]. We detail the propagation graph model and demonstrate its versatility for channel modeling. The versatility is demonstrated by relating the model to previous published models, e.g. Turin et al. [77] and Saleh&Valenzuela [75]. The propagation graph model consists of a directed graph in which vertices represent transmitters, receivers, and scatterers, while edges represent propagation conditions between vertices. A representation of such a graph can be seen in Fig. 5.1.

The propagation graph model includes recursive scattering, see the scatterer vertex set $\mathcal{V}_\mathrm{s}$ in Fig. 5.1. The recursive scattering inherently accounts for the avalanche effect. The recursive structure of the model allows to derive in closed form the channel response for infinitely many specular components. The computational complexity of the propagation graph is dominated by the number of scatterers rather than the "infinite" number of specular components in the impulse response. We detail in Paper B how partial responses can be obtained in closed form. Partial responses contain only an arbitrary

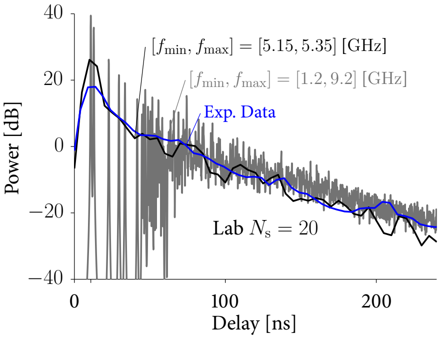

*Fig. 5.2: Delay power spectra obtained from experiments and simulations. Two different frequency bands are used in the simulations. The smaller bandwidth corresponds to the one used to collect the experimental data. The larger bandwidth allows to see the avalanche effect.*

number of interactions between scatterer vertices. These partial responses may be of interest in combination with ray-tracing tools.

We present an application of the propagation graph model to an in-room channel. In this example we consider a geometric interpretation of the graph. Positions of scatterer vertices are drawn independently from a uniform distribution in the volume of the room. The interactions are assumed to cause no delay dispersion and thus delay dispersion occurs only due to propagation times between vertices. The propagation time between vertices are obtained as the ratio of the euclidian distance between the vertice positions and the speed of light. The gain coefficients along edges are inspired from Friis equation (2.3), except the gains for the edges which connect scatterer to scatterer vertices. These edge gains are set to a fixed value. The results reveal that the graph's recursive structure yields both an exponential power decay and an avalanche effect in the generated impulse responses. An example of a power delay spectrum obtained from local spatial averages is shown in Fig. 5.2. For these results, the gains for the edges between scatterers were selected such that the tail of the experimental and simulated delay power spectra have the same decay rate. We see a good agreement between the experimental and simulated delay power spectra. The simulations with larger bandwidth show clearly the avalanche effect in Fig. 5.2.

## 5.3 Predict the Delay Power Spectrum for Specific Environments Using Reverberation Models

In Section 4.1 we posed the research question: "Which physical propagation mechanisms govern the diffuse component?". We know that reverberation models from room acoustics and electromagnetic fields in cavities provide a possible physical interpretation of the observed diffuse component. This physical interpretation explains the avalanche effect, the exponential decay and the behavior with respect to transmitter-receiver distance of the diffuse component. Therefore, we investigate in Paper C if Sabine's and Eyring's acoustical reverberation models are valid for electromagnetics in typical in-room environments. The results from the validation procedure indicate that the reverberation is contained in a single room. Furthermore, the reverberation models from acoustics remain valid when transcribed to room electromagnetics. We make controlled changes to the absorbtion coefficient and predict with Sabine's and Eyring's models the changes in the reverberant component. The models predictions are in good agreement with the experimental results. The observed absorbtion coefficients are large in comparison to typical values in acoustics. For these large absorbtion coefficients, Eyring's model provides a better prediction than Sabine's. This is expected as Eyring's model was developed under the consideration of rooms with large absorbtion coefficients. We use the models of Sabine and Eyring to predict the parameters of the reverberant component for a neighboring room. The volume and the surface of this neighboring room differ from the original room the model was fitted too. Again, we observe good agreement between model predictions and experimental results. Details on this validation can be found in Paper C.

As an example application, we consider the prediction of the parameters of the reverberant component in the DPS model. This prediction can be done either for different absorbtion coefficients in a room or for rooms with different size but known average absorption coefficient. An example is presented in Paper C. In this example we predict the path gain, mean delay and rms delay spread versus distance using the secondary models of the delay power spectrum. This is done for a specific room under the assumption of knowing the average absorption coefficient. The value of this coefficient is set equal to the value obtained for an adjacent room. The rooms share similar wall properties but differ slightly in furniture. With Eyring's model, we predict the reverberation time and the reference gain of the reverberant component of the delay power spectrum. The parameter settings of the primary component are assumed equal to the values obtained for the adjacent room. We observe in general good agreement between the predicted and the experimental values of mean delay and rms delay spread. The path gain has a slight offset due to a mismatch in parameter values of the primary primary component in the two rooms. However, the root mean squared errors for the predictions are close to the ones obtained when fitting the DPS model to the measurements. Details of this application can be found in Paper C.

We investigate the effect on the reverberant component when emulating a meeting (multiple humans) in the investigated room. The absorption due to human bodies significantly affects the reverberant component. This is of importance in the design of communication systems, e.g. for a large auditorium. The audience causes smaller reverberation times. Thus, the reverberant component of the delay power spectrum changes. This change in the spectrum reduces the coverage and affects the performance of the communication system. Having information on the impact of the humans allows to adjust appropriately the communication system in an auditorium.

## 5.4 The DPS Model and its Secondary Models

In Papers D and E, we investigate the distance dependency of the delay dispersion of the in-room radio channel to answer the homonymic research question posed in Section 4.1.These papers introduce the distance dependent DPS model. In this model the delay power spectrum is assumed to be composed of a "primary" and a "reverberant" component. The early part in the delay power spectrum is named primary component. We model the primary component as a dirac delta function weighted according to an inverse distance power law ($d^{-n}$). The model of the reverberant component is based on empirical observations from the open literature [67, 69]: the reverberant component decays exponentially[1] in delay with an onset equal to the propagation delay between transmitter and receiver, see Fig. 5.3. The reverberant component coincides, except the onset, for all transmitter and receiver positions in the room.

The DPS model was first proposed in a preliminary version in Paper D. Paper E explores the idea in full detail: specifically, we focus on the model validation and a more thorough comparison with previous models. Two applications are presented in Paper E too. One application is the design of a model of the Rice factor as a function of distance and the other application is a tapped delay line model for the impulse response.

The validation procedure in Paper E reveals good agreement between experimental data and the predictions from the secondary models. We compare the root mean squared error (RMSE) of the path gains obtained by fitting the commonly used one-slope model and the secondary path gain model of the delay power spectrum. Due to a higher number of model parameters, the secondary path gain model obtains lower RMSE values, in comparison to the values of the one-slope model. However, the proposed secondary path gain model not only fits better, but also predicts better the path gains estimated from the validation data set. Thus the higher model complexity is justified. Besides the path gain, we obtain, with the same parameter set, predictions

---

[1] We remark that, the model for the tail derived in [67] is non-exponential in delay. However, the measured delay power spectra reported in [67] are close to exponential. A delay power spectrum model considering other shapes of the tail may be proposed in a way similar to the one described in this thesis.

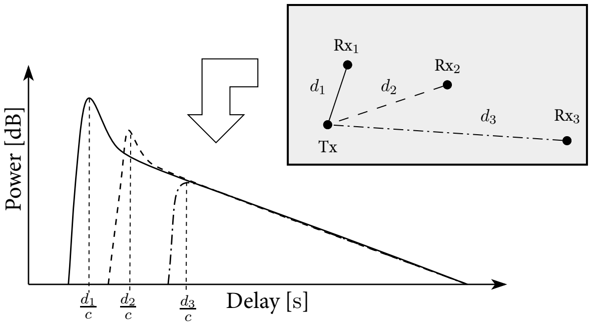

*Fig. 5.3: Typical behavior of the bandlimited delay power spectrum experimentally observed at three different transmitter-receiver distances in an in-room environment (schematically presented by the grey box).*

of the mean delay, rms delay spread, and kurtosis versus distance using the remaining secondary models. The predictions of mean delay, etc., show good agreement in trend versus distance with the experimental data of both the fitting and validation data sets.

In the following, we present a few remarks on the estimated parameters of the DPS model. By using the proposed model, we obtain an estimated path gain exponent of the primary component close to 2, i.e. the free-space propagation. Note that a value close to the free-space exponent is expected, specifically when the primary component consists only of the line of sight component. In comparison, by fitting the one-slope model (2.4), we obtain an exponent close to unity. This value, significantly below the free-space exponent, is due to the inability of the one-slope model to separate the contributions from the primary and reverberant component. For the investigated environments the ratio of the reverberant component and the total power are 0.41 and 0.35 at $1\,\mathrm{m}$. Thus the reverberant component is prominent for the considered rooms. The reverberation distance is below $1.5\,\mathrm{m}$. Therefore, despite having line of sight conditions in the entire room, the reverberant component is stronger then the direct component for distances above the reverberation distance. This contradicts the intuition inherited from outdoor scenarios, that in line of sight all other components are of little importance.

One final remark on the one-slope model: The one-slope model's inability to separate the primary and the reverberant components leads to different values of the path loss exponent for the same room but at different measurement locations. To illustrate this, we consider the following two cases:

1. The transmitter is placed in the center of the room. Measurements are obtained for various receiver locations. In this case, the measurements are obtained mainly for distances where the primary component dom-

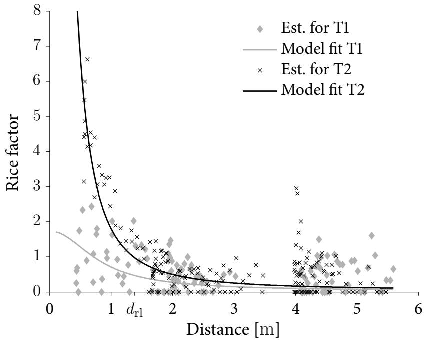

*Fig. 5.4: Estimated Rice factors obtained from measurements collected along two transmitter tracks (T1 and T2) in a room. The graphs of the fitted Rice factor models are also depicted. We observe a good fit. Some outliers are observed around 4* m. *For further details see Section E.5.1 in Paper E.*

inates. Thus the estimated value of the path loss exponent of the one-slope model is close to the value of the primary component.

2. The transmitter is placed in a corner of the room and the receiver is displaced throughout the entire room. A large number of measurements is obtained for distances where the reverberant component dominates. Thus the estimated value of the path loss exponent of the one-slope model is determined by the reverberant component.

We consider this observation important for cooperative localization where the nodes can move freely in the room. In such a scenario, what is the appropriate path loss exponent for the one-slope model to infer distances? Note that the secondary path gain model does not suffer from this problem.

We detail here one useful application of the DPS model for communication purpose. In this application we use the DPS model to devise a distance dependent model of the Rice factor. The model consists of two random processes, one describing the impact of the primary component of the delay power spectrum and one representing the effect of the reverberant component, see Paper E. The random processes inherit the distance dependency of the delay power spectrum. Based on the two random processes, we characterize the narrowband Rice factor versus distance. More details on the Rice factor model and a comparison to related models [55, 96] are presented in Paper E. Almost all parameters of the probability density functions of the two random processes are obtained from the DPS model. The only missing parameter characterizes the fading of the primary component. Either this parameter is obtained from measurement data or is set based on assumptions. One such assumption could be that the primary component does not fade. This

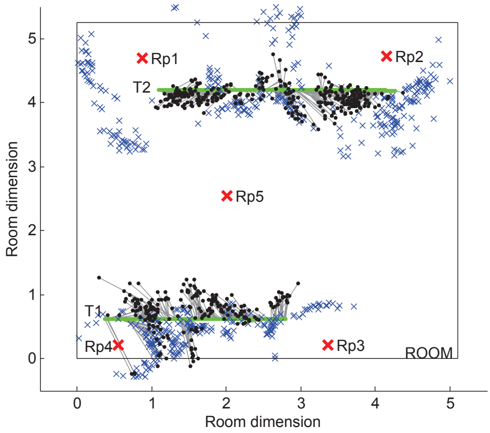

*Fig. 5.5: Location estimates obtained for scenarios where the transmitter moves along tracks T1 and T2. Results are presented for the one-step algorithm when this algorithm uses either the estimated received powers (crosses) or the estimated mean delays (dot). The estimated locations obtained in the second setup are closer to the true positions (green tracks). The grey lines connect the location estimates to the true positions.*

means that the primary component consists only of the contribution from the line of sight propagation path. Our experimental Rice factors show two cases of distinct behavior with distance, see Fig. 5.4. In one case the primary component does not exhibit fading and primarily consists of the line of sight component. Thus, the Rice factor is large at short distances and decreases as the distance increases, see T2 in Fig. 5.4. In the other case, the primary component fades due to relatively strong first order reflections. This leads to small Rice factor values at small distances and a progressive decay with increasing distance. The proposed model in Paper E represents well these two distinct cases and allows for a continuous transition between them. The experimental results indicate that knowledge on the fading behavior of the primary component is essential to model the Rice factor accurately at short distances. Furthermore, even though line of sight is present at all distances, the reverberant component prevents large Rice factors over the entire room.

## 5.5 Application of the DPS Model in Localization

In Paper F we investigate the cross covariance of the received powers of multiple links. The experimental results indicate an insignificant correlation between the log power values of different links. This is in accordance with the observations in [97]. The log power values appear to be Gaussian distributed with a range dependent mean. The variance of the log power values appears to be constant regardless of distance. As a result, the received log power of

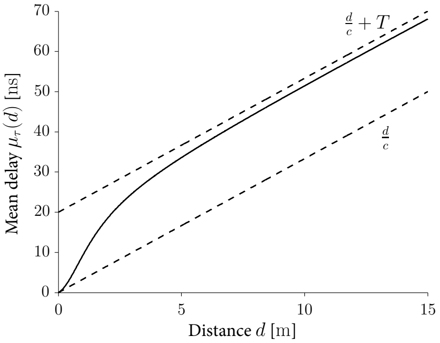

*Fig. 5.6: Mean delay versus distance predicted by the secondary model of the DPS model.*

any link can be modeled as the sum of two terms, a distance dependent mean value plus a zero mean Gaussian term with a fixed variance. The Gaussian terms of multiple links are drawn independently. The behavior of the mean versus distance can be described with an appropriate path gain model such as for instance the secondary model described in Paper D and E. Preliminary observations in ongoing work indicate similar small correlation for the mean delay and rms delay spread.

The results of these multi-link investigations are used in Paper G where we propose a stochastic model for the received power and the mean delay for localization. The stochastic model is used to derive one-step and two-step localization algorithms. In the one-step case, we estimate the location directly from the channel observations (received power and/or mean delay). In the two-step case, we first infer the transmitter-receiver distances and secondly we use these distances to estimate the location. We compare the location estimates using i) the path gain, ii) the mean delay and iii) jointly the path gain and mean delay. This comparison is done for both one-step and two-step location estimators. Path gain and mean delay are correlated as both parameters are derived from the delay power spectrum, see (2.8) and (2.9). However, for simplicity we assume in Paper G that these parameters are independent.

We observe an improvement in the location estimation accuracy when using the observations of the mean delay in comparison to using the received power, see Fig. 5.5. For the one-step estimator which uses the received power and the mean delay jointly we observe a location error below 0.5 m for 90% of the observations. The corresponding value is roughly 1.3 m when the estimator uses the received power only. The improved performance, due to including the mean delay, may be explained by the distinct behavior of the mean delay and the received power versus distance. The experimental data shows that the received power follows roughly an inverse distance power law ($d^{-n}$) and the variance of the log power values is constant with respect to distance. When inferring the distance from the received power, the estimation error increases, when the transmitter receiver distance increases. The mean delay observations show that the variance is constant with respect to distance. The analytical expression of the mean delay, plotted in Fig. 5.6, consists of the sum of two terms. One term grows linearly with distance and the second term is a plateau/mesa function, which is upper bounded by the reverberation time $T$. For possible distance ranges in typical environments we observe only a monotonic increase with distance from zero to approximately the reverberation time $T$. Thus the mean delay follows roughly $d/c$ for short distances and $d/c + T$ for large distances. This behavior is beneficial for inferring the distance from observations of the mean delay. The obtained results clearly indicate an improvement of the location estimation accuracy when using the proposed DPS model of Paper E to infer the location.

Chapter 6

# Conclusions and Outlook

In this thesis, we propose and validate several models for the reverberant channel based on experimental observations, both from open literature and our own. The proposed models are important for communications and localization. Our proposals cover models for impulse responses, the DPS model and its secondary models, etc. In this thesis we pursue several research questions. In this Chapter, we structure the conclusions and the outlook according to these questions.

## 6.1 Conclusions

One of the questions raised in Section 4.1 focuses on the physical propagation mechanisms that govern the diffuse component and how to characterize these mechanisms in channel models for communications and localization. Reverberation models of room acoustics and electromagnetic fields in cavities predict an avalanche effect and an exponentially decaying diffuse component in the delay power spectrum. Thus, these models provide a possible answer but they are not directly applicable to electromagnetics in typical home and office environments and need to be validated for our purpose. We investigated and validated reverberation models transcribed from acoustics to electromagnetics. Sofar, these models have been fitted to measurement data in the open literature but a validation was missing. We designed and conducted a specific experiment to gather data for the validation process. This experiment is similar to that presented in the original work by Sabine in acoustics. We validate two models from acoustics which characterize the diffuse component: Sabine's model and Eyring's model. From the open literature it appears that the former is more widely adopted for electromagnetics. Our investigations validate Sabine's and Eyring's models for the prediction of parameters, i.e. the reverberation time and the reference path gain of the reverberant component. Sabine's and Eyring's models allow to predict the reverberation time for a room, based on its average absorption coefficient and its dimensions. Due to the fact that the observed absorption coefficients are large in comparison to acoustics, Eyring's model predicts the reverberation time better than Sabine's model. In conclusion, Eyring's model is more appropriate for electromagnetics in typical in-room environments than Sabine's.

Another research question focuses on the modeling aspects of impulse responses, e.g. if specular components can recreate the observed phenomena of the avalanche effect and the diffuse tail. To answer this question, we investigate the dispersion of per-path components in an indoor scenario. Our results show that the estimated components have very small spreads. These spreads are close to or below the resolution of the measurement equipment. Following Occam's razor, we conclude that these components can be considered to be specular. We use the specular component assumption in the propagation graph model for the simulation of impulse responses. The simulated impulse responses reproduce the avalanche effect and exhibit an exponentially decaying tail. The avalanche effect and the exponentially decaying tail result from the recursive structure of the graph. As demonstrated by simulations, the avalanche effect and the diffuse component are observed even when considering only specular components. The diffusion process leading to the diffuse component is created by the increasing arrival rate of specular components. We present a geometrical interpretation of the propagation graph suitable for modeling the reverberation phenomenon of in-room environments. Edge gains follow a distance dependent weighting inspired by Friis equation. However, the edges between scatterer vertices have a fixed gain adjusted to meet the required exponential decay rate of the reverberant component. Note that the decay rate used in the propagation graph model can be obtained from or predicted with Sabine's or Eyring's model.

The next question focuses on a distance dependent characterization of the delay dispersion of the reverberant channel. We answer this question with the proposed distance dependent DPS model. The DPS model is composed of a primary component which follows an inverse distance power law ($d^{-n}$) and a reverberant component. The reverberant component decays exponentially versus delay and its onset is distance dependent: The onset time corresponds to $d/c$ where $c$ is the speed of propagation. By computing the moments of the delay power spectrum we obtain distance dependent secondary models of path gain, mean delay, rms delay spread, kurtosis, and higher order centered moments. From our experimental data we conclude that the reverberation distance is less than 1.5 $\mathrm{m}$. This indicates that the power of the reverberant component exceeds the primary one for large portions of the room. The primary component has a path gain exponent close to the free-space exponent. By contrast, the exponent of the one-slope model of the path gain is close to unity. The one-slope model provides a fit to the path gain that blends the primary and the reverberant components. As a consequence the one-slope model leads to different path gain exponents for different measurement locations in the same environment. This makes it difficult to i) compare path gain exponents of the one-slope model found in the open literature and ii) select values of the exponent for predictions. Thus, we propose to use the delay power spectrum model and its secondary model of the path gain, as the later allows to characterize the path gain for the entire room independent of the transmitter receiver positions. In addition, the predictions of mean delay, rms delay spread, etc., with the remaining secondary models of the delay power spectrum, agree well with experimental results.

In the following we answer the remaining questions of Chapter 4 on applications of the reverberant channel models. The questions related to localization are answered simply by combining all presented models. We utilize Eyring's model to predict the characteristics of the reverberant component, e.g. the reverberation time, from the room geometry and an average absorption coefficient. The reverberation time is used as a parameter in the propagation graph model and in the DPS model. Our proposed geometric interpretation of the propagation graph model leads to impulse responses that include an avalanche effect that is related to the room geometry. This makes the propagation graph model suitable for testing localization algorithms based on time of arrival estimates. Alternatively, characterizing the delay power spectrum with the reverberation time allows to make use of the distance dependent secondary models. These secondary models are analytically simple and can be used to infer the location using for instance observations of the path gain and/or mean delay. We detail one example of localization using these secondary models in a multi link scenario. The algorithm using the mean delay performs better than the one using the path gain. This is due to the fact that the behavior of the mean delay versus distance is better suited for localization than the behavior versus distance of the path gain.

We also present other applications of the distance dependent DPS model useful for communications, e.g. a Rice factor model and a tapped delay line model of the distance dependent impulse response. The experimental values of the Rice factor versus distance are good approximated by the model. A prerequisite is, however, that the fading behavior of the primary component is known. This knowledge can be based on assumptions or gathered from measurements. Our observations show that the reverberant component prevents large Rice factors in the entire room, even though line of sight is present at all distances.

## 6.2 Outlook

The validation of Eyring's model leads us to suggest that experimental results of reverberation time, absorption coefficient and room geometry be gathered in a database. Such a database would be of great use in the radio channel modeling community similar as various collections of, e.g. wall attenuations in [31] or parameters of the one-slope model in [28]. The database of parameters for the reverberation models, in combination with the delay power spectrum model, would allow for the prediction of distance dependent path gain, mean delay, rms delay spread, etc. for rooms with different size and shape. Besides the obvious benefits for communications and localization, this would be useful for inferring parameters of other channel models too, i.e. the calibration of ray-tracing models in the absence of detailed wall material properties.

In this thesis, we consider only the delay dispersion of the reverberant channel. The reverberation models from acoustics or electromagnetic fields in cavities predict an electromagnetic field isotropic in direction under ideal conditions. As indicated by Richardson in [65], this does not hold for moderately reverberant environments. Thus, future investigations should consider the directional dispersion in the validation process of reverberation models.

Sofar, we considered Sabine's and Eyring's reverberation models for in-room scenarios. Further investigations should be conducted with respect to coupling between rooms and the absorption by humans in large auditoria. Models exist already in room acoustics and electromagnetic fields in cavities which consider coupling between rooms. However, these models still need a thorough experimental validation for typical indoor environments. A first attempt was done in [98]. The extension to coupling between rooms allows to extend the work to scenarios where the transmitter and the receiver are placed separately into two adjacent rooms or placed within the entire building. If the transmitter and the receiver are separated by several walls, our previous assumption that power leaving a room is lost may not hold anymore. For example, a signal leaving via a window and re-entering via a reflection on a neighboring building may be as strong as or even stronger than the signals originating from propagation through multiple walls.

Although several investigations of the absorption due to the human body have been made, their focus was mainly on the specific absorption rate. The specific absorption rate is useful for investigations on health issues. These investigations all indicate a noticeable change in reverberation time due to rather small groups of humans. A large audience in e.g. an auditorium significantly changes the propagation conditions such that the performance of communication systems may degrade severely. This knowledge is useful in planning communication systems in large auditoria. Note that in future investigations on absorption by humans one may consider the recent work in [99, 100] on loading reverberation chambers with large-form-factor devices.

As to future applications of the propagation graph model, we envision hybrid models. As an example, one such hybrid model would combine, e.g., a ray-tracing tool that represents specular components and the propagation graph model that mimics the reverberant component. In combination with

Sabine's or Eyring's model, we can predict the decay rate of the reverberant component which is used in the calibration of the propagation graph model.

The propagation graph model and associated analytical results encompass MIMO and multi-link systems. However, an open issue is to incorporate multiple links and their appropriate correlation. Such an extension will enable the study of avalanche effects in multi-link channels via numerical simulations. An additional open issue is the validation of such multi-link models using measurement data.

We consider our work presented in the extended abstract [101] as a concrete future investigation. This work, which is not part of this thesis, includes a preliminary calibration process of the propagation graph model for reverberant rooms. We investigate stochastic models for placing scatterers in two rooms. Two different models are proposed according to the geometric description of the room and the placement of furniture therein. We describe how to model and calibrate the gain coefficients of the edges for both scatterer placement models. The calibration procedure uses the reverberation time obtained from measurement data collected in the two rooms. Alternatively, the reverberation time may be predicted with Sabine's or Eyring's model. This ongoing work needs further investigations of the arrival rate of components obtained from measurements.

One open aspect, when using the mean delay for localization, is the synchronization between terminals. In the localization application presented in this thesis, the transmitter and all receivers were perfectly synchronized. In realistic localization scenarios this is not the case. One envisioned possibility to circumvent the synchronization problem is to use a similar approach as in localization with time difference of arrival algorithms. Another future topic is to extend the localization algorithm with a joint model which takes into account the correlation between the path gain, mean delay and rms delay spread.

# References

[1] ICT Data and Statistics Division, "ICT Facts and Figures - The World in 2013," International Telecommunication Union (ITU), Geneva, Switzerland, Tech. Rep., February 2013.

[2] A. F. Molisch, *Wireless Communications*, 2nd ed. Wiley, Dec. 2010.

[3] R. Vaughan and J. B. Andersen, *Channels, Propagation and Antennas for Mobile Communications*. Institution of Electrical Engineers, 2003.

[4] WHERE1 Partners, "Deliverable D3.4: Location based optimisation for PHY algorithms/protocols," WHERE1, Deliverable FP7-ICT-217033, 2010.

[5] S. Majhi, Y. Nasser, J. Hélard, R. Raulefs, and A. Dammann, "Geo-Location Aided Cooperative Communications," in *Positioning Navigation and Communication (WPNC), 2010 7th Workshop on*, 2010, pp. 264–269.

[6] L. Brunel, M. Plainchault, N. Gresset, A. Dammann, C. Mensing, and R. Raulefs, "Inter-Cell Interference Coordination and Synchronization based on Location Information," in *Positioning Navigation and Communication (WPNC), 2010 7th Workshop on*, 2010, pp. 224–232.

[7] S. K. Jayaweera, "Virtual MIMO-based cooperative communication for energy-constrained wireless sensor networks," *IEEE Trans. Wireless Commun.*, vol. 5, no. 5, pp. 984–989, 2006.

[8] WHERE1 Partners, "Deliverable D3.5: Location based cross-layer optimisation for PHY/MAC," WHERE1, Deliverable FP7-ICT-217033, 2010.

[9] F. C. Commission and et al., "OET Bulletin No. 71 Guidelines for Testing and Verifying the Accuracy of Wireless E911 Location Systems," *Federal Communication Commission*, 2000.

[10] S. Wang, M. Green, and M. Malkawi, "Mobile Positioning Technologies and Location Services," in *Radio and Wireless Conference, 2002. RAWCON 2002. IEEE*, 2002, pp. 9–12.

[11] R. Zekavat and R. M. Buehrer, *Handbook of Position Location: Theory, Practice and Advances*, 1st ed. Wiley-IEEE Press, 11 2011.

[12] F. Izquierdo, M. Ciurana, F. Barcelo, J. Paradells, and E. Zola, "Performance evaluation of a TOA-based trilateration method to locate terminals in WLAN," in *Wireless Pervasive Computing, 2006 1st International Symposium on*, 2006, pp. 1–6.

[13] Z. Sahinoglu, S. Gezici, and I. Güvenc, *Ultra-wideband Positioning Systems: Theoretical Limits, Ranging Algorithms, and Protocols*. Cambridge University Press, 6 2011.

[14] W. Figel, N. Shepherd, and W. Trammell, "Vehicle Location by a Signal Attenuation Method," in *Vehicular Technology Conference, 1968. 19th IEEE*, vol. 19, 1968, pp. 105–109.

[15] T. Roos, P. Myllymaki, and H. Tirri, "A Statistical Modeling Approach to Location Estimation," *IEEE Trans. Mobile Comput.*, vol. 1, no. 1, pp. 59–69, 2002.

[16] I. Jami, M. Ali, and R. Ormondroyd, “Comparison of Methods of Locating and Tracking Cellular Mobiles,” in *Novel Methods of Location and Tracking of Cellular Mobiles and Their System Applications (Ref. No. 1999/046), IEE Colloquium on*, 1999, pp. 1–6.

[17] M. Triki and D. T. M. Slock, “Mobile Localization for NLOS Propagation,” in *Personal, Indoor and Mobile Radio Communications, 2007. PIMRC 2007. IEEE 18th International Symposium on*, 2007, pp. 1–4.

[18] J. Kunisch and J. Pamp, “Measurement results and modeling aspects for the UWB radio channel,” in *Ultra Wideband Systems and Technologies, 2002. Digest of Papers. 2002 IEEE Conf. on*, May 2002, pp. 19–24.

[19] A. Richter, J. Salmi, and V. Koivunen, “Distributed Scattering in Radio Channels and its Contribution to MIMO Channel Capacity,” in *Antennas and Propagation, 2006. EuCAP 2006. First European Conference on*, 2006, pp. 1–7.

[20] A. Richter, “The Contribution of Distributed Scattering in Radio Channels to Channel Capacity: Estimation and Modeling,” in *Signals, Systems and Computers, 2006. ACSSC ’06. Fortieth Asilomar Conference on*, 2006, pp. 951–955.

[21] F. Quitin, C. Oestges, F. Horlin, and P. De Doncker, “Diffuse Multipath Component Characterization for Indoor MIMO Channels,” in *Antennas and Propagation (EuCAP), 2010 Proceedings of the Fourth European Conference on*, 2010, pp. 1–5.

[22] N. Czink, A. Richter, E. Bonek, J.-P. Nuutinen, and J. Ylitalo, “Including Diffuse Multipath Parameters in MIMO Channel Models,” in *Proc. of the 66th IEEE Veh. Technol. Conf. (VTC)*, A. Richter, Ed., 2007, pp. 874–878.

[23] M. Landmann, M. Kaeske, R. Thoma, J. Takada, and I. Ida, “Measurement Based Parametric Channel Modeling Considering Diffuse Scattering and Specular Components,” in *International Symposium on Antennas and Propagation*, Niigata, Japan, Aug. 2007, pp. 1–5.

[24] G. D. Durgin, *Space-Time Wireless Channels*. Prentice Hall, 2003.

[25] B. H. Fleury, “First- and Second-Order Characterization of Direction Dispersion and Space Selectivity in the Radio Channel,” *IEEE Trans. Inf. Theory*, vol. 46, no. 6, pp. 2027–2044, Sept. 2000.

[26] H. Hashemi, “The Indoor Radio Propagation Channel,” *Proc. IEEE*, vol. 81, no. 7, pp. 943–968, July 1993.

[27] H. T. Friis, “A Note on a Simple Transmission Formula,” *Proceedings of the I.R.E.*, vol. 34, no. 5, pp. 254–256, may 1946.

[28] E. Damosso, Ed., *Digital mobile radio towards future generation systems: COST 231 Final Report*. Bruxelles, Belgium: European Commission, 1999.

[29] A. Motley and J. Keenan, “Personal Communication Radio Coverage in Buildings at 900 MHz and 1700 MHz,” *Electronics Letters*, vol. 24, no. 12, pp. 763–764, 1988.

[30] J. Keenan and A. Motley, “Radio coverage in buildings,” in *Br. Telecom Technol. J.*, vol. 8, no. 1, Jan. 1990, pp. 19–24.

[31] T. S. Rappaport, *Wireless Communications: Principles and Practice (2nd Edition)*, 2nd ed. Prentice Hall, 12 2001.

[32] R. Valenzuela, "A Ray Tracing Approach to Predicting Indoor Wireless Transmission," in *Vehicular Technology Conference, 1993., 43rd IEEE*, 1993, pp. 214–218.

[33] S. Y. Seidel and T. S. Rappaport, "Site-specific propagation prediction for wireless in-building personal communication system design," *IEEE Trans. Veh. Technol.*, vol. 43, no. 4, pp. 879–891, 1994.

[34] H. G. Gauch, *Scientific Method in Practice*. Cambridge University Press, 2002.

[35] M. Jakobsen, T. Pedersen, and B. Fleury, "Time-Dynamic Stochastic Channel Modeling and Analysis by use of Marked Spatial Point Processes," *IEEE Trans. Antennas Propag.*, submitted.

[36] B. Fleury, "An Uncertainty Relation for WSS Processes and Its Application to WSSUS Systems," *IEEE Trans. Commun.*, vol. 44, no. 12, pp. 1632–1634, Dec. 1996.

[37] M. Janson, "Hybride Funkkanalmodellierung für ultrabreitbandige MIMO-Systeme," Ph.D. dissertation, Karlsruher Institut für Technologie, Fakultät für Elektrotechnik and Informationstechnik, Dec. 2010.

[38] V. Degli-Esposti, "A Diffuse Scattering Model for Urban Propagation Prediction," *IEEE Trans. Antennas Propag.*, vol. 49, no. 7, pp. 1111–1113, 2001.

[39] V. Degli-Esposti, D. Guiducci, A. de'Marsi, P. Azzi, and F. Fuschini, "An Advanced Field Prediction Model Including Diffuse Scattering," *IEEE Trans. Antennas Propag.*, vol. 52, no. 7, pp. 1717–1728, 2004.

[40] V. Degli-Esposti, F. Fuschini, E. M. Vitucci, and G. Falciasecca, "Measurement and Modelling of Scattering From Buildings," *IEEE Trans. Antennas Propag.*, vol. 55, no. 1, pp. 143–153, 2007.

[41] E. M. Vitucci, F. Mani, V. Degli-Esposti, and C. Oestges, "Polarimetric Properties of Diffuse Scattering From Building Walls: Experimental Parameterization of a Ray-Tracing Model," *IEEE Trans. Antennas Propag.*, vol. 60, no. 6, pp. 2961–2969, 2012.

[42] J. Jarvelainen, K. Haneda, M. Kyro, V.-M. Kolmonen, J. Takada, and H. Hagiwara, "60 GHz radio wave propagation prediction in a hospital environment using an accurate room structural model," in *Antennas and Propagation Conference (LAPC), 2012 Loughborough*, 2012, pp. 1–4.

[43] J. Medbo, M. Riback, H. Asplund, and J. Berg, "MIMO Channel Characteristics in a Small Macrocell Measured at 5.25 GHz and 200 MHz Bandwidth," in *Vehicular Technology Conference, 2005. VTC-2005-Fall. 2005 IEEE 62nd*, vol. 1, Sept., 2005, pp. 372–376.

[44] A. Richter, "Estimation of Radio Channel Parameters: Models and Algorithms," Ph. D. dissertation, Ilmenau, Techn. University, February 2005, ISBN: 978-3-938843-02-4.

[45] C. Ribeiro, A. Richter, and V. Koivunen, "Joint Angular- and Delay-Domain MIMO Propagation Parameter Estimation Using Approximate ML Method," *IEEE Trans. Signal Process.*, vol. 55, no. 10, pp. 4775–4790, 2007.

[46] F. Heereman, W. Joseph, E. Tanghe, D. Plets, and L. Martens, "Prediction of Range, Power Consumption and Throughput for IEEE 802.11n in Large Conference Rooms," in *Antennas and Propagation (EUCAP), Proceedings of the 5th European Conference on*, 2011, pp. 692–696.

[47] ——, "Development of Path Loss Model for 802.11n in Large Conference Rooms," in *Antennas and Propagation (APSURSI), 2011 IEEE International Symposium on*, 2011, pp. 2785–2788.

[48] ——, "Small-scale Fading and Delay in Conference Room with 802.11 Coverage Problems," in *Antennas and Propagation (EUCAP), 2012 6th European Conference on*, 2012, pp. 2021–2024.

[49] F. Heereman, W. Joseph, E. Tanghe, D. Plets, A. Bamba, L. Verloock, and L. Martens, "Performance Loss Due to Multipath Propagation for IEEE 802.11 Systems," in *Antennas and Propagation (EuCAP), 2013 7th European Conference on*, 2013, pp. 2610–2613.

[50] P. Meissner and K. Witrisal, "Analysis of position-related information in measured UWB indoor channels," in *Antennas and Propagation (EUCAP), 2012 6th European Conference on*, 2012, pp. 6–10.

[51] K. Witrisal and P. Meissner, "Performance bounds for multipath-assisted indoor navigation and tracking (MINT)," in *Communications (ICC), 2012 IEEE International Conference on*, 2012, pp. 4321–4325.

[52] W. C. Sabine, *Collected papers on acoustics*. Cambridge: Harvard University Press, 1922.

[53] C. F. Eyring, "Reverberation Time in 'Dead' rooms," *The Journal of the Acoustical Society of Amarica*, vol. 1, no. 2, p. 241, 1930.

[54] H. Kuttruff, *Room Acoustics*. London: Taylor & Francis, 2000.

[55] D. A. Hill, *Electromagnetic Fields in Cavities: Deterministic and Statistical Theories*, ser. IEEE Press Series on Electromagnetic Wave Theory. Piscataway, NJ: Wiley/IEEE Press, 2009.

[56] T. H. Lehman, "A Statistical Theory of Electromagnetic Fields in Complex Cavities," Otto von Guericke University of Magdeburg, Tech. Rep., May 1993.

[57] C. Holloway, H. Shah, R. Pirkl, K. Remley, D. Hill, and J. Ladbury, "Early Time Behavior in Reverberation Chambers and Its Effect on the Relationships Between Coherence Bandwidth, Chamber Decay Time, RMS Delay Spread, and the Chamber Buildup Time," *IEEE Trans. Electromagn. Compat.*, vol. 54, no. 4, pp. 714–725, 2012.

[58] C. Holloway, D. Hill, J. Ladbury, P. Wilson, G. Koepke, and J. Coder, "On the Use of Reverberation Chambers to Simulate a Rician Radio Environment for the Testing of Wireless Devices," *IEEE Trans. Antennas Propag.*, vol. 54, no. 11, pp. 3167–3177, 2006.

[59] J. Sanchez-Heredia, J. Valenzuela-Valdes, A. Martinez-Gonzalez, and D. Sanchez-Hernandez, "Emulation of MIMO Rician-Fading Environments With Mode-Stirred Reverberation Chambers," *IEEE Trans. Antennas Propag.*, vol. 59, no. 2, pp. 654–660, 2011.

[60] J. Valenzuela-Valdes, A. Martinez-Gonzalez, and D. Sanchez-Hernandez, “Diversity Gain and MIMO Capacity for Nonisotropic Environments Using a Reverberation Chamber,” *IEEE Antennas Wireless Propag. Lett.*, vol. 8, pp. 112–115, 2009.

[61] O. Delangre, S. Van Roy, P. De Doncker, M. Lienard, and P. Degauque, “Modeling in-Vehicle Wideband Wireless Channels Using Reverberation Chamber Theory,” in *2007 IEEE 66th Vehicular Technology Conference, 2007. VTC-2007 Fall.* , Sept. 2007, pp. 2149–2153.

[62] F. Bellens, F. Quitin, F. Horlin, and P. De Doncker, “Channel Measurements and MB-OFDM Performance Inside a Driving Car,” in *International Conference on Electromagnetics in Advanced Applications, 2009. ICEAA ’09.* , Sept. 2009, pp. 392–395.

[63] M. Heddebaut, V. Deniau, and K. Adouane, “In-Vehicle WLAN Radio-Frequency Communication Characterization,” *Intelligent Transportation Systems, IEEE Transactions on*, vol. 5, no. 2, pp. 114–121, 2004.

[64] K. Hurst and S. Ellingson, “Path Loss From a Transmitter Inside an Aircraft Cabin to an Exterior Fuselage-Mounted Antenna,” *IEEE Trans. Electromagn. Compat.*, vol. 50, no. 3, pp. 504–512, Aug. 2008.

[65] R. E. Richardson, “Reverberant Microwave Propagation,” Naval Surface Warfare Center, Dahlgreen Division, Tech. Rep. NSWCDD/TR-08/127, Oct. 2008.

[66] E. Genender, C. Holloway, K. Remley, J. Ladbury, G. Koepke, and H. Garbe, “Simulating the Multipath Channel With a Reverberation Chamber: Application to Bit Error Rate Measurements,” *IEEE Trans. Electromagn. Compat.*, vol. 52, no. 4, pp. 766–777, 2010.

[67] C. Holloway, M. Cotton, and P. McKenna, “A model for predicting the power delay profile characteristics inside a room,” *IEEE Trans. Veh. Technol.*, vol. 48, no. 4, pp. 1110–1120, July 1999.

[68] R. Rudd, “Statistical prediciton of indoor radio channel impulse response,” Ph.D. dissertation, University of Surrey, Sept. 2007.

[69] J. B. Andersen, J. O. Nielsen, G. F. Pedersen, G. Bauch, and J. M. Herdin, “Room electromagnetics,” *IEEE Antennas Propag. Mag.*, vol. 49, no. 2, pp. 27–33, apr 2007.

[70] J. Nielsen, J. Andersen, G. Pedersen, and M. Pelosi, “On Polarization and Frequency Dependence of Diffuse Indoor Propagation,” in *Vehicular Technology Conference, 2011 IEEE 74th*, Sept. 2011.

[71] J. Andersen, K. L. Chee, M. Jacob, G. Pedersen, and T. Kurner, “Reverberation and Absorption in an Aircraft Cabin With the Impact of Passengers,” *IEEE Trans. Antennas Propag.*, vol. 60, no. 5, pp. 2472–2480, 2012.

[72] V. Degli-Esposti and H. L. Bertoni, “Evaluation of the Role of Diffuse Scattering in Urban Microcellular Propagation,” in *Vehicular Technology Conference, 1999. VTC 1999 - Fall. IEEE VTS 50th*, vol. 3, 1999, pp. 1392–1396.

[73] G. Rougeron, F. G. nd Yannik Gabillet, and K. Boutouch, “Simulation of the Indoor Propgation of a 60 GHz Electromagnetic Wave with a Time-

Dependent Radiosity Algorithm," *Computers & Graphics*, vol. 26, pp. 125–141, 2002.

[74] O. Franek, J. B. Andersen, and G. F. Pedersen, "Diffuse Scattering Model of Indoor Wideband Propagation," *IEEE Trans. Antennas Propag.*, vol. 59, no. 8, pp. 3006–3012, 2011.

[75] A. Saleh and R. Valenzuela, "A Statistical Model for Indoor Multipath Propagation," *IEEE J. Sel. Areas Commun.*, vol. 5, no. 2, pp. 128–137, 1987.

[76] M. Jakobsen, T. Pedersen, and B. Fleury, "Analysis of the Stochastic Channel Model by Saleh & Valenzuela via the Theory of Point Processes," in *International Zurich Seminar on Communications*. Zurich, Switzerland: Eidgenössische Technische Hochschule Zürich, Mar. 2012, http://dx.doi.org/10.3929/ethz-a-007023900.

[77] G. Turin, F. Clapp, T. Johnston, S. Fine, and D. Lavry, "A statistical model of urban multipath propagation channel," *IEEE Trans. Veh. Technol.*, vol. 21, pp. 1–9, Feb. 1972.

[78] J. Kunisch and J. Pamp, "An ultra-wideband space-variant multipath indoor radio channel model," in *Ultra Wideband Systems and Technologies, 2003 IEEE Conf. on*, Nov. 2003, pp. 290–294.

[79] M. Kaeske, M. Landmann, and R. Thoma, "Modelling and Synthesis of Dense Multipath Propagation Components in the Angular Domain," in *Antennas and Propagation, 2009. EuCAP 2009. 3rd European Conference on*, 2009, pp. 2641–2645.

[80] X. Yin, "High-Resolution Parameter Estimation for MIMO Channel Sounding," Ph.D. dissertation, Aalborg University, July 2006.

[81] N. Czink, P. Cera, J. Salo, E. Bonek, J.-P. Nuutinen, and J. Ylitalo, "A Framework for Automatic Clustering of Parametric MIMO Channel Data Including Path Powers," in *Proc. of the 64th IEEE Veh. Technol. Conf. (VTC)*, 2006, pp. 1–5.

[82] N. Czink, "The Random-Cluster Model - A Stochastic MIMO Channel Model for Broadband Communication Systems of the 3rd Generation and Beyond," Ph.D. dissertation, Institut für Nachrichtentechnik und Hochfrequenztechnik, Vienna University of Technology, 2007.

[83] N. Czink, E. Bonek, J. Nuutinen, and J. Ylitalo, "Parameterizing Geometry Based Stochastic MIMO Channel Models From Measurements Using Correlated Clusters," in *Proc. of the ITG Workshop on Smart Antennas*, Vienna, Austria, February 2007.

[84] K. Yu, Q. Li, D. Cheung, and C. Prettie, "On the Tap and Cluster Angular Spreads of Indoor WLAN Channels," in *Proc. of the 59th IEEE Veh. Technol. Conf. (VTC)*, vol. 1, 2004, pp. 218–222 Vol.1.

[85] X. Yin, T. Pedersen, N. Czink, and B. H. Fleury, "Parametric Characterization and Estimation of Bi-Azimuth and Delay Dispersion of Path Components," in *Proceedings of The First European Conf. on Antennas and Propagation (EuCAP)*, Acropolis, Nice, France, Nov. 2006.

[86] X. Yin, L. Liu, D. Nielsen, T. Pedersen, and B. Fleury, "A SAGE Algorithm for Estimation of the Direction Power Spectrum of Individual Path Components,"

in *Proc. IEEE Global Telecommunications Conference GLOBECOM '07*, Nov. 2007, pp. 3024–3028.

[87] X. Yin, L. Liu, T. Pedersen, D. K. Nielsen, and B. H. Fleury, "Modeling and estimation of the direction-delay power spectrum of the propagation channel," in *Proc. 3rd International Symposium on Communications, Control and Signal Processing ISCCSP 2008*, Mar. 2008, pp. 225–230.

[88] L. M. Correia, *Wireless Flexible Personalised Communications: COST 259: European Co-operation in Mobile Radio Research*. John Wiley and Sons Ltd, 3 2001.

[89] ——, *Mobile Broadband Multimedia Networks: Techniques, Models and Tools for 4G*. Academic Press, 5 2006.

[90] R. Verdone and A. Zanella, Eds., *Pervasive Mobile and Ambient Wireless Communications: COST Action 2100 (Signals and Communication Technology)*. Springer, jan 2012.

[91] J. Poutanen, "Geometry-based Radio Channel Modeling: Propagation Analysis and Concept Development," Ph.D. dissertation, Aalto University, School of Electronic Engineering, Mar. 2011.

[92] J. Salmi, J. Poutanen, K. Haneda, A. Richter, V. M. Kolmonen, P. Vainikainen, and A. Molisch, "Incorporating Diffuse Scattering in Geometry-based Stochastic MIMO Channel Models," in *Antennas and Propagation (EuCAP), 2010 Proceedings of the Fourth European Conference on*, 2010, pp. 1–5.

[93] C. M. Bishop and N. M. Nasrabadi, *Pattern recognition and machine learning*. springer New York, 2006, vol. 1.

[94] Q. H. Spencer, B. Jeffs, M. Jensen, and A. Swindlehurst, "Modeling the statistical time and angle of arrival characteristics of an indoor multipath channel," *IEEE J. Sel. Areas Commun.*, vol. 18, no. 3, pp. 347–360, 2000.

[95] C.-C. Chong, C.-M. Tan, D. Laurenson, S. McLaughlin, M. Beach, and A. Nix, "A New Statistical Wideband Spatio-Temporal Channel Model for 5-GHz Band WLAN Systems," *IEEE J. Sel. Areas Commun.*, vol. 21, no. 2, pp. 139–150, 2003.

[96] Y. Lustmann and D. Porrat, "Indoor Channel Spectral Statistics, K-Factor and Reverberation Distance," *IEEE Trans. Antennas Propag.*, vol. 58, no. 11, pp. 3685–3692, Nov. 2010.

[97] N. Jalden, P. Zetterberg, B. Ottersten, A. Hong, and R. Thomä, "Correlation Properties of Large Scale Fading Based on Indoor Measurements," in *Wireless Communications and Networking Conference (WCNC)*, March 2007.

[98] A. Bamba, W. Joseph, J. Andersen, E. Tanghe, G. Vermeeren, D. Plets, J. Nielsen, and L. Martens, "Experimental Assessment of Specific Absorption Rate Using Room Electromagnetics," *IEEE Trans. Electromagn. Compat.*, vol. 54, no. 4, pp. 747–757, Aug. 2012.

[99] S. van de Beek, K. Remley, C. Holloway, J. Ladbury, and F. Leferink, "Characterizing Large-Form-Factor Devices in a Reverberation Chamber," in *International Symposium on Electromagnetic Compatibility (EMC EUROPE)*, Sept. 2013, pp. 375–380.

[100] W. Burger, K. Remley, C. Holloway, and J. Ladbury, "Proximity and Antenna Orientation Effects for Large-Form-Factor Devices in a Reverberation Chamber," in *International Symposium on Electromagnetic Compatibility (EMC)*, Aug. 2013, pp. 671–676.

[101] G. Steinböck, T. Pedersen, B. Fleury, W. Wang, and R. Raulefs, "Calibration of the Propagation Graph Model in Reverberant Rooms," in *URSI Commission F Triennial Open Symposium on Radiowave Propagation and Remote Sensing*, May 2013.

Paper A

# Experimental Characteristics of Indoor Wideband MIMO Radio Channels and their Impact on Stochastic Modeling

Gerhard Steinböck, Xuefeng Yin, Troels Pedersen and Bernard H. Fleury

*IEEE 13th Digital Signal Processing Workshop and 5th IEEE Signal Processing Education Workshop. DSP/SPE 2009*

© 2009 IEEE
*The layout has been revised.*

## Abstract

We compare two methods for estimation of path-component spreads in bi-azimuth and delay, namely the clustering approach and the density approach, in indoor environments. Monte Carlo simulations reveal possible shortcomings of the clustering approach. Published estimates of component spreads in delay, azimuth of departure and azimuth of arrival obtained with the clustering approach are reviewed and contrasted with estimates gathered using the density approach. A detailed study of these experimental data, aided with the insight gained from the simulation results, leads to the conjecture that in some cases the estimated spreads computed with the clustering approach are too large. The settings of the path component spreads of two widely used models including bi-azimuth delay dispersion, namely the Winner II Model and the 802.11 Tgn Model are revisited based on these findings. The investigations stress the obvious, but apparently sometimes forgotten, importance of validating the behavior and performance of channel parameter estimation techniques before using these tools to extract empirical information from measurement data.

## A.1 Introduction

The response of the radio channel is commonly modeled as a superposition of a number of "path components". Each of these components represents the contribution of some electromagnetic wave, propagating from the transmitter to the receiver via a specific propagation path. Along this path the wave may interact with a number of objects called "scatterers". The path components may be dispersive in delay, direction of departure (DoD), direction of arrival (DoA), Doppler frequency and in polarizations, due to the electromagnetic and geometric properties of the scatterers (see Fig. A.1). In the sequel, we refer to these dimensions as dispersion dimensions. In [1–3] it is stressed that stochastic models need to include the dispersive behavior of individual path components in order to accurately emulate real propagation channels.

The Bartlett spectral estimator [4] is widely used to assess dispersion of the radio channel in DoA, DoD or jointly in both directions. The direction or bi-direction Bartlett spectrum usually provides a good insight into the distribution of dominant path components, especially in wide-band scenarios, when it is computed as a function of the delay. Indeed, the nominal values, or centers of gravity, of these components in these dimensions can usually be assessed with a reasonable accuracy. The Bartlett spectrum is, however, not appropriate to assess the dispersive behavior of these individual components, because the spreads of these components are typically below the resolution of practical antenna arrays.

High resolution methods rely on parametric models that aim at circumventing the impact of the system response by exploiting certain assumptions

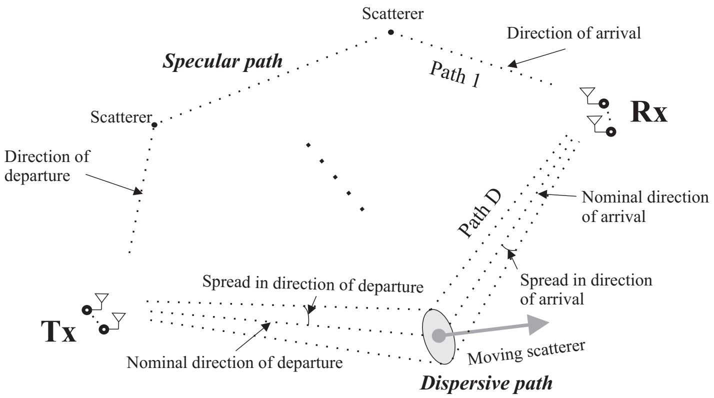
Scatterer
Direction of arrival
Specular path
Path 1
Rx
Scatterer
Direction of departure
Path D
Nominal direction of arrival
Spread in direction of arrival
Spread in direction of departure
Tx
Nominal direction of departure
Moving scatterer
Dispersive path

*Fig. A.1: Schematic representation of multipath propagation.*

on the channel property. In our particular application it is assumed that waves can be considered as planar and specular, or nearly specular, over small regions including the transmit and receive arrays. Two main approaches for characterization of dispersive path components have been proposed in the literature. The first approach uses density functions to describe the power spectral density of dispersive path components and directly estimates the parameters of these density functions [5–10]. We refer to this approach as the "density approach". The second, so-called "clustering approach", attempts to approximate the dispersive path components by superpositions of specular components [11–15]. In a first stage a feasible high-resolution technique, commonly based on the SAGE (Space Alternating Generalized Expectation-maximization) algorithm [16], is applied on measurement data to estimate the characteristics of these specular components. In a second stage the estimated components undergo a manual or automated pruning process based on a predetermined selection criterion. Those components retained are grouped in "clusters", each cluster representing an individual dispersive path component. The dispersion characteristics of each dispersive path component, i.e. nominal values and spreads, are then extracted from the parameters of the specular components in the corresponding cluster.

The paper is organized as follows. The signal model of the radio channel including dispersive path components is introduced in Section A.2. Section A.3 gives a short literature review of previous works on the clustering and density approaches. The performances of the clustering and density approaches are investigated in Section A.4. This section also reviews values of component spreads obtained experimentally with both approaches, as well as such values specified in two widely used channel models including bi-azimuth-delay dispersion. Concluding remarks are stated in Section A.5.

## A.2 Signal Model

We consider the propagation environment depicted in Fig. A.1. The components of the complex baseband signal vector $\mathbf{s}(t) \in \mathbb{C}^{M_1}$ are fed to the inputs of the $M_1$ transmit antennas. The signals radiated by these antennas propagate via $D$ paths to the $M_2$ receive antennas. The signal $\mathbf{Y}(t) \in \mathbb{C}^{M_2}$ at the outputs of these antennas reads [9]

$$\mathbf{Y}(t) = \int_{-\infty}^{\infty} \int_{\mathbb{S}_2} \int_{\mathbb{S}_2} \mathbf{c}_2(\boldsymbol{\Omega}_2)\mathbf{c}_1(\boldsymbol{\Omega}_1)^T \mathbf{s}(t-\tau) \\ h(\boldsymbol{\Omega}_1, \boldsymbol{\Omega}_2, \tau) d\boldsymbol{\Omega}_1 d\boldsymbol{\Omega}_2 d\tau + \mathbf{W}(t), \quad \text{(A.1)}$$

where $\tau$ is the propagation delay and $\mathbf{c}_i(\boldsymbol{\Omega}_i)$ is the response in direction $\boldsymbol{\Omega}_i$ of the transmit ($i = 1$) or the receive ($i = 2$) array. Here, $(\cdot)^T$ denotes the transpose operation. A direction $\boldsymbol{\Omega}$ is an element of the unit sphere $\mathbb{S}_2$. It is specified by its azimuth $\phi \in [-\pi, \pi)$ and co-elevation $\theta \in [0, \pi]$ according to $\boldsymbol{\Omega} = [\cos(\phi)\sin(\theta), \sin(\phi)\cos(\theta), \cos(\theta)]^T$. The noise vector $\mathbf{W}(t) \in \mathbb{C}^{M_2}$ is a spatially and temporarily white circularly symmetric complex Gaussian process.

It is assumed that the bi-direction-delay spread function $h(\boldsymbol{\Omega}_1, \boldsymbol{\Omega}_2, \tau)$ of the radio channel can be decomposed into $D$ uncorrelated (or orthogonal) processes:

$$h(\boldsymbol{\Omega}_1, \boldsymbol{\Omega}_2, \tau) = \sum_{d=1}^{D} h_d(\boldsymbol{\Omega}_1, \boldsymbol{\Omega}_2, \tau). \quad \text{(A.2)}$$

Each process is meant to be contributed by a wave propagating along a specific propagation path. Assuming that the $D$ processes in (A.2) are uncorrelated, the bi-direction-delay power spectrum is of the form

$$\begin{aligned} P(\boldsymbol{\Omega}_1, \boldsymbol{\Omega}_2, \tau) &= \mathbb{E}\left[ |h(\boldsymbol{\Omega}_1, \boldsymbol{\Omega}_2, \tau)|^2 \right] && \text{(A.3)} \\ &= \sum_{d=1}^{D} P_d(\boldsymbol{\Omega}_1, \boldsymbol{\Omega}_2, \tau), && \text{(A.4)} \end{aligned}$$

where $\mathbb{E}[\cdot]$ denotes the expectation operator and

$$P_d(\boldsymbol{\Omega}_1, \boldsymbol{\Omega}_2, \tau) = \mathbb{E}\left[ |h_d(\boldsymbol{\Omega}_1, \boldsymbol{\Omega}_2, \tau)|^2 \right] \quad \text{(A.5)}$$

is the bi-direction-delay power spectrum of the $d$th path component.

## A.3 Dispersive Path Parameter Estimators

In this section we briefly review two proposed high-resolution techniques for estimating dispersive path components, namely the clustering approach, which represents dispersive path components with a sum of specular components, and the density approach, which models the power spectral densities of individual dispersive path components by means of a parametric family of density functions.

### A.3.1 Clustering Approach

In the clustering approach the power spectrum of the $d$th dispersive path component of (A.5) is represented by $N_d$ specular components:

$$P_d(\mathbf{\Omega}_1, \mathbf{\Omega}_2, \tau) = \sum_{j=1}^{N_d} P_{d,j} \cdot \delta(\mathbf{\Omega}_1 - \mathbf{\Omega}_{1,d,j}) \cdot \delta(\mathbf{\Omega}_2 - \mathbf{\Omega}_{2,d,j}) \cdot \delta(\tau - \tau_{d,j}), \quad \text{(A.6)}$$

where $P_{d,j}$, $\mathbf{\Omega}_{1,d,j}$, $\mathbf{\Omega}_{2,d,j}$ and $\tau_{d,j}$ are respectively the power, the DoD, the DoA, and the delay of the $j$th specular component of the $d$th dispersive path component, and $\delta(\,\cdot\,)$ denotes the Dirac delta function. The number of specular components $N_d$ may depend on $d$. The nominal and spread parameters of each dispersive path component are calculated as

$$\bar{\eta}_d = \frac{\sum_{j=1}^{N_d} P_{d,j}\eta_{d,j}}{\sum_{j=1}^{N_d} P_{d,j}} \quad \text{(A.7)}$$

$$\sigma_{\eta_d} = \sqrt{\frac{\sum_{j=1}^{N_d} P_{d,j}(\eta_{d,j} - \bar{\eta}_d)^2}{\sum_{j=1}^{N_d} P_{d,j}}}, \quad \text{(A.8)}$$

where $\eta$ may stand for $\phi_1$, $\theta_1$, $\phi_2$, $\theta_2$, or $\tau$.

In the clustering approach estimation of dispersive path components is performed in two stages. In the first stage, the bi-direction-delay spread function is represented as a sum of specular components:

$$h(\mathbf{\Omega}_1, \mathbf{\Omega}_2, \tau) = \sum_{n=1}^{N} h_n \cdot \delta(\mathbf{\Omega}_1 - \mathbf{\Omega}_{1,n}) \cdot \delta(\mathbf{\Omega}_2 - \mathbf{\Omega}_{2,n}) \cdot \delta(\tau - \tau_n). \quad \text{(A.9)}$$

A high-resolution estimator, usually based on the SAGE algorithm, is used to extract the parameters $h_n$, $\mathbf{\Omega}_{1,n}$, $\mathbf{\Omega}_{2,n}$, and $\tau_n$, $n = 1 \ldots N$ from each channel realization. In the second stage, the estimated specular components gathered from $N_c$ realizations, undergo a selection process and those components retained are grouped into clusters. The components allocated to one cluster form an estimate of its power spectrum (A.6). The corresponding component parameters are plugged in (A.7) and (A.8) to obtain estimates of the nominal values and spreads of the cluster in the dispersion dimensions.

The various implementations of the clustering approach found in the literature differ in the pruning and grouping methods in the second stage and in the investigated dispersion dimensions. In the sequel we shortly review these implementations. All of them consider horizontal-only propagation, i.e., a direction is specified by its azimuth only: $\boldsymbol{\Omega} = [\cos(\phi), \sin(\phi)]^T$.

In [13] static multiple-input multiple-output (MIMO) indoor channel measurements are processed to assess dispersion in azimuth of arrival (AoA) and azimuth of departure (AoD). The measurement data is partitioned into subsets collected in frequency sub-bands and using specific sub-arrays. The sub-bands and sub-arrays are selected in such a way that the channel transfer functions corresponding to any two subsets of data are nearly uncorrelated. Several thousand of specular path components are estimated from these subsets. The estimated components are selected and grouped into clusters by means of a visual inspection procedure relying on a computed bi-azimuth Bartlett spectrum.

In [11, 14] delay-AoA dispersion in large office, foyer, and laboratory environments is experimentally investigated from single-input multiple-output (SIMO) measurement data. The delay-AoA spread function reconstructed from estimated specular components is convolved with either a 2-dimensional Gaussian density kernel [11] or a Hanning window [14]. Pruning and grouping of the estimated components are carried out by visual inspection of the squared-magnitude of the smoothed delay-AoA spread functions.

The clustering approaches discussed so far rely all on visual inspection by a "trained" person. This step introduces a significant amount of heuristic. Indeed, the individual decisions of the trained person regarding the pruning and grouping of the specular path components heavily influence the results and make them difficult to compare. Moreover, the visual cluster identification is time-consuming and therefore inappropriate for processing large amounts of measurement data. A framework for automatic clustering of the estimated specular path components, using the $k$-means algorithm, is introduced in [15] and applied in [12].

### A.3.2 Density Approach

In the density approach the power spectral density (A.5) of path component $d$ is recast according to

$$P_d(\boldsymbol{\Omega}_1, \boldsymbol{\Omega}_2, \tau) = P_d \cdot f(\boldsymbol{\Omega}_1, \boldsymbol{\Omega}_2, \tau; \boldsymbol{\theta}_d), \tag{A.10}$$

where $P_d$ denotes the average power of the $d$th component. The normalized bi-direction-delay power spectral density $f(\boldsymbol{\Omega}_1, \boldsymbol{\Omega}_2, \tau; \boldsymbol{\theta}_d)$ is an element of a family of density functions indexed by the parameter vector $\boldsymbol{\theta}_d$ .

*Table A.1: Parameter settings for the simulations.*

| | | |
|---|---|---|
| $f_c$ = 5.25 GHz | $\bar{\tau}$=15 ns | $\sigma_\tau$=3.5 ns |
| Bandwidth = 100 MHz | $\bar{\phi}_1$=0° | $\sigma_{\phi_1}$=11° |
| SNR=30 dB, $N_c$=4 | $\bar{\phi}_2$=0° | $\sigma_{\phi_2}$=2° |

In [9] the constrained maximum-entropy principle is proposed to select the family. More specifically, the family is the solution of the problem of finding the density function maximizing the entropy, under the constraint that density's first and second moments are specified. Various solutions for various subsets of dispersion dimensions have been published [9, 10]. They all lead to density functions of the von-Mises-Fisher kind. The investigations performed in [9] aim at experimentally characterizing bi-azimuth and delay dispersion. Moreover, horizontal-only propagation is assumed. The maximum-likelihood estimator of the parameters $\boldsymbol{\Theta} = [\boldsymbol{\theta}_1, \ldots \boldsymbol{\theta}_D]$ is approximated using the SAGE algorithm [9]. The method is applied in Section A.4.2. The reader is referred to [9] for a detailed description of the family of density functions and the maximum-likelihood estimator.

For the sake of completeness it should be mentioned that early implementations of the density approach have been already proposed, however with a different application in mind [5–8].

## A.4 Numerical and Experimental Results

The density and clustering approaches are compared by simulation in Section A.4.1. In Section A.4.2 the density approach is applied to measurement data. These obtained experimental results are compared to empirical values found in literature in Section A.4.3 and parameter settings of stochastic models in Section A.4.4.

### A.4.1 Accuracy of Spread Estimators

We consider the scenario described by the the settings in Table A.1 for the Monte Carlo simulation. The arrays at the transmitter and the receiver have the same response, which coincides with that of the 9-element circular array used to collect the measurement data processed in Section A.4.2 and [9]. In each simulation run the signal model described in Section A.2 is used to generate the signal contributed by one dispersive path component with dispersion characteristics reported in Table A.1. The density estimator described in [9] is applied to estimate the parameters of the bi-azimuth-delay power spectrum.

We now describe the generic clustering approach considered for the simulations. This approach applies a pruning procedure similar to the clustering

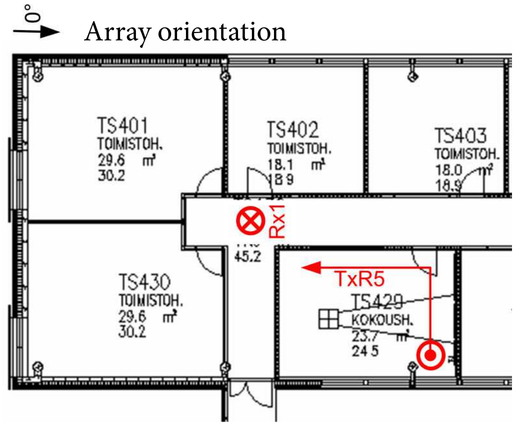

*Fig. A.2: The investigated environment [17, Scenario TxR5].*

approaches described in Section A.3.1, and therefore is equivalent to share their behaviors. The SAGE algorithm [16] processes the signals generated in each run to estimate a certain fixed number $N$ of specular path components, i.e. to compute an estimate of (A.9); $N_c$ consecutive runs are processed in this way to obtain $N_c \cdot N$ specular component estimates. Pruning of the path components is conducted as follows: Among the $N_c \cdot N$ components, only those with power larger than a given dynamic range (DR) with respect to the maximum component power are retained. The power of a component is its squared absolute weight. The retained set of path components form an estimate of (A.10). Estimates of the nominal azimuth and azimuth spread are computed by plugging the parameters of these estimates in (A.7) and (A.8). The average of 100 azimuth spread estimates is depicted in Fig. A.3 versus $N$ for different DRs. Notice that no component is discarded when DR=$\infty$.

The results depicted in Fig. A.3 show that the choice of the DR and the parameter $N$ heavily influence the behavior of the clustering approach. For instance for the large true spread in Fig. A.3 (a) with $N$=4 and DR$\geq$18 dB, the cluster based method underestimates the spread. For a small true spread as in Fig. A.3 (b), the same setting leads to overestimation of the spread. This example clearly exposes the difficulty in optimizing the setting of DR; the appropriate setting depends on the true spread value as well as the number of components $N$ extracted for a cluster — both of which are unknown in real measurements. Notice that $N$=4 is a typical value returned by the high-resolution estimation algorithms used in the clustering approaches.

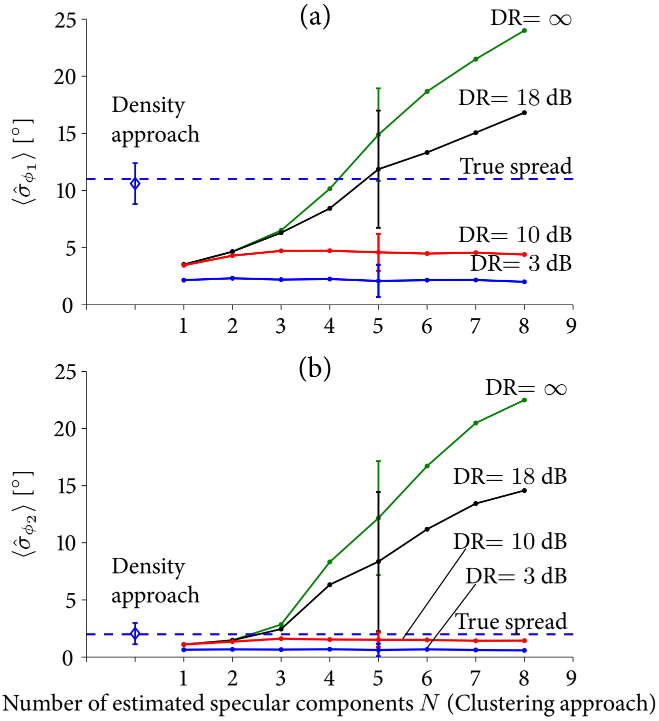

*Fig. A.3: Comparison of the estimated AoD spread (a) and AoA spread (b) computed with the density estimator and the clustering method. The clustering method uses different settings of the number of specular components $N$ and DR. The error bars indicate the standard deviations of the estimates.*

## *A.4.2 Component Spreads of Measured Data Estimated with the Density Approach*

Measurement data collected in an office environment with a channel sounder operating with the settings reported in the first column in Table A.1 are used to experimentally assess the performance of the density estimator. A map of the investigated environment including the transmitter trajectory (in red) and the receiver position is shown in Fig. A.2. The transmitter was pushed with an approximate speed of 0.5 $\mathrm{m/s}$. The data collected within the first $N_c$=20 measurements from the instant the transmitter started moving are considered in this investigation. The traveled distance between the data acquisitions of 20 consecutive measurements is approximately 14 $\mathrm{cm}$. We assume that the propagation conditions are approximately constant over this distance. A more detailed explanation of the measurement campaign, referred to as TxR5, can be found in [17]. The estimator described in [9] is used to estimate the bi-azimuth-delay power spectral density of individual path components.

*Table A.2: Parameter estimates of the power spectral density of individual components.*

| $d$ | $\hat{P}_d$ [dB] | $\hat{\sigma}_{\tau,d}$ [ns] | $\hat{\sigma}_{\phi_1,d}$ [°] | $\hat{\sigma}_{\phi_2,d}$ [°] | $\hat{\rho}_{\phi_1,\tau,d}$ | $\hat{\rho}_{\phi_2,\tau,d}$ | $\hat{\rho}_{\phi_1,\phi_2,d}$ |
|---|---|---|---|---|---|---|---|
| 1 | −54 | $\leq 0.5$ | 3.7 | 3.0 | – | – | −0.90 |
| 2 | −56 | $\leq 0.5$ | 5.9 | 6.0 | – | – | 0.39 |
| 3 | −56 | 1.8 | 14.7 | 0.7 | −0.42 | 0.06 | 0.39 |
| 4 | −59 | 0.9 | 6.0 | 3.5 | 0.35 | 0.06 | −0.90 |
| 5 | −60 | $\leq 0.5$ | 5.7 | 14.1 | – | – | 0.82 |
| 6 | −58 | $\leq 0.5$ | 3.5 | 4.1 | – | – | −0.90 |
| 7 | −59 | 3.5 | 13.5 | 3.2 | 0.40 | −0.01 | −0.79 |
| 8 | −64 | 5.3 | 2.9 | 8.0 | −0.42 | −0.01 | −0.90 |
| avg. | | 1.7 | 7.0 | 5.3 | | | |
| std. | | 1.8 | 4.5 | 4.1 | | | |

–: values are neglected due to small delay spread estimates.

Due to the limited bandwidth of the sounding signal, we set the minimum delay spread to be estimated to one tenth of the sample interval, i.e. 0.5 $\mathrm{ns}$. Moreover, the coupling coefficients between the spreads in delay and azimuths are only considered when the delay spread is strictly larger than this value. To avoid numerical problems, we set the maximum absolute value of the coupling coefficients between AoA and AoD to 0.9 instead of 1.

The SAGE algorithm [9] estimates $D$=8 path components, using 6 iterations (per component). The dynamic range of the component power is set to 30 dB, i.e. the components found with power 30 dB less than the largest component power are discarded. The results are reported in Table A.2. In this table, $(\hat{\cdot})$ denotes an estimate of the parameter given as an argument. It can be seen that some of the dispersed components are highly concentrated with small delay spread ($\leq$0.5 $\mathrm{ns}$).

Bi-azimuth Bartlett spectra computed at different delay bins from the sample covariance matrix $(\widehat{\mathbf{\Sigma}})$ are reported in the first column of Fig. A.4. The third column depicts the contour plots of the bi-azimuth power spectra $(\hat{P}(\phi_1, \phi_2, \tau))$ derived from the estimated bi-azimuth-delay power spectrum computed with the density approach. Finally, the second column depicts the bi-azimuth Bartlett spectra computed from the covariance matrix $(\mathbf{\Sigma}(\widehat{\mathbf{\Theta}}))$ reconstructed from the estimated bi-azimuth-delay power spectrum. Most of the estimated components have their delays in the three considered bins. The shape and size of the corresponding footprints of the dispersive components in two adjacent Bartlett spectra are very similar. The estimated component power densities are much more concentrated than the corresponding footprints in the Bartlett spectra.

### A.4.3 Comparison of Experimentally Obtained Path Component Spreads

The upper part of Table A.3 summarizes published estimates of path-component spreads experimentally obtained using the clustering methods described in Section A.3, as well as the results presented in [18]. Minima, maxima and means of average values computed over different environments and positions are reported. The number of dispersive components $D$ and the number of specular components $N_d$ are average values as well. The results presented in this paper using the density approach are summarized in Table A.3 for comparison.

It can be observed from Table A.3 that all cluster approaches lead to larger delay spread compared to the values obtained with the density approach. The same observation holds for the minimum azimuth spreads, apart from [13]. It appears that the reported maximum azimuth spreads are in accordance for both approaches. All clustering approaches but [13] lead to larger average values for the azimuth spreads. The range and average of azimuth spread estimates presented in [13] are more or less in agrement with the results obtained with the density approach. Fig. 8 in reference [13] shows that this "manual" clustering approach leads to an unbiased estimator when the true azimuth spread is lower that $5°$. Above $5°$, the estimator under estimates the true spread.

Although clear and definitive conclusions can be hardly drawn from Table A.3, the observed trend is that the considered clustering approaches but [13] tend to lead to larger spreads compared to the density approach. Two theses are proposed that can explain this discrepancy: 1) The spread values are obtained from experimental investigations of delay-azimuth dispersion in specific indoor channels [11, 13, 14, 18]. Some path components with small spreads that might be resolvable in the bi-azimuth delay dimensions, i.e. with the density approach in [9], might appear as one component with larger spreads when resolved in the delay-azimuth dimensions only; 2) As discussed in Section 4.1 over-estimation of the spreads might be a result of the inherent behavior of the clustering approach.

### A.4.4 Component Spreads in Standard Models, Revisited

The settings of the spread parameters of two widely used indoor channel models supporting per-cluster direction and delay spreads are included in the bottom part of Table A.3. The reader is referred to the provided references for a detailed description of these models. The 802.11 Tgn channel Model B (typical large open space and office environments, NLOS conditions, and 100 ns rms delay spread) [19] is based on a tapped delay line with inter-tap spacing of 10 $\mathrm{ns}$. All cluster taps exhibit the same azimuth spread. The Winner II Model scenario A1 (Indoor Office) [20] relies on a geometric cluster representation.

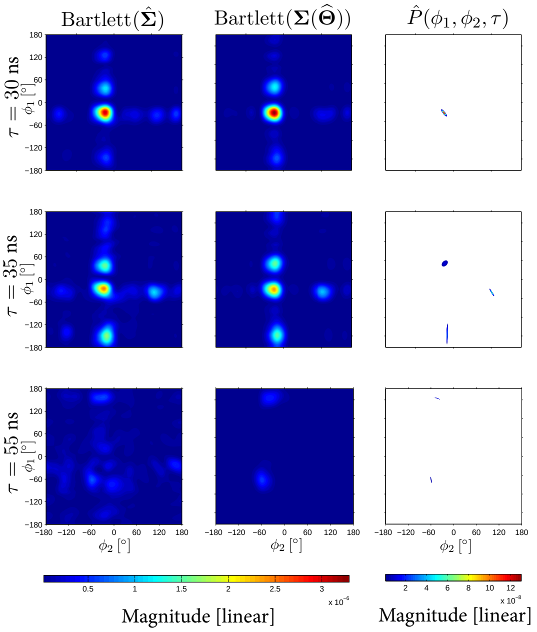

*Fig. A.4: Bi-azimuth spectra versus delay in an indoor environment. (for more details see Section A.4.2)*

A less complex implementation, based on a "cluster delay line" in which each tap is considered as a cluster, is suggested too. The inter-tap spacing is 5 ns. The tap spacings of these two models are of the same order as the resolution of the sounding equipments used to collect the measurement data based on which the results depicted in the top part of Table A.3 are obtained. For instance, the sounder used to gather the data processed in Section A.4.2 has a 10 ns resolution. We conclude from this observation that the taps in the 802.11 Tgn and Winner II models can be viewed as dispersive path components in the sense described in this paper.

The component spreads specified in the Winner II Model A1 rely partly on the experimental results of [12, 13] and correspond to mean values reported in these references. They are in accordance with the experimental values found in Table A.2. The setting of spread values of the 802.11 Tgn Model B has been selected based on the results of [11, 14, 18]. The specified spread values are significantly larger that those given in Table A.2. The over-estimation trend of the clustering approach mentioned in the previous section might partly explain this observation.

The COST273 [21] model supports dispersion in bi-azimuth and delay of so-called clusters of path components. The values provided for the cluster spreads in picocell environments [21] are usually much larger, e.g. $\sigma_\tau$=300 ns

*Table A.3: Selected published values of spread parameters for indoor environments.*

| Ref. | $D$ | $N_d$ | $\sigma_\tau$ [ns] | | | $\sigma_{\phi,1}$ [°] | | | $\sigma_{\phi,2}$ [°] | | |
|---|---|---|---|---|---|---|---|---|---|---|---|
| | | | min | max | avg. | min | max | avg. | min | max | avg. |
| **Experimental Results** | | | | | | | | | | | |
| Table A.2 | 8.0 | | $\leq$0.5 | 5.3 | 1.7 | 2.9 | 14.7 | 7.0 | 0.7 | 14.1 | 5.3 |
| [11] | 8.0 | 5.0 | 13.4 | 37.9 | – | | | | 3.3 | 9.5 | – |
| [12] | 11.0 | 8.0 | 6.0 | 10.0 | 7.8 | 10.8 | 19.0 | 15.7 | 9.3 | 14.9 | 12.2 |
| [13] | 8.8 | | | | | 2.4 | 11.1 | 5.2 | 2.6 | 8.2 | 5.5 |
| [14] | 4.5 | | | | | | | | 5 | 25 | 13.7 |
| [18] | 4.0 | | | | | | | | 22.0 | 26.0 | – |
| **Settings in Two Commonly Used Channel Models** | | | | | | | | | | | |
| Winner II [20] | 13.3 | 20.0 | 6.0 | 10.0 | – | 5.0 | 6.0 | – | 5.0 | 13.0 | – |
| 802.11 Tgn [19] | 9.0 | | | | | 14.4 | 25.4 | – | 14.4 | 25.2 | – |

and $\sigma_{\phi,2}$=30°. This indicates that these clusters cannot be identified with the dispersive components described in Section A.3. Clusters defined in the COST273 sense appear to be clusters of such dispersive components. Further studies are, however, necessary to clarify this conjecture.

## *A.5 Discussion and Conclusion*

The paper addresses some important aspects related to the high-resolution estimation of dispersion in radio channels. To this end, we have studied the behavior and performance of two approaches for estimating the spreads of individual path components in indoor environments, namely the clustering approach and the density approach.

The reported simulation results reveal the shortcomings of the clustering approach, when it is used to estimate component spreads. The method, combined with a trained visual inspection, seems to work appropriately [13]. The heuristic and manual steps in the selection of the clusters, however, make it difficult to accept it as a qualitative tool. The simulation results also show that the density approach is an efficient alternative to the clustering approach. The review of experimental component spreads presented in Section A.4.3 demonstrates the difficulty of comparing similar experimental qualities, when they are gathered in different environments and processed using different methods. It is conjectured that some of the spread values reported in the literature are too large to characterize bi-azimuth-delay dispersion of path components. Two possible theses have been formulated to explain this effect: 1) the intrinsic behavior of the clustering approach and 2) the fact that the experimental investigations were limited to azimuth-delay dispersion of the radio channel, so another additional dimension, i.e. azimuth of departure, was not exploited to resolve path components.

Some of the reported experimental results have been used to specify the settings of the component spreads of the Winner II Model A1 (Indoor Office) and the 802.11 Tgn Model B (typical NLOS large open space and office environments). The discussion shows that the values selected in the parameter settings of these models are as reliable as the estimators used to extract the empirical information based on which these parameters are selected. This – apparently obvious observation – stresses the necessity to validate channel parameter estimators in order to clearly understand their behavior and performance.

The discussions in Section A.4.3 and Section A.4.4 rely on limited experimental evidence gathered from a small set of results obtained with the density approach. However, further experimental observations not reported here confirm the presented theses. Nevertheless, a more comprehensive study is necessary in order to definitely confirm them, and especially to confirm the conjecture that path component spreads in bi-direction and delay are typically smaller that commonly believed.

## *References*

[1] K.-H. Li, M. Ingram, and A. Van Nguyen, "Impact of Clustering in Statistical Indoor Propagation Models on Link Capacity," *IEEE Trans. Commun.*, vol. 50, no. 4, pp. 521–523, 2002.

[2] Z. Tang and A. S. Mohan, "Impact of Clustering in Indoor MIMO Propagation Using a Hybrid Channel Model," *EURASIP J. Appl. Signal Process.*, vol. 2005, no. 1, pp. 1698–1711, 2005.

[3] T. Betlehem, T. Abhayapala, and T. Lamahewa, "Space-Time MIMO Channel Modelling Using Angular Power Distributions," in *Proc. of Australian Commun. Theory Workshop*, 2006, pp. 165–170.

[4] M. Bartlett, "Smoothing periodograms from time series with continuous spectra," *Nature*, vol. 161, 1948.

[5] M. Bengtsson and B. Ottersten, "Low-Complexity Estimators for Distributed Sources," *IEEE Trans. Signal Process.*, vol. 48, no. 8, pp. 2185–2194, 2000.

[6] T. Trump and B. Ottersten, "Estimation of Nominal Direction of Arrival and Angular Spread Using an Array of Sensors," *Signal Process.*, vol. 50, no. 1-2, pp. 57–69, 1996.

[7] O. Besson and P. Stoica, "Decoupled Estimation of DOA and Angular Spread for a Spatially Distributed Source," *IEEE Trans. Signal Process.*, vol. 48, no. 7, pp. 1872–1882, 2000.

[8] C. Ribeiro, A. Richter, and V. Koivunen, "Joint Angular- and Delay-Domain MIMO Propagation Parameter Estimation Using Approximate ML Method," *IEEE Trans. Signal Process.*, vol. 55, no. 10, pp. 4775–4790, 2007.

[9] X. Yin, T. Pedersen, N. Czink, and B. H. Fleury, "Parametric Characterization and Estimation of Bi-Azimuth and Delay Dispersion of Path Components," in *Proc. of the First European Conf. on Antennas and Progation (EuCAP)*. Acropolis, Nice, France: EuCAP, November 2006.

[10] X. Yin, L. Liu, T. Pedersen, D. K. Nielsen, and B. H. Fleury, "Modeling and estimation of the direction-delay power spectrum of the propagation channel," in *Proc. 3rd Int. Symposium on Commun., Control and Signal Process. ISCCSP 2008*, Mar. 2008, pp. 225–230.

[11] C.-C. Chong, C.-M. Tan, D. Laurenson, S. McLaughlin, M. Beach, and A. Nix, "A New Statistical Wideband Spatio-Temporal Channel Model for 5-GHz Band WLAN Systems," *IEEE J. Sel. Areas Commun.*, vol. 21, no. 2, pp. 139–150, 2003.

[12] N. Czink, E. Bonek, J. Nuutinen, and J. Ylitalo, "Parameterizing Geometry Based Stochastic MIMO Channel Models From Measurements Using Correlated Clusters," in *Proc. of the ITG Workshop on Smart Antennas*, Vienna, Austria, February 2007.

[13] N. Czink, X. Yin, H. Özcelik, M. Herdin, E. Bonek, and B. Fleury, "Cluster Characteristics in a MIMO Indoor Propagation Environment," *IEEE Trans. Wireless Commun.*, vol. 6, no. 4, pp. 1465–1475, 2007.

[14] K. Yu, Q. Li, D. Cheung, and C. Prettie, "On the Tap and Cluster Angular Spreads of Indoor WLAN Channels," in *Proc. of the 59th IEEE Veh. Technol. Conf. (VTC)*, vol. 1, 2004, pp. 218–222 Vol.1.

[15] N. Czink, P. Cera, J. Salo, E. Bonek, J.-P. Nuutinen, and J. Ylitalo, "A Framework for Automatic Clustering of Parametric MIMO Channel Data Including Path Powers," in *Proc. of the 64th IEEE Veh. Technol. Conf. (VTC)*, 2006, pp. 1–5.

[16] B. Fleury, M. Tschudin, R. Heddergott, D. Dahlhaus, and K. Pedersen, "Channel Parameter Estimation in Mobile Radio Environments Using the SAGE Algorithm," *IEEE J. Sel. Areas Commun.*, vol. 17, no. 3, pp. 434–450, March 1999.

[17] N. Czink, "The Random-Cluster Model - A Stochastic MIMO Channel Model for Broadband Communication Systems of the 3rd Generation and Beyond," Ph.D. dissertation, Institut für Nachrichtentechnik und Hochfrequenztechnik, Vienna University of Technology, 2007.

[18] Q. Spencer, B. Jeffs, M. Jensen, and A. Swindlehurst, "Modeling the statistical time and angle of arrival characteristics of an indoor multipath channel," *IEEE J. Sel. Areas Commun.*, vol. 18, no. 3, pp. 347–360, 2000.

[19] V. Erceg, L. Schumacher, P. Kyritsi, and et al., "TGn Channel Models," Garden Grove, Calif, USA, Tech. Rep. IEEE P802.11, Wireless LANs IEEE 802.11-03/940r4, May 2004.

[20] P. Kyösti, J. Meinilä, and et al., "WINNER II Channel Models D1.1.2 V1.1," IST Winner II Project, Tech. Rep. IST-4-027756 WINNER II, D1.1.2 V1.1, 11 2007.

[21] L. M. Correia, *Mobile Broadband Multimedia Networks: Techniques, Models and Tools for 4G*. Academic Press, 5 2006.

# Modeling of Reverberant Radio Channels Using Propagation Graphs

Troels Pedersen, Gerhard Steinböck, and Bernard H. Fleury

*IEEE Transactions Antennas and Propagation, 2012*

© 2012 IEEE
*The layout has been revised.*
*Errata:* (B.32) *was corrected to* $\frac{g^2}{\mathrm{odi}(e)}$.

## *Abstract*

In measurements of in-room radio channel responses an avalanche effect can be observed: earliest signal components, which appear well separated in delay, are followed by an avalanche of components arriving with increasing rate of occurrence, gradually merging into a diffuse tail with exponentially decaying power. We model the channel as a propagation graph in which vertices represent transmitters, receivers, and scatterers, while edges represent propagation conditions between vertices. The recursive structure of the graph accounts for the exponential power decay and the avalanche effect. We derive a closed form expression for the graph's transfer matrix. This expression is valid for any number of interactions and is straightforward to use in numerical simulations. We discuss an example where time dispersion occurs only due to propagation in between vertices. Numerical experiments reveal that the graph's recursive structure yields both an exponential power decay and an avalanche effect.

## *B.1 Introduction*

Engineering of modern indoor radio systems for communications and geolocation relies heavily on models for the time dispersion of the wideband and ultrawideband radio channels [1–3]. From measurement data, as exemplified in Fig. B.1, it appears that the spatial average of the channel impulse response's squared magnitude (referred to as the spatially averaged delay-power spectrum) observed in in-room scenarios exhibits an avalanche effect: The earliest signal components, which appear well separated in time, are followed by an avalanche of components arriving with increasing rate of occurrence, gradually merging into a diffuse tail with exponentially decaying power. The diffuse tail is often referred to as a "dense multipath component" and is commonly attributed to diffuse scattering from rough surfaces and objects which are small compared to the wavelength [5, 6]. A similar avalanche effect is well-known in room acoustics [7] where it is attributed to recursive scattering of sound waves. Indoor radio propagation environments are particularly exposed to recursive scattering as electromagnetic waves may be reflected back and forth in between walls, floor, and ceiling. Thus, the avalanche effect and the exponential power decay may occur due to recursive scattering rather than diffuse scattering.

Recursive scattering phenomena have been previously taken into account in a number of radio channel models. The works [8–11] use the analogy to acoustical reverberation theory to predict the exponential decay. As a matter of fact, there exists a well-developed theory of electromagnetic fields in cavities [12, 13], but in this context too the avalanche effect has received little attention. Recursive scattering between particles in a homogeneous medium

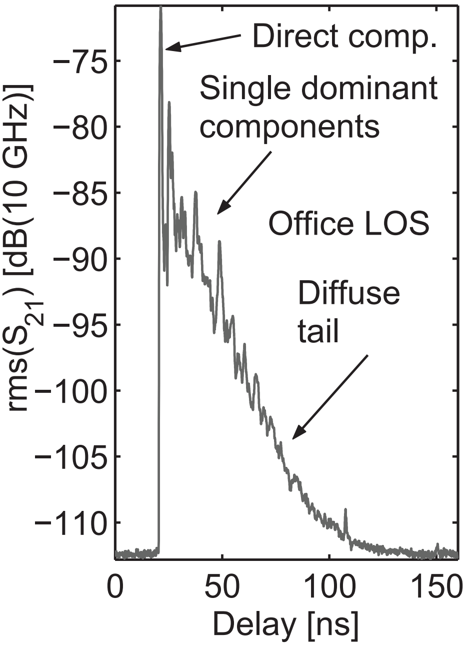

*Fig. B.1: Spatially averaged delay-power spectrum measured within an office of* $5\times5\times2.6\,\mathrm{m}^3$ *obtained as the rms value of impulse response for* $30\times30$ *receiver positions on a square horizontal grid with steps of* 1 cm. *Abscissa includes cable delays; reference to signal bandwidth (*10 GHz*) shifts ordinate by* −100 dB. *Reprinted from [4] with permission (© 2002 IEEE).*

is a well-known phenomenon studied by Foldy [14] and Lax [15, 16]. The solution, given by the so-called Foldy-Lax equation [17], has been applied in the context of time-reversal imaging by Shi and Nehorai [18]. The solution is, however, intractable for heterogeneous indoor environments. In [19] the radio propagation mechanism is modeled as a "stream of photons" performing continuous random walks in a homogeneously cluttered environment. The model predicts a delay-power spectrum consisting of a single directly propagating "coherent component" followed by an incoherent tail. Time-dependent radiosity [20–23] accounting for delay dispersion has been recently applied to design a model for the received instantaneous power [24]. Thereby, the exponential power decay and the avalanche effect can be predicted.

Simulation studies of communication and localization systems commonly rely on synthetic realizations of the channel impulse response. A multitude of impulse response models exist [2, 3, 25], but only few account for the avalanche effect. The models [26–28] treat early components via a geometric model whereas the diffuse tail is generated via another stochastic process;

the connection between the propagation environment and the diffuse tail is, however, not considered. Ray tracing methods may also be used for site-specific simulations [29]. However, ray tracing methods commonly predict the signal energy to be concentrated into the single dominant components whereas the diffuse tail is not well represented.

In this contribution, we model the channel impulse response for the purpose of studying the avalanche effect and, in particular, its relation to recursive scattering. The objective is a model for which analytical results can be obtained allowing for computer simulation of channel realization as well as average entities, such as the delay-power spectrum, without the need for truncating the recursive scattering process. Expanding on a previous work [30, 31], we propose a unified approach for modeling of the transition from single dominant components to the diffuse tail. The propagation environment is represented in terms of a propagation graph, with vertices representing transmitters, receivers, and scatterers, while edges represent propagation conditions between vertices. The propagation graph accounts inherently for recursive scattering and thus signal components arriving at the receiver may have undergone any number of scatterer interactions. Furthermore, we are able to express the channel transfer matrix in closed form for an unlimited number of interactions. With this closed form expression it is possible in praxis to numerically compute the channel recursive scattering with infinite number of bounces. The proposed formalism also enables a virtual "dissection" of the impulse response in so-called partial responses to inspect how recursive scattering leads to a gradual buildup of the diffuse tail.

Propagation graphs may be defined according to a specific scenario for site-specific prediction, or be generated as outcomes of a stochastic process for use in e.g. Monte Carlo simulations. In the present contribution we consider an example of a stochastically generated propagation graph suitable for Monte Carlo simulations on a desktop computer. In this example model, delays occur only due to propagation in between vertices; the interactions with the scatterers cause no additional delay. The simulations reveal that the graph's recursive structure yields both an exponential power decay and an avalanche effect in the generated impulse responses.

## *B.2 Representing Radio Channels as Graphs*

In a typical propagation scenario, the electromagnetic signal emitted by a transmitter propagates through the environment while interacting with a number of objects called scatterers. The receiver, which is usually placed away from the transmitter, senses the electromagnetic signal. If a line of sight exists between the transmitter and the receiver, direct propagation occurs. Also, the signal may arrive at the receiver indirectly via one or more scatterers. In the following we represent propagation mechanisms using graphs allowing for both recursive and non-recursive scattering. We first introduce the necessary definitions of directed graphs.

### B.2.1 Directed Graphs

Following [32], we define a directed graph $\mathcal{G}$ as a pair $(\mathcal{V}, \mathcal{E})$ of disjoint sets of vertices and edges. Edge $e \in \mathcal{E}$ with initial vertex denoted by $\operatorname{init}(e)$ and terminal vertex denoted by $\operatorname{term}(e)$ is said to be outgoing from vertex $\operatorname{init}(e)$ and ingoing to $\operatorname{term}(e)$. We consider graphs without parallel edges. Thus, there exists no pair of edges $e$ and $e'$ such that $\operatorname{init}(e) = \operatorname{init}(e')$ and $\operatorname{term}(e) = \operatorname{term}(e')$. In this case an edge $e$ can be identified by the vertex pair $(\operatorname{init}(e), \operatorname{term}(e)) \in \mathcal{V}^2$ and with a slight abuse of notation we write $e = (\operatorname{init}(e), \operatorname{term}(e))$ and $\mathcal{E} \subseteq \mathcal{V} \times \mathcal{V}$.

### B.2.2 Propagation Graphs

We define a propagation graph as a directed graph where vertices represent transmitters, receivers and scatterers. Edges represent the propagation conditions between the vertices. Thus, the vertex set $\mathcal{V}$ of a propagation graph is a union of three disjoint sets: $\mathcal{V} = \mathcal{V}_\mathrm{t} \cup \mathcal{V}_\mathrm{r} \cup \mathcal{V}_\mathrm{s}$, the set of transmitters $\mathcal{V}_\mathrm{t} = \{\mathrm{Tx}1, \ldots, \mathrm{Tx}N_\mathrm{t}\}$, the set of receivers $\mathcal{V}_\mathrm{r} = \{\mathrm{Rx}1, \ldots, \mathrm{Rx}N_\mathrm{r}\}$, and the set of scatterers $\mathcal{V}_\mathrm{s} = \{\mathrm{S}1, \ldots, \mathrm{S}N_\mathrm{s}\}$. The transmit vertices are considered as sources and have only outgoing edges. Likewise, the receivers are considered as sinks with only incoming edges. The edge set $\mathcal{E}$ can thus be partitioned into four disjunct sets as $\mathcal{E} = \mathcal{E}_\mathrm{d} \cup \mathcal{E}_\mathrm{t} \cup \mathcal{E}_\mathrm{r} \cup \mathcal{E}_\mathrm{s}$, with direct edges in $\mathcal{E}_\mathrm{d} = \mathcal{E} \cap (\mathcal{V}_\mathrm{t} \times \mathcal{V}_\mathrm{r})$, transmitter-scatterer edges in $\mathcal{E}_\mathrm{t} = \mathcal{E} \cap (\mathcal{V}_\mathrm{t} \times \mathcal{V}_\mathrm{s})$, scatterer-receiver edges in $\mathcal{E}_\mathrm{r} = \mathcal{E} \cap (\mathcal{V}_\mathrm{s} \times \mathcal{V}_\mathrm{r})$, and inter-scatterer edges in $\mathcal{E}_\mathrm{s} = \mathcal{E} \cap (\mathcal{V}_\mathrm{s} \times \mathcal{V}_\mathrm{s})$. Fig. B.2 shows an example propagation graph.

The signals propagate in the graph in the following way. Each transmitter emits a signal that propagates via its outgoing edges. The signal observed by a receiver vertex is the sum of the signals arriving via the ingoing edges. A scatterer sums up the signals on its ingoing edges and re-emits the sum-signal on the outgoing edges. As a signal propagates along an edge, or interacts with a scatterer, it undergoes delay and dispersion in time. The specific delay dispersion endured by a signal depends on the particular propagation mechanism along its edges. Assuming these mechanisms to be linear and time-invariant, this effect can be represented as a convolution with an impulse response or, in the Fourier domain, as a multiplication with a transfer function. Hence, the signal arriving to vertex $v_{n'}$ via edge $e = (v_n, v_{n'})$ reads $A_e(f)C_n(f)$, where $C_n(f)$ is the signal emitted by vertex $v_n$ and $A_e(f)$ denotes the transfer function associated to edge $e$. In other words, the transfer function $A_e(f)$

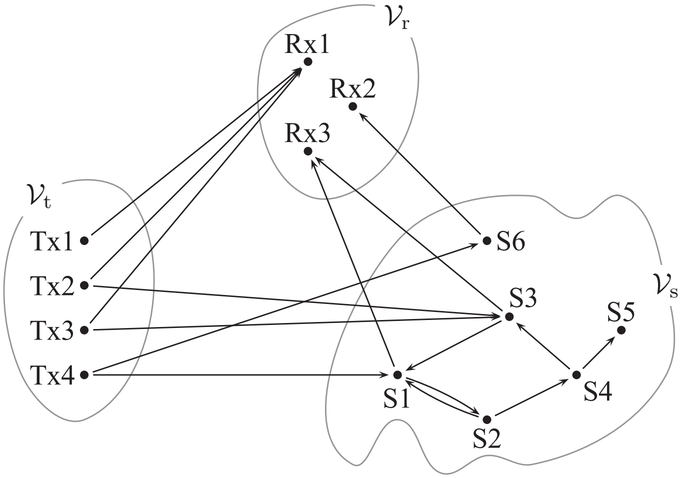
$\mathcal{V}_{\mathrm{r}}$
Rx1
Rx2
Rx3
$\mathcal{V}_{\mathrm{t}}$
Tx1
Tx2
Tx3
Tx4
S6
S3
S5
$\mathcal{V}_{\mathrm{s}}$
S1
S4
S2

$$\begin{aligned}
\mathcal{E}_{\mathrm{d}} &= \{(\mathrm{Tx1},\mathrm{Rx1}),(\mathrm{Tx2},\mathrm{Rx1}),(\mathrm{Tx3},\mathrm{Rx1})\}\\
\mathcal{E}_{\mathrm{t}} &= \{(\mathrm{Tx2},\mathrm{S3}),(\mathrm{Tx3},\mathrm{S3}),(\mathrm{Tx4},\mathrm{S6}),(\mathrm{Tx4},\mathrm{S1})\}\\
\mathcal{E}_{\mathrm{r}} &= \{(\mathrm{S1},\mathrm{Rx3}),(\mathrm{S3},\mathrm{Rx3}),(\mathrm{S6},\mathrm{Rx2})\}\\
\mathcal{E}_{\mathrm{s}} &= \{(\mathrm{S1},\mathrm{S2}),(\mathrm{S2},\mathrm{S1}),(\mathrm{S3},\mathrm{S1}),(\mathrm{S2},\mathrm{S4}),(\mathrm{S4},\mathrm{S3}),(\mathrm{S4},\mathrm{S5})\}
\end{aligned}$$

*Fig. B.2: A propagation graph with four transmit vertices, three receive vertices and six scatterer vertices.*

describes the interaction at the initial vertex $v_n$ and the propagation from $v_n$ to $v_{n'}$.

### *B.2.3 Weighted Adjacency Matrix of a Propagation Graph*

Propagation along the edges is described via a transfer matrix $\mathbf{A}(f)$ which can be viewed as an adjacency matrix with each entry coinciding with the edge transfer function of the corresponding edge. Thus, the weighted adjacency matrix $\mathbf{A}(f) \in \mathbb{C}^{(N_{\mathrm{t}}+N_{\mathrm{r}}+N_{\mathrm{s}})\times(N_{\mathrm{t}}+N_{\mathrm{r}}+N_{\mathrm{s}})}$ of the propagation graph $\mathcal{G}$ is defined as

$$[\mathbf{A}(f)]_{nn'} = \begin{cases} A_{(v_n,v_{n'})}(f) & \text{if } (v_n,v_{n'}) \in \mathcal{E}, \\ 0 & \text{otherwise}, \end{cases} \tag{B.1}$$

i.e., entry $n, n'$ of $\mathbf{A}(f)$ is the transfer function from vertex $v_n$ to vertex $v_{n'}$ of $\mathcal{G}$. Selecting the indexing of the vertices according to

$$v_n \in \begin{cases} \mathcal{V}_{\mathrm{t}}, & n = 1,\dots,N_{\mathrm{t}} \\ \mathcal{V}_{\mathrm{r}}, & n = N_{\mathrm{t}}+1,\dots,N_{\mathrm{t}}+N_{\mathrm{r}} \\ \mathcal{V}_{\mathrm{s}}, & n = N_{\mathrm{t}}+N_{\mathrm{r}}+1,\dots,N_{\mathrm{t}}+N_{\mathrm{r}}+N_{\mathrm{s}}, \end{cases} \tag{B.2}$$

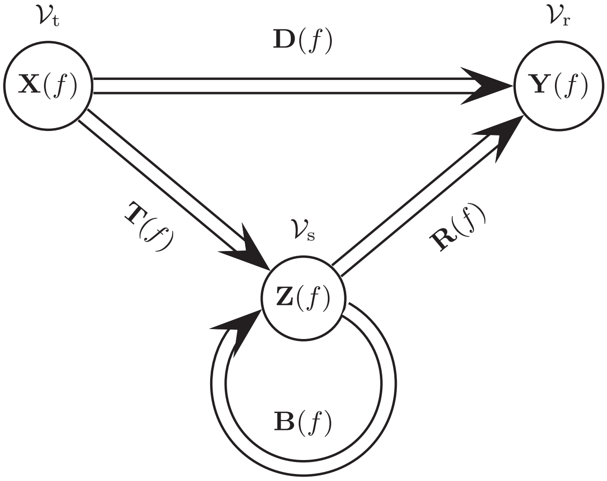

*Fig. B.3: Vector signal flow graph representation of a propagation graph. Vertices represent vertex sets of the propagation graph with associated vector signals. Signal transmission between the sets are represented by the edges and associated transfer matrices.*

the weighted adjacency matrix takes the form

$$\mathbf{A}(f) = \begin{bmatrix} \mathbf{0} & \mathbf{0} & \mathbf{0} \\ \mathbf{D}(f) & \mathbf{0} & \mathbf{R}(f) \\ \mathbf{T}(f) & \mathbf{0} & \mathbf{B}(f) \end{bmatrix}, \tag{B.3}$$

where **0** denotes the all-zero matrix of the appropriate dimension and the transfer matrices

$$\mathbf{D}(f) \in \mathbb{C}^{N_\mathrm{r} \times N_\mathrm{t}} \quad \text{connecting } \mathcal{V}_\mathrm{t} \text{ to } \mathcal{V}_\mathrm{r}, \tag{B.4}$$

$$\mathbf{R}(f) \in \mathbb{C}^{N_\mathrm{r} \times N_\mathrm{s}} \quad \text{connecting } \mathcal{V}_\mathrm{s} \text{ to } \mathcal{V}_\mathrm{r}, \tag{B.5}$$

$$\mathbf{T}(f) \in \mathbb{C}^{N_\mathrm{s} \times N_\mathrm{t}} \quad \text{connecting } \mathcal{V}_\mathrm{t} \text{ to } \mathcal{V}_\mathrm{s}, \text{ and} \tag{B.6}$$

$$\mathbf{B}(f) \in \mathbb{C}^{N_\mathrm{s} \times N_\mathrm{s}} \quad \text{interconnecting } \mathcal{V}_\mathrm{s}. \tag{B.7}$$

The special structure of $\mathbf{A}(f)$ reflects the structure of the propagation graph. The first $N_\mathrm{t}$ rows are zero because we do not accept incoming edges into the transmitters. Likewise columns $N_\mathrm{t} + 1, \dots, N_\mathrm{t} + N_\mathrm{r}$ are all zero since the receiver vertices have no outgoing edges.

The input signal vector $\mathbf{X}(f)$ is defined as

$$\mathbf{X}(f) = [X_1(f), \dots, X_{N_\mathrm{t}}(f)]^\mathrm{T}, \tag{B.8}$$

where $X_m(f)$ is the spectrum of the signal emitted by transmitter $\mathrm{Tx}m$, and $[\cdot]^\mathrm{T}$ denotes the transposition operator. The output signal vector $\mathbf{Y}(f)$ is defined as

$$\mathbf{Y}(f) = [Y_1(f), \ldots, Y_{N_\mathrm{r}}(f)]^\mathrm{T}, \tag{B.9}$$

where $Y_m(f)$ is the Fourier transform of the signal observed by receiver $\mathrm{Rx}m$. Similar, to $\mathbf{X}(f)$ and $\mathbf{Y}(f)$ we let $\mathbf{Z}(f)$ denote the output signal vector of the scatterers:

$$\mathbf{Z}(f) = [Z_1(f), \ldots, Z_{N_\mathrm{s}}(f)]^\mathrm{T} \tag{B.10}$$

with the $n$th entry denoting the Fourier transform of the signal observed at scatterer vertex $\mathrm{S}n$. By the definition of the propagation graph, there are no other signal sources than the vertices in $\mathcal{V}_\mathrm{t}$. Assuming linear and time-invariant propagation mechanisms, the input-output relation in the Fourier domain reads

$$\mathbf{Y}(f) = \mathbf{H}(f)\mathbf{X}(f), \tag{B.11}$$

where $\mathbf{H}(f)$ is the $N_\mathrm{r} \times N_\mathrm{t}$ transfer matrix of the propagation graph.

The structure of the propagation graph unfolds in the vector signal flow graph depicted in Fig. B.3. The vertices of the vector signal flow graph represent the three sets $\mathcal{V}_\mathrm{t}$, $\mathcal{V}_\mathrm{r}$, and $\mathcal{V}_\mathrm{s}$ with the associated signals $\mathbf{X}(f)$,$\mathbf{Y}(f)$, and $\mathbf{Z}(f)$. The edge transfer matrices of the vector signal flow graph are the sub-matrices of $\mathbf{A}(f)$ defined in (B.4)–(B.7).

## B.3 Transfer Matrix of a Propagation Graph

In the following we derive the transfer matrix of a propagation graph. In Subsection B.3.1 we first discuss how the response of a graph is composed of signal contributions propagating via different propagation paths. This representation is, albeit intuitive, impractical for computation of the transfer matrix of graphs with cycles. Thus in Subsections B.3.2 and B.3.3 we give the transfer matrix and partial transfer matrices of a general propagation graph in closed form. Subsection B.3.4 treats the graphical interpretation of reciprocal channels. The section concludes with a discussion of related results in the literature.

### B.3.1 Propagation Paths and Walks

The concept of a propagation path is a corner stone in modeling multipath propagation. In the literature, this concept is most often defined in terms of the resulting signal components arriving at the receiver. A shortcoming of this definition is that it is often hard to relate to the propagation environment. The graph terminology offers a convenient alternative. A walk $\ell$ (of length $K$) in a graph $\mathcal{G} = (\mathcal{V}, \mathcal{E})$ is defined as a sequence $\ell = (v^{(1)}, v^{(2)}, \ldots, v^{(K+1)})$ of vertices in $\mathcal{V}$ such that $(v^{(k)}, v^{(k+1)}) \in \mathcal{E}, k = 1, \ldots K$. We say that $\ell$

is a walk from $v^{(1)}$ to $v^{(K+1)}$ where $v^{(1)}$ is the start vertex and $v^{(K+1)}$ is the end vertex; $v^{(2)}, \ldots, v^{(K)}$ are called the inner vertices of $\ell$. We define a propagation path as a walk in a propagation graph from a transmitter to a receiver. Consequently, all (if any) inner vertices of a propagation path are scatters. A signal that propagates along propagation path $\ell$ traverses $K+1$ (not necessarily different) edges and undergoes $K$ interactions. We refer to such a propagation path as a $K$-bounce path. The zero-bounce path $\ell = (v, v')$ is called the direct path, from transmitter $v$ to receiver $v'$. As an example, referring to the graph depicted in Fig. B.2, it is straightforward to verify that $\ell_1 = (\mathrm{Tx1}, \mathrm{Rx1})$ is a direct path, $\ell_2 = (\mathrm{Tx4}, \mathrm{S6}, \mathrm{Rx2})$ is a single-bounce path, and $\ell_3 = (\mathrm{Tx4}, \mathrm{S1}, \mathrm{S2}, \mathrm{S1}, \mathrm{Rx3})$ is a 3-bounce path.

We denote by $\mathcal{L}_{vv'}$ the set of propagation paths in $\mathcal{G}$ from transmitter $v$ to receiver $v'$. The signal received at $v'$ originating from transmitter $v$ is the superposition of signal components each propagating via a propagation path in $\mathcal{L}_{vv'}$. Correspondingly, entry $(v, v')$ of $\mathbf{H}(f)$ reads

$$H_{vv'}(f) = \sum_{\ell \in \mathcal{L}_{vv'}} H_\ell(f), \tag{B.12}$$

where $H_\ell(f)$ is the transfer function of propagation path $\ell$.

The number of terms in (B.12) equals the cardinality of $\mathcal{L}_{vv'}$, which may, depending on the structure of the graph, be finite or infinite. As an example, the number of propagation paths is infinite if $v$ and $v'$ are connected via a directed cycle in $\mathcal{G}$, i.e. if a propagation path contains a walk from an inner vertex back to itself. The graph in Fig. B.2 contains two directed cycles which are connected to both transmitters and receivers.

In the case of an infinite number of propagation paths, computing $H_{vv'}(f)$ directly from (B.12) is infeasible. This problem is commonly circumvented by truncating the sum in (B.12) to approximate $H_{vv'}(f)$ as a finite sum. This approach, however, calls for a method for determining how many terms of the sum should be included in order to achieve reasonable approximation.

In the frequently used "$K$-bounce channel models", propagation paths with more than $K$ interactions are ignored. This approach is motivated by the rationale that at each interaction, the signal is attenuated, and thus terms in (B.12) resulting from propagation paths with a large number of bounces are weak and can be left out as they do not affect the sum much. This reasoning, however, holds true only if the *sum* of the components with more than $K$ interactions is insignificant, which may or may not be the case. From this consideration, it is clear that the truncation criterion is non-trivial as it essentially necessitates computation of the whole sum before deciding whether a term can be ignored or not.

### B.3.2 Transfer Matrix for Recursive and Non-Recursive Propagation Graphs

As an alternative to the approximation methods applied to the sum (B.12) we now give an exact closed-form expression for the transfer matrix $\mathbf{H}(f)$. Provided that the spectral radius of $\mathbf{B}(f)$ is less than unity, the expression holds true for any number of terms in the sum (B.12) and thus holds regardless whether the number of propagation paths is finite or infinite.

*Theorem* B.3.1: *If the spectral radius of* $\mathbf{B}(f)$ *is less than unity, then the transfer matrix of a propagation graph reads*

$$\mathbf{H}(f) = \mathbf{D}(f) + \mathbf{R}(f)[\mathbf{I} - \mathbf{B}(f)]^{-1}\mathbf{T}(f). \tag{B.13}$$

According to Theorem B.3.1 the transfer matrix $\mathbf{H}(f)$ consists of the two following terms: $\mathbf{D}(f)$ representing direct propagation between the transmitters and receivers and $\mathbf{R}(f)[\mathbf{I} - \mathbf{B}(f)]^{-1}\mathbf{T}(f)$ describing indirect propagation. The condition that the spectral radius of $\mathbf{B}(f)$ be less than unity implies that for any vector norm $\|\cdot\|$, $\|\mathbf{Z}(f)\| > \|\mathbf{B}(f)\mathbf{Z}(f)\|$ for non-zero $\|\mathbf{Z}(f)\|$, cf. [33]. For the Euclidean norm in particular this condition implies the sensible physical requirement that the signal power strictly decreases for each interaction.

*Proof.* Let $\mathbf{H}_k(f)$ denote the transfer matrix for all $k$-bounce propagation paths, then $\mathbf{H}(f)$ can be decomposed as

$$\mathbf{H}(f) = \sum_{k=0}^{\infty} \mathbf{H}_k(f), \tag{B.14}$$

where

$$\mathbf{H}_k(f) = \begin{cases} \mathbf{D}(f), & k = 0 \\ \mathbf{R}(f)\mathbf{B}^{k-1}(f)\mathbf{T}(f), & k > 0. \end{cases} \tag{B.15}$$

Insertion of (B.15) into (B.14) yields

$$\mathbf{H}(f) = \mathbf{D}(f) + \mathbf{R}(f)\left(\sum_{k=1}^{\infty} \mathbf{B}^{k-1}(f)\right)\mathbf{T}(f). \tag{B.16}$$

The infinite sum in (B.16) is a Neumann series converging to $[\mathbf{I} - \mathbf{B}(f)]^{-1}$ if the spectral radius of $\mathbf{B}(f))$ is less than unity. Inserting this in (B.16) completes the proof. ☐

The decomposition introduced in (B.14) makes the effect of the recursive scattering directly visible. The received signal vector is a sum of infinitely many components resulting from any number of interactions. The structure of the propagation mechanism is further exposed by (B.16) where the emitted vector signal is re-scattered successively in the propagation environment leading to the observed Neumann series. This allows for modeling of channels with infinite impulse responses by expression (B.13).

It is possible to arrive at (B.13) in an alternative, but less explicit, manner:

*Proof.* It is readily observed from the vector signal flow graph in Fig. B.3 that $\mathbf{Z}(f)$ can be expressed as

$$\mathbf{Z}(f) = \mathbf{T}(f)\mathbf{X}(f) + \mathbf{B}(f)\mathbf{Z}(f). \tag{B.17}$$

Since the spectral radius of $\mathbf{B}(f)$ is less than unity we obtain for $\mathbf{Z}(f)$ the solution

$$\mathbf{Z}(f) = [\mathbf{I} - \mathbf{B}(f)]^{-1}\mathbf{T}(f)\mathbf{X}(f). \tag{B.18}$$

Furthermore, according to Fig. B.3 the received signal is of the form

$$\mathbf{Y}(f) = \mathbf{D}(f)\mathbf{X}(f) + \mathbf{R}(f)\mathbf{Z}(f). \tag{B.19}$$

Insertion of (B.18) in this expression yields (B.13). ☐

We remark that the above two proofs allow for propagation paths with any number of bounces. This is highly preferable, as the derived expression (B.13) is not impaired by approximation errors due to the truncation of the series into a finite number of terms as it occurs when using $K$-bounce models.

A significant virtue of the expression (B.13) is that propagation effects related to the transmitters and receivers are accounted for in the matrices $\mathbf{D}(f)$, $\mathbf{T}(f)$ and $\mathbf{R}(f)$, but do not affect $\mathbf{B}(f)$. Consequently, the matrix $[\mathbf{I} - \mathbf{B}(f)]^{-1}$ only needs to be computed once even though the configuration of transmitters and receivers changes. This is especially advantageous for simulation studies of e.g. spatial correlation as this leads to a significant reduction in computational complexity.

### *B.3.3 Partial Transfer Matrices*

The closed form expression (B.13) for the transfer matrix of a propagation graph accounts for propagation via an arbitrary number of scatterer interactions. For some applications it is, however, relevant to study only some part of the impulse response associated with a particular number of interactions. One case is where a propagation graph is used to generate only a part of the response and other techniques are used for the remaining parts. Another case is when one must assess the approximation error when the infinite series is truncated. In the following we derive a few useful expressions for such partial transfer matrices.

We define the $K : L$ partial transfer matrix as

$$\mathbf{H}_{K:L}(f) = \sum_{k=K}^{L} \mathbf{H}_k(f), \quad 0 \leq K \leq L, \tag{B.20}$$

i.e., we include only contributions from propagation paths with at least $K$, but no more than $L$ bounces. It is straightforward to evaluate (B.20) for $K = 0$, and $L = 0, 1, 2$:

$$\mathbf{H}_{0:0}(f) = \mathbf{D}(f) \tag{B.21}$$
$$\mathbf{H}_{0:1}(f) = \mathbf{D}(f) + \mathbf{R}(f)\mathbf{T}(f) \tag{B.22}$$
$$\mathbf{H}_{0:2}(f) = \mathbf{D}(f) + \mathbf{R}(f)\mathbf{T}(f) + \mathbf{R}(f)\mathbf{B}(f)\mathbf{T}(f). \tag{B.23}$$

This expansion of the truncated series is quite intuitive but the obtained expressions are increasingly complex for large $L$. Theorem B.3.2 gives a closed form expression of the partial transfer function $\mathbf{H}_{K,L}(f)$ for arbitrary $K$ and $L$:

*Theorem* B.3.2: *The partial response $\mathbf{H}_{K:L}(f)$ is given by*

$$\mathbf{H}_{K:L}(f) = \begin{cases} \mathbf{D}(f) + \mathbf{R}(f)[\mathbf{I} - \mathbf{B}^L(f)][\mathbf{I} - \mathbf{B}(f)]^{-1}\mathbf{T}(f), \\ \hfill K = 0, L \geq 0 \\ \mathbf{R}(f)[\mathbf{B}^{K-1}(f) - \mathbf{B}^L(f)][\mathbf{I} - \mathbf{B}(f)]^{-1}\mathbf{T}(f), \\ \hfill 0 < K \leq L, \end{cases}$$

*provided that the spectral radius of $\mathbf{B}(f)$ is less than unity.*

*Proof.* The partial transfer function for $0 \leq K \leq L$ reads

$$\begin{aligned} \mathbf{H}_{K:L}(f) &= \sum_{k=K}^{\infty} \mathbf{H}_k(f) - \sum_{k'=L+1}^{\infty} \mathbf{H}_{k'}(f) \\ &= \mathbf{H}_{K:\infty}(f) - \mathbf{H}_{L+1:\infty}(f). \end{aligned} \tag{B.24}$$

For $K = 0$ we have $\mathbf{H}_{0:\infty}(f) = \mathbf{H}(f)$ by definition; for $K \geq 1$ we have

$$\begin{aligned} \mathbf{H}_{K:\infty}(f) &= \mathbf{R}(f) \sum_{k=K-1}^{\infty} \mathbf{B}^k(f)\mathbf{T}(f) \\ &= \mathbf{R}(f)\mathbf{B}^{K-1}(f) \sum_{k=0}^{\infty} \mathbf{B}^k(f)\mathbf{T}(f) \\ &= \mathbf{R}(f)\mathbf{B}^{K-1}(f)[\mathbf{I} - \mathbf{B}(f)]^{-1}\mathbf{T}(f). \end{aligned} \tag{B.25}$$

Inserting (B.25) into (B.24) completes the proof. □

Theorem B.3.2 enables closed-form computation of $\mathbf{H}_{K:L}(f)$ for any $K \geq L$. We have already listed a few partial transfer matrices in (B.21), (B.22), and (B.23). By definition the partial response $\mathbf{H}_{K:K}(f)$ equals $\mathbf{H}_K(f)$ for which an expression is provided in (B.15). The transfer function of the $K$-bounce approximation is equal to $\mathbf{H}_{0:K}(f)$. Another special case worth mentioning is $\mathbf{H}_{K+1:\infty}(f) = \mathbf{H}(f) - \mathbf{H}_{0:K}(f)$ available from (B.25), which gives the error due to the $K$-bounce approximation. Thus the validity of the $K$-bounce approximation can be assessed by evaluating some appropriate norm of $\mathbf{H}_{K+1:\infty}(f)$.

### *B.3.4 Reciprocity and Reverse Graphs*

In most cases, the radio channel is considered reciprocal. As we shall see shortly, the graph terminology accommodates an interesting interpretation of the concept of reciprocity. For any propagation graph we can define the reverse graph in which the roles of transmitter and receiver vertices are swapped. The principle of reciprocity states that the transfer matrix of the reverse channel is equal to the transposed transfer matrix of the forward channel, i.e., a forward channel with transfer matrix $\mathbf{H}(f)$ has a reverse channel with transfer matrix $\tilde{\mathbf{H}}(f) = \mathbf{H}^{\mathrm{T}}(f)$. In the sequel we mark all entities related to the reverse channel with a tilde.

We seek the relation between the forward graph $\mathcal{G} = (\mathcal{V}, \mathcal{E})$ and its reverse $\tilde{\mathcal{G}} = (\tilde{\mathcal{V}}, \tilde{\mathcal{E}})$ under the assumption of reciprocity. More specifically, we are interested in the relation between the weighted adjacency matrix $\mathbf{A}(f)$ of $\mathcal{G}$ and the weighted adjacency matrix $\tilde{\mathbf{A}}(f)$ of $\tilde{\mathcal{G}}$. We shall prove the following theorem:

Theorem B.3.3: *For a propagation graph $\mathcal{G} = (\mathcal{V}, \mathcal{E})$ with weighted adjacency matrix $\mathbf{A}(f)$ and transfer matrix $\mathbf{H}(f)$ there exists a reverse graph $\tilde{\mathcal{G}} = (\tilde{\mathcal{V}}, \tilde{\mathcal{E}})$ such that $\tilde{\mathcal{V}} = \mathcal{V}$, $\tilde{\mathcal{E}} = \{(v, v') : (v', v) \in \mathcal{E}\}$, $\tilde{\mathbf{A}}(f) = \mathbf{A}^{\mathrm{T}}(f)$, and $\tilde{\mathbf{H}}(f) = \mathbf{H}^{\mathrm{T}}(f)$.*

*Proof.* We prove the Theorem by constructing a suitable propagation graph such that the reciprocity condition is fulfilled. We first note that the set of transmitters, receivers, and scatterers is maintained for the reverse channel, thus the vertex set of $\tilde{\mathcal{G}}$ is $\mathcal{V}$ with $\tilde{\mathcal{V}}_{\mathrm{t}} = \mathcal{V}_{\mathrm{r}}$, $\tilde{\mathcal{V}}_{\mathrm{r}} = \mathcal{V}_{\mathrm{t}}$, and $\tilde{\mathcal{V}}_{\mathrm{s}} = \mathcal{V}_{\mathrm{s}}$. It is immediately clear from the structure of $\mathcal{G}$ that the reverse graph $\tilde{\mathcal{G}}$ has no ingoing edges to $\tilde{\mathcal{V}}_{\mathrm{t}}$ and no outgoing edges from $\tilde{\mathcal{V}}_{\mathrm{r}}$ and $\tilde{\mathcal{G}}$ is thus a propagation graph. Assuming the vertex indexing as in (B.2), the weighted adjacency matrix of $\tilde{\mathcal{G}}$ is of the form

$$\tilde{\mathbf{A}}(f) = \begin{bmatrix} \mathbf{0} & \tilde{\mathbf{D}}(f) & \tilde{\mathbf{T}}(f) \\ \mathbf{0} & \mathbf{0} & \mathbf{0} \\ \mathbf{0} & \tilde{\mathbf{R}}(f) & \tilde{\mathbf{B}}(f) \end{bmatrix}, \tag{B.26}$$

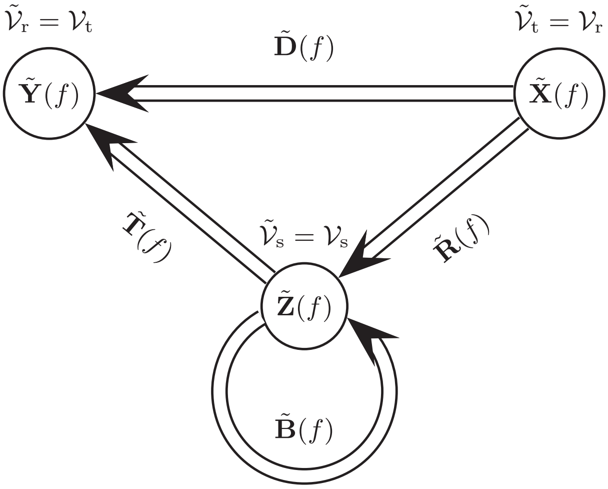
$\tilde{\mathcal{V}}_{\mathrm{r}} = \mathcal{V}_{\mathrm{t}}$
$\tilde{\mathbf{D}}(f)$
$\tilde{\mathcal{V}}_{\mathrm{t}} = \mathcal{V}_{\mathrm{r}}$
$\tilde{\mathbf{Y}}(f)$
$\tilde{\mathbf{X}}(f)$
$\tilde{\mathbf{T}}(f)$
$\tilde{\mathcal{V}}_{\mathrm{s}} = \mathcal{V}_{\mathrm{s}}$
$\tilde{\mathbf{R}}(f)$
$\tilde{\mathbf{Z}}(f)$
$\tilde{\mathbf{B}}(f)$

*Fig. B.4: Vector signal flow graph representation of a reverse propagation graph. Compared to the forward graph depicted in Fig. B.3 all edges are reversed.*

where the transfer matrices $\tilde{\mathbf{D}}(f), \tilde{\mathbf{R}}(f), \tilde{\mathbf{T}}(f)$, and $\tilde{\mathbf{B}}(f)$ are defined according to Fig. B.4. Equating $\tilde{\mathbf{A}}(f)$ and $\mathbf{A}(f)$ we obtain the identities $\tilde{\mathbf{D}}(f) = \mathbf{D}^{\mathrm{T}}(f), \tilde{\mathbf{B}}(f) = \mathbf{B}^{\mathrm{T}}(f), \tilde{\mathbf{T}}(f) = \mathbf{R}^{\mathrm{T}}(f)$, and $\tilde{\mathbf{R}}(f) = \mathbf{T}^{\mathrm{T}}(f)$. The relation between $\tilde{\mathcal{E}}$ and $\mathcal{E}$ now follows from the definition of the weighted adjacency matrix. The input-output relation of the reverse channel reads $\tilde{\mathbf{Y}}(f) = \tilde{\mathbf{H}}(f)\tilde{\mathbf{X}}(f)$ where $\tilde{\mathbf{X}}(f)$ is the signal vector emitted by the vertices in $\tilde{\mathcal{V}}_{\mathrm{t}}$ and $\tilde{\mathbf{Y}}(f)$ is the signal vector received by the vertices in $\tilde{\mathcal{V}}_{\mathrm{t}}$. Considering Fig. B.4 and arguing as in Section B.3.2 yields for the reverse channel

$$\tilde{\mathbf{H}}(f) = \tilde{\mathbf{D}}(f) + \tilde{\mathbf{R}}(f)\left[\mathbf{I} - \tilde{\mathbf{B}}(f)\right]^{-1}\tilde{\mathbf{T}}(f) \tag{B.27}$$

Inserting for $\tilde{\mathbf{D}}(f), \tilde{\mathbf{R}}(f), \tilde{\mathbf{T}}(f)$, and $\tilde{\mathbf{B}}(f)$ leads to

$$\begin{aligned}\tilde{\mathbf{H}}(f) &= \mathbf{D}^{\mathrm{T}}(f) + \mathbf{T}^{\mathrm{T}}(f)\left[\mathbf{I} - \mathbf{B}^{\mathrm{T}}(f)\right]^{-1}\mathbf{R}^{\mathrm{T}}(f)\\ &= \mathbf{H}^{\mathrm{T}}(f),\end{aligned} \tag{B.28}$$

where the last equality results from (B.13). □

In words Theorem B.3.3 says that for a propagation graph there exists a reverse graph which fulfills the reciprocity condition. Furthermore, an example of a propagation graph fulfilling the reciprocity condition is the reverse graph $\tilde{\mathcal{G}}$ obtained by reversing all edges of $\mathcal{G}$ while maintaining the edge transfer functions.

### B.3.5 Related Recursive Scattering Models

We provide a few examples of recursive models to assist the reader in recognizing models which can be represented by the graphical structure.

In [18] Shi and Nehorai consider a model for recursive scattering between point scatterers in a homogeneous background. The propagation between any point in space is described by a scalar Green's function. The transfer function obtained by applying the Foldy-Lax equation can also be obtained from a propagation graph by defining the sub-matrices of $\mathbf{A}(f)$ as follows. The model does not include a directed term and thus $\mathbf{D}(f) = \mathbf{0}$. The entry of $[\mathbf{T}(f)]_{m_1 n}$ is the Green's function from transmit vertex $m_1$ to scatterer $n$ times the scattering coefficient of scatterer $n'$. Similarly, the entry $[\mathbf{R}(f)]_{nm_2}$ is the Green's function from the position of scatterer $n$ to receiver $m_2$. The entry $[\mathbf{B}(f)]_{nn'}, n \neq n'$ is the Green's function from the position of scatterer $n$ to the position of scatterer $n'$ times the scattering coefficient of scatterer $n$. Since a point scatterer does not scatter back on itself, the diagonal entries of $\mathbf{B}(f)$ are all zero. As can be observed from the above definitions, the assumption of homogeneous background medium leads to the special case with $\mathcal{E}_\mathrm{d} = \emptyset$, $\mathcal{E}_\mathrm{t} = \mathcal{V}_\mathrm{t} \times \mathcal{V}_\mathrm{s}$, $\mathcal{E}_\mathrm{r} = \mathcal{V}_\mathrm{s} \times \mathcal{V}_\mathrm{r}$, and $\mathcal{E}_\mathrm{s} = \mathcal{V}_\mathrm{s} \times \mathcal{V}_\mathrm{s}$.

Another modeling method that can be conveniently described using propagation graphs is (time-dependent) radiosity [20–24]. In these methods, the surfaces of the objects in the propagation environment are first divided in smaller patches, then the power transfer between pairs of patches is defined in terms of the so-called "delay-dependent form factor", and finally the power transfer from the transmitter to the receiver is estimated. The delay-dependent form factor is essentially a power impulse response between patches. It appears that for these algorithms no closed-form solution feasible for numerical evaluation is available in the literature. Thus [20–24] resort to iterative solutions which can be achieved after discretizing the inter-patch propagation delays. The time-dependent radiosity problem can be expressed in the Fourier domain in terms of a propagation graph where each patch is represented by a scatterer, while the entries of $\mathbf{A}(f)$ are defined according to delay dependent form factor. Using this formulation, a closed form expression of the channel transfer matrix appears immediately by Theorem B.3.1 with no need for quantization of propagation delays.

### B.3.6 Revisiting Existing Stochastic Radio Channel Models

It is interesting to revisit existing radio channel models by means of the just defined framework of propagation graphs. Such an effort may reveal some structural differences between models, which are not apparent merely from the mathematical formulation. It is, however, a fact that the interpretation of a transfer function as a propagation graph is not unique—it is straightforward to construct different propagation graphs which yield the same transfer matrix. Thus different propagation graphs may be associated to the same radio channel model. In the sequel we construct graphs for two well-known stochastic channel models, i.e., the model by Turin *et al.* [34] and the model by Saleh and Valenzuela [35]. We include here only enough detail to allow for the discussion of the structure of the associated graphs and refer the reader to the original papers for the full description.

The seminal model [34] by Turin *et al.* can be expressed in the frequency domain as

$$H(f) = \sum_{\ell=0}^{\infty} \alpha_\ell \exp(-j2\pi f \tau_\ell), \tag{B.29}$$

where $\alpha_\ell$ is the complex gain and $\tau_\ell$ denotes the delay of component $\ell$. Apart from the direct component, to which we assign index $\ell = 0$, the index $\ell$ is merely a dummy index which does not indicate any ordering of terms in (B.29). The set, $\{(\tau_\ell, \alpha_\ell) : \ell = 1, 2, \dots\}$ is a marked Poisson point process on $[\tau_0, \infty)$ with complex marks $\{\alpha_\ell : \ell = 1, 2, \dots\}$.

The propagation graph we seek should contain a propagation path for each term in the sum (B.29). We notice that modifying the term $\alpha_\ell \exp(-j2\pi f \tau_\ell)$ has no effect on the other terms in (B.29). This structure can be captured by constructing a propagation graph in which modifying vertices or edges in a propagation path leaves others unchanged. Graph theory offers the convenient notion of "independent walks" [32]: Two or more walks are called independent if none of them contains an inner vertex of another. In particular, propagation paths are independent if they do not traverse the same scatterers. Thus for independent propagation paths $\ell, \ell'$, changing path $\ell$ by changing its edge transfer functions or by deleting edges from it, has no effect on path $\ell'$. We therefore associate to each term in (B.29) an independent propagation path. Assuming for simplicity all paths to be single bounce paths this results in the graph shown in Fig. B.5(a).

The model by Saleh and Valenzuela [35] can be formulated as a second-order Turin model:

$$H(f) = \sum_{\ell=0}^{\infty} \exp(-j2\pi f \tau_\ell) \sum_{\ell'=0}^{\infty} \alpha_{\ell\ell'} \exp(-j2\pi f \tau_{\ell\ell'}), \tag{B.30}$$

where $\ell$ is a cluster index and $\ell'$ is a index for the components within a cluster. The set $\{\tau_\ell : \ell = 1, 2, \dots\}$ is a Poisson process on $[\tau_0, \infty)$ and conditioned on the cluster delays $\{\tau_\ell; \ell = 0, 1, \dots\}$, the family of sets $\{(\alpha_{\ell\ell'}, \tau_{\ell\ell'}) : \ell' = 1, 2, \dots\}$, $\ell = 0, 1, \dots,$ are independent marked Poisson processes. Using a similar argument as for the Turin model, leads to the graph depicted in Fig. B.5(b). The transmitter is connected to a set of super-ordinate scatterers, each scatterer corresponding to a "cluster". These

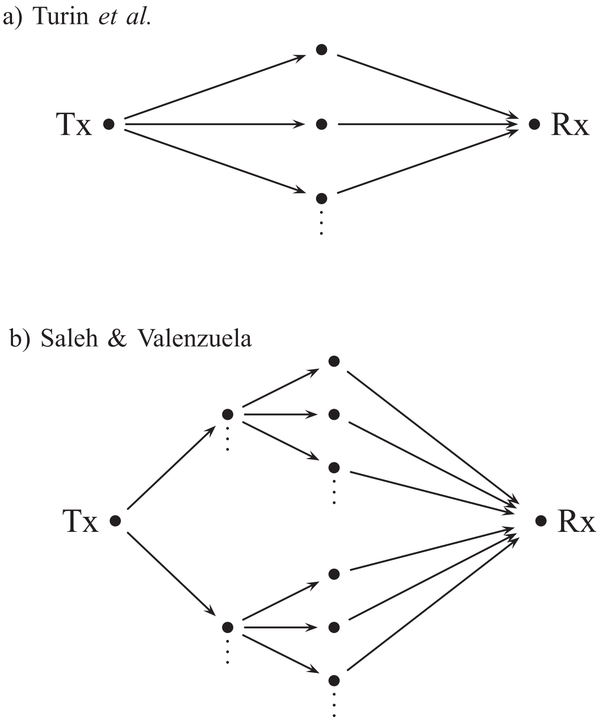

*Fig. B.5: Propagation graph representations of: a) a realization of the model by Turin* et al. *[34]; and b) a realization of the Saleh-Valenzuela model [35].*

cluster-scatters are then connected to the receiver via independent single-bounce paths passing through sub-ordinate scatterers. In this graph, deleting cluster scatterer $\ell$ makes a whole signal cluster $\ell$ disappear in (B.30). Similarly, removing the sub-ordinate scatterer $\ell'$ the component with index $\ell\ell'$ in (B.30) vanishes.

We end the discussion of the Saleh-Valenzuela model by mentioning that many equivalent graphical interpretations may be given. As an example, one may consider a graph structure as that of the reverse graph of Fig. B.5(b). In such a structure, the transmitter is directly connected to the sub-ordinate scatterers whereas the receiver is connected to the clusters. Indeed by reversing any number of clusters we obtain an equivalent propagation graph. These graphs share the common property that they contain no cycles.

## *B.4 Example: Stochastic Model for In-Room Channel*

The concept of propagation graph introduced until now can be used for describing a broad range of channel models. In this section we apply these general results to a specific example scenario where scatterer interactions are considered to be non-dispersive in delay. This resembles the case where all wave interactions can be considered as specular reflections, or considering points scatterers. The intent is to exemplify that the experimentally observed avalanche effect and diffuse tail can be explained using only scatterer interactions that by themselves yield no delay dispersion. We specify a method feasible for generating such a graph in Monte Carlo simulations. The model discussed in this example is a variant of the model proposed in [30, 31].

### *B.4.1 Weighted Adjacency Matrix*

We define the weighted adjacency matrix according to a geometric model of the environment. We consider a scenario with a single transmitter, a single receiver, and $N_\mathrm{s}$ scatterers, i.e., the vertex set reads $\mathcal{V} = \mathcal{V}_\mathrm{t} \cup \mathcal{V}_\mathrm{r} \cup \mathcal{V}_\mathrm{s}$ with $\mathcal{V}_\mathrm{t} = \{\mathrm{Tx}\}, \mathcal{V}_\mathrm{r} = \{\mathrm{Rx}\}$, and $\mathcal{V}_\mathrm{s} = \{\mathrm{S1}, \ldots, \mathrm{S}N_\mathrm{s}\}$. To each vertex $v \in \mathcal{V}$ we assign a displacement vector $\mathbf{r}_v \in \mathbb{R}^3$ with respect to a coordinate system with arbitrary origin. To edge $e = (v, v')$ we associate the Euclidean distance $d_e = \|\mathbf{r}_v - \mathbf{r}_{v'}\|$, the gain $g_e$, the phase $\phi_e$, and the propagation delay $\tau_e = d_e/c$, where $c$ is the speed of light. The edge transfer functions are defined as

$$A_e(f) = \begin{cases} g_e(f) \exp j(\phi_e - 2\pi\tau_e f); & e \in \mathcal{E} \\ 0; & e \notin \mathcal{E}. \end{cases} \tag{B.31}$$

The edge gains $\{g_e(f)\}$ are defined according to

$$g_e^2(f) = \begin{cases} \frac{1}{(4\pi f\tau_e)^2}; & e \in \mathcal{E}_\mathrm{d} \\ \frac{1}{4\pi f \mu(\mathcal{E}_\mathrm{t})} \cdot \frac{{\tau_e}^{-2}}{S(\mathcal{E}_\mathrm{t})}; & e \in \mathcal{E}_\mathrm{t} \\ \frac{1}{4\pi f \mu(\mathcal{E}_\mathrm{r})} \cdot \frac{{\tau_e}^{-2}}{S(\mathcal{E}_\mathrm{r})}; & e \in \mathcal{E}_\mathrm{r} \\ \frac{g^2}{\mathrm{odi}(e)}; & e \in \mathcal{E}_\mathrm{s} \end{cases} \tag{B.32}$$

where $\mathrm{odi}(e)$ denotes the number of edges from $\mathrm{init}(e)$ to other scatterers and for any $\mathcal{E}' \subseteq \mathcal{E}$

$$\mu(\mathcal{E}') = \frac{1}{|\mathcal{E}'|} \sum_{e \in \mathcal{E}'} \tau_e \qquad \text{and} \qquad S(\mathcal{E}') = \sum_{e \in \mathcal{E}'} {\tau_e}^{-2}, \tag{B.33}$$

with $|\cdot|$ denoting cardinality. The weight of the direct edge is selected according to the Friis equation [36] assuming isotropic antennas at both ends. The weights of edges in $\mathcal{E}_\mathrm{t}$ and $\mathcal{E}_\mathrm{r}$ also account for the antenna characteristics. They are computed at the average distance to avoid signal amplification when scatterers are close to a transmitter or receiver, namely when the far-field assumption is invalid. The value of inter-scatterer gain is for simplicity assumed fixed, i.e., $g_e(f) = g, e \in \mathcal{E}_\mathrm{s}$.

### *B.4.2 Stochastic Generation of Propagation Graphs*

We now define a stochastic model of the sets $\{\mathbf{r}_v\}$, $\mathcal{E}$, and $\{\phi_e\}$ as well as a procedure to compute the corresponding transfer function and impulse response. The vertex positions are assumed to reside in a bounded region $\mathcal{R} \subset \mathbb{R}^3$ corresponding to the region of interest. The transmitter and receiver positions are assumed to be fixed, while the positions of the $N_\mathrm{s}$ scatterers $\{\mathbf{r}_v : v \in \mathcal{V}_s\}$ are drawn independently from a uniform distribution on $\mathcal{R}$.

Edges are drawn independently such that a vertex pair $e \in \mathcal{V} \times \mathcal{V}$ is in the edge set $\mathcal{E}$ with probability $P_e = \Pr[e \in \mathcal{E}]$ defined as

$$P_e = \begin{cases} P_\mathrm{dir}, & e = (\mathrm{Tx}, \mathrm{Rx}) \\ 0, & \mathrm{term}(e) = \mathrm{Tx} \\ 0, & \mathrm{init}(e) = \mathrm{Rx} \\ 0, & \mathrm{init}(e) = \mathrm{term}(e) \\ P_\mathrm{vis} & \text{otherwise} \end{cases} . \tag{B.34}$$

The first case of (B.34) controls the occurrence of a direct component. If $P_\mathrm{dir}$ is zero, $D(f)$ is zero with probability one. If $P_\mathrm{dir}$ is unity, the direct term $D(f)$ is non-zero with probability one. The second and third cases of (B.34) exclude ingoing edges to the transmitter and outgoing edges from the receiver. Thus the generated graphs will have the structure defined in Section B.2.2. The fourth case of (B.34) excludes the occurrence of loops in the graphs. This is sensible as a specular scatterer cannot scatter a signal back to itself. A consequence of this choice is that any realization of the graph is loopless and therefore $\mathbf{A}(f)$ has zeros along its main diagonal. The last case of (B.34) assigns a constant probability $P_\mathrm{vis}$ of the occurrence of edges from $\mathcal{V}_t$ to $\mathcal{V}_s$, from $\mathcal{V}_s$ to $\mathcal{V}_s$ and from $\mathcal{V}_s$ to $\mathcal{V}_r$.

Finally, the phases $\{\phi_e : e \in \mathcal{E}\}$ are drawn independently from a uniform distribution on $[0; 2\pi)$.

Given the deterministic values of parameters $\mathcal{R}$, $\mathbf{r}_\mathrm{Tx}$, $\mathbf{r}_\mathrm{Rx}$, $N_\mathrm{s}$, $P_\mathrm{dir}$, $P_\mathrm{vis}$ and $g$, realizations of the (partial) transfer function $H_{K:L}(f)$ and corresponding (partial) impulse response $h_{K:L}(\tau)$ can now be generated for a preselected frequency range $[f_\mathrm{min}, f_\mathrm{max}]$, using the algorithm stated in Fig. B.6 and Appendix.

The algorithm in Appendix invokes (B.13) once at each frequency point considered. The computational complexity is thus of order $M$. Evaluation of

```
1. Draw $\mathbf{r}_v,\ v \in \mathcal{V}_\mathrm{s}$ uniformly on $\mathcal{R}$
2. Generate $\mathcal{E}$ according to (B.34)
3. Draw independent phases $\{\phi_e : e \in \mathcal{E}\}$ uniformly on $[0, 2\pi)$
4. Compute $\mathbf{A}(f)$ within the frequency bandwidth using (B.31)
5. IF spectral radius of $\mathbf{B}(f)$ is larger than unity for some frequency within
   the bandwidth THEN GOTO step 1
6. Estimate $H_{K:L}(f)$ and $h_{K:L}(\tau)$ as described in Appendix B.I
```

*Fig. B.6: Algorithm for generating full or partial transfer functions and impulse responses for a preselected bandwidth.*

(B.13) at one frequency calls for computation of the term $\mathbf{R}(f)(\mathbf{I} - \mathbf{B}(f))^{-1}\mathbf{T}(f)$. If this is done by inverting the matrix $\mathbf{I} - \mathbf{B}(f)$ the complexity is of order $N_\mathrm{s}^3$. If there are fewer transmitters or receivers than scatterers the complexity of computing (B.13) can be reduced somewhat depending on the particular numerical implementation. Thus the complexity of the algorithm in Appendix is *at most* cubic in $N_\mathrm{s}$. In practice, e.g. with the settings in Table B.1, the complexity of this algorithm is low enough to be run on a standard desktop computer in less than a second per channel realization.

### *B.4.3 Numerical Experiments*

The effect of the recursive scattering phenomenon can now be illustrated by numerical experiments. The parameter settings given in Table B.1 are selected to mimic the experimental setup of [27] used to acquire the measurements reported in Fig. B.1. The room size and positions of the transmitter and receiver are chosen as in [27]. We consider the case where direct propagation occurs and set $P_\mathrm{dir}$ to unity. The probability of visibility $P_\mathrm{vis}$ and the number of scatterers $N_\mathrm{s}$ are chosen to mimic the observed avalanche effect. The value of $g$ is set to match the tail slope $\rho \approx -0.4\,\mathrm{dB/ns}$ of the delay-power spectrum depicted in Fig. B.1. The value of $g$ can be related to the slope $\rho$ of the log delay-power spectrum via the approximation $\rho \approx 20\log_{10}(g)/\mu(\mathcal{E}_\mathrm{s})$. This approximation arises by considering the power balance for a scatterer: assuming the signal components arriving at the scatterer to be statistically independent, neglecting the probability of scatterers with outdegree zero, and approximating the delays of edges in $\mathcal{E}_\mathrm{s}$ by the average $\mu(\mathcal{E}_\mathrm{s})$ defined in (B.33). We remark that since $\mu(\mathcal{E}_\mathrm{s})$ depends on the realization of the graph, the gain coefficient $g$ is a random variable.

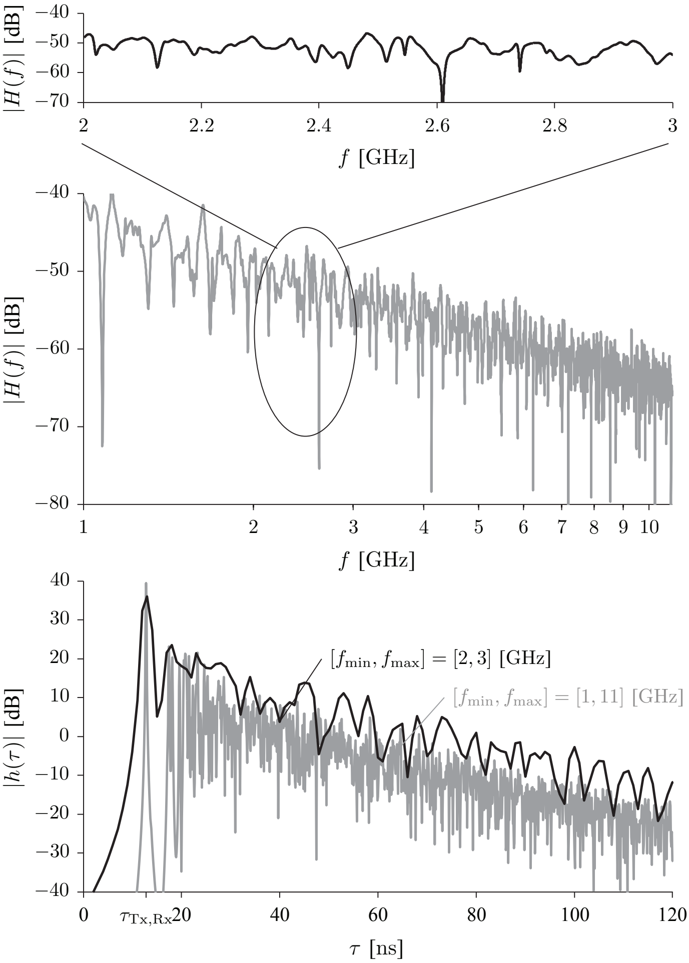

*Fig. B.7: Channel response for a specific realization of the propagation graph. Top: Transfer function in dB* $(20\log_{10}|H(f)|)$*. Bottom: Impulse responses in dB* $(20\log_{10}|h(\tau)|)$ *computed for two frequency bandwidths.*

*Table B.1: Parameter Settings for the Numerical Examples*

| Parameters | Symbol | Values |
|---|---|---|
| Room size | $\mathcal{R}$ | $[0, 5] \times [0, 5] \times [0, 2.6]\,\mathrm{m}^3$ |
| Transmitter position | $\mathbf{r}_{\mathrm{Tx}}$ | $[1.78,\ 1.0,\ 1.5]^{\mathrm{T}}\ \mathrm{m}$ |
| Receiver position | $\mathbf{r}_{\mathrm{Rx}}$ | $[4.18,\ 4.0,\ 1.5]^{\mathrm{T}}\ \mathrm{m}$ |
| Number of scatterers | $N_{\mathrm{s}}$ | 10 |
| Tail slope | $\rho$ | $-0.4\,\mathrm{dB/ns}$ |
| Prob. of visibility | $P_{\mathrm{vis}}$ | 0.8 |
| Prob. of direct propagation | $P_{\mathrm{dir}}$ | 1 |
| Speed of light | $c$ | $3 \cdot 10^8\ \mathrm{m/s}$ |
| Transmit signal | $X[m]$ | Unit power Hann pulse |
| Number of frequency samples | $M$ | 8192 |

Fig. B.7 shows the amplitude of a single realization of the transfer function. Overall, the squared amplitude of the transfer function decays as $f^{-2}$ due to the definition of $\{g_e(f)\}$. Furthermore, the transfer function exhibits fast fading over the considered frequency band. The lower panel of Fig. B.7 reports the corresponding impulse response for two different signal bandwidths. Both impulse responses exhibit an avalanche effect as well as a diffuse tail of which the power decays nearly exponentially with $\rho \approx -0.4\,\mathrm{dB/ns}$. As anticipated, the transition to the diffuse tail is most visible in the response obtained with the larger bandwidth.

The build up of the impulse response can be examined via the partial impulse responses given in Fig. B.8. Inspection of the partial responses when $K = L$ reveals that the early part of the tail is due to signal components with a low $K$ while the late part is dominated by higher-order signal components. It can also be noticed that as $K$ increases, the delay at which the maximum of the $K$-bounce partial response occurs and the spread of this response are increasing.

Fig. B.9 shows two types of delay-power spectra. The upper panel shows the ensemble average of squared amplitudes of 1000 independently drawn propagation graphs for the two signal bandwidths also considered in Fig. B.7. Both spectra exhibit the same trend: A clearly visible peak due to the direct signal is followed by a tail with nearly exponential power decay. As expected, the first peak is wider for the case with 1 GHz bandwidth than for the case with 10 GHz bandwidth. The tails differ by approximately 7 dB. This shift arises due to the $f^{-2}$ trend of the transfer function resulting in a higher received power for the lower frequencies considered in the 1 GHz bandwidth case. For the 1000 generated propagation graphs, the gain coefficient appears approximately Gaussian distributed with mean $0.65$ and standard deviation $0.029$. The bottom panel shows spatially averaged delay-power spectra obtained for one particular realization of the propagation graph. The simulated spatial averaged delay-power spectra exhibit the avalanche effect similar to the one

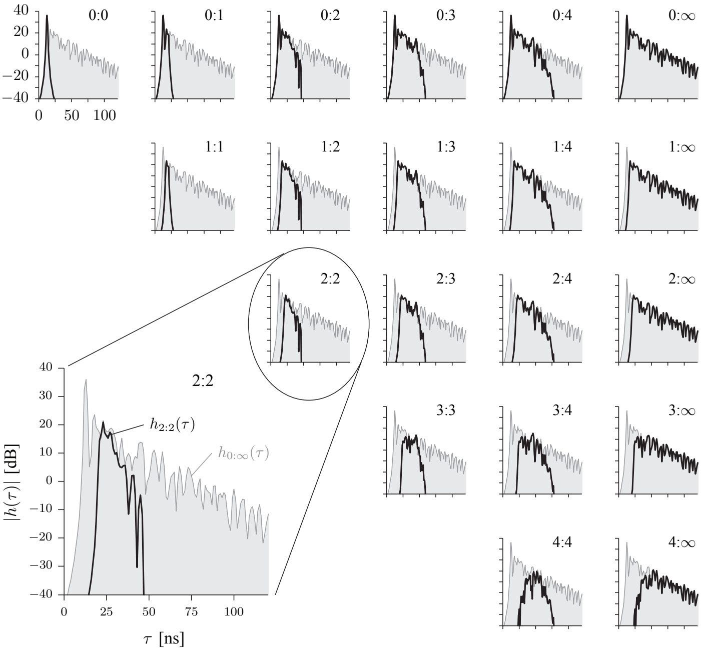

*Fig. B.8: Partial responses obtained for one graph realization for the bandwidth* $[2, 3]$ GHz. *The* $K : L$ *settings are indicated in each miniature. Top row:* $K$*-bounce approximations. Right-most column: error terms resulting from* $(K - 1)$*-bounce approximations. Main diagonal* $(K = L)$*:* $K$*-bounce contributions.*

observed in Fig. B.1. For the 10 GHz bandwidth case the power level of the diffuse tails agrees remarkably well with the measurement in Fig. B.1. The modest deviation of about 3 dB can be attributed to antenna losses in the measurement.

## B.5 Conclusions

The outset for this work was the observation that the measured impulse responses and delay-power spectra of in-room channels exhibit an avalanche effect: Multipath components appear at increasing rate and gradually merge into a diffuse tail with an exponential decay of power. We considered the question whether the avalanche effect is due to recursive scattering. To this end we modelled the propagation environment as a graph in which vertices represent transmitters, receivers, and scatterers and edges represent propagation conditions between vertices. From this general structure the graph's full and partial frequency transfer matrices were derived in closed form. These

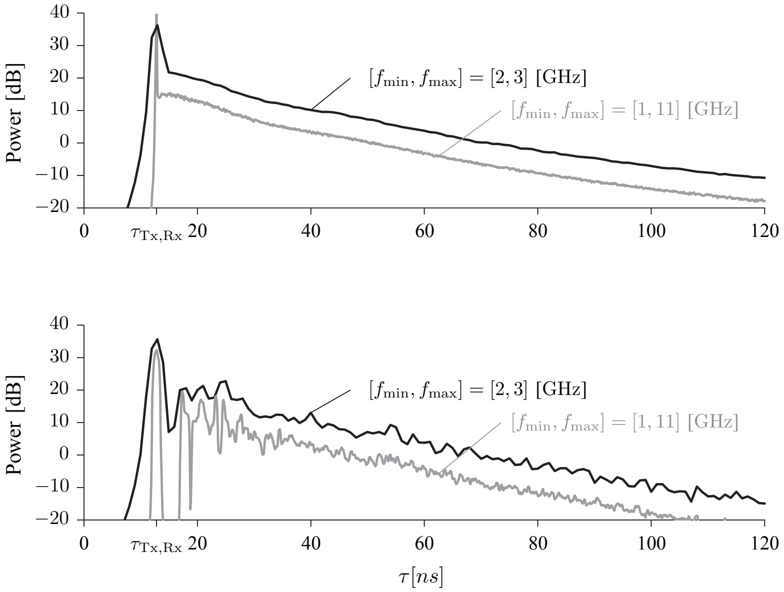

*Fig. B.9: Simulated delay-power spectra. Top panel: Ensemble average of 1000 Monte Carlo runs. Bottom panel: Spatial average of a single graph realization assuming the same grid as in Fig. B.1, i.e., 900 receiver positions on a 30×30 horizontal square grid with* $1 \times 1$ cm□ *mesh centered at position* $\mathbf{r}_{\mathrm{Rx}}$ *given in Table B.1.*

expressions can, by specifying the edge transfer functions, be directly used to perform numerical simulations.

We considered as an example a graph-based stochastic model where all interactions are non-dispersive in delay in a scenario similar to an experimentally investigated scenario where the avalanche effect was observed. The impulse responses generated from the model also exhibit an avalanche effect. This numerical experiment lead to the observation that the diffuse tail can be generated even when scatterer interactions are non-dispersive in delay. Furthermore, the exponential decay of the delay-power spectra can be explained by the presence of recursive scattering. As illustrated by the simulation results the proposed model, in contrast to existing models which treat dominant and diffuse components separately, provides a unified account by reproducing the avalanche effect.

## *B.I Appendix*

The transfer function $\mathbf{H}(f)$ and impulse response $\mathbf{h}(\tau)$ can be estimated as follows:

1. Compute $M$ samples of the transfer matrix within the bandwidth $[f_{\text{min}}, f_{\text{max}}]$

$$\mathbf{H}[m] = \mathbf{H}(f_{\text{min}} + m\Delta_f), \quad m = 0, 1, \ldots M-1, \tag{B.35}$$

where $\Delta_f = (f_{\text{max}} - f_{\text{min}})/(M-1)$ and $\mathbf{H}(\,\cdot\,)$ is obtained using Theorem B.3.1.

2. Estimate the received signal $\mathbf{y}(\tau)$ via the inverse discrete Fourier transform

$$\mathbf{y}(i\Delta_\tau) = \Delta_f \sum_{m=0}^{M-1} \mathbf{H}[m]\mathbf{X}[m] \exp(j2\pi im/M),$$

$i = 0, \ldots M-1$, with $\mathbf{X}[m] = \mathbf{X}(f_{\text{min}} + m\Delta_f)$ and $\Delta_\tau = 1/(f_{\text{max}} - f_{\text{min}})$.

The impulse response can be estimated by letting $\mathbf{X}[f]$ be a window function of unit power

$$\int_{f_{\text{min}}}^{f_{\text{max}}} |\mathbf{X}(f)|^2 \mathrm{d}f \approx \sum_{m=0}^{M} |\mathbf{X}[m]|^2 \Delta_f = 1, \tag{B.36}$$

where $\mathbf{X}[m] = \mathbf{X}(f_{\text{min}} + m\Delta_f)$. The window function must be chosen such that its inverse Fourier transform exhibits a narrow main-lobe and sufficiently low side-lobes; $\mathbf{y}(\tau)$ is then regarded as a good approximation of the impulse response of the channel and by abuse of notation denoted by $\mathbf{h}(\tau)$. Samples of the partial transfer matrix are obtained by replacing $\mathbf{H}(\,\cdot\,)$ by $\mathbf{H}_{K:L}(\,\cdot\,)$ in (B.35). The corresponding received partial impulse response is denoted by $\mathbf{h}_{K:L}(\tau)$.

## Acknowledgment

We wish to thank Dr. -Ing. Jürgen Kunisch and Dipl.-Ing. Jörg Pamp for their kind permission to use Fig. B.1.

## References

[1] H. Hashemi, "Simulation of the urban radio propagation," *IEEE Trans. Veh. Technol.*, vol. 28, pp. 213–225, Aug. 1979.

[2] D. Molkdar, "Review on radio propagation into and within buildings," *Microwaves, Antennas and Propagation, IEE Proceedings H*, vol. 138, no. 1, pp. 61–73, 1991.

[3] N. Alsindi, B. Alavi, and K. Pahlavan, “Measurement and modeling of ultrawideband TOA-based ranging in indoor multipath environments,” *IEEE Trans. Veh. Technol.*, vol. 58, no. 3, pp. 1046–1058, Mar. 2009.

[4] J. Kunisch and J. Pamp, “Measurement results and modeling aspects for the UWB radio channel,” in *IEEE Conf. on Ultra Wideband Systems and Technologies, 2002. Digest of Papers*, May 2002, pp. 19–24.

[5] J. Poutanen, J. Salmi, K. Haneda, V. Kolmonen, F. Tufvesson, and P. Vainikainen, “Propagation characteristics of dense multipath components,” *Antennas and Wireless Propagation Letters, IEEE*, vol. 9, pp. 791–794, 2010.

[6] J. Poutanen, J. Salmi, K. Haneda, V. Kolmonen, and P. Vainikainen, “Angular and shadowing characteristics of dense multipath components in indoor radio channels,” *IEEE Trans. Antennas Propagat.*, vol. 59, no. 1, pp. 245–253, Jan. 2011.

[7] H. Kuttruff, *Room Acoustics*. London: Taylor & Francis, 2000.

[8] C. Holloway, M. Cotton, and P. McKenna, “A model for predicting the power delay profile characteristics inside a room,” *IEEE Trans. Veh. Technol.*, vol. 48, no. 4, pp. 1110–1120, July 1999.

[9] R. Rudd and S. Saunders, “Statistical modelling of the indoor radio channel – an acoustic analogy,” in *Proc. Twelfth International Conf. on Antennas and Propagation (Conf. Publ. No. 491)*, vol. 1, 31 March–3 April 2003, pp. 220–224.

[10] R. F. Rudd, “The prediction of indoor radio channel impulse response,” in *The Second European Conf. on Antennas and Propagation, 2007. EuCAP 2007.*, Nov. 2007, pp. 1–4.

[11] J. B. Andersen, J. Ø. Nielsen, G. F. Pedersen, G. Bauch, and J. M. Herdin, “Room electromagnetics,” *IEEE Antennas Propagat. Mag.*, vol. 49, no. 2, pp. 27–33, Apr. 2007.

[12] T. H. Lehman, “A statistical theory of electromagnetic fields in complex cavities,” Otto von Guericke University of Magdeburg, Tech. Rep., May 1993.

[13] D. A. Hill, *Electromagnetic Fields in Cavities: Deterministic and Statistical Theories*. Wiley-IEEE Press, 2009.

[14] L. L. Foldy, “The multiple scattering of waves — I. General theory of isotropic scattering by randomly distributed scatterers,” *Physical Review*, vol. 67, pp. 107–119, Feb. 1945.

[15] M. Lax, “Multiple scattering of waves,” *Reviews of Modern Physics*, vol. 23, no. 4, pp. 287–310, Oct. 1951.

[16] ——, “Multiple scattering of waves. II. The effective field in dense systems,” *Physical Review*, vol. 85, no. 4, pp. 621–629, Feb. 1952.

[17] M. I. Mishchenko, L. D. Travis, and A. A. Lacis, *Multiple Scattering of Light by Particles: Radiative Transfer and Coherent Backscattering*. Cambridge University Press, May 2006.

[18] G. Shi and A. Nehorai, “Cramér-Rao bound analysis on multiple scattering in multistatic point-scatterer estimation,” *IEEE Trans. Signal Processing*, vol. 55, no. 6, pp. 2840–2850, June 2007.

[19] M. Franceschetti, “Stochastic rays pulse propagation,” *IEEE Trans. Antennas Propagat.*, vol. 52, no. 10, pp. 2742–2752, Oct. 2004.

[20] E.-M. Nosal, M. Hodgson, and I. Ashdown, "Investigation of the validity of radiosity for sound-field prediction in cubic rooms," *The Journal of the Acoustical Society of America*, vol. 116, no. 6, pp. 3505–3514, 2004.

[21] M. Hodgson and E.-M. Nosal, "Experimental evaluation of radiosity for room sound-field prediction," *The Journal of the Acoustical Society of America*, vol. 120, no. 2, pp. 808–819, 2006.

[22] S. Siltanen, T. Lokki, S. Kiminki, and L. Savioja, "The room acoustic rendering equation," *The Journal of the Acoustical Society of America*, vol. 122, no. 3, pp. 1624–1635, 2007.

[23] R. T. Muehleisen and C. W. Beamer, IV, "Steady state acoustic radiosity for the prediction of sound pressure levels in enclosures with diffuse surfaces," *Noise Control Engineering Journal*, vol. 57, no. 3, pp. 244–262, 2009.

[24] G. Rougeron, F. G. nd Yannik Gabillet, and K. Boutouch, "Simulation of the indoor propgation of a 60 GHz electromagnetic wave with a time-dependent radiosity algorithm," *Computers & Graphics*, vol. 26, pp. 125–141, 2002.

[25] H. Hashemi, "The indoor radio propagation channel," *Proc. IEEE*, vol. 81, no. 7, pp. 943–968, July 1993.

[26] J. Kunisch and J. Pamp, "UWB radio channel modeling considerations," in *Proc. International Conference on Electromagnetics in Advanced Applications 2003*, Turin, Sept. 2003.

[27] ——, "An ultra-wideband space-variant multipath indoor radio channel model," in *IEEE Conf. on Ultra Wideband Systems and Technologies, 2003*, Nov. 2003, pp. 290–294.

[28] ——, "Locally coherent ultra-wideband radio channel model for sensor networks in industrial environment," in *Proc. IEEE 2006 International Conf. on Ultra-Wideband*, Sept. 2006, pp. 363–368.

[29] O. Fernandez, L. Valle, M. Domingo, and R. P. Torres, "Flexible rays," *IEEE Veh. Technol. Mag.*, vol. 3, pp. 18–27, Mar. 2008.

[30] T. Pedersen and B. Fleury, "Radio channel modelling using stochastic propagation graphs," in *Proc. IEEE International Conf. on Communications ICC '07*, June 2007, pp. 2733–2738.

[31] T. Pedersen and B. H. Fleury, "A realistic radio channel model based on stochastic propagation graphs," in *Proceedings 5th MATHMOD Vienna – 5th Vienna Symposium on Mathematical Modelling*, vol. 1,2, Feb. 2006, p. 324, ISBN 3–901608–30–3.

[32] R. Diestel, *Graph Theory*. Springer-Verlag, 2000.

[33] R. A. Horn and C. A. Johnson, *Matrix Analysis*. Cambridge University Press, 1985.

[34] G. Turin, F. Clapp, T. Johnston, S. Fine, and D. Lavry, "A statistical model of urban multipath propagation channel," *IEEE Trans. Veh. Technol.*, vol. 21, pp. 1–9, Feb. 1972.

[35] A. A. M. Saleh and R. A. Valenzuela, "A statistical model for indoor multipath propagation channel," *IEEE J. Select. Areas Commun.*, vol. SAC-5, no. 2, pp. 128–137, Feb. 1987.

[36] H. T. Friis, “A note on a simple transmission formula,” *Proceedings of the I.R.E.*, vol. 34, no. 5, pp. 254–256, may 1946.

# *Experimental Validation of the Reverberation Effect in Room Electromagnetics*

Gerhard Steinböck, Troels Pedersen, Bernard H. Fleury, Wei Wang
and Ronald Raulefs

*IEEE Transactions Antennas and Propagation, to be submitted.*

© 2013 IEEE

*The layout has been revised.*

## Abstract

Knowledge of the time dispersion of the radio channel is important for wireless communication and localization. One tool to characterize the dispersion is the delay power spectrum. In-room experimental investigations indicate that the tail of the delay power spectrum has a behavior like a declining diffuse field and may be characterized with Sabine's reverberation model translated from room acoustics to electromagnetics. However, this translated model was sofar only fitted to experimental data, and no thorough validation of the models prediction abilities has been performed. In this contribution we experimentally validate Sabine's and Eyring's reverberation models. We follow Sabine's original approach of modifying wall absorption coefficients. For those modifications we compare predictions and experimental observations. We observe that Eyring's model predicts better than Sabine's, specifically with increasing absorption coefficients. After validating the models we present two applications. One focuses on the difference between Sabine's and Eyring's model for the estimation of human absorbtion cross section. The other application uses the reverberation models to predict parameters for the delay power spectrum in a neighboring room. From the delay power spectrum we predict the path loss or path gain, mean delay and rms delay spread and compare them with experimental observations and observe good agreement.

## C.1 Introduction

Models of the time dispersion of the radio channel are important tools in the engineering of wireless communication and localization systems. The time dispersion is of concern since it determines in part the coherence bandwidth and the intersymbol interference which are directly related to the bit error rate [1, 2] of communication systems. For these systems the time dispersion information may be used to decide upon the modulation, coding, equalization and diversity schemes. The time dispersion can be characterized by the delay power spectrum. Models for the delay power spectrum for different environments are thus an essential tool in the design of communication systems and many such models have been proposed [3, 4]. In [5] a distance dependent delay power spectrum was proposed allowing to characterize the narrow band parameter path loss and the wide band parameters mean delay and rms delay spread versus distance. These parameters are not only important in communications but in addition the distance dependent wideband parameters can enhance the localization performance [6].

Acoustical Reverberation models, such as Sabine's and Eyring's models, have been transcribed to characterize the delay power spectrum [7–11]. Sabine [12] and Eyring [13] characterized the tail of the delay power spectrum for room acoustics for a single source inside the room and no contributions from outside. They require few parameters, such as the volume, surface and an average absorption coefficient of the room. This simplicity makes the models very attractive for the use in electromagnetics too. For electromagnetics similar models exist for reverberation chambers [11]. However, those chambers have highly conductive walls and use a steerer to create a diffuse field. Therefore we focus here on the transcribed reverberation models from acoustics.

It is not apparent that the acoustical analogy is valid for room electromagnetics. For instance, it is unclear if the reverberation is determined by a single room, or by the outer structure of the building. Single rooms typically consist of several "light walls" and possibly one "heavy" wall. Radio waves may propagate easily through light walls. The outer structure, however, consists of heavy walls such as concrete or thick brick walls which are harder to penetrate. As such the presented results in previous publications of estimated reverberation times or estimated average absorption coefficients highly depend on the assumption which surface and volume to be used, e.g. the single room, the entire floor or the entire building. Although measurements in rooms with different sizes have been conducted, these rooms have different wall absorption coefficients too. Therefore, one cannot conclude if changes in the observations are caused by the room size or the changed absorption coefficients. To our knowledge no systematic evaluation of the reverberation phenomenon has appeared in the literature for electromagnetics. For indoor environments a thorough validation of the reverberation models for electromagnetics is missing.

In this contribution we validate and compare the reverberation models for electromagnetics for indoor environments. Inspired by Sabine's original experiments [12] we carry out an experiment where we change in a controlled systematic manner the average absorption coefficient in a room and observe the effect on the reverberation time. This approach enables the validation of the prediction accuracy of the reverberation models. We compare predictions of Sabine's [12, 14] and Eyring's [13, 14] reverberation models with our experimental results. This allows to i) identify if the reverberation is confined within a single room, ii) compare the prediction accuracy of the two models and iii) evaluate their validity for room electromagnetics. After the validation of the models we discuss two possible applications. The first application focuses on a discussion of the differences between Sabine's and Eyring's model for the estimation of the average human absorption cross section. This cross section may be used for determining the specific absorption rate (SAR) for the whole human body [15, 16]. In the second application we use a prediction of the delay power spectrum for an adjacent room to predict path loss, mean delay and rms delay spread versus distance. We compare those predictions with their respective experimental observations.

The obtained results indicate that the reverberation models are valid for room electromagnetics and that Eyring's model predicts better. The models can be used to characterize the delay power spectrum and predict it for various environments.

## C.2 Reverberation Models

In the following a short overview of Sabine's and Eyring's reverberation models and their use in the delay power spectrum is presented in the context of radio channels. The delay power spectrum is defined as

$$G(d,\tau) = \mathrm{E}[|h\,(d,\tau)|^2], \tag{C.1}$$

where $h\,(d,\tau)$ denotes the impulse response obtained for distance $d$ between transmitter and receiver. [1] As shown in [5] and sketched in Fig. C.1 $G(d,\tau)$ can be modeled as the sum of a primary and a reverberant component

$$G(d,\tau) = \underbrace{G_0 \left(\tfrac{d_0}{d}\right)^n \delta\left(\tau - \tfrac{d}{c}\right)}_{G_{\mathrm{pri}}(d,\tau)} + \underbrace{G_{0,\mathrm{rev}}\, e^{-\tau/T}\, u(\tau - \tfrac{d}{c})}_{G_{\mathrm{rev}}(d,\tau)}. \tag{C.2}$$

The primary component, denoted $G_{\mathrm{pri}}(d,\tau)$, represents the early part of the delay power spectrum and consists of the direct propagation and possibly first-order reflections. The parameters of $G_{\mathrm{pri}}(d,\tau)$ are the reference path gain $G_0$ at reference distance $d_0$, the path gain exponent $n$, the speed of light $c$ and $d$ the distance between transmitter and receiver. The Dirac delta function is denoted by $\delta(\,\cdot\,)$. The reverberant component $G_{\mathrm{rev}}(d,\tau)$ is contributed by the multitude of higher order reflections in the room, which yield the tail in the measured delay power spectra. It decays exponentially with rate $T$, referred to as the reverberation time and $G_{0,\mathrm{rev}}$ corresponding to the reverberant power at delay zero. The unit step function $u(\tau)$ ensures causality and creates the onset of the reverberant component at $\frac{d}{c}$. The delay power spectrum is sketched in Fig. C.1. The received power $P_{\mathrm{R}}(t,d)$ of the reverberant component reads

$$P_{\mathrm{R}}(t,d) = \int P_{\mathrm{I}}(t-\tau)\, G_{\mathrm{rev}}(d,\tau)\, \mathrm{d}\tau, \tag{C.3}$$

where $P_{\mathrm{I}}(t)$ is the radiated power and we assume that any losses from the transmit and receive antennas are included in $G_{\mathrm{rev}}(d,\tau)$. The main concern of this contribution is to obtain predictions of $G_{0,\mathrm{rev}}$ and $T$ necessary to describe $G_{\mathrm{rev}}(d,\tau)$.

---

[1] The expectation operator E[] represents the mathematical abstraction of an averaging procedure to suppress variations due to small and large scale fading. This averaging procedure is used in [17] to obtain the so called long-term power delay profile. Realizations of $|h\,(\tau,d)|^2$ are sampled at different transmitter and receiver locations in the room.

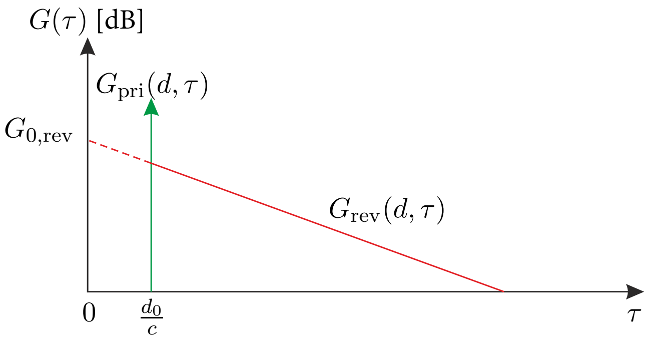

*Fig. C.1: The delay power spectrum and relevant parameters for the model in [5]. The spectrum is shown for distance $d = d_0$.*

The reverberation models allow for predictions for different environments of the tail of the delay power spectrum. Thus, in the following we focus on $G_{\text{rev}}(d,\tau)$. In [9, 11] is shown that the average received power $P_{\text{R}}(t)$ of an antenna in an isotropic diffuse field is related to the energy density $W(t)$ in the room as

$$P_{\text{R}}(t) = c\,A_{\text{R}}\,W(t). \tag{C.4}$$

The proportionality constant $A_{\text{R}}$ accounts for the receive and transmit antenna parameters and polarization loss. The isotropic diffuse field makes the directivity of the antennas negligible. In the following investigations we do not know the antenna parameters in detail, instead we use a reference measurement and will compare only relative results. Reverberation models of room acoustics, which were translated to room electromagnetics, have been used in [7–11, 15, 16] to characterize $W(t)$. Similar models for $W(t)$ exist for electromagnetic fields in reverberation chambers [11]. However, these chambers have highly conductive walls and a stirrer is used to obtain a diffuse field. Obviously, this situation is very different from “normal” rooms we consider.

### C.2.1 Sabine’s Model

The well-known room acoustics model by Sabine [12] has been considered for modeling of the parameters of the reverberant component in in-room radio channels [9, 10, 16, 18]. The assumption of a diffuse field contained in a room leads to Sabine’s model. Sabine’s model yields an expression for the $W(t)$ by considering a closed room with volume $V$ and surface $S$, a single source inside the room and no contributions from outside the room. Upon wall interactions some power remains in the room and the rest is absorbed as sketched in Fig. C.2. It is shown in [9, 14, 18] that for an isotropic diffuse

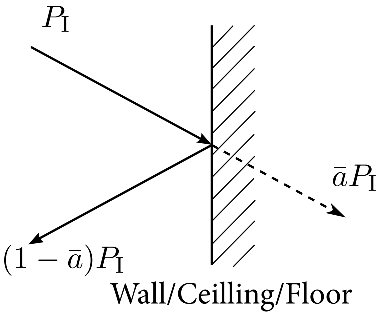

*Fig. C.2: Absorption on the room boundaries with average absorbtion coefficient $\bar{a}$ obtained from* (C.6).

field the power balance of radiated input power $P_\mathrm{I}(t)$, reverberant power and absorbed power leads to the differential equation

$$P_\mathrm{I}(t) = \underbrace{V\frac{\mathrm{d}W(t)}{\mathrm{d}t}}_{\text{Reverberant Power}} + \underbrace{\frac{\bar{a}\,S\,c}{4}W(t)}_{\text{Absorbed Power}} \,. \tag{C.5}$$

The average absorption coefficient $\bar{a}$ is defined as

$$\bar{a} = \frac{\sum_i S_i a_i}{S}, \qquad S = \sum_i S_i. \tag{C.6}$$

with $S_i$ denoting the area of surface $i$ with absorption coefficient $a_i$. The general solution of the first order differential equation (C.5) is a convolutional integral

$$W(d,t) = \int_{-\infty}^{\infty} P_\mathrm{I}(t-\tau)\frac{1}{V}\exp\left(-\frac{\tau}{T_\mathrm{Sab}}\right)u(\tau-\tfrac{d}{c})\,\mathrm{d}\tau \tag{C.7}$$

with the exponential decay rate (reverberation time)

$$T_\mathrm{Sab} = \frac{4\,V}{\bar{a}\,S\,c}. \tag{C.8}$$

The step function $u(\tau-\frac{d}{c})$ ensures causality. From Sabine's modeling approach we obtain a model for $G_\mathrm{rev}(d,\tau)$ in room electromagnetics. Inserting (C.7) into (C.5) and comparing to (C.3) leads to the model

$$G_\mathrm{rev,Sab}(d,\tau) = c\,A_\mathrm{R}\,\frac{1}{V}\exp\left(-\frac{\tau}{T_\mathrm{Sab}}\right)u(\tau-\tfrac{d}{c}). \tag{C.9}$$

### C.2.2 *Eyring's Model*

As already pointed out by Eyring in [13], in "dead" rooms with an average absorption coefficient of unity such that no reverberation occurs, Sabine's model still provides a value different from zero for the reverberation time in (C.8). This nonphysical effect lead Eyring to propose for acoustics a model [13] suitable for large absorption coefficients or so called "dead" rooms. In the following we present Eyring's modeling approach for room electromagnetics.

Eyring's model was based on the mirror source theory. Upon a specular reflection on a wall, a "virtual" mirror source behind the wall is assumed. This can be extended for infinitely many reflections between walls, creating infinitely many of such mirror sources outside the room. The distance between a mirror source and the receiver corresponds to the distance the wave travels between transmitter and receiver via the reflection point(s). Thus instead of considering reflections one may assume that the walls do not exist and all mirror sources including the original source in the room transmit the signal simultaneously to the receiver. Using this approach Eyring [13] obtained a differential equation similar to (C.5). The main difference, however, is that Eyring did not make any prior assumptions on the diffuse field in the room. Instead, Eyring considered only specular reflections and derived the reverberation model via the mirror theory. The received power obtained for $k$th mirror source is

$$P_{\mathrm{R},k}(t,\tau_k) \approx A_{\mathrm{R}} \underbrace{\frac{1}{4\,\pi\,d_k^2}}_{\text{Free space attenuation}} \underbrace{(1-\bar{a})^{w_k}}_{\text{Wall attenuation}} P_{\mathrm{I}}(t-\tau_k), \qquad \text{(C.10)}$$

where $(1-\bar{a})$ is the average wall reflection coefficient, $(1-\bar{a})^{w_k}$ is the attenuation for $w_k$ wall interactions, $\tau_k = \frac{d_k}{c}$ is the propagation time of the transmit signal for distance $d_k$ between the mirror source and the receiver. We assume $A_{\mathrm{R}}$ to be a constant for all $k$ directions by either considering omnidirectional antennas or by utilizing the assumption of an isotropic diffuse field as in (C.4). The attenuation due to wall interactions is approximated as

$$(1-\bar{a})^{w_k} \approx (1-\bar{a})^{\bar{w}\,\tau_k} = \exp(\bar{w}\,\tau_k\,\ln(1-\bar{a})), \qquad \text{(C.11)}$$

where the average number of wall interactions per second may be approximated as [14]

$$\bar{w} \approx \frac{c\,S}{4\,V}. \qquad \text{(C.12)}$$

With these approximations, the power of a single mirror source reads

$$P_{\mathrm{R},k}(t,\tau_k) \approx A_{\mathrm{R}} \frac{1}{4\,\pi\,(c\,\tau_k)^2} \exp(\bar{w}\,\tau_k\,\ln(1-\bar{a}))\,P_{\mathrm{I}}(t-\tau_k). \qquad \text{(C.13)}$$

The average number of mirror sources with delay $\tau$ is approximately [14]

$$r(\tau) \approx 4\pi \frac{c^3 \tau^2}{V}. \tag{C.14}$$

This approximation is valid if the reflections are uncorrelated. The received power at delay $\tau$ is given as $\sum_k^{r(\tau)} P_{\mathrm{R},k}(t,\tau) = r(\tau)\, P_{\mathrm{R},k}(t,\tau)$. We then obtain the total received power for an infinite number of mirror sources as the integral

$$\begin{aligned} P_\mathrm{R}(t) &= \int_{-\infty}^{\infty} r(\tau)\, P_{\mathrm{R},k}(t,\tau) u(\tau - \tfrac{d}{c})\, \mathrm{d}\tau, && \text{(C.15)} \\ &= \int_{-\infty}^{\infty} P_\mathrm{I}(t-\tau) \underbrace{c\, A_\mathrm{R}\, \frac{1}{V} \exp\left(-\frac{\tau}{T_\mathrm{Eyr}}\right) u(\tau - \tfrac{d}{c})}_{G_{\mathrm{rev,Eyr}}(d,\tau)}\, \mathrm{d}\tau. && \text{(C.16)} \end{aligned}$$

The reverberation time $T_\mathrm{Eyr}$ is

$$T_\mathrm{Eyr} = -\frac{4\,V}{c\,S\, \ln(1-\bar{a})}. \tag{C.17}$$

### C.2.3 Remarks

For both, Sabine's and Eyring's models, we identify the reverberant gain at delay zero as

$$G_{0,\mathrm{rev}} = c\, A_\mathrm{R}\, \frac{1}{V}. \tag{C.18}$$

Thus Eyring's $G_{\mathrm{rev,Eyr}}(d,\tau)$ and Sabine's (C.9) model only differ by their respective decay rates (C.17) and (C.8). Both decay rates are of the form:

$$T = f(\bar{a})\, \frac{4\,V}{c\,S}, \qquad f(\bar{a}) = \begin{cases} 1/\bar{a}, & \text{Sabine, } f_\mathrm{Sab}(\bar{a}) \\ -1/\ln(1-\bar{a}), & \text{Eyring, } f_\mathrm{Eyr}(\bar{a}). \end{cases} \tag{C.19}$$

In [13] was shown that $f_\mathrm{Sab}(\bar{a})$ can be considered as a first order Tailor series expansion of $f_\mathrm{Eyr}(\bar{a})$ and is well approximated for small absorption coefficients. A comparison of the dependency on the absorption coefficient of Sabine's and Eyring's models can be seen in Fig. C.3 for the reverberation time and in Fig. C.4 for $G_\mathrm{rev}(d,\tau)$. From Fig. C.3 we see that (C.8) and (C.17) are very steep functions at small $\bar{a}$ and flatten at large values. This different behavior may be of importance for experimental investigations of the reverberation time, specifically for room electromagnetics where typical experimentally observed absorption coefficients are larger as in room acoustics. Therefore we expect in electromagnetics only small changes in the reverberation time

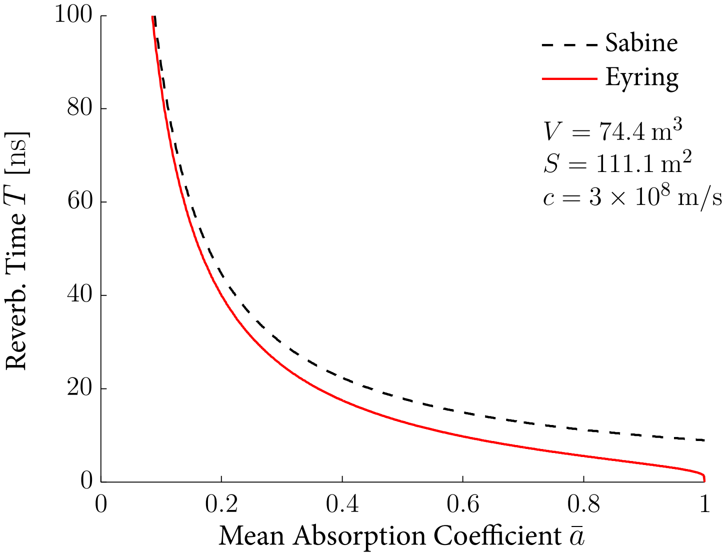

*Fig. C.3: The reverberation time versus the average absorption coefficient is shown for Sabine's and Eyring's model for the electromagnetic case.*

when varying the absorption coefficient. Important for the prediction of the reverberation time is that it only depends on the volume-surface ratio $V/S$ with unit [m], if $f(\bar{a})$ is the same for different rooms. Thus both models predict the same change in reverberation time for different rooms with equal $f(\bar{a})$.

The absorption coefficient $\bar{a}$ can be obtained from experimental observations of the reverberation time $\widehat{T}$ by rearranging (C.8) and (C.17) as

$$\bar{a}_{\mathrm{Sab}} = \frac{4\,V}{c\,S\,\widehat{T}}, \tag{C.20}$$

$$\bar{a}_{\mathrm{Eyr}} = 1 - \exp\left(\frac{-4\,V}{c\,S\,\widehat{T}}\right), \tag{C.21}$$

for Sabine's and Eyring's model, respectively. Since

$$\bar{a}_{\mathrm{Eyr}} = 1 - \exp\left(-\bar{a}_{\mathrm{Sab}}\right), \tag{C.22}$$

we can transform the absorption coefficient obtained with one model into the other. Using this transform in Table C.4 we provide an overview of observed reverberation times and their corresponding absorption coefficients from open literature.

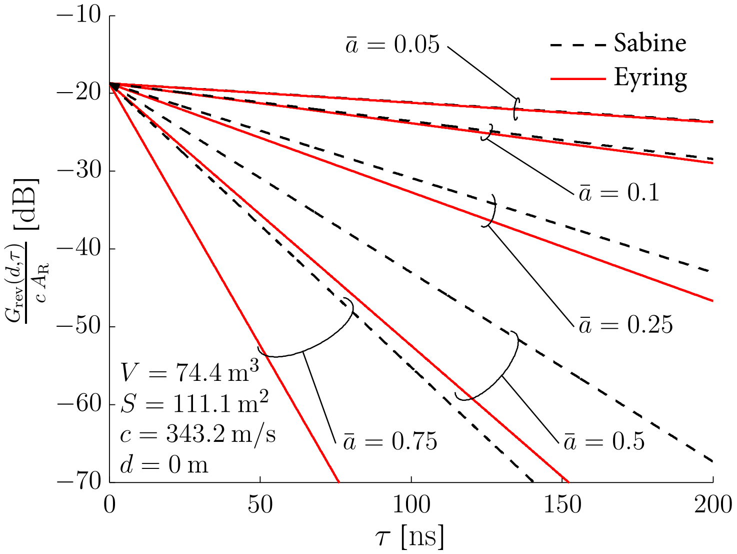

*Fig. C.4: The reverberant component $G_{\text{rev}}(d,\tau)$ with the decay rates obtained with Sabine's and Eyring's model,* (C.8) *and* (C.17)*, respectively are scaled by the constant $c\ A_{\text{R}}$ and shown for different average absorption coefficients.*

## C.3 Model Validation

Model validation here means verification of the models prediction abilities, i.e. to test that the models predictions are in line with measurement results which were not used in the model fitting process. This should be done by carefully designing the experiments and by a proper evaluation in order to avoid circular reasoning when proposing a model. In the following we present a short overview of previous literature applying the reverberation models in room electromagnetics. Thereafter, we propose a general validation methodology followed by a detailed description specific for our experiments.

### C.3.1 Background on Validation

Previously, the reverberation models were fitted to electromagnetic measurements [9, 10, 18]. Sabine's model was transcribed from acoustics to electromagnetics in [9, 18]. The transcribed model was fitted to measurement data of a single room but predictions of the model were not tested. Thus, the model is not validated. In [7] a model of the delay power spectrum was proposed. The model builds partly upon Eyring's [13] results to obtain a model that considers the transition from a non-reverberant to a reverberant field, however this leads to a non-exponential $G_{\text{rev}}(\tau, d)$. In [8] the work of [7] was extended. A model specifically for asymmetrical rooms, where the mean free path length is different from $c/\bar{w}$, is proposed. A partial validation was done for the models in [7] and [8]. For the validation both contribution consider experimental observations of delay power spectra in two differently sized rooms. To predict the shape of the delay power spectrum in these rooms, the average absorption coefficients were calculated from the wall materials. The predicted delay power spectra and the measured ones were normalized and afterwards their shape, specifically the decay of the tail was used to validate the models[2]. Due to the normalization and the non-exponential tail, they did not consider the intersection of the tail at zero delay in their validation procedure. Neither contribution considers modifying the absorption coefficient in a single room and check if the predicted changes in $T$ are valid. Furthermore the influence of neighboring rooms was not considered. This, however, maybe critical as radio waves propagate through walls and may be reflected backwards into the room under consideration. No comparison to the simpler models as Sabine's and Eyring's were considered to justify the proposed modifications.

### C.3.2 Validation Procedure

We propose to follow a validation procedure based on predictions of the reverberation time and the power of the tail at delay zero for changes of the average absorption coefficient and the volume-surface ratio. To do such a validation of the Sabine's and Eyring's models we "change" the environment and verify if the reverberation time changes according to predictions of the models. One approach similar to [7] and [8] could be to measure in different rooms with different sizes. However, the interior will most likely differ, i.e. other furniture or other wall materials, and thus the volume-surface ratio and the average wall absorption coefficient will change, hindering a comparison. To circumvent the problem of changing all parameters of the models, we follow the approach of Sabine's original work [12] and modify the average wall absorption coefficient and predict the change in reverberation time in the considered room. Additionally we modify the average absorbtion coefficient in neighboring rooms to investigate their influence on the reverberation time. Besides the reverberation time of the model we investigate as well the power of the tail at zero delay. The models predict that this power solely depends on the volume of the room. Thus by changing the average absorption coefficient we expect no changes of the power at delay zero. After validating the models dependency on the average absorbtion coefficient, we predict the reverberation time and the power of the tail at zero delay for a smaller room. This allows us to validate the volume-surface ratio dependency of the models.

---

[2] We remark that in [8] the model of [7] did not provide a valid result for their measurements. In fact an absorption coefficient of 0.6 instead of 0.3 provided a good fit, this large discrepancy lead the author in [8] to their modifications.

In the validation procedure for the models we verify the dependency i) on the average absorption coefficient, ii) the volume-surface ratio, and iii) the power at delay zero $G_{0,\mathrm{rev}}$. In part the following procedure is the same as in the original work by Sabine [12].

### *Verification of Absorbtion Coefficient Dependency*

This dependency of the models is validated by comparing predictions of the reverberation time against experimental observations for controlled changes of the average absorption coefficient. For the purpose of validation we consider an environment, where the windows cover a large portion of the outer wall. By opening windows, one at the time, we change the absorption coefficient for parts of the room surface. An overview of the different number of open windows and the corresponding scenarios see Table C.2. While the walls average absorption coefficient $a_w$ ranges from zero to unity, the absorption coefficient $a_o$ of an opening can be set to unity. This corresponds to the assumption, which was also assumed by Sabine [12], that power leaving the room via the opening never reenters the room. The average absorbtion coefficient of the room is modeled as

$$\bar{a} = \frac{S_w \cdot a_w + S_o \cdot a_o}{S_w + S_o} = \frac{S_w \cdot a_w + S_o}{S_w + S_o}, \qquad \text{(C.23)}$$

where $S_o$ is the surface area corresponding to the window openings and $S_w$ is the area with the average wall absorption coefficient $a_w$. We assume that $a_w$ is equal to the average absorption coefficient estimated for the closed room. In the considered environment the windows open inwards which needs to be considered for the value of $S_w$. For instance $S_w$ of scenario B is equal to the room surface of scenario A plus one extra window area. In scenario C open the two windows back to back and are very close. Therefore we set $S_w$ equal to that of scenario A. For these investigations we assume that the single room in which transmitter and receiver are placed is responsible for the reverberation and thus defines the volume and surface used for the model predictions.

### *Verification of Volume-Surface Ratio Dependency*

The volume-surface ratio verification is done by considering a second, similarly furnished neighboring room with a smaller volume. Both rooms share the same wall properties and thus we assume $f(\bar{a})$ in (C.19) to be the same for them. Using (C.19) we predict the reverberation time for the smaller room R3. For this analysis we use an estimate of the reverberation time for the closed room R4 as reference.

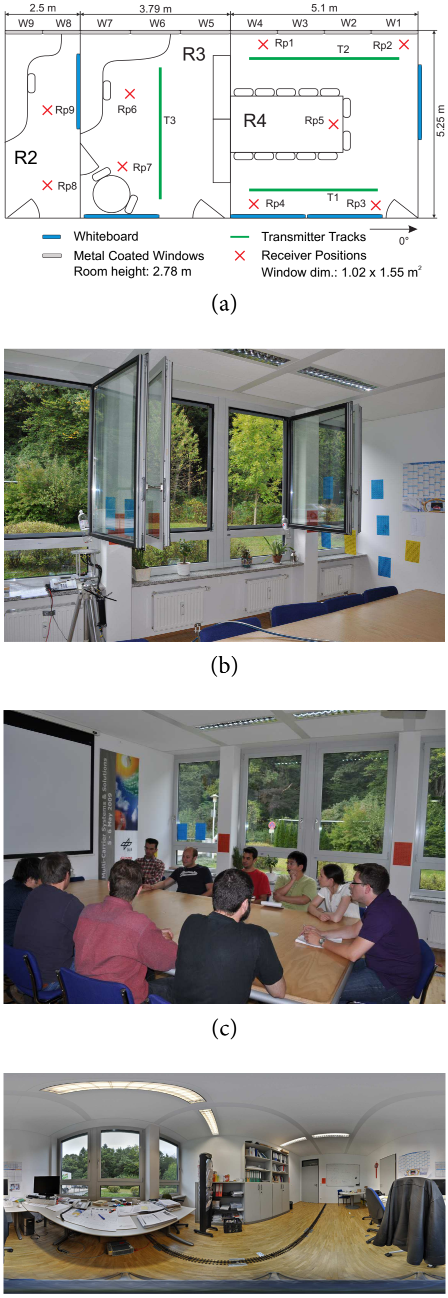
2.5 m
3.79 m
5.1 m
W9
W8
W7
W6
W5
W4
W3
W2
W1
R2
R3
R4
Rp1
Rp2
Rp3
Rp4
Rp5
Rp6
Rp7
Rp8
Rp9
T1
T2
T3
5.25 m
0°
Whiteboard
Metal Coated Windows
Room height: 2.78 m
Transmitter Tracks
Receiver Positions
Window dim.: 1.02 x 1.55 m²

(a)

(b)

(c)

(d)

*Fig. C.5: Schematic of the measurement scenario is shown in (a) and (b) is a photo of the investigated room R4 seen from the starting point of track T1 with the open window configuration "E". The panels (c) and (d) shown the simulated conference and a panograph in spherical coordinates of* $360^\circ \times 180^\circ$ *at receiver position Rp6 of room R3, respectively.*

*Verification of the Volume Dependency of the Power at Delay Zero*

The verification of $G_{0,\mathrm{rev}}$ is done by using the reference measurement in R4 and make predictions for the volume in R3. As we can see from (C.18) the value of $G_{0,\mathrm{rev}}$ depends only on the volume of the room, the antenna properties and not on the absorption coefficient. Therefore we expect only small changes in the estimates of $G_{0,\mathrm{rev}}$ caused by estimation errors when opening windows in R4. Thus confirming that $G_{0,\mathrm{rev}}$ does not depend on the average absorption coefficient. Using $G_{0,\mathrm{rev}}$ of room R4 as a reference, we expect $G_{0,\mathrm{rev}}$ to be 1.3 $\mathrm{dB}$ larger for room R3 according to the room volumes and confirm thereby the volume dependency.

## C.4 Measurements and Results

### C.4.1 Measurements

The measurement environment shown in Fig. C.5 consists of the meeting room R4 and the two adjacent offices R3 and R2. The dimensions of room R2 to R4 and the window dimensions are reported in Table C.1. The inner walls are made of plaster boards. As visible in Fig. C.5b, the outer "wall" consists mainly of windows (W1–W9) and concrete pillars. The frames of the windows are metallic and the glass is metal coated. The height of the transmit and receive antenna was 1.26 $\mathrm{m}$ and 1.1 $\mathrm{m}$, respectively. The environment was static and no one was in the room while the measurements were taken, except for the measurement scenario which "simulated" an ongoing meeting in room R4. For the placement of metallic whiteboards in the different rooms see Fig. C.5a.

The measurements have been conducted using the RUSK-DLR channel-sounder [19] with the settings specified in Table C.1. The transmitter and receiver were synchronized to a common clock via cables throughout the measurements. The transmit antenna [20] was omni-directional with 3 $\mathrm{dBi}$ gain. The receiver was equipped with eight monopoles arranged as a uniform circular array with diameter 75.18 $\mathrm{mm}$.

Channel measurements were obtained for fixed receive antenna array locations (Rp1 to Rp9), shown in Fig. C.5a. The transmit antenna was mounted on a model train which moved on the three tracks. The positions Rp1 to Rp9 and the trajectories along the tracks were measured with a tachymeter. The model train is equipped with a tachymeter which is connected to the channel sounder to obtain the Tx antenna locations during the movement. Frequency responses were measured for each receiver position while the transmitter moved along the tracks with a constant speed of approximately 0.05 $\mathrm{m/s}$ corresponding to a movement of $0.0035\lambda$ within a burst. Over this distance the channel response can be considered constant. Between two consecutive bursts, the transmitter moved $\lambda/8.8$.

*Table C.1: Settings of the channel sounder and parameters for data post-processing.*

| Sounder Settings | Value |
|---|---|
| Carrier frequency $f_c$ | 5.2 GHz |
| Bandwidth $B$ | 120 MHz |
| Number of sub-carriers $N_c$ | 1536 |
| Carrier separation $\Delta f$ | 78.125 kHz |
| Signal duration $T_{\mathrm{S}}$ | 12.8 µs |
| Cycle duration $T_{\mathrm{C}}$ | 204.8 µs |
| Cycles per burst $C$ | 20 |
| Burst duration $T_{\mathrm{B}}$ | 4096 µs |
| Burst repetition time $T_{\mathrm{BR}}$ | 131.072 ms |
| Transmit power | 0 dBm |
| Delay MUX and cable $\tau_{\mathrm{mux}}$ | 3.86 ns |

### C.4.2 Postprocessing

We estimate the reverberation time $T$ and the power of the reverberant component at delay zero $G_{0,\mathrm{rev}}$ from the tails of the estimated delay power spectra. The delay power spectra are estimated from the measured frequency response. We first average over the cycles in a burst to reduce the influence of noise resulting in the averaged measured frequency response $H_{m,r,p,t}[f]$ for receive array element $m$ at receiver position $r$ and at transmitter positions $p$ along track $t$ for frequency $f$. The delay power spectra are estimated by averaging over the receive antennas as

$$\widehat{G}_{r,p,t}[\tau] = \frac{1}{M}\sum_{m=1}^{M} \left|\mathrm{IFFT}\left\{H_{m,r,p,t}[f]\, W[f]\right\}\right|^2 , \tag{C.24}$$

where $\mathrm{IFFT}\{\cdot\}$ is the inverse fast fourier transform and $W[f]$ denotes a Hann window applied to suppress sidelobes. The samples in the delay domain are indexed by $\tau$. The reverberation time is estimated as the slope of the log of the delay power spectrum within the delay range $\tau_{\mathrm{s}} \leq \tau \leq \tau_{\mathrm{max}}$. This is done via least squares fitting of a straight line. The value of $\tau_{\mathrm{s}}$ should be chosen to reduce the influence of the primary component on the estimate of the slope. We chose $\tau_{\mathrm{s}} = 24\,\mathrm{ns}$ to be the maximum transmitter-receiver distance in the experimental data plus one pulse duration. The value of $\tau_{\mathrm{max}} = 150$ ns is chosen such that the slope of $\widehat{G}_{r,p,t}[\tau]$ is not influenced from the noise floor for all measurement scenarios.

### C.4.3 Results

The delay power spectra and the estimation of the parameters of their tails is essential for the results on the model prediction. Therefore, we start presenting the results on the delay power spectra. In Fig. C.6 $\widehat{G}(\tau)$ is obtained

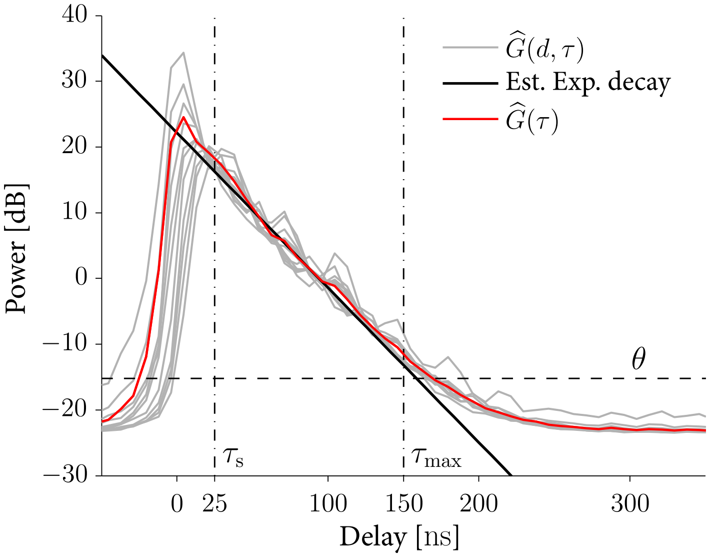

*Fig. C.6: Experimental delay power spectra obtained from spatial averages in distance sectors of length $4\lambda$ in room R4. The delay power spectrum $\widehat{G}(\tau)$ is obtained as the average of all receiver and all transmitter positions. The reverberation time and $\widehat{G}_{0,\mathrm{rev}}$ are estimated using the delay power spectra in the range $\tau_s < \tau < \tau_{\max}$ indicated with the dash-dot lines.*

as the spatial average over all transmitter positions along tracks T1 and T2 and receiver positions Rp1 to Rp4. We observe that the tail in the range $\tau_\mathrm{s} < \tau < \tau_{\max}$ is well approximated by exponential decaying function. The delay power spectra $\widehat{G}(d,\tau)$ are obtained from spatial averages of the transmitter and receiver locations with distances within sectors of length $4\lambda$. We clearly observe for short distances the early peak for $\tau < \tau_\mathrm{s}$. This peak, corresponding to the primary component, decays with increasing distance as predicted by the model (C.2). Similarly a good fit of the model (C.2) and the tails is observed. However, for some distances we observe multiple peaks in $\widehat{G}(d,\tau)$ for the range $\tau_\mathrm{s} < \tau < \tau_{\max}$. The delay interval between those peaks corresponds roughly to crossing twice the room between the white board and windows. It therefore seems plausible to assume that the peaks are caused by strong back and forth reflections between the metallic whiteboard and the metal coated windows. Similarly, we observe these peaks in the open window scenario for $\widehat{G}(\tau)$, see Fig. C.7. We remark that in the open window scenario track T2 and Rp1 could not be measured due to obstruction by the open windows and Rp5 was not measured due to practical reasons. Due to the given geometries of the used track and the receiver positions in the open window scenario it is not possible to obtain a spatial average for the entire room which reduces the peaks in $\widehat{G}(\tau)$. Specifically for the open window scenarios A to D are the peaks present. In scenarios E and F all windows are open and thus the back and forth reflections between the whiteboard and the windows cannot occur. In Fig. C.7 we see that the peaks in scenarios A to D coincide with $\tau_{\max}$, which possibly influences the estimates of $T$. Note that for the investigations in room R3 the track is perpendicular to the whiteboard and the windows. This geometrical difference reduces by spatial averaging the peaks caused by back and forth reflections similarly as in Fig. C.6. This different behavior for the open window and neighboring room scenarios is important for the following investigations of the model predictions.

For the predictions and the experimental results with open windows only the data from track T1 and receiver positions Rp2 to Rp4 were considered. The results for changing the average absorption coefficient by opening windows are reported in Table C.2 and shown in Fig. C.7 and Fig. C.8. The errorbars in Fig. C.8 represent the 95 % confidence intervals from the closed room estimates of $\widehat{T}$ and their respective predictions for Eyring's and Sabine's model. Sabine's model generally seems to predict to large reverberation times and the prediction error increases with increasing average absorption coefficients. These observations are in line with the theoretical results shown for instance in Fig. C.3 or Fig. C.4 and observed similarly for acoustics by [13]. The predictions with Eyring's model shown in Fig. C.8 are very close to the measured results and their respective confidence intervals overlap except in scenario E. Scenario E lacks the multiple peaks in the delay power spectrum which may cause the lower experimental value.

Eyring's and Sabine's model predict that $\widehat{G}_{0,\text{rev}}$ is independent on the average absorption coefficient. Our experimental observations reported in Table C.2 for scenarios B to F confirm this. The values exhibit only small deviations from the experimental value obtained in the closed room. The 95 % confidence intervals for the estimated values are overlapping, except for scenario E and F, where the difference to the closed room is 0.67 $\mathrm{dB}$. We identified two possible causes. One being the missing back and forth reflections between the windows and the whiteboards when all windows are open. The other being estimation errors caused by the used pulse shape and the change of the reverberation time. To exclude a possible influence of the pulse shaping filter on the observed difference of $\widehat{G}_{0,\text{rev}}$ we conducted simulations for the used pulse shape and the experimental reverberation times. The simulations showed a negligible difference due to the pulse shape. Therefore we conclude that the missing back and forth reflections are the cause in the larger difference.

The dependency of the models on the volume-surface ratio for room R3 and R4 is reported in Fig. C.9 and Table C.3. The estimates are obtained from the estimated delay power spectra of receiver positions Rp1 to Rp4 and both

*Table C.2: Estimated and predicted model parameters for open window scenarios A to F.*

| Scenario | | | Meas. Est. | | Fit | |
|---|---|---|---|---|---|---|
| | Pictograph | $S$ [m$^2$] | $\widehat{G}_{0,\mathrm{rev}}$ [dB] | $\widehat{T}$ [ns] | $\widehat{a}_{\mathrm{Sab}}$ | $\widehat{a}_{\mathrm{Eyr}}$ |
| A | 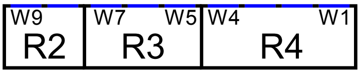 | 111.1 | 22.89 | 18.95 | 0.47 | 0.38 |

| Scenario | | | | Meas. Est. | | Prediction | |
|---|---|---|---|---|---|---|---|
| | Pictograph | $S_w$ [m$^2$] | $S_o$ [m$^2$] | $\widehat{G}_{0,\mathrm{rev}}$ [dB] | $\widehat{T}$ [ns] | $T_{\mathrm{Sab}}$ [ns] | $T_{\mathrm{Eyr}}$ [ns] |
| B† | 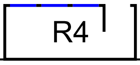 | 112.68 | 1.58 | 22.92 | 18.07 | 18.14 | 17.9 |
| C† | 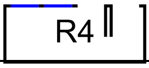 | 111.1 | 3.16 | 22.87 | 17.37 | 17.87 | 17.4 |
| D† | 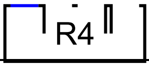 | 112.68 | 4.74 | 22.72 | 16.4 | 17.15 | 16.49 |
| E† | 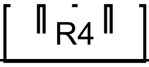 | 111.1 | 6.32 | 22.35 | 15.74 | 16.91 | 16.04 |
| F‡ | 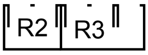 | 111.1 | 6.32 | 22.22 | 15.8 | 16.91 | 16.04 |

† windows in R2 and R3 closed; ‡ windows in R4 open as in scenario E

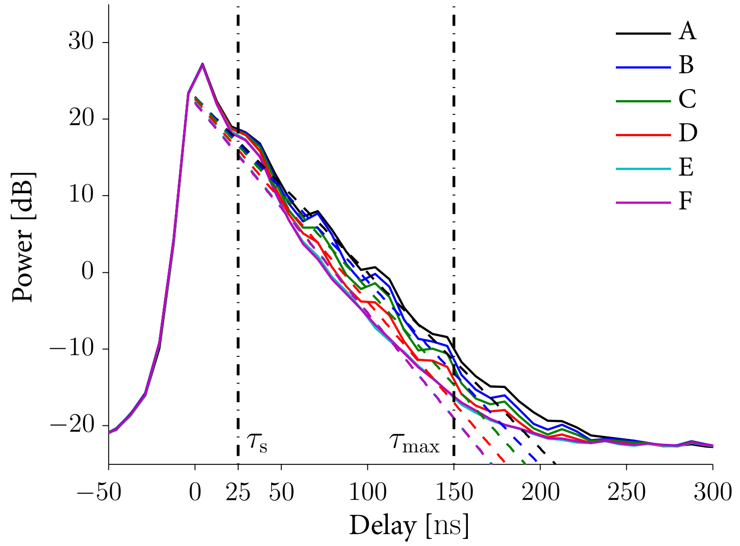

*Fig. C.7: The delay power spectra $\widehat{G}(\tau)$, obtained as the average of receiver positions Rp2 to Rp4 and all transmitter positions along track T1, are shown for the different window configurations. A change of slope, steeper for configurations with more open windows, is visible. The dashed lines correspond to $\widehat{G}_{\mathrm{rev}}(d,\tau)$ with d equal to zero. The dash-dot lines mark the delay range used for estimating the parameters of $\widehat{G}_{\mathrm{rev}}(d,\tau)$. We remark scenarios E and F coincide.*

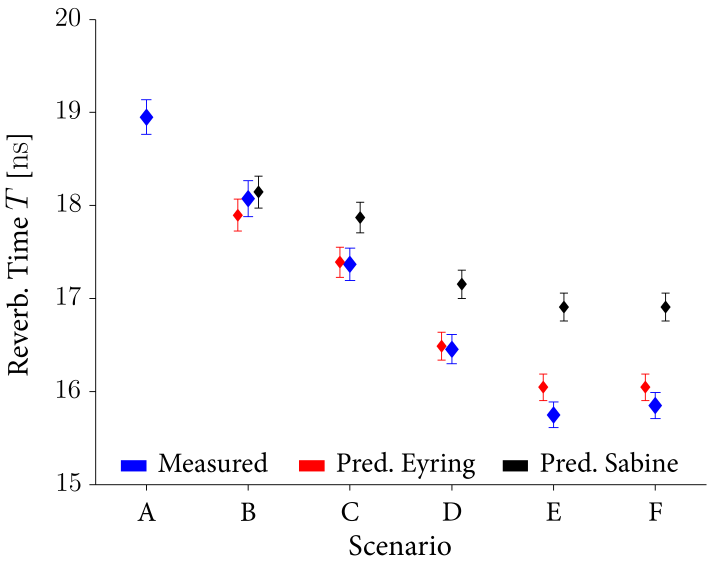

*Fig. C.8: Estimated and predicted reverberation times with 95% confidence intervals. The predictions for the Eyring and Sabine models for the different window configurations B to F are shown including the 95% confidence interval obtained from the reverberation time for the closed room.*

*Table C.3: Estimated and predicted model parameters for room R4 and R3.*

| Scenario | | | Meas. Est. | | Prediction | |
|---|---|---|---|---|---|---|
| Room | $S$ [m$^2$] | $V$ [m$^3$] | $\widehat{G}_{0,\text{rev}}$ [dB] | $\widehat{T}$ [ns] | $G_{0,\text{rev}}$ [dB] | $T$[ns] |
| R4 | 111.1 | 74.4 | 22.16 | 18.43 | – | – |
| R3 | 90.1 | 55.3 | 22.75 | 16.52 | 23.45 | 16.9 |

tracks in room R4. We use both tracks to obtain a better "spatial" approximation of $T$ for entire R4. For details see the previous results on the delay power spectra. We obtain predictions for room R3 from experimental observations of R4 and applying (C.19) and (C.18) with the appropriate room geometry changes. The experimental observations and their respective predictions in R3 are close. The difference of predicted and experimentally obtained $T$ and $G_{0,\text{rev}}$ are 0.38 ns and 0.7 dB, respectively. We remark that R3 is equipped with more furniture and this may results in additional surfaces. These extra surface areas were ignored in our prediction of $T$.

We report in Table C.4 reverberation times and average absorption coefficients from R3, R4 and open literature. Some references did not state values of

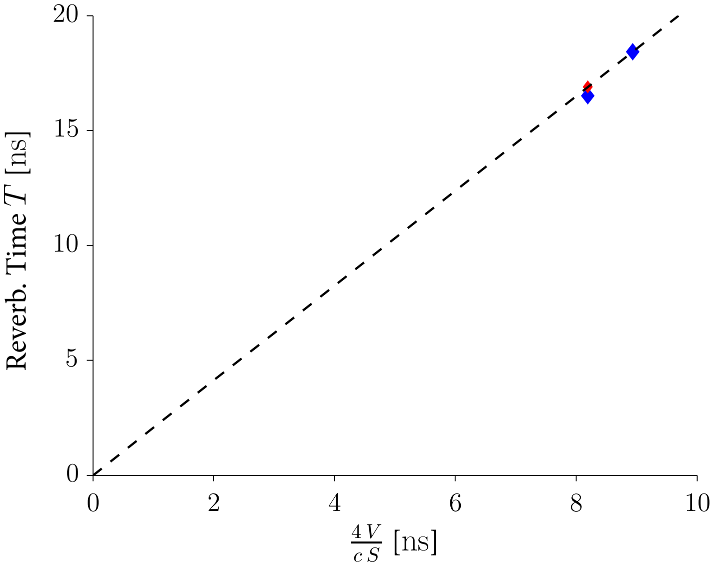

*Fig. C.9: Reverberation time versus the volume-surface ratio. The blue diamonds indicate the experimental results for room R3 and R4 and the red diamond corresponds to the prediction for R3. All predictions for various volume-surface ratios will located on the dashed line.*

the reverberation times. Thus, we obtained them manually by reading them of the graphed delay power spectra. We did not extract $G_{0,\text{rev}}$ as many reported delay power spectra are normalized in power and differ in antenna losses. Thus considering the information at hand, a fair comparison is not possible.

To Table C.4 we have the following remarks:

- Large absorption coefficients, for Sabine's model even greater unity, are observed for 60 GHz in [21]. Even though the volume is doubled for the larger office and the volume-surface ratio changed from 0.7 to 0.8, the reverberation time only increases by 1.2 ns. Eyring's and Sabine's model both predict for large absorption coefficients only small variations in the reverberation time when the volume-surface ratio changes.
- The references [16] and [10] considered the same environment. They vary in their respective carrier frequency, used bandwidth and investigated polarizations.
  - The respective absorption coefficients and reverberation times in [16] are close for different bandwidths and measurement systems.
  - For the two carrier frequencies 2.3 GHz and 5.7 GHz is the reverberation time the same [10]. A difference is reported for $G_{0,\text{rev}}$ which is close to the expected difference for the antenna losses.

- Apart from the 60 GHz measurements, the absorption coefficients for Eyring's model fall in the range of 0.31 to 0.6 with an average of 0.4.
- Reported reverberation times range from $7.5\ \mathrm{ns}$ to $25.8\ \mathrm{ns}$ and are in the range of typically reported rms delay spread values [22] for indoor environments.

## *C.5 Discussion*

Our experimental results show that the reverberation is confined in a single room. Scenario F, when opening the windows in the neighboring rooms did not lead to a change in the reverberation time, where as opening windows in the same room did. This indicates that the reverberation can be characterized by the single room. Furthermore, using the single room assumption, the experimental validation of the model predictions due to the absorption coefficient changes confirms i) the single room assumption and ii) the validity of the reverberation models. Specifically for increasing absorption coefficients predicts Eyring's model the reverberation time better. As predicted by the reverberation models our experimental results confirm that $G_{0,\mathrm{rev}}$ does not depend on the average absorption coefficient.

The prediction of the reverberation time for the smaller adjacent room confirms its volume-surface ratio dependency. Even though our assumptions for the neighboring room surface and the absorption coefficient are crude we obtain a good prediction for the neighboring room. The predicted reverberation time of $16.9\ \mathrm{ns}$ is only 2.25% larger than the experimentally obtained value. Thus the models are well suited for the prediction of reverberation times in differently sized rooms with similar absorption coefficients.

The reverberation models predict a volume dependency of $G_{0,\mathrm{rev}}$. We use this dependency to predict $G_{0,\mathrm{rev}}$ of the delay power spectrum for different environments. The volume of room R3 is 74% of R4, which amounts to a change of $1.3\ \mathrm{dB}$ for $G_{0,\mathrm{rev}}$. The experimentally obtained $G_{0,\mathrm{rev}}$ is $0.7\ \mathrm{dB}$ below the predicted value. This difference is similar to the variation we observed over the open window scenarios when comparing scenarios A to D with E and F. From this we have two observations: i) for further validation investigations rooms with larger volume differences are required and ii) for prediction purposes $G_{0,\mathrm{rev}}$ is insensitive to small changes in the volume.

We remark, that for the closed room we observed slightly different values for the reverberation time with the data set composed of receiver positions Rp2 to Rp4 and track T1 as compared to the data set with Rp1 to Rp4 and tracks T1 and T2. We conjecture that this is due the peaks from back and forth reflections which are not smoothed out by the spatial averaging with the data set considering only T1.

Table C.4: *Overview of reverberation times and average absorbtion coefficients found in open literature.*

| Room Dim. [m$^3$] | V [m$^3$] | S [m$^2$] | Freq. Band [GHz] | $\widehat{\rho}$ [dB/ns] | $\widehat{T}$ [ns] | $\bar{a}_{\mathrm{Sab}}$ | $\bar{a}_{\mathrm{Eyr}}$ | Comments |
|---|---|---|---|---|---|---|---|---|
| $5 \times 5 \times 2.6$ | 65 | 102 | $1 \ldots 11$ | $-0.19$ | 22.9 | 0.37 | 0.31 | Office, read of Fig. 1b NLOS, [23] |
| $11 \times 20 \times 2.5$ | 550 | 595 | $5.75 \ldots 5.85$ | $-0.18$ | 24.1 | 0.51 | 0.4 | Office, data provided in text, [9] |
| $7.73 \times 5.85 \times 2.6$ | 118 | 161 | $2.25 \ldots 2.35$ | $-0.18$ | 24.5 | 0.4 | 0.33 | Conference room†, [16] |
| | | | $2.05 \ldots 2.55$ | $-0.17$ | 25.8 | 0.38 | 0.32 | |
| $7.73 \times 5.85 \times 2.6$ | 118 | 161 | $2.25 \ldots 2.35$<br>$5.75 \ldots 5.85$ | $-0.20 \ldots -0.18$ | $22.1 \ldots 24.6$ | $0.4 \ldots 0.44$ | $0.33 \ldots 0.36$ | Conference room‡, [10] |
| $12 \times 7 \times 2.8$ | 235.2 | 274.4 | $2.35 \ldots 2.45$ | $-0.35$ | 12.4 | 0.92 | 0.6 | Conference room, read of Fig. 8, [24] |
| $3.8 \times 3.5 \times 2.5$ | 33.25 | 63.1 | | $-0.36$ | 12 | 0.59 | 0.44 | Living room, read of Fig. 9, [24] |
| $4.65 \times 6 \times 3$ | 83.7 | 119.7 | $59 \ldots 62.5$ | $-0.58$ | 7.5 | 1.23 | 0.71 | Office, read of Fig. 12a, [21] |
| $6 \times 9 \times 3$ | 162 | 198 | | $-0.5$ | 8.7 | 1.26 | 0.72 | Office, read of Fig. 12b, [21] |
| $9.35 \times 7.18 \times 5$ | 335.7 | 299.6 | $1.25 \ldots 1.75$ | $-0.2$ | 21.8 | 0.69 | 0.5 | Laboratory, read of Fig. 13, [7] |
| $5.1 \times 5.25 \times 2.78$ | 74.4 | 111.1 | $5.15 \ldots 5.25$ | $-0.24$ | 18.4 | 0.48 | 0.38 | R4 with T1 and T2 for Rp1 to Rp4 |
| $3.79 \times 5.25 \times 2.78$ | 55.3 | 90.1 | | $-0.26$ | 16.5 | 0.5 | 0.39 | R3 with T3 for Rp6 and Rp7 |

† The value of $\widehat{T}$ is provided in the publication however it is unclear how the values were obtained from the measurements with varying number of people.

‡ A range of median values of $\widehat{T}$ is provided for different polarizations.

We observe that our values of the average absorption coefficients obtained for room R3 and R4 are in the range of values found in the open literature in Table C.4. Furthermore the gathered average absorption coefficient is close to 0.5. In acoustics [25] is suggested that predictions with Sabine's model for average absorption coefficients above 1/3 could be inaccurate and it is suggested to use Eyring's model. This is further confirmed by our experimental results where Eyring's model predicts better, see Fig. C.8 and Table C.2.

Our validation procedure suggests that acoustical reverberation models, translated to electromagnetics, are applicable and allow for predicting the tail of the delay power spectra. Note that within this investigation we did not confirm that the observed tail of the delay power spectrum is truly caused by a diffuse field. In [7, 26] is suggested that the tail has an initial build up phase after which the diffuse field occurs. The authors in [7, 26] state that the duration of the build up phase and typical dynamic ranges used in wireless communications do not allow to observe a truly diffuse field. We remark that specifically for large absorption coefficients a truly diffuse field will be difficult to observe. Nevertheless, the reverberation models seem to be applicable and Eyring's model predicts the reverberation time well for modified absorption coefficients. In [14] is stated that in real environments for acoustics a truly diffuse field is similarly difficult to observe.

## *C.6 Applications*

In the following we present two applications of the reverberation models. One focuses on the differences between Sabine's and Eyring's model when used to experimentally asses the specific absorption rate of the human body as done in [15] and [16]. The other application focuses on the possibility of using a distance dependent delay power spectrum model [5] together with the reverberation models to predict for the neighboring room the path gain, mean delay and rms delay spread versus distance. Such predictions are of interest for localization and communication purposes.

### *C.6.1 Human Absorption Cross Section Estimation*

In [15, 16] Sabine's model is used to experimentally investigate the human absorption cross section which is used to obtain experimental estimates of the specific absorption rate (SAR) for health issues. It is not our primary focus to obtain SAR values but to point out differences in obtaining the human absorption cross section with Sabine's and Eyring's model, respectively. In [15, 16] is assumed that additional human bodies in the room will introduce a change in the average absorption coefficient of the room and this is observable for instance in the reverberation time. The average absorption coefficient

(C.6) with humans in the room is rearranged to obtain an expression for the human absorption cross section as

$$\ell \times \underbrace{S_{\mathrm{H}}\, a_{\mathrm{H}}}_{ACS_{\mathrm{H}}} = \bar{a}(S + \ell \times S_{\mathrm{H}}) - \bar{a}_{\mathrm{E}}\, S, \tag{C.25}$$

where $\ell$ is the number of humans, $S_{\mathrm{H}}$ and $a_{\mathrm{H}}$ are the humans surface area and absorption coefficient, respectively. The superscripts “H” and “E” stand for human and empty room. The human absorption cross section is denoted $ACS_{\mathrm{H}}$ and for the empty room $S$ and $\bar{a}_{\mathrm{E}}$ are the room surface and the average absorption coefficient, respectively. The average absorption coefficient of the room with humans $\bar{a}$ can be estimated from Sabine’s model with (C.20) which leads to the expression

$$\ell \times ACS_{\mathrm{Sab,H}} = \frac{4\,V}{c}\left(\tfrac{1}{\widehat{T}_{\mathrm{H}}} - \tfrac{1}{\widehat{T}_{\mathrm{E}}}\right), \tag{C.26}$$

where $\widehat{T}_{\mathrm{H}}$ and $\widehat{T}_{\mathrm{E}}$ are the experimentally obtained reverberation times with $\ell$ or without humans, respectively. By multiple measurements with varying $\ell$ or by a reference measurement with an empty room one can estimate $ACS_{\mathrm{H}}$ from Sabine’s model. Note, this can be done without the knowledge of $S_{\mathrm{H}}$. For Eyring’s model, we use (C.25) but insert for the average absorption coefficients (C.21) to obtain

$$\begin{aligned} \ell \times ACS_{\mathrm{Eyr,H}} = \left(1 - \exp\left(\tfrac{-4\,V}{c\,(S+\ell\times S_{\mathrm{H}})\,\widehat{T}_{\mathrm{H}}}\right)\right)(S + \ell \times S_{\mathrm{H}}) \\ - \left(1 - \exp\left(\tfrac{-4\,V}{c\,S\,\widehat{T}_{\mathrm{E}}}\right)\right) S. \end{aligned} \tag{C.27}$$

Thus $ACS_{\mathrm{Eyr,H}}$ depends on $S_{\mathrm{H}}$. This dependency is shown in Fig. C.10 for experimental observations from empty and with ten humans in room R4. Numerical values are shown in Table C.5, where two human surface areas are used. Those two human surface areas are obtained as follows: i) Assuming for the ten humans in the conference room an average height 175 $\mathrm{cm}$ and weight 70 $\mathrm{kg}$ with Fujimotos formula [27] we obtain a surface area of $S_{\mathrm{H},1} = 1.79\mathrm{m}^2$ [3]. ii) In [30] the surface area of a 22 year old Japanese male human is given as $S_{\mathrm{H},2} = 2.45\ \mathrm{m}^2$ from a whole-body voxel model[4].

We observe from the estimated absorption cross sections that depending on the chosen human surface area, the values with Eyring’s model are 23 % to 40 % larger compared to Sabine’s model. Notice, this leads to under- or

---

[3] Applying different formulas such as Du Bois [28] or Mosteller [29] gives 1.85 $\mathrm{m}^2$ or 1.84 $\mathrm{m}^2$, respectively.

[4] For the voxel model the true persons height and weight and respective surface area result with Fujimotos formula are, 173 $\mathrm{cm}$, 65 $\mathrm{kg}$ and 1.73 $\mathrm{m}^2$ [30].

*Table C.5: Estimated human absorbtion cross sections.*

| Model | Results | Parameters | | | | | |
|---|---|---|---|---|---|---|---|
| | $ACS$ [$\mathrm{m}^2$] | $S_\mathrm{H}$ [$\mathrm{m}^2$] | $V$ [$\mathrm{m}^3$] | $S$ [$\mathrm{m}^2$] | $\ell$ | $\widehat{T}_\mathrm{E}$ [ns] | $\widehat{T}_\mathrm{H}$ [ns] |
| Sabine | 0.22 | — | 74.4 | 111.1 | 10 | 18.95 | 18.2 |
| Eyring | 0.27<br>0.31 | 1.79<br>2.45 | | | | | |

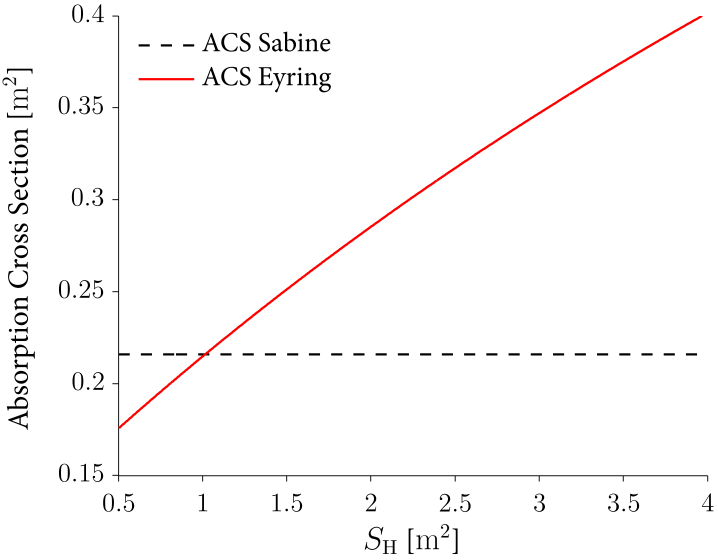

*Fig. C.10: Human absorption cross section versus the human surface area. Model parameters are given in Table C.5.*

overestimation of the SAR values. In the following we compare our values to the open literature. Absorption cross-sections reported in [15, 31] are 0.33 $\mathrm{m}^2$ and 0.4 $\mathrm{m}^2$, respectively. Values in [30] range from 0.38 $\mathrm{m}^2$ to 0.48 $\mathrm{m}^2$, depending on the used human surface approximations. In [16] are absorption cross-sections reported in the range of 0.24 $\mathrm{m}^2$ to 0.42 $\mathrm{m}^2$. Averaged values of 0.34 $\mathrm{m}^2$ and 0.36 $\mathrm{m}^2$ are reported for two carrier frequencies of 2.3 GHz and 3 GHz, respectively. We remark that [15, 16] used Sabine's model to obtain the absorption cross section. In comparison to these values are our findings for Sabine's and Eyring's model close to or at the lower end. For future investigations of the human absorption cross section, we propose to use rooms with low absorption coefficients, for instance reverberation chambers. This would have the benefits: i) the difference between Sabine's and Eyring's model is smaller and thus allowing Sabine's model to be used and ii) a small change in the average absorption coefficient, for instance caused by presence of humans, will result in larger changes in the reverberation time which could be more reliably observed.

We remark, in room acoustics the audience in concert halls is often considered in a different manner [32]. There the surface of a concert hall is split into the area where the orchestra is situated, the audience and the remaining surface. An empty room measurement similar to our measurements is used as a reference to obtain the absorption for the "remaining" surface of the concert hall. The absorption coefficients of the audience and orchestra are calculated, however, only for the respective parts of the room surface covered by them. The audience, the chairs or the orchestra introduce no additional surface area. Only a change in the absorption coefficient is considered. Note, differences in acoustics compared to our findings in electromagnetics are the low average absorption coefficients for the empty room (roughly 0.1 or below) and absorption coefficients close to unity for seats and humans [14, 32].

### C.6.2 Prediction of Path loss, Mean Delay and Rms Delay Spread

The reverberation models allow to predict parameters of the delay power spectrum for the adjacent room. These parameters applied to the distance dependent model of the delay power spectrum in (C.2) of [5]. This combination of the two models allows a prediction of the distance dependent path gain (path loss), mean delay and rms delay spread. In order to evaluate our prediction quality for room R3 we consider two cases. In the one case we predict from room R4 all model parameters of (C.2) where as in the other case we estimate all parameters from the experimental values (model fitting). In the prediction case the parameters $T$ and $G_{0,\mathrm{rev}}$ of the delay power spectrum tail are predicted from R4 with the reverberation models (see Table C.3) and the primary component parameters $G_0$ and $n$ are predicted to be the same as in R4. In the parameter estimation case we consider the experimental delay power spectra of R3 and estimate the parameters $T$ and $G_{0,\mathrm{rev}}$ of the tail (see Table C.3). The remaining parameters of the primary component $G_0$ and $n$ are obtained by fitting (C.2) to the experimental path gain values for R3. We remark, we did not use the experimental values of mean delay and rms delay spread in the fitting procedure. The parameters for the two cases are summarized in Table C.6. The respective model predictions together with the experimental values of path gain, mean delay and rms delay spread are shown in Fig. C.11.

For room R4 the estimated model parameters are reported in Table C.2 together with the root mean square error (RMSE) values. The RMSE values using the predicted model parameters are close to the fitted values in R4. When using the fitted model parameters for R3, we see only a marginal improvement

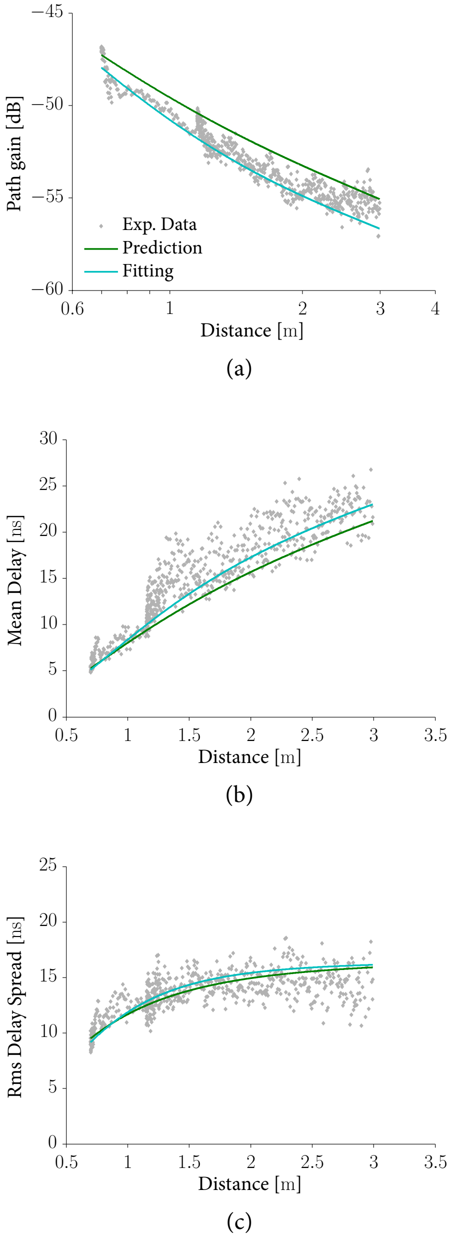

*Fig. C.11: Path gain (a), mean delay (b) and rms delay spread (c): Experimental values and model predictions for parameter settings reported in Table C.6.*

*Table C.6: Parameter estimates and predictions for the delay power spectrum model for room R3 and R4 and root mean squared errors for fitting and prediction, respectively.*

| Model | Parameters | | | | RMSE | | |
|---|---|---|---|---|---|---|---|
| | $G_0$ | $n$ | $G_{0,\mathrm{rev}}$ [dB] | $T$ [ns] | $G$ [dB] | $\mu$ [ns] | $\sigma$ [ns] |
| R4 | $7.97 \cdot 10^{-6}$ | 1.85 | 22.16 | 18.43 | 1.2 | 3.1 | 2.5 |
| Prediction | $7.97 \cdot 10^{-6}$ | 1.85 | 23.45 | 16.9 | 1.1 | 3 | 1.4 |
| Fitting | $5.81 \cdot 10^{-6}$ | 2.32 | 22.75 | 16.52 | 0.8 | 2.2 | 1.5 |

in the RMSE values. The trends of the model predictions and experimental results shown in Fig. C.11a for path gain, mean delay and rms delay spread are similar versus distance. However, we see for the prediction of the path gains an overestimation between 0.5 to 2 dB in the considered distance range. This is caused by a prediction error in the primary component. Not shown here, we observe for R4 a different behavior of the primary component for track T1 and T2. For T1 the primary component is much stronger due to an additional very strong first order reflection from the metallic whiteboard. For T2 this first order reflection is weaker leading to a slightly weaker primary component which is close to the one fitted in R3. However, we require that the delay power spectrum model is fitted for the entire room. This leads to a strong primary component in R4 and in the prediction for R3 to an overestimation in the path gains. We can see that this overestimation of the primary component has an impact on the mean delay prediction in Fig. C.11a. The predictions is slightly below the fitted curve. The error in the prediction of the primary component has negligible impact on the predicted rms delay spread and therefore are the curves for the predicted and fitted model almost on top of each other.

Considering the offset in the path gain our prediction for R3 seems crude, however, the RMSE values are similar to the ones for the fitted model in R4. The improvements in RMSE values for fitting all model parameters in R3 are only marginal. In case of additional or differently chosen tracks in R3, for instance close to the whiteboard, we may observe experimental values closer to our predictions. We conclude that the reverberation models and the distance dependent delay power spectrum from [5] allow in our case for predictions of path gain, mean delay and rms delay spread for the neighboring room.

## C.7 Conclusion

Our findings confirm that the reverberation is confined in the investigated room and that the reverberation models developed in acoustics can be transposed in electromagnetics. Eyring's model predicts better than Sabine's for the obtained absorption coefficients. This we validated with a specifically designed experiment. In the experiment we changed the average absorption coefficient and predicted the reverberation time and the reverberant power at delay zero using Eyring's and Sabine's model. We observe good agreement between these predictions and their experimental counterparts. Specially for the higher absorption coefficients are the predictions of Eyring's model better compared to Sabine's. Furthermore, we validated the models predicted volume-surface ratio dependency of $G_{0,\mathrm{rev}}$ with experimental observations of different rooms. Our data set is limited to measurements collected in an office and a meeting room but experimental values in the open literature indicate similar average absorption coefficients and reverberation times. In particular, it appears that the available values indicate that the average absorption coefficients are in the regime where Eyring's model is most appropriate.

We present two applications of the reverberation models. From the first application we conclude that the absorption due to humans is significant enough to be measured with a wideband channel sounder. Furthermore, the estimates of the human absorption cross section obtained with Sabine's and Eyring's models differ. In the latter the absorbtion cross section is obtained as a function of the human surface area. The obtained values of the human cross section are in the lower range of reported values in the literature. Based on our observations we suggest to use environments with low average absorption coefficients for investigating the human cross section. This has two benefits: i) Sabine's model can be used and thus no knowledge of the human surface area is necessary, and ii) changes in the absorption coefficient due to humans result in larger changes in the reverberation times, which is easier to observe and estimate.

In the second application of the reverberation models we predict parameters of the delay power spectrum model for an adjacent room and use those parameters in the models proposed in [5] to forecast path gain, mean delay and rms delay spread versus distance. The predictions of the parameters of the delay power spectrum model, path gain, mean delay and rms delay spread are in good agreement with their experimental counterparts. Thus the reverberation models can be used to predict parameters for the delay power spectrum and its secondary models for differently sized rooms.

## References

[1] A. F. Molisch, *Wireless Communications*, 2nd ed. Wiley, 12 2010.

[2] T. S. Rappaport, *Wireless Communications: Principles and Practice (2nd Edition)*, 2nd ed. Prentice Hall, 12 2001.

[3] H. Hashemi, "The Indoor Radio Propagation Channel," *Proc. IEEE*, vol. 81, no. 7, pp. 943–968, July 1993.

[4] A. Saleh and R. Valenzuela, "A statistical model for indoor multipath propagation," *IEEE J. Sel. Areas Commun.*, vol. 5, no. 2, pp. 128–137, 1987.

[5] G. Steinböck, T. Pedersen, B. Fleury, W. Wang, and R. Raulefs, "Distance Dependent Model for the Delay Power Spectrum of In-room Reverberant Channels," *IEEE Trans. Antennas Propagat.*, in Press, 2013.

[6] S. Begusic, D. Nygaard Urup, J. Kolonic, H. Holbæk Pedersen, W. Wang, R. Raulefs, M. Jakobsen, G. Steinböck, and T. Pedersen, "Wireless Indoor Positioning Relying on Observations of Received Power and Mean Delay," in *IEEE ICC 2013 Workshop on Advances in Network Localization and Navigation (ANLN)*, June 2013.

[7] C. Holloway, M. Cotton, and P. McKenna, "A model for predicting the power delay profile characteristics inside a room," *IEEE Trans. Veh. Technol.*, vol. 48, no. 4, pp. 1110–1120, 1999.

[8] R. Rudd, "Statistical prediction of indoor radio channel impulse response," Ph.D. dissertation, University of Surrey, Sept. 2007.

[9] J. Andersen, J. Nielsen, G. Pedersen, G. Bauch, and J. Herdin, "Room electromagnetics," *IEEE Antennas Propag. Mag.*, vol. 49, no. 2, pp. 27–33, 2007.

[10] J. Nielsen, J. Andersen, G. Pedersen, and M. Pelosi, "On Polarization and Frequency Dependence of Diffuse Indoor Propagation," in *Vehicular Technology Conference, 2011 IEEE 74th*, Sept. 2011.

[11] D. A. Hill, *Electromagnetic Fields in Cavities: Deterministic and Statistical Theories*, ser. IEEE Press Series on Electromagnetic Wave Theory. Piscataway, NJ: Wiley/IEEE Press, 2009.

[12] W. C. Sabine, *Collected papers on acoustics*. Cambridge: Harvard University Press, 1922.

[13] C. F. Eyring, "Reverberation time in "dead" rooms," *J. Acoust. Soc. Am.*, vol. 1, no. 2A, pp. 217–241, Jan. 1930.

[14] H. Kuttruff, *Room Acoustics*, 4th ed. London: Taylor & Francis, 2000.

[15] J. Andersen, K. L. Chee, M. Jacob, G. Pedersen, and T. Kurner, "Reverberation and Absorption in an Aircraft Cabin With the Impact of Passengers," *IEEE Trans. Antennas Propag.*, vol. 60, no. 5, pp. 2472–2480, May 2012.

[16] A. Bamba, W. Joseph, J. Andersen, E. Tanghe, G. Vermeeren, D. Plets, J. Nielsen, and L. Martens, "Experimental Assessment of Specific Absorption Rate Using Room Electromagnetics," *IEEE Trans. Electromagn. Compat.*, vol. 54, no. 4, pp. 747–757, Aug. 2012.

[17] ITU-R, "Recommendation ITU-R P.1407-4 (10/2009): Multipath propagation and parameterization of its characteristics," Nov. 2009.

[18] J. B. Andersen, J. O. Nielsen, G. Bauch, and M. Herdin, "The large office environment - measurement and modeling of the wideband radio channel," in *Proc. IEEE 17th Int. Symposium on Personal, Indoor and Mobile Radio Commun. PIMRC 2006*, 2006, pp. 1–5.

[19] J. Stephan, Y. Lostanlen, J. Keignart, W. Wang, D. Slock, and F. Kaltenberger, "Measurements of location-dependent channel features," ICT- 217033 WHERE, Deliverable 4.1, Oct. 2008, http://www.ict-where.eu/.

[20] Huber+Suhner, "Datasheet for Sencity Antenna For In-Carriage Wireless Communication, Type: SOA 5600/360/3/20/V_1," Document No. 01.02.1358, May 2007.

[21] G. Rougeron, F. Gaudaire, Y. Gabillet, and K. Boutouch, "Simulation of the indoor propgation of a 60 GHz electromagnetic wave with a time-dependent radiosity algorithm," *Computers & Graphics*, vol. 26, pp. 125–141, 2002.

[22] M. Awad, K. Wong, and Z. bin Li, "An Integrated Overview of the Open Literature's Empirical Data on the Indoor Radiowave Channel's Delay Properties," *IEEE Trans. Antennas Propag.*, vol. 56, no. 5, pp. 1451–1468, May 2008.

[23] J. Kunisch and J. Pamp, "Measurement results and modeling aspects for the UWB radio channel," *Ultra Wideband Systems and Technologies, 2002. Digest of Papers. 2002 IEEE Conf. on*, pp. 19–23, 2002.

[24] R. F. Rudd, "The prediction of indoor radio channel impulse response," in *The Second European Conf. on Antennas and Propagation, 2007. EuCAP 2007.*, Nov. 2007, pp. 1–4.

[25] A. D. Pierce, *Acoustics: An Introduction to Its Physical Principles and Applications*. Acoustical Society of America, June 1989.

[26] C. Holloway, H. Shah, R. Pirkl, K. Remley, D. Hill, and J. Ladbury, "Early Time Behavior in Reverberation Chambers and Its Effect on the Relationships Between Coherence Bandwidth, Chamber Decay Time, RMS Delay Spread, and the Chamber Buildup Time," *IEEE Trans. Electromagn. Compat.*, vol. 54, no. 4, pp. 714–725, Aug. 2012.

[27] S. Fujimoto and T. Watanabe, "Studies on the body surface area of Japanese," *Acta medica Nagasakiensia*, vol. 14, no. 1-2, pp. 1–13, 1969.

[28] D. Du Bois and E. F. Du Bois, "A formula to estimate the approximate surface area if height and weight be known. 1916." *Nutrition (Burbank, Los Angeles County, Calif.)*, vol. 5, no. 5, p. 303, 1989.

[29] R. Mosteller, "Simplified Calculation of Body-Surface Area," *New England Journal of Medicine*, vol. 317, no. 17, pp. 1098–1098, 1987, pMID: 3657876.

[30] A. Hirata, Y. Nagaya, F. Osamu, A. Nagaoka, and S. Watanabe, "Correlation Between Absorption Cross Section and Body Surface Area of Human for Far-Field Exposure at GHz Bands," in *Electromagnetic Compatibility, 2007. EMC 2007. IEEE International Symposium on*, July 2007, pp. 1–4.

[31] K. Hurst and S. Ellingson, "Path Loss From a Transmitter Inside an Aircraft Cabin to an Exterior Fuselage-Mounted Antenna," *IEEE Trans. Electromagn. Compat.*, vol. 50, no. 3, pp. 504–512, Aug. 2008.

[32] L. L. Beranek and T. Hidaka, "Sound absorption in concert halls by seats, occupied and unoccupied, and by the hallŠs interior surfaces," *The Journal of the Acoustical Society of America*, vol. 104, p. 3169, 1998.

# Model for the Path Loss of In-room Reverberant Channels

Gerhard Steinböck, Troels Pedersen, Bernard H. Fleury, Wei Wang,
Thomas Jost and Ronald Raulefs

*IEEE Vehicular Technology Conference Spring, 2011*

© 2013 IEEE
*The layout has been revised.*

## *Abstract*

A general path loss model for in-room radio channels is proposed. The model is based on experimental observations of the behavior of the delay-power spectrum in closed rooms. In such a room, the early part of the spectrum observed at different positions typically consists of a dominant component (peak) that vanishes as the transmitter-receiver distance increases; the late part decays versus distance according to the same exponential law in delay regardless of the distance. These observations motivate the proposed model of the delay-power spectrum with an early dominant component and a reverberant component. The dominant component is modeled as a Dirac delta function weighted with a factor decaying according to an inverse distance power law ($d^{-n}$). The reverberant component is an exponentially decaying function versus delay with distance-dependent onset. Its power decays exponentially with distance. The proposed model allows for the prediction of path loss, mean delay, and rms delay spread versus distance. We use measurements to validate the model. We observe good agreement of the model prediction for mean delay and rms delay spread.

## *D.1 Introduction*

The field of indoor radio-localization has recently attracted significant interest. One approach for solving the localization problem is to rely on the measured power of the received signal [1] and to use a path loss model to infer the corresponding length of a radio link. Knowledge of the received power is often used for localization in already deployed systems (e.g. WiFi) where received signal strength is readily available or with cheap low power devices in sensor networks. Even when deploying localization techniques with higher accuracy, path loss models are used to predict the signal-to-noise ratio and the probability of connectivity [2], which are both important criteria for system analysis.

Indoor path loss models, relating the received power to the transmitter-receiver distance, have been a valuable instrument to the communication engineer [3]. A vast amount of such models have been proposed for various propagation scenarios and environments and have been validated for diverse purposes in wireless communications. The primary concern so far has been to predict the power loss with respect to distance. These models consider indoor scenarios in which path loss is caused by transmission across multiple walls and floors, and multi-path fading [4, 5]. Thus, they cover a whole building. Only few models are available in the literature that characterize propagation in a single room [6].

In this contribution we propose an in-room path loss model based on experimental observations of the behavior of the delay-power spectrum [7, 8] and on analogies to models used in room acoustics [9] and electromagnetic

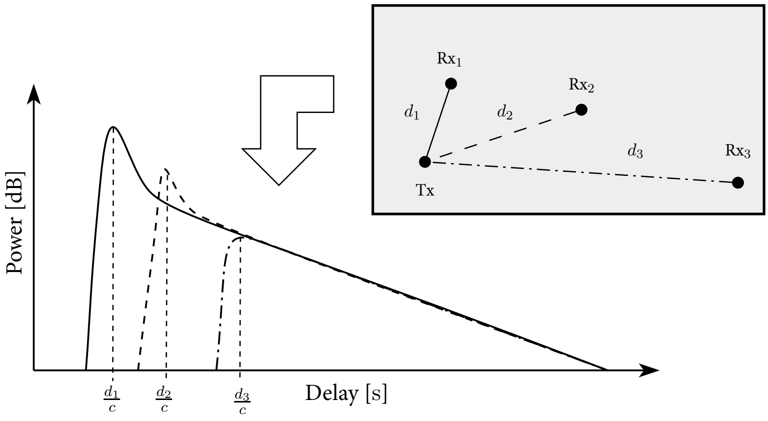

*Fig. D.1: Typical behavior of the bandlimited delay-power spectrum experimentally observed in an in-room environment at three different transmitter-receiver distances (schematically presented by the grey box).*

fields in cavities [10]. In our model the delay-power spectrum consists of a dominant and a reverberant component. The model allows for the prediction of the path loss, the mean delay and the rms delay spread versus transmitter-receiver distance. The proposed model is validated with a new set of measurement data.

## D.2 Delay Power Spectrum Model

We consider an in-room scenario as illustrated in Fig. D.1. The delay-power spectrum is observed at different transmitter and receiver locations. A system bandwidth high enough to observe frequency fading (delay dispersion), but to low to separate single propagation paths in the environment is considered. The regarded carrier frequencies are high enough, such that the smallest dimension of the room is large compared to the wavelength $\lambda$. The delay-power spectrum is the expectation of the squared magnitude of the impulse response $h\left(\tau, d\right)$:

$$G(\tau, d) = \mathrm{E}[|h\left(\tau, d\right)|^2]. \tag{D.1}$$

Here $\tau$ is the delay and $d$ is the transmitter-receiver distance. In [8] it is observed that the delay-power spectrum in such an in-room scenario exhibits the typical behavior depicted in Fig. D.1. The tail of the delay-power spectrum exhibits the same constant exponential decay regardless of the transmitter-receiver distance. The early part is strong at short distance and gradually vanishes as this distance increases.

*Table D.1: Parameters of the proposed model.*

| Parameter | Meaning |
|---|---|
| $G_0$ | Path gain at reference distance $d_0$. |
| $d_0$ | Reference distance, typically 1 m. |
| $n$ | Path gain decay exponent of the dominant component. |
| $q$ | Ratio $G_{\mathrm{rev}}(d_0)/G_{\mathrm{dom}}(d_0)$. |
| $T$ | Reverberation time of the reverberant component. |

Based on these observations, we model the delay-power spectrum as a dominant component plus a reverberant component:

$$\begin{aligned} G(\tau, d) &= \mathrm{E}[|h_{\mathrm{dom}}(\tau, d)|^2] + \mathrm{E}[|h_{\mathrm{rev}}(\tau, d)|^2] \\ &= G_{\mathrm{dom}}(\tau, d) + G_{\mathrm{rev}}(\tau, d). \end{aligned} \tag{D.2}$$

Subscript dom indicates the dominant component and subscript rev denotes the reverberant component. The dominant component represents the early part of the delay-power spectrum consisting of a directly propagating component and possible first-order reflections from the floor, ceiling and walls. The reverberant component represents the multitude of higher order reflections in the room which yield the diffuse tail of the delay-power spectrum.

We model the delay-power spectrum of the dominant component as

$$G_{\mathrm{dom}}(\tau, d) = G_0 \left(\frac{d_0}{d}\right)^n \delta\left(\tau - \frac{d}{c}\right), \tag{D.3}$$

where $n$ is the power decay exponent, $\delta(\,\cdot\,)$ is the Dirac delta function, $c$ the speed of light, and $G_0 > 0$ is the gain at the reference distance $d_0$.

We model the reverberant delay-power spectrum as an exponentially decaying function with onset determined by the transmitter-receiver distance:

$$G_{\mathrm{rev}}(\tau, d) = \begin{cases} G_{0,\mathrm{rev}}\, e^{-\frac{\tau}{T}}, & \tau > \frac{d}{c} \\ 0, & \text{otherwise} \end{cases} \tag{D.4}$$

where $G_{0,\mathrm{rev}}$ is the reference gain of the reverberant component. In analogy to acoustics [8, 9] we call $T$ the reverberation time.

We remark that the models in [7] and [8] are based on the room acoustic theory. They both neglect the transmitter-receiver distance. In [7] the delay-power spectrum of the reverberant component, i.e. corresponding to (D.4), is non-exponential. It has maximum power one and constant onset at delay zero. In [8] the model only accounts for the exponentially decaying delay-power spectrum of the reverberant component in (D.2).

## D.3 Predictions of the Delay Power Spectrum Model

Based on the model (D.2) we now derive expressions for the path gain, mean delay, and rms delay spread as a function of the transmitter-receiver distance.

### D.3.1 Path gain

The path gain at distance $d$ is

$$\begin{aligned} G(d) &= \int G(\tau, d)\mathrm{d}\tau \\ &= \underbrace{G_0 \left(\tfrac{d_0}{d}\right)^n}_{G_{\mathrm{dom}}(d)} + \underbrace{G_{0,\mathrm{rev}}\, T\, e^{\frac{-d}{c\,T}}}_{G_{\mathrm{rev}}(d)} . \qquad \text{(D.5)} \end{aligned}$$

The component $G_{\mathrm{dom}}(d)$ decays with $d^{-n}$, while $G_{\mathrm{rev}}(d)$ decays exponentially. Denoting by $q$ the ratio of reverberant to dominant gain at reference distance $d_0$:

$$q = \frac{G_{\mathrm{rev}}(d_0)}{G_{\mathrm{dom}}(d_0)} = \frac{G_{0,\mathrm{rev}}}{G_0}\, T\, e^{\frac{-d_0}{c\,T}}, \qquad \text{(D.6)}$$

the path gain can be recast as

$$G(d) = G_0 \left(\tfrac{d_0}{d}\right)^n + G_0\, q\, e^{\frac{d_0 - d}{c\,T}} . \qquad \text{(D.7)}$$

Examples of $G(d)$ are graphed in Fig. D.2a. At small distances $G_{\mathrm{dom}}(d)$ dominates and the path gain decays as $d^{-n}$. Beyond a certain distance, the contribution of the reverberant component $G_{\mathrm{rev}}(d)$ in $G(d)$ leads to a deviation from $G_{\mathrm{dom}}(d)$. This effect occurs over a certain distance interval, denoted as the reverberation region $D_{\mathrm{rev}} = \{d : G_{\mathrm{rev}}(d) \geq G_{\mathrm{dom}}(d)\}$. At larger distances $G_{\mathrm{rev}}(d)$ vanishes and $G(d)$ approaches $G_{\mathrm{dom}}(d)$ again.

We remark that the path loss is defined as the inverse of the path gain: $L(d) = G(d)^{-1}$. For notational convenience we consider only path gain in the sequel.

### D.3.2 Mean Delay and Root Mean Squared Delay Spread

The mean delay at distance $d$ as is derived from (D.2) as

$$\begin{aligned} \mu_\tau(d) &= \frac{1}{G(d)} \int \tau\, G(\tau, d)\mathrm{d}\tau \qquad \text{(D.8)} \\ &= \tfrac{d}{c} + T \frac{1}{1 + \left(\tfrac{d_0}{d}\right)^n \tfrac{1}{q}\, e^{\frac{d - d_0}{c\,T}}} . \qquad \text{(D.9)} \end{aligned}$$

In (D.9) the first term is the delay of a directly propagating component and the second term results from the reverberant component. Fig. D.2b depicts the mean delay versus distance with the settings specified in the legend of the figures. The mean delay increases with distance. For distances in the reverberation region, the curves approximately follow the straight line $\frac{d}{c}+T$ . It can be seen from (D.9) that $\lim_{d\to 0} \mu_{\mathcal{T}}(d) = 0$ and that $\mu_{\mathcal{T}}(d)$ has the asymptote $\frac{d}{c}$ for $d \to \infty$. Note that the range of distance considered in the plot of Fig. D.2b is to small to observe the convergence of $\mu_{\mathcal{T}}(d)$ towards its asymptote.

Similarly, (D.2) enables computation of the rms delay spread: $\sigma_{\mathcal{T}}(d)$:

$$\sigma_{\mathcal{T}}^2(d) = \frac{1}{G(d)} \int \tau^2\, G(\tau,d)\mathrm{d}\tau - \left(\mu_{\mathcal{T}}(d)\right)^2 . \tag{D.10}$$

Insertion of (D.7) and (D.9) into (D.10) leads to

$$\sigma_{\mathcal{T}}^2(d) = \frac{T^2}{1+\left(\frac{d_0}{d}\right)^n \frac{1}{q}\, e^{\frac{d-d_0}{c\,T}}} \left(2 - \frac{1}{1+\left(\frac{d_0}{d}\right)^n \frac{1}{q}\, e^{\frac{d-d_0}{c\,T}}}\right) . \tag{D.11}$$

Fig. D.2c depicts the rms delay spread versus distance. Notice, $\sigma_{\mathcal{T}}(d)$ in (D.11) has the following limits

$$\lim_{d\to 0} \sigma_{\mathcal{T}}(d) = \lim_{d\to\infty} \sigma_{\mathcal{T}}(d) = 0. \tag{D.12}$$

Here again, the range of the distance considered in Fig. D.2c is to small to observe the convergence of $\sigma_{\mathcal{T}}(d)$ towards 0 as $d \to \infty$. For distances in the reverberation region $\sigma_{\mathcal{T}}(d)$ approaches the reverberation time $T$. Indeed it can be shown that

$$T = \sup_{d,n,q} \{\sigma_{\mathcal{T}}(d) : d \geq 0, n \geq 0, q \geq 0\}, \tag{D.13}$$

i.e. the rms delay spread is upper bounded by $T$ for any distance.

## D.4 Measurement Data

We validate the proposed model by means of measurement data from a campaign conducted at DLR in Oberpfaffenhofen, Germany. The investigated room is sketched in Fig. D.3. A panograph of it is depicted in Fig. D.4. The environment was static and no one was in the room while the measurements were taken.

The dimensions of the room are 5.1×5.25×2.78 $\mathrm{m}^3$. The three inner walls are made of plaster boards. As visible in the panograph, the outer “wall”

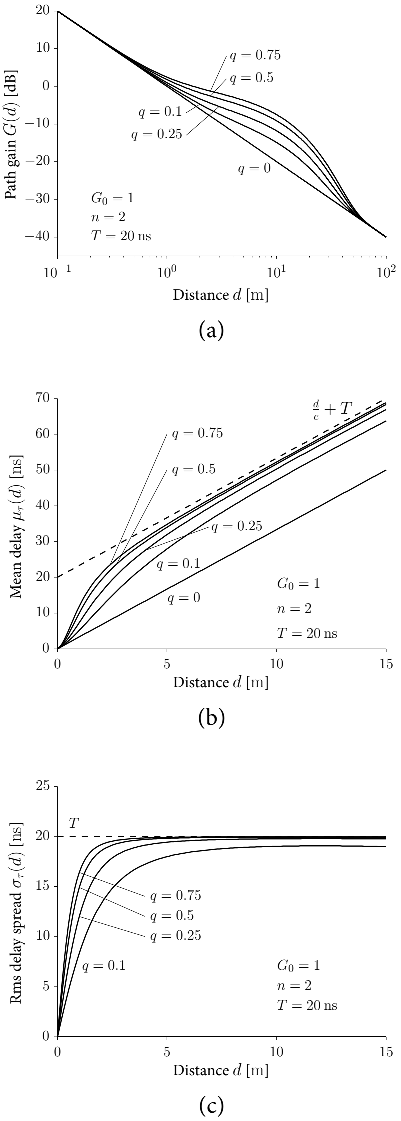

*Fig. D.2: Path gain (a), mean delay (b) and rms delay spread (c) versus distance predicted by the proposed model for* $d_0 = 1$ m.

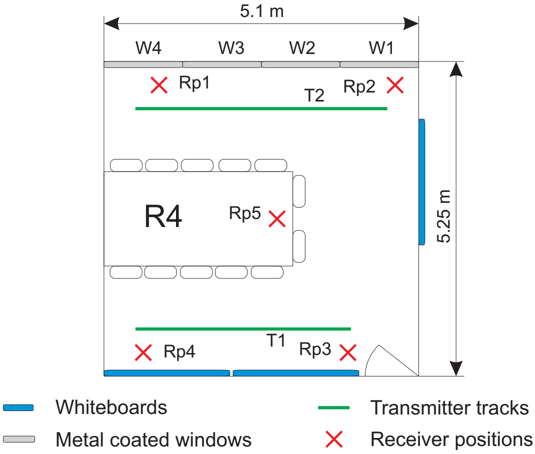
5.1 m
W4
W3
W2
W1
Rp1
T2
Rp2
R4
Rp5
5.25 m
T1
Rp4
Rp3
Whiteboards
Metal coated windows
Transmitter tracks
Receiver positions

*Fig. D.3: Schematic of the investigated room.*

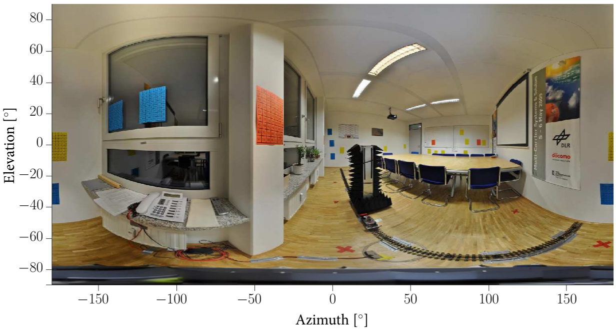
Elevation [°]
80
60
40
20
0
−20
−40
−60
−80
−150
−100
−50
0
50
100
150
Azimuth [°]

*Fig. D.4: Panograph (spherical panoramic photo) of the investigated room seen from Rp1 using an equi-rectangular projection.*

consists mainly of four windows (W1–W4) and two pillars made of concrete. The frames of the windows are metallic and the glass is metal coated. The height of the transmit and receive antenna was 1.26 m and 1.1 m, respectively.

The measurement data were collected using the Rusk-DLR channel sounder [11] operating at 5.2 GHz. The settings of the sounder are summarized in Table D.2. The transmit antenna [12] was omni-directional with 3 dBi gain. A uniform circular array of eight monopoles with diameter 75.18 mm was used at the receiver. The transmitter and receiver were synchronized to a common clock via cables throughout the measurements.

The equipment used a multiplexer to sequentially sound the eight channels between the port of the transmit antenna and the ports of the eight elements of the receive array. One measurement cycle, in which all eight channel frequency responses were measured, was completed in 204.8 µs. The sounder

*Table D.2: Settings of the channel sounder.*

| Parameter | Value |
|---|---|
| Carrier frequency $f_c$ | 5.2 GHz |
| Bandwidth $B$ | 120 MHz |
| Number of sub-carriers $N_c$ | 1536 |
| Carrier separation $\Delta f$ | 78.125 kHz |
| Signal duration | 12.8 µs |
| Cycle duration | 204.8 µs |
| Cycles per burst | 20 |
| Burst duration | 4096 µs |
| Burst repetition time | 131.072 ms |
| Transmit power | 0 dBm |

was operating in "burst" mode. In each burst 20 consecutive measurement cycles were performed. One burst lasted $20 \cdot 204.8\ \mu\mathrm{s} = 4096\ \mu\mathrm{s}$. Between each burst, the sounder paused for data storage; the burst repetition time was $131.072\ \mathrm{ms}$.

The receive antenna array was placed at five fixed locations labeled as Rp1 to Rp5 respectively in Fig. D.3. The transmit antenna was mounted on a model train which moved on two tracks labeled as T1 and T2. Frequency responses were measured for each receiver position while the transmitter moved along the two tracks with a constant speed of approximately $0.05\ \mathrm{m/s}$. During one measurement burst the transmitter moved $204.8\ \mu\mathrm{m} = 0.0035\lambda$. Over this distance the channel response can be considered constant. Between two consecutive bursts, the transmitter moved $6.55\ \mathrm{mm} \approx \lambda/8.8$.

The positions Rp1-Rp5 and the trajectory along the track were measured with a tachymeter. The odometer of the model train was connected to the channel sounder to record the measurement locations.

## D.5 Results

We compute the received power at all receiver and transmitter positions. Notice that one measurement burst corresponds uniquely to one pair of transmitter and receiver positions. Let us consider one specific burst. The frequency responses of each of the eight channels measured during the burst are averaged. The averaged responses are then squared and integrated to obtain the power values of the eight channels. Averaging these values yields the power measured in the burst. Fig. D.5 reports the scatter plot of power values computed for all bursts versus transmitter-receiver distance. Since the noise-floor is below $-70$ dBm in all measurements, we disregard the noise.

We compute the mean delay estimate $\widehat{\mu}_\tau$ and rms delay spread estimates $\widehat{\sigma}_\tau$ for each burst. We multiply the averaged frequency responses of the eight channels obtained for a given burst (see above) with a Hann window. Taking

*Table D.3: Parameter estimates for the standard and proposed models.*

| Model | $\widehat{G}_0$ | $\widehat{n}$ | $\widehat{q}$ | $\widehat{T}$ [ns] |
|---|---|---|---|---|
| Standard | $1.11 \cdot 10^{-5}$ | 1.14 | — | — |
| Proposed $\widehat{T} = 18.73$ ns | $6.42 \cdot 10^{-6}$ | 2.26 | 0.56 | 18.73 |
| Proposed $\widehat{T} = 16.02$ ns | $5.79 \cdot 10^{-6}$ | 2.39 | 0.71 | 16.02 |

the inverse Fourier transform of the filtered frequency responses yields estimates of the impulse responses of the eight channels. The mean delay and delay spread estimates for the burst are obtained by inserting the squared average of the eight impulse responses in (D.8) and (D.10), respectively. These estimates computed for all bursts are reported versus transmitter-receiver distance in Fig. D.6. These values are in accordance with values reported in [5] for office environments.

We use the model assumption (D.4) on the behavior of the tail of the delay-power spectrum versus $\tau$ to estimate $T$ from experimental delay-power spectra. More specifically, an estimate of $T$ is obtained from a linear least squares estimate of the slope of the late part of the experimental log power spectra. As can be seen in Fig. D.7 the underlying model assumption (D.4) holds true for the experimental delay-power spectra. Considering the restriction of the log spectra obtained for any transmitter and receiver positions in the delay range $40 \text{ ns} \leq \tau \leq 150 \text{ ns}$, the linear least squares estimator yields $\widehat{T} = 18.73 \text{ ns}$.

We test the behavior of the mean delay ($\mu_\mathcal{T} \rightarrow \frac{d}{c} + T$, see Fig. D.2b) and the rms delay spread ($\sigma_\mathcal{T} \approx T$, see Fig. D.2c) predicted by the model when $d$ ranges in the reverberation region. The scatter plot of estimates of the rms delay spread in Fig. D.6 shows a constant behavior for distances larger than $3 \text{ m}$. Therefore, we estimate $T$ by taking the average of these estimates for $d > 3 \text{m}$. This yields $\widehat{T} = 16.02 \text{ns}$. Similarly we estimate $T$ from the scatter plot of estimates of the mean delay versus distance. For each estimate, say $\widehat{\mu}_\mathcal{T}(d)$, the difference $\widehat{\mu}_\mathcal{T}(d) - \frac{d}{c}$ is computed for $d > 3 \text{ m}$. The estimate $\widehat{T}$ is the average of these differences. Doing so yields $\widehat{T} = 13.07 \text{ ns}$. The theoretical results for $\mu_\mathcal{T}$ and $\sigma_\mathcal{T}$ in Fig. D.2b and Fig. D.2c, respectively, show that for some model parameter settings, the bound $\sigma_\mathcal{T} \approx T$ and specifically the asymptote of the mean delay $\mu_\mathcal{T} \rightarrow \frac{d}{c} + T$ are not reached. Thus we proceed with the analysis by considering the two close estimates $\widehat{T} = 18.73 \text{ ns}$ and $\widehat{T} = 16.02 \text{ ns}$.

We estimate the parameters of both the standard path loss model ($G(d) = G_0 \left(\frac{d_0}{d}\right)^n$) and the proposed model from the estimated power values reported in Fig. D.5. More specifically, the estimates are computed by considering the log-power domain. For the standard path loss model a linear least squares estimation is performed. We use the Matlab curve fitting toolbox [13], which provides a non-linear least squares estimator, to fit the proposed path

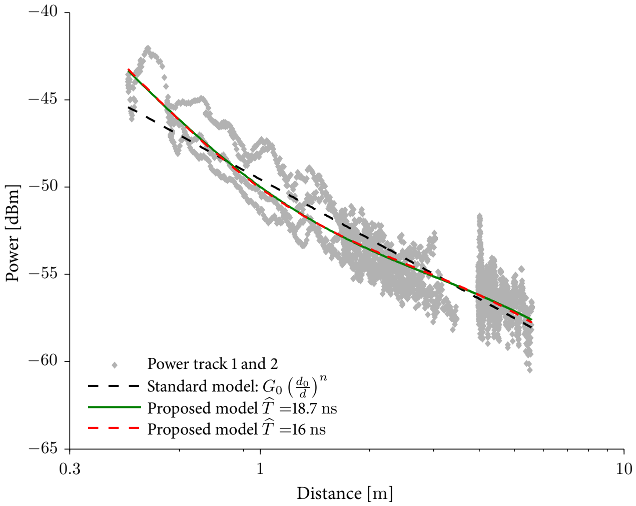

*Fig. D.5: Estimated received power versus distance with the predictions computed using the standard and the proposed path gain models.*

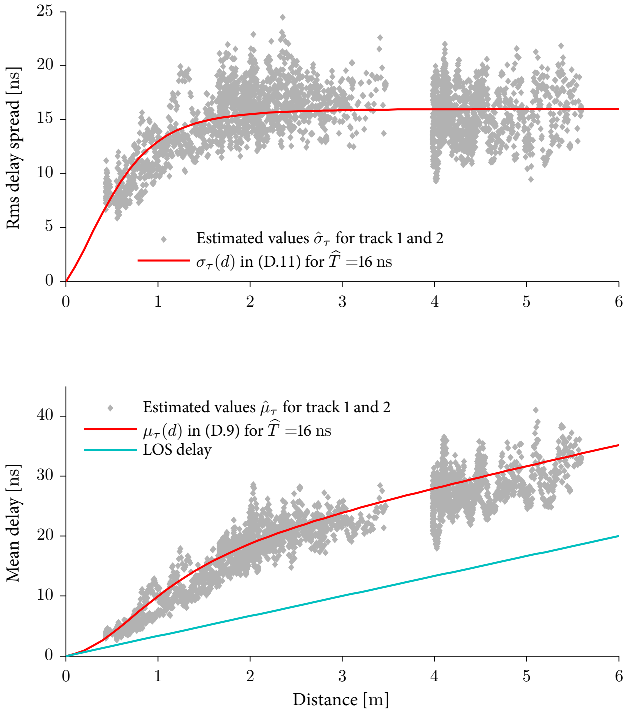

*Fig. D.6: Scatter plots of estimates of the rms delay spread and the mean delay versus distance. The solid lines depict the predicted rms delay spread and mean delay obtained with the proposed model. For reference we also plot the line corresponding to $\frac{d}{c}$.*

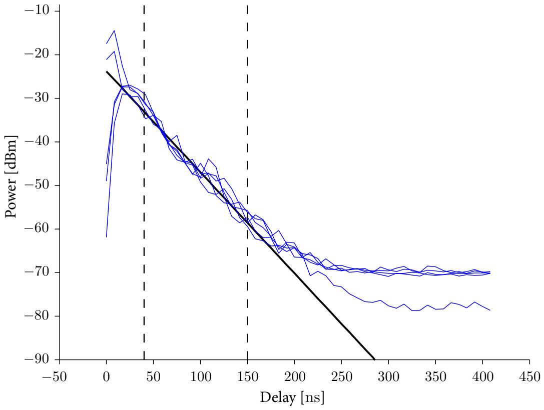

*Fig. D.7:* *Spatially averaged delay-power profiles obtained for the receiver positions Rp1 to Rp5 when the transmitter was at the start position on track T1. The straight line depicts an exponentially decaying function with decay factor* $\widehat{T} = 18.73$ ns. *The dashed lines indicate the range* $40$ ns $\leq \tau \leq 150$ ns *used for the estimation of* $\widehat{T}$.

gain model (D.7). This toolbox returns estimates of the parameters $G_0$, $n$ and $q$ with the estimate $\widehat{T}$ provided as input.

The estimates of the parameters of the models are reported in Table D.3 and the path gains versus distance computed from the models with these parameter settings are shown in Fig. D.5. The path gain predictions of the standard and proposed models (for the two sets of parameter estimates) almost overlap.

## D.6 Discussion

The estimate $\widehat{n} = 1.14$ of the path loss exponent of the standard path gain model is in the range of published values obtained from in-room measurement data [6] and references therein. Traditionally, exponent values lower than 2 are attributed to wave guiding effects. However, the dimensions of the room do not advocate this interpretation. A reverberation phenomenon in the room provides a more plausible explanation to the observed low exponent.

The estimates of the mean delay $\widehat{\mu}_\tau(d)$ and rms delay spread $\widehat{\sigma}_\tau(d)$ shown in Fig. D.6 are in accordance with the model prediction obtained with $\widehat{T} = 16.02\,\text{ns}$. The predicted transition of the mean delay and the rms delay spread from zero at $d = 0$ to respectively $\frac{d}{c} + T$ and $T$ for $d$ ranging in the reverberation region is well observed.

The parameter estimates of the model computed from the two estimated reverberation times slightly differ (see Table D.3). However, the path gains predicted by the two model estimates fall on top of each other as shown in Fig. D.7.

The estimate $\widehat{T} = 18.73\ \mathrm{ns}$ obtained directly from the delay-power spectra deviates by only 14.5 % from $\widehat{T} = 16.02\ \mathrm{ns}$ obtained from (D.13). These observations support the hypothesis that the reverberant component impacts significantly the received power, mean delay, and rms delay spread.

The estimated values for $q$, which characterize the ratio between the power of the dominant and reverberant components, is 0.56 and 0.71 respectively. Thus, the reverberant component plays an important role in the description of the path gain. The estimates $\widehat{n} = 2.26$ and 2.39 of the path gain decay exponent of the dominant component are close to the exponent of free-space propagation.

The estimated reverberation times are close to typical rms delay spreads observed in office environments [5]. This suggests that these rms delay spreads might have been measured in the reverberation region and are thus dominated by the reverberation term. This interpretation is further supported by the fact that the reverberation region starts as close a distance as 1.2 $\mathrm{m}$ in the considered scenario.

## D.7 Conclusions

A model of the delay-power spectrum of an in-room reverberant channel has been proposed. The model includes a dominant and a reverberant component. The dominant component follows an inverse distance power law ($d^{-n}$). The reverberant component decays exponentially versus delay and exhibits a distance dependent onset. As a result, its power decays exponentially with distance. The proposed model allows for the prediction of path gain, mean delay and rms delay spread. The model was validated using measurement data and compared to the standard path loss model. The predictions of mean delay and rms delay spread agree well with the estimates obtained from the measurement data. In the investigated environment the ratio of the gain of the reverberant component to the gain of the dominant component is 0.56. Hence, the reverberant component is prominent in this environment. The estimated path gain exponent of the dominant component in the proposed model is close to the free-space path gain exponent. Due to its inability to separate the dominant component from the reverberant component the standard path gain model yields a path gain exponent close to unity. This model merely provides a fit of the path gain that blends the contributions from the dominant and reverberant component.

## References

[1] H. Liu, H. Darabi, P. Banerjee, and J. Liu, “Survey of Wireless Indoor Positioning Techniques and Systems,” *IEEE Trans. Syst., Man, Cybern. C*, vol. 37, no. 6, pp.

1067–1080, Nov. 2007.

[2] D. Dardari, A. Conti, C. Buratti, and R. Verdone, "Mathematical Evaluation of Environmental Monitoring Estimation Error through Energy-Efficient Wireless Sensor Networks," *IEEE Trans. Mobile Comput.*, vol. 6, no. 7, pp. 790–802, July 2007.

[3] R. Vaughan and J. B. Andersen, *Channels, Propagation and Antennas for Mobile Communications*. Institution of Engineering and Technology, 2003.

[4] J. Keenan and A. Motley, "Radio coverage in buildings," in *Br. Telecom Technol. J.*, vol. 8, no. 1, Jan. 1990, pp. 19–24.

[5] E. Damosso, Ed., *Digital mobile radio towards future generation systems: COST 231 Final Report*. Bruxelles, Belgium: European Commission, 1999.

[6] D. Xu, J. Zhang, X. Gao, P. Zhang, and Y. Wu, "Indoor Office Propagation Measurements and Path Loss Models at 5.25 GHz," *IEEE Veh. Technol. Conf. (VTC)*, pp. 844–848, Oct. 2007.

[7] C. Holloway, M. Cotton, and P. McKenna, "A model for predicting the power delay profile characteristics inside a room," *IEEE Trans. Veh. Technol.*, vol. 48, no. 4, pp. 1110–1120, 1999.

[8] J. B. Andersen, J. Ø. Nielsen, G. F. Pedersen, G. Bauch, and J. M. Herdin, "Room electromagnetics," *IEEE Antennas Propag. Mag.*, vol. 49, no. 2, pp. 27–33, 2007.

[9] H. Kuttruff, *Room Acoustics*, 4th ed. London: Taylor & Francis, 2000.

[10] D. A. Hill, *Electromagnetic Fields in Cavities: Deterministic and Statistical Theories*, ser. IEEE Press Series on Electromagnetic Wave Theory. Piscataway, NJ: Wiley/IEEE Press, 2009.

[11] J. Stephan, Y. Lostanlen, J. Keignart, W. Wang, D. Slock, and F. Kaltenberger, "Measurements of location-dependent channel features," ICT-217033 WHERE, Del. 4.1, Oct. 2008, http://www.ict-where.eu/.

[12] Huber+Suhner, "Datasheet for Sencity Antenna For In-Carriage Wireless Communication, Type: SOA 5600/360/3/20/V_1," Document No. 01.02.1358, May 2007.

[13] Mathworks, "Matlab Curve Fitting Toolbox, Version 1.2.2 (r2008b)," 2008.

# Distance Dependent Model for the Delay Power Spectrum of In-room Radio Channels

Gerhard Steinböck, Troels Pedersen, Bernard H. Fleury, Wei Wang
and Ronald Raulefs

*IEEE Transactions Antennas and Propagation, 2013*

© 2013 IEEE

*The layout has been revised.*

## Abstract

A model based on experimental observations of the delay power spectrum in closed rooms is proposed. The model includes the distance between the transmitter and the receiver as a parameter which makes it suitable for range based radio localization. The experimental observations motivate the proposed model of the delay power spectrum with a primary (early) component and a reverberant component (tail). The primary component is modeled as a Dirac delta function weighted according to an inverse distance power law ($d^{-n}$). The reverberant component is an exponentially decaying function with onset equal to the propagation time between transmitter and receiver. Its power decays exponentially with distance. The proposed model allows for the prediction of e.g. the path loss, mean delay, root mean squared (rms) delay spread, and kurtosis versus the distance. The model predictions are validated by measurements: they show good agreement with respect to distance dependent trends.

## E.1 Introduction

Range based radio localization relies on models of the radio channel that incorporate distance as a parameter [1]. Such models allow for inferring on the transmitter-receiver distance from observations of range dependent channel features. For example currently deployed communication systems estimate the distance from the received signal strength based on a validated path loss model [1]. Wideband communication systems potentially allow for the exploitation of additional distance dependent information inherent in the dispersive behavior of the radio channel for localization purposes. Delay dispersion is characterized by means of the delay power spectrum, which is defined as the expectation of the squared impulse response. Thus, models describing the behavior of the delay power spectrum versus distance are in demand.

The delay power spectrum is a key component in wireless communications research of most stochastic models of the channel impulse response. The delay power spectrum is typically modeled as a one-sided exponentially decaying function of the delay [2]. Moreover, the power is normalized and the reference delay (origin) is selected to coincide with the onset delay. These transformations do not affect the bit error rate performance of communication systems operating in these stochastic channels, but the distance information potentially exploitable for localization is removed. Distance information is included in separate path loss models for an entire building [2–5] or for a single room [6–8] to perform coverage analysis.

We consider models for the in-room scenario as a basic element to cover entire buildings. Models of the delay power spectrum of in-room channels

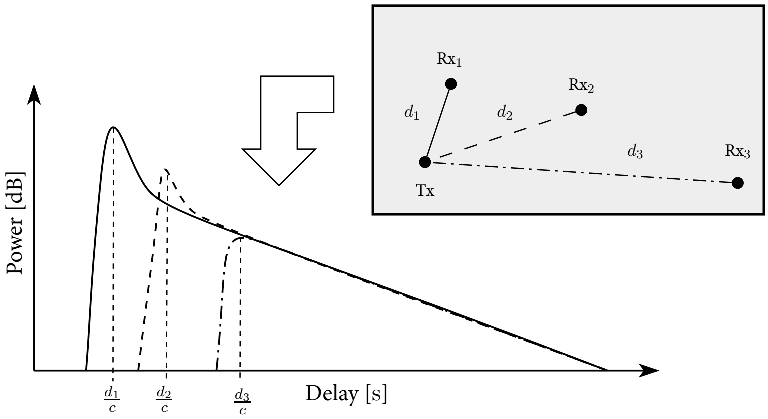

*Fig. E.1: Typical behavior of the bandlimited delay power spectrum experimentally observed at three different transmitter-receiver distances in an in-room environment (schematically presented by the grey box).*

relying on reverberation theory, or room electromagnetics, have been recently proposed in [9–13]. These room electromagnetic models characterize the tail of the delay power spectrum, which is caused by reverberation, an effect similar to that occurring in room acoustics [14]. However, these models ignore the early part of the delay power spectrum, which is typically exploited for localization.

In the present contribution, the distance dependent model of the delay power spectrum is motivated by experimental observations [9, 11, 15] indicating that it exhibits an early, or primary, spike-like component followed by an exponential decaying tail. A model with a similar shape ("spike plus exponential tail") for outdoor scenarios was considered in [16] without including the distance dependence. The model proposed here consists of a primary and a reverberant component. The primary component is a Dirac delta function weighted according to an inverse distance power law ($d^{-n}$). The reverberant component is exponentially decaying with a distance-dependent onset and a reverberant field like behavior [11]. We denote the latter component as reverberant component, even though a reverberant field might not be entirely formed [9].

In this contribution, we extend the work presented in [17]. We derive the moment generating function and the kurtosis of the delay power spectrum. Additionally, a detailed investigation of the distance dependence of the primary and reverberant component is provided. This study leads to the concept of reverberation region. Furthermore, this contribution focuses on the validation of the model and uses additional experimental data in comparison to [17]. The relevance of the proposed delay power spectrum model is demonstrated by relating it to other published models and by means of two applications. These applications are a distance dependent model for the Rice factor and a time-discrete model to generate impulse responses.

The path loss prediction shows good agreement with the two distinct behaviors observed at both short and medium transmitter-receiver distances. So far this different behavior was not considered in path loss models, see e.g. [7] and references therein. We observe a good agreement between predicted values and estimates of the mean delay together with a predictable distance dependency, which is critical for localization purposes. The predicted and estimated values of the root mean squared (rms) delay spread are close with a distance behavior similar to that reported in [18, 19] for small to intermediate ranges.

## *E.2 Model of the Delay Power Spectrum*

We consider an in-room environment as illustrated in Fig. E.1 and assume that the wavelength is small compared to the smallest dimension of the room. The bandwidth of the considered system is assumed high enough to observe frequency fading (delay dispersion), but too low to separate single propagation paths in the environment.

We define the delay power spectrum as the expectation of the squared magnitude of the impulse response $h\left(\tau,d\right)$:

$$G(\tau,d) = \mathrm{E}[|h\left(\tau,d\right)|^2], \tag{E.1}$$

where $\tau$ is the delay and $d$ is the transmitter-receiver distance. The expectation operator represents the mathematical abstraction of an averaging procedure to suppress variations due to small and large scale fading. This averaging procedure is used in [20] to obtain the so called long-term power delay profile. Realizations of $|h\left(\tau,d\right)|^2$ are sampled at different transmitter and receiver locations.

Fig. E.1 illustrates the empirical observation that the delay power spectra in such an in-room scenario consist of an early part and a tail [9–11, 15]. The early part is strong at short distance and gradually vanishes as the distance increases and the tail has the same exponential decay[1] regardless of the transmitter-receiver distance.

We propose to model the delay power spectrum as a superposition of a primary and a reverberant component, each of which is distance dependent (see Appendix E.I):

$$G(\tau,d) = G_{\mathrm{pri}}(\tau,d) + G_{\mathrm{rev}}(\tau,d). \tag{E.2}$$

---

[1] The theoretical investigations in [9] lead to a non-exponential tail, however some of the reported experimental results are close to exponential.

*Table E.1: Parameters of the proposed model.*

| Parameter | Meaning |
|---|---|
| $G_0$ | Path gain at reference distance $d_0$. |
| $d_0$ | Reference distance, typically 1 m. |
| $n$ | Path gain exponent. |
| $R_0$ | Ratio $G_{\text{rev}}(d_0)/(G_{\text{pri}}(d_0)+G_{\text{rev}}(d_0))$. |
| $T$ | Reverberation time. |

Subscript "pri" indicates the primary component and subscript "rev" the reverberant component. The primary component represents the early part of the delay power spectrum. It consists of the component resulting from direct propagation and possibly a superposition of components that may originate from first-order reflections on the floor, ceiling, and walls. We model the primary component as

$$G_{\text{pri}}(\tau, d) = G_0 \left(\frac{d_0}{d}\right)^n \delta\left(\tau - \frac{d}{c}\right), \tag{E.3}$$

where $n$ is the path gain exponent, $\delta(\,\cdot\,)$ is the Dirac delta function, $c$ the speed of light, and $G_0 > 0$ is the gain at an arbitrary reference distance $d_0$. We chose the Dirac delta function as an approximation of the superimposed multipath components resulting from direct propagation and first order reflections as they cannot be resolved due to the bandwidth limitation.

The reverberant component is contributed by the multitude of higher order reflections in the room, which yield the tail in the measured delay power spectra. We model it as an exponentially decaying function with onset equal to the propagation time between the transmitter and receiver:

$$G_{\text{rev}}(\tau, d) = \begin{cases} G_{0,\text{rev}}\, e^{-\tau/T}, & \tau > \frac{d}{c} \\ 0, & \text{otherwise}, \end{cases} \tag{E.4}$$

where $G_{0,\text{rev}}$ is the reference gain of the reverberant component. In analogy to room acoustics [11, 14] we term $T$ the reverberation time.

The assumed exponential decay in (E.4) is inspired from experimental observations from literature [9–11, 15]. Reverberation theory [11, 13, 14, 21] predicts an exponentially decaying tail that exhibits a behavior with distance similar to (E.4). However, there may be other propagation phenomena leading to such an exponential decay. In this contribution we do not validate if the tail is created by reverberation; instead we rely only on experimental evidence to model the tail. Reverberation theory provides counterparts to some of the parameters that we use in the following sections. Therefore we use a terminology inspired by reverberation theory. The parameters of the model of the delay power spectrum are summarized in Table E.1.

We will see in the following sections that the model (E.2)–(E.4) allows for the derivation of secondary models characterizing the behavior versus distance of narrowband parameters, like path loss and K-factor, and wideband parameters, like mean delay and rms delay spread.

### *E.2.1 Path Gain and Path Loss*

The average path gain at distance $d$ is obtained by integration of the delay power spectrum (E.2) with respect to delay:

$$G(d) = \int G(\tau, d)\,\mathrm{d}\tau, \tag{E.5}$$

$$= \underbrace{G_0 \left(\tfrac{d_0}{d}\right)^n}_{G_{\mathrm{pri}}(d)} + \underbrace{G_{0,\mathrm{rev}}\, T\, e^{\frac{-d}{c\,T}}}_{G_{\mathrm{rev}}(d)}. \tag{E.6}$$

The component $G_{\mathrm{pri}}(d)$ decays as $d^{-n}$, while $G_{\mathrm{rev}}(d)$ decays exponentially. Note that the average path loss is defined as the inverse of the average path gain: $L(d) = G(d)^{-1}$. For mathematical convenience we consider the average path gain in the sequel and refer to it as path gain.

It is convenient to define a reverberation ratio $R(d)$ as the fraction of the total power contained in the reverberant component:

$$R(d) = \frac{G_{\mathrm{rev}}(d)}{G(d)}. \tag{E.7}$$

By definition $R(d)$ ranges from zero to unity. The introduction of the reverberation ratio simplifies the equations in the sequel. Furthermore, we chose to parameterize the model in terms of the reverberation ratio at the reference distance $d_0$, i.e. we recast (E.6) and (E.7) with $R_0 = R(d_0)$ as a parameter:

$$G(d) = G_0 \left(\tfrac{d_0}{d}\right)^n + G_0\, \tfrac{R_0}{1-R_0}\, e^{\frac{d_0-d}{c\,T}}, \tag{E.8}$$

$$R(d) = \frac{1}{1 + \frac{1-R_0}{R_0} \left(\frac{d_0}{d}\right)^n\, e^{\frac{d-d_0}{c\,T}}}. \tag{E.9}$$

The parameter $R_0 \in [0, 1]$ indicates the balance between the primary and reverberant components at the reference distance. The ratio $\frac{1-R_0}{R_0}$ corresponds to the ratio of primary versus reverberant component $(G_{\mathrm{pri}}(d_0)/G_{\mathrm{rev}}(d_0))$ at the reference distance. The special case $R_0 = 0$, i.e. the reverberant component vanishes, leads to the "one-slope" model [4]

$$G(d) = G_{\mathrm{pri}}(d) = G_0 \left(\tfrac{d_0}{d}\right)^n. \tag{E.10}$$

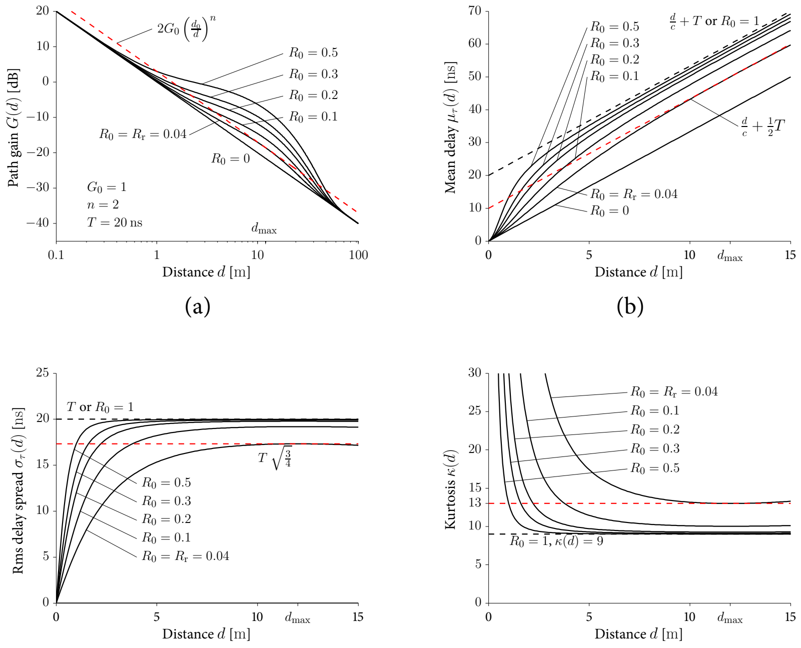

(a) (b)

(c) (d)

*Fig. E.2: Path gain (a), mean delay (b), rms delay spread (c) and kurtosis (d) versus distance predicted by the proposed model for $d_0 = 1$ m. The intersections of the various functions with the red dashed line mark the beginning and end of the reverberation region. The intersection at the end or the reverberation is not visible in (b), (c) and (d) due to chosen axis limitation. The reverberation region is observed if, and only if, $R_0 \geq R_r = 0.04$ for these settings.*

This occurs when either $G_{0,\text{rev}} = 0$ or the tail decays very fast, i.e. $T \approx 0$.

In the other extreme where the primary component vanishes, i.e. $R(d) = R_0 = 1$, (E.8) simplifies to

$$G(d) = G_{\text{rev}}(d) = G_{0,\text{rev}}\, T\, e^{-\frac{d}{c\,T}}. \tag{E.11}$$

Blockage of the line-of-sight path will not lead to a vanishing primary component as the primary component may include additional first order reflections according to its definition.

Fig. E.2a depicts example graphs of $G(d)$. For small distances $d$, the primary component dominates and the path gain decays as $d^{-n}$. For intermediate distances we observe a deviation from $d^{-n}$ due to the reverberant component. For very large distances the influence of the reverberant component vanishes again.

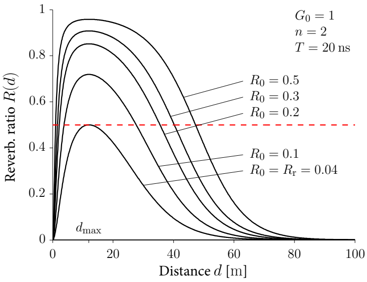

*Fig. E.3: Reverberation ratio versus the distance in linear scale. The intersections of $R(d)$ with the red dashed line mark the beginning and end of the reverberation region for the various parameter settings.*

### E.2.2 Properties of the Reverberation Ratio

The reverberation ratio ranges by definition between zero and unity. In the following we derive properties of $R(d)$ under the assumption that $R_0 \neq 0$. We observe from (E.9) and Fig. E.3 that $R(d)$ vanishes for very small and very large distances, where the primary component dominates the reverberant component. More specifically,

$$\lim_{d \to 0} R(d) = 0 \qquad \text{and} \qquad \lim_{d \to \infty} R(d) = 0. \tag{E.12}$$

For intermediate distances $R(d)$ approaches its maximum when the reverberant component dominates over the primary component. The distance $d_{\max}$ where $R(d)$ is maximum is obtained by differentiation of (E.9) and equating the result to zero:

$$d_{\max} = c\,T\,n. \tag{E.13}$$

At this distance the reverberation ratio is

$$R(d_{\max}) = \frac{1}{1 + \frac{1-R_0}{R_0} e^{-\frac{d_0}{c\,T}} \left( \frac{d_0\, e}{c\,T\,n} \right)^n}. \tag{E.14}$$

Notice that $d_{\max}$ only depends on $n$, $T$ and $c$, the speed of light. The value $R(d_{\max})$ depends in addition on $R_0$ and $d_0$. It is less than unity except for the case $R_0 = 1$, i.e. when only the reverberant component is present. For the examples shown in Fig. E.3, $d_{\max}$ is 12 m.

### E.2.3 Mean Delay and Root Mean Squared Delay Spread

The mean delay is obtained from the delay power spectrum (E.2) as

$$\begin{aligned} \mu_\tau(d) &= \frac{1}{G(d)} \int \tau \, G(\tau, d) \, \mathrm{d}\tau && \text{(E.15)} \\ &= \tfrac{d}{c} + T\,R(d). && \text{(E.16)} \end{aligned}$$

The first term in (E.16) is the delay of a directly propagating component and the second term results from the reverberant component. The mean delay is a function of the distance between transmitter and receiver and its value increases with distance. Fig. E.2b depicts examples of the mean delay versus distance for different values of $R_0$. Using $R(d_{\max})$ and the upper bound of $R(d)$, which is unity, in (E.16), we can establish the following bounds for $\mu_\tau(d)$:

$$0 \le \mu_\tau(d) \le \tfrac{d}{c} + T\,R(d_{\max}) \le \tfrac{d}{c} + T. \tag{E.17}$$

From the limits of $R(d)$ given in (E.12) and from (E.16) we conclude that

$$\lim_{d \to 0} \mu_\tau(d) = 0 \qquad \text{and} \qquad \lim_{d \to \infty} \mu_\tau(d) - \tfrac{d}{c} = 0. \tag{E.18}$$

Note that the distance range considered in the plot of Fig. E.2b is too small to observe the convergence of $\mu_\tau(d)$ towards its asymptote $\frac{d}{c}$ for $d \to \infty$. The mean delay approaches $\frac{d}{c} + T$ for intermediate distances when $R(d)$ is close to unity.

The rms delay spread $\sigma_\tau(d)$ is computed as

$$\begin{aligned} \sigma_\tau^2(d) &= \frac{1}{G(d)} \int \tau^2 \, G(\tau, d) \, \mathrm{d}\tau - (\mu_\tau(d))^2 && \text{(E.19)} \\ &= T^2 R(d) \, (2 - R(d)) \, . && \text{(E.20)} \end{aligned}$$

Hence the behavior of $R(d)$ determines that of $\sigma_\tau^2(d)$. Using (E.14) and the fact that $R(d)$ is unity in the case where there is only a reverberant component we obtain the following upper bounds:

$$\sigma_\tau^2(d) \le T^2 R(d_{\max}) \; (2 - R(d_{\max})) \le T^2. \tag{E.21}$$

Furthermore, it can be seen from (E.12), that

$$\lim_{d \to 0} \sigma_\tau^2(d) = 0 \qquad \text{and} \qquad \lim_{d \to \infty} \sigma_\tau^2(d) = 0. \tag{E.22}$$

The rms delay spread is depicted as a function of distance in Fig. E.2c. As for Fig. E.2b the distance range considered in Fig. E.2c is too small to observe the convergence of $\sigma_\tau(d)$ towards zero as $d$ approaches infinity.

### E.2.4 Centered Moment of Order k and Kurtosis

Analytical expressions for the centered moments of the delay power spectrum (E.2)–(E.4) are given in Appendix E.II. The third and fourth moments show similar dependency versus distance as the rms delay spread and therefore we omit presenting these results.

The kurtosis of $|h(\tau,d)|$ is used in localization to distinguish between line of sight or non-line of sight situations [22–26]. The kurtosis of the delay power spectrum is

$$\kappa(d)=\frac{\mu_4(d)}{\mu_2^2(d)}, \tag{E.23}$$

where $\mu_k(d)$ is the normalized $k$th centered moment of the delay power spectrum (E.55) derived in Appendix E.II. After inserting $\mu_2(d)$ and $\mu_4(d)$ in (E.23) we see that for small and large distances $\kappa(d)$ approaches infinity. For intermediate distances $\kappa(d)$ approaches its minimum value of nine, which coincides with the kurtosis of the exponential distribution [27]. Fig. E.2d shows (E.23) for different settings of $R_0$.

We find the maximum of the moments of order $k\geq 2$ by equating the derivative of $\mu_k(d)$ to zero. Since these moments depend only on $d$ via $R(d)$, we can write

$$\frac{\mathrm{d}\mu_k(d)}{\mathrm{d}d}=\frac{\mathrm{d}\mu_k(d)}{\mathrm{d}R(d)}\frac{\mathrm{d}R(d)}{\mathrm{d}d}. \tag{E.24}$$

The first factor in the right-hand product is positive, and therefore the root of (E.24) coincides with the root of the second factor, which is $d_{\max}$. Thus, all moments of order $k\geq 2$ attain their maximum value at distance $d_{\max}$. Furthermore, since $R(d)<1$ we obtain

$$\mu_k(d)\leq T^k\sum_{\ell=0}^{k}\frac{k!}{\ell!}(-1)^{\ell}\qquad k\geq 2. \tag{E.25}$$

For $k=2$, (E.25) combined with the identity $\sigma_\tau=\sqrt{\mu_2}$ yields the upper bound of the rms delay spread in (E.21).

### E.2.5 Reverberation Region

For particular parameter values, it may occur that the power of the reverberant component equals or exceeds the power of the primary component at some distances, i.e. $G_{\text{rev}}(d)\geq G_{\text{pri}}(d)$ or equivalently $R(d)\geq\frac{1}{2}$. The reverberation region is the interval of distances for which $G_{\text{rev}}(d)\geq G_{\text{pri}}(d)$:

$$D_{\text{rev}}=\{d\geq 0; R(d)\geq\tfrac{1}{2}\}. \tag{E.26}$$

The reverberation region is non empty if, and only if,

$$R_0 \geq \frac{1}{1 + e^{\frac{d_0}{c\,T}} \left(\frac{d_0\,e}{c\,T\,n}\right)^{-n}} = R_{\mathrm{r}}. \tag{E.27}$$

We define the reverberation distance as $d_{\mathrm{rl}} = \min D_{\mathrm{rev}}$. We consider the following three cases:

*Case* $R_0 < R_{\mathrm{r}}$*:* In this case the primary component is dominating over the reverberant component over all distances and $D_{\mathrm{rev}}$ is the empty set.

*Case* $R_0 = R_{\mathrm{r}}$*:* The reverberation region is a singleton: $D_{\mathrm{rev}} = \{d_{\max}\}$. In the graph of the path gain versus distance we observe a maximum of 3 dB deviation from $G_{\mathrm{pri}}(d_{\mathrm{rl}})$ (see Fig. E.2a). We denote this largest possible reverberation distance $d_{\mathrm{rl,max}} = d_{\max}$. The parameter $d_{\mathrm{rl,max}}$ is of importance since it can be used for interpreting measurements: If the measured power does not exceed $G_{\mathrm{pri}}(d)$ by 3 dB at distances smaller than $d_{\mathrm{rl,max}}$, it will never occur. This result may be useful e.g. for the planning of in-room channel measurements.

*Case* $R_0 > R_{\mathrm{r}}$*:* In this case $D_{\mathrm{rev}} = [d_{\mathrm{rl}}, d_{\mathrm{ru}}]$, with $d_{\mathrm{rl}} < d_{\mathrm{ru}}$. The endpoints of the reverberation region are the two solutions of the identity $G_{\mathrm{pri}}(d) = G_{\mathrm{rev}}(d)$. After some algebraic manipulations this identity can be written as

$$-\tfrac{d_0}{c\,T\,n} \left(\tfrac{R_0}{1-R_0}\, e^{\frac{d-d_0}{c\,T}}\right)^{-\frac{1}{n}} = -\tfrac{1}{c\,T\,n}\, d\, e^{-\frac{1}{c\,T\,n} d}. \tag{E.28}$$

This expression can be solved in terms of the Lambert $W$ function[2] [28]. For $z \in (-e^{-1}, 0)$, the Lambert $W$ function provides two real solutions denoted by $W_0(z)$ and $W_{-1}(z)$), respectively [28]. By inserting the left hand side of (E.28) for $z$ in $W_0(z)$ we obtain

$$d_{\mathrm{rl}} = -c\,T\,n\,W_0\left(-\tfrac{d_0}{c\,T\,n}\left(\tfrac{R_0}{1-R_0}\, e^{\frac{d_0}{c\,T}}\right)^{-\frac{1}{n}}\right). \tag{E.29}$$

We obtain $d_{\mathrm{ru}}$ by replacing $W_0(\,\cdot\,)$ with $W_{-1}(\,\cdot\,)$ in (E.29).

We derive the following special values for the boundaries of the reverberation region:

$$\mu_\tau(d_{\mathrm{rl}}) = \tfrac{d_{\mathrm{rl}}}{c} + \tfrac{T}{2}, \tag{E.30}$$

$$\mu_\tau(d_{\mathrm{ru}}) = \tfrac{d_{\mathrm{ru}}}{c} + \tfrac{T}{2}, \tag{E.31}$$

$$\sigma_\tau(d_{\mathrm{rl}}) = \sigma_\tau(d_{\mathrm{ru}}) = T\,\sqrt{\tfrac{3}{4}}, \tag{E.32}$$

$$\kappa(d_{\mathrm{rl}}) = \kappa(d_{\mathrm{ru}}) = 13. \tag{E.33}$$

---

[2] The Lambert $W$ function is the (multi-valued) inverse of the complex function $w \mapsto w\,e^{w}$. For any complex number $z$, the values of $W(z)$ satisfy $z = W(z)\,e^{W(z)}$ [28].

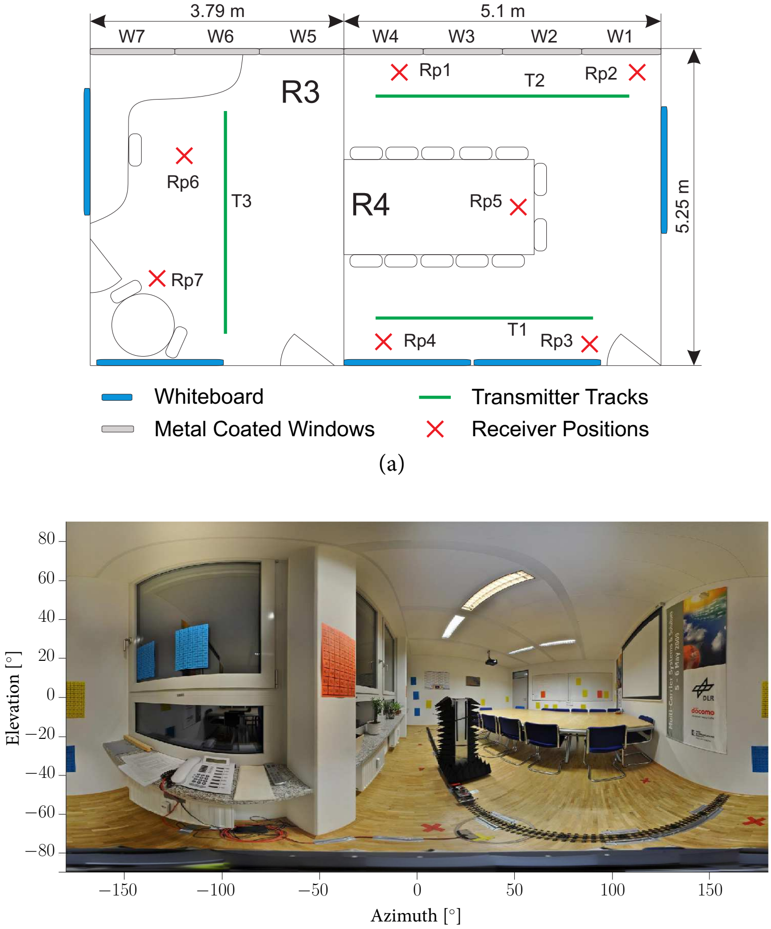
3.79 m
5.1 m
W7
W6
W5
W4
W3
W2
W1
R3
Rp1
T2
Rp2
Rp6
T3
R4
Rp5
5.25 m
Rp7
T1
Rp4
Rp3
Whiteboard
Transmitter Tracks
Metal Coated Windows
Receiver Positions
Elevation [°]
80
60
40
20
0
−20
−40
−60
−80
−150
−100
−50
0
50
100
150
Azimuth [°]

(a)

(b)

*Fig. E.4: Schematic of room R3 and R4 where the measurements were performed (a) and panograph (spherical panoramic photo) of R4 seen from Rp1 using an equi-rectangular projection (b).*

We see from (E.32) that $\sigma_\tau(d_{\mathrm{rl}})$ depends only on the reverberation time. We can use this result, together with an estimate of $T$, to estimate $d_{\mathrm{rl}}$ for a given room. To obtain an estimate of $T$ from the rms delay spread one might simply average the rms delay spread estimates obtained for distances within an interval where these estimates show a constant trend. For the case that $R_0 \leq R_{\mathrm{r}}$ the maximum of the rms delay spread is $\max_{d\geq 0}\{\sigma_\tau(d)\} \leq T\sqrt{\frac{3}{4}}$ and, similarly, $\max_{d\geq 0}\{\mu_\tau(d) - \frac{d}{c}\} \leq \frac{T}{2}$.

### *E.2.6 Relation to Other Models and Measurements*

The contributions [9, 11] investigate the delay power spectrum in reverberant environments. In [11] it is shown that a diffuse field induces a delay power spectrum with an exponentially decaying tail. As shown in [9], the diffuse field occurs after an initial build up phase. The analysis in [9] indicates that the buildup phase lasts for so long that it cannot be neglected. This leads the authors to propose a model of the delay power spectrum with a non-exponentially decaying tail. The exponentially decaying tail in the model (E.2)–(E.4) is motivated solely by empirical observations. Therefore, the model is valid as long as (E.4) holds. A modification of (E.4) towards a non-exponential decay as in [9] is straightforward. Note that one of the two measurements in [9] is well described by an exponentially decaying tail.

Neither [9] nor [11] report the delay power spectrum in a form suitable to derive secondary models for path loss, mean delay, etc. versus distance. The model in [9] characterizes the delay power spectrum as a direct ray plus a non-exponential tail[3] for an average transmitter-receiver distance corresponding to the mean-free path[4] of the room. In [11] the early part of the delay power spectrum and the distance dependent onset of the tail are not specified. The way the models in [9, 11] are constructed hinders the derivation of secondary models. In contrast, the model (E.2)–(E.4) induces such secondary models (see (E.8), (E.16), and (E.20)).

Published measurements of the received power [29, 30] indicate a distinct behavior at short, intermediate and large distances. The decay of the total power versus distance, however, is commonly approximated with a one-slope model [7, 29, 30]. The approximation with a single path loss exponent leads to estimates of the path loss exponents smaller than the free space exponent and an overall poor model prediction. The path gain model in (E.8) mimics the difference in behavior at short, intermediate and large distances, as can be seen in Section E.2.1.

We introduce in Section E.2.5 the new concept of reverberation region, where the reverberant component dominates. Furthermore, we define the reverberation distance to be the lower boundary of the reverberation region, cf. $d_{\mathrm{rl}}$ in (E.29). At this distance the primary and reverberant components have equal power, so our definition is in line with the classical definition of the reverberation distance or "effective radius" well known in room acoustics [14] and room electromagnetics [11, 31]. Note, however, that in our model, a second such distance might exist, namely $d_{\mathrm{ru}}$, due to the fact that the power of the tail decays exponentially versus distance.

---

[3] More specifically, the direct ray and the tail's onset are both shifted to delay zero and the delay power spectrum is normalized such that the power of the direct ray is unity.

[4] In [9] the mean-free path is obtained as the product of the speed of light and the average number of wall reflections per second.

According to the model (E.20), the rms delay spread increases with distance up to the reverberation distance, stabilizes at a constant plateau within the reverberation region, and decreases outside the reverberation region. The empirical values of the rms delay spread reported in the survey [32] exhibit inconclusive behavior with respect to distance dependence: the rms delay spread is reported to both increase and decrease with distance. We conjecture that this behavior may be due to the used rms delay spread estimators. The measurements and results from ray-tracing simulations reported in [18, 19] agree with (E.20).

In summary, the model (E.2)–(E.4) of the delay power spectrum induces secondary models for the path gain, mean delay and rms delay spread etc. versus distance. These secondary models are interconnected via the initial model (E.2)–(E.4), in the sense that they share common parameters and are thus consistent. This consistency cannot be ensured when the models are derived independently from each other, as currently done in the literature. Our secondary models show good agreement with experimental data published in [7, 11, 18, 19, 29–32]. In the following two sections, we validate the model (E.2)–(E.4) by comparing the predictions achieved with the secondary models to measurements.

## *E.3 Measurement Data*

We validate the proposed model by means of measurement data from a campaign [33] conducted at the DLR premises in Oberpfaffenhofen, Germany. In the following we describe in detail the measurement campaign and the post-processing of the measurement data.

### *E.3.1 Measurement Campaign*

Measurements were collected in a meeting room (R4) and an adjacent office (R3) depicted in Fig. E.4. The dimensions of R4 and R3 are $5.1\times5.25\times2.78\ \mathrm{m}^3$ and $3.79\times5.25\times2.78\ \mathrm{m}^3$, respectively. The inner walls are made of plaster boards. As visible in the panograph, the outer "wall" consists mainly of four windows (W1–W4) and two concrete pillars in R4. The office has only three windows (W5–W7). The window frames are metallic and the glass is metal coated. In both rooms the heights of the transmit and receive antennas were 1.26 m and 1.1 m, respectively. The environment was static and no one was in the room while the measurements were taken.

The measurement data were collected using the Rusk-DLR channel sounder [34] operating at 5.2 GHz. The transmitter and receiver were synchronized to a common Rubidium clock via cables throughout the measurements. The used transmit antenna [35] is omni-directional with 3 dBi gain. The receiver

*Table E.2: Setting of the channel sounder and parameters for data post-processing.*

| Sounder Settings | Value |
|---|---|
| Carrier frequency $f_c$ | 5.2 GHz |
| Bandwidth $B$ | 120 MHz |
| Number of sub-carriers $N_c$ | 1537 |
| Carrier separation $\Delta_f$ | 78.125 kHz |
| Signal duration $T_\mathrm{S}$ | 12.8 µs |
| Cycle duration $T_\mathrm{C}$ | 204.8 µs |
| Cycles per burst $C$ | 20 |
| Burst duration $T_\mathrm{B}$ | 4096 µs |
| Burst repetition time $T_\mathrm{BR}$ | 131.072 ms |
| Transmit power | 0 dBm |
| Delay MUX and cable $\tau_\mathrm{mux}$ | 3.86 ns |
| Number of receive antennas $M$ | 8 |
| **Post-processing Settings** | |
| Threshold $\theta$ | -61 dB |
| Start delay range $T$ estimator $\tau_\mathrm{s}$ in R4 | 25 ns |
| Start delay range $T$ estimator $\tau_\mathrm{s}$ in R3 | 16.7 ns |
| End delay range $T$ estimator $\tau_\mathrm{max}$ | 150 ns |
| Reference distance $d_0$ | 1 m |

was equipped with a uniform circular array of $M = 8$ monopoles with diameter 75.18 $\mathrm{mm}$. These monopoles were connected to the receiver via a multiplexer. The multiplexer and the cables connecting the receive antennas to it introduce an additional known delay $\tau_\mathrm{mux}$ which could not be removed in the calibration process but can be accounted for during the post-processing. In a measurement cycle $T_\mathrm{C}$ all eight channel frequency responses are sequentially measured. The sounder was operating in "burst" mode. In each burst $C$ consecutive measurement cycles are performed. The duration of one burst is $T_\mathrm{B} = C \cdot T_\mathrm{C}$. In between bursts, the sounder pauses for data storage, resulting in the burst repetition time $T_\mathrm{BR}$. The setting of the sounder selected for the measurement campaign is reported in Table E.2.

Channel measurements were obtained for seven fixed receive antenna array locations (Rp1 to Rp7), shown in Fig. E.4a. The transmit antenna was mounted on a model train which moved on three tracks (T1 to T3). The positions Rp1 to Rp7 and the trajectories along the tracks were measured with a tachymeter. The odometer of the model train was connected to the channel sounder to record the traveled distance during the movement. For each receiver position the frequency response was measured while the trans-

---

[5] The spatially averaged delay power spectrum $\widehat{G}[\tau]$ is obtained as the average of $\widehat{G}_{r,p,q}[\tau]$ over all transmitter and receiver positions in room R4. For a given distance $d$, $\widehat{G}[\tau, d]$ is the spatial average of $\widehat{G}_{r,p,q}[\tau]$ over all transmitter and receiver positions with distance belonging to a section centered around $d$. Distance sections have a length of 4 wavelengths and stretch over the full range of transmitter-receiver distances.

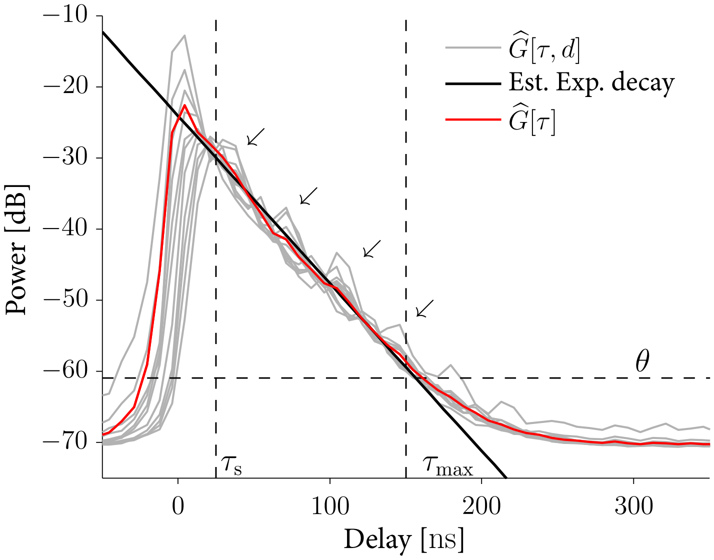

*Fig. E.5: Spatially averaged delay power spectrum $\widehat{G}[\tau]$ and $\widehat{G}[\tau, d]$ [5]. For displaying convenience $\widehat{G}[\tau, d]$ is shown for every second distance section. The straight line depicts an exponentially decaying function with decay constant $\widehat{T} = 18.4\,\mathrm{ns}$ corresponding to $-0.24\,\mathrm{dB/ns}$. The arrows indicate the delays of the reoccurring peaks in the spectrum estimates (see also Fig. E.6), caused by propagation paths with multiple reflections between the metallic whiteboard and the windows.*

mitter was moving along a track. The transmitter moved with a constant speed of approximately 0.07 $\mathrm{m/s}$. According to the setting of $T_\mathrm{B}$ in Table E.2 this corresponds to a movement of $0.005$ wavelengths within a burst. Over this distance the channel response can be considered quasi-static. Between two consecutive bursts ($T_\mathrm{BR}$), the transmitter moved $1/6.3$ wavelengths.

### E.3.2 Post-processing of the Measurement Data

We apply the following post-processing procedure on the experimental data. The measured frequency responses are averaged over all cycles in each burst to reduce noise. The resulting averaged frequency response is denoted by $\widehat{H}_{m,r,p,q}[f]$ where $m$ is the index of the receive array element at receiver position index $r$ and at transmitter position $p$ along track $q$. The brackets around $f$ indicate that the frequency variable has been discretized, due to the measurement process. We estimate the path gain of the channel for the

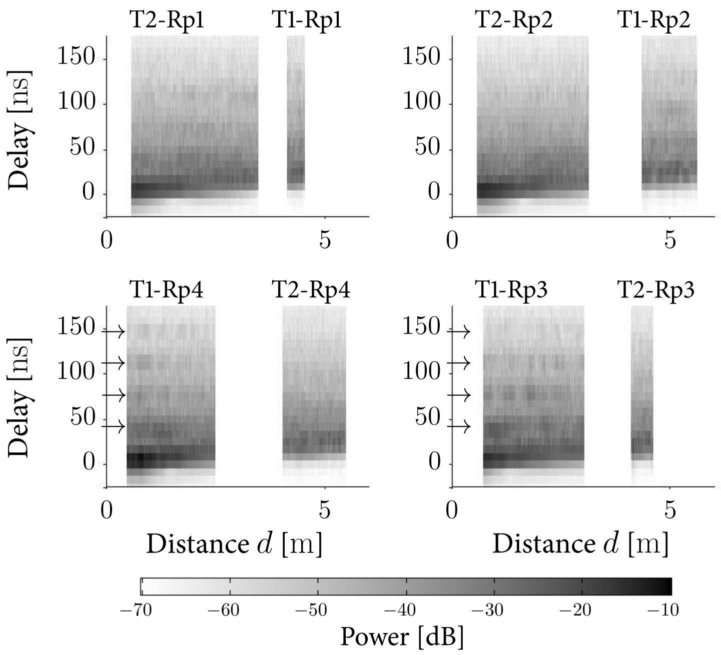

*Fig. E.6: Estimates of the delay power spectrum (see* (E.36)*) for room R4 versus transmitter-receiver distance. Results are shown for the receiver positions Rp1 to Rp4 and the tracks T1 and T2. The arrows on the lower panel indicate the delays of the reoccurring peaks in the spectrum estimates (see also Fig. E.5), caused by propagation paths with multiple reflections between the metallic whiteboard and the windows.*

transmitter at position $p$ along track $q$ and the receiver at position $r$ as

$$\widehat{G}_{r,p,q} = \frac{1}{M}\sum_{m=1}^{M}\frac{1}{B}\sum_{i=0}^{N_c-1}|\widehat{H}_{m,r,p,q}[i\Delta_f]|^2\Delta_f. \tag{E.34}$$

To estimate the delay power spectrum of the said channel we first average the modified periodograms of $\widehat{H}_{m,r,p,q}[f]$, $m = 1, \ldots, M$:

$$\widehat{G}'_{r,p,q}[\tau] = \frac{1}{M}\sum_{m=1}^{M}\left|\mathrm{IDFT}\left\{\widehat{H}_{m,r,p,q}[f]\,W[f]\right\}[\tau]\right|^2. \tag{E.35}$$

In this expression IDFT$\{\cdot\}$ is the inverse discrete Fourier transform of the function given as an argument and $W[f]$ denotes a Hann window applied to suppress sidelobes. We obtain the estimated delay power spectrum by shifting (E.35) ahead by $\tau_{\mathrm{mux}}$ to remove the additional delay due to the cables and multiplexer:

$$\widehat{G}_{r,p,q}[\tau] = \widehat{G}'_{r,p,q}[\tau + \tau_{\mathrm{mux}}]. \tag{E.36}$$

Note that, the positions at which the measurements used in the average in (E.35) were taken only span one wavelength. Therefore the estimate $\widehat{G}_{r,p,q}[\tau]$ undergoes large scale fading. The mean delay estimate is obtained by numerical integration of (E.15) with $G(\tau, d)$ replaced by a truncated version of $\widehat{G}_{r,p,q}[\tau]$. Indeed, to reduce the effect of noise we use only the parts of $\widehat{G}_{r,p,q}[\tau]$ exceeding a threshold $\theta$; see Fig. E.5. The rms delay spread and higher order moments are estimated similarly, e.g. using (E.19). The limited bandwidth of the measurement system affects the estimation of the rms delay spread of the channel. We compensate for this by subtracting the second central moment of the inverse Fourier transform of $W[f]$ from the second central moment of the truncated version of $\widehat{G}_{r,p,q}[\tau]$.

By applying the above post-processing to any of the average frequency responses gathered from the measurements in room R3 and R4 we obtain data sets denoted as $\mathcal{D}3$ and $\mathcal{D}4$, respectively. These data sets are used for the validation of the model. Each set consists of estimates of the delay power spectrum, path gain, mean delay, rms delay spread, higher moments, the kurtosis and the corresponding transmitter-receiver distances inside the room.

## *E.4 Validation of the Proposed Model*

The estimated delay power spectra in Fig. E.5 confirm the observations from [9–11, 15] that: i) the reverberant tails coincide and ii) the primary component vanishes for large distances. Thus, the assumptions underlying the model (E.2)–(E.4) of the delay power spectrum are fulfilled. Fig. E.6 shows the estimates of the delay power spectrum versus transmitter-receiver distance for room R4. The estimates are shown for distances obtained from receiver positions Rp1 to Rp4 and all transmitter locations along the two tracks. We apply no spatial averaging within distance sections as done to obtain the delay power spectrum estimates depicted in Fig. E.5. The similarity of the reverberant tails is apparent for the four receiver positions and all transmitter locations along the two tracks.

We now validate the model (E.2)–(E.4) by checking its predictions of path gain, mean delay, rms delay spread and kurtosis. To this end, we split the data set $\mathcal{D}4$ into a fitting set $\mathcal{D}4_F$ and a validation set $\mathcal{D}4_V$. We let $\mathcal{D}4_F$ be the data set for receiver positions Rp1 to Rp4 and $\mathcal{D}4_V$ be the data for receiver position Rp5 in room R4. Notice that $\mathcal{D}4 = \mathcal{D}4_F \bigcup \mathcal{D}4_V$, and $\mathcal{D}4_F \bigcap \mathcal{D}4_V = \emptyset$. Similarly $\mathcal{D}3$ is split into $\mathcal{D}3_F$ and $\mathcal{D}3_V$ corresponding to receiver positions Rp6 and Rp7, respectively, in room R3.

For $\mathcal{D}4$ we fit the model (E.2)–(E.4) by first estimating $T$ from the estimated delay power spectra and afterwards estimating the remaining model parameters by non-linear least squares fitting of (E.8) to the scatter plot of estimated path gains versus distance. The reverberation time is the least

Table E.3: *Parameter estimates and Root Mean Squared Errors (RMSEs) of path gains for room R3 and R4.*

| Model | Parameter estimates | | | | RMSE† [dB] | |
|---|---|---|---|---|---|---|
| | $\widehat{G}_0$ | $\widehat{n}$ | $\widehat{R}_0$ | $\widehat{T}$ [ns] | Fit to $\mathcal{D}(\cdot)_F$ | Pred. of $\mathcal{D}(\cdot)_V$ |
| One-slope R4 | $1.14 \cdot 10^{-5}$ | 1.13 | — | — | 1.27 | 1.33 |
| Proposed R4 | $6.85 \cdot 10^{-6}$ | 2.2 | 0.35 | 18.4 | 1.17 | 1 |
| One-slope R3 | $9.28 \cdot 10^{-6}$ | 1.27 | — | — | 0.66 | 0.73 |
| Proposed R3 | $5.06 \cdot 10^{-6}$ | 2.67 | 0.41 | 16.7 | 0.5 | 0.65 |

Reverberation region R4: $\widehat{d}_{\mathrm{rl}} = 1.39$ m, $\widehat{d}_{\mathrm{ru}} = 42$ m, $\widehat{d}_{\mathrm{max}} = 12$ m.
Reverberation region R3: $\widehat{d}_{\mathrm{rl}} = 1.16$ m, $\widehat{d}_{\mathrm{ru}} = 52$ m, $\widehat{d}_{\mathrm{max}} = 13.4$ m.
† The path gain values in dB are used to obtain the RMSE.

square estimate of the slope of the estimated log delay power spectra within the delay range $\tau_{\mathrm{s}} \leq \tau \leq \tau_{\mathrm{max}}$ as indicated in Fig. E.5. The value of $\tau_{\mathrm{s}}$ is chosen to reduce the influence of the primary component on the slope estimate. We chose $\tau_{\mathrm{s}}$ to be the delay sample closest to the propagation time between transmitter and receiver at the maximum transmitter-receiver distance occurring in $\mathcal{D}4$ plus one pulse duration. The value of $\tau_{\mathrm{max}}$ is the largest delay sample such that $\widehat{G}_{r,p,q}[\tau]$ exceeds the threshold $\theta$. For $\mathcal{D}4_F$, we obtain in this way $\widehat{T} = 18.4$ ns. We obtain the same value for $\mathcal{D}4_V$. The parameters $G_0$, $n$ and $R_0$ are estimated by fitting the path gain model (E.8) with reference distance $d_0 = 1$ m to the scatter plot of estimated path gain values versus distance for $\mathcal{D}4_F$. We use a non-linear least squares estimator [36] with $\widehat{T}$ as input. This procedure is repeated for $\mathcal{D}3$. The estimates of $T$ for $\mathcal{D}3$ and $\mathcal{D}4$ are listed in Table E.3. For comparison we also report the estimates of the parameters of the one-slope model obtained via linear least squares fitting.

The ability of the two models to fit and predict the experimental power values in dB is evaluated by comparing their respective root mean squared errors (RMSEs), which are reported in Table E.3. The model (E.2)–(E.4) yields a lower RMSE for $\mathcal{D}4_F$ and $\mathcal{D}3_F$ than the one-slope model. This is expected since the former model contains more parameters than the latter and includes it as a special case. Furthermore, when comparing the RMSE values for the fitting and validation data in room R4, we see that the one-slope model yields a higher value for the validation data, while the proposed model achieves a lower value. Compared to the one-slope model, our model not only fits the data better, but also yields a better prediction, thus justifying its added complexity. The reason for the proposed model's superior prediction ability appears from Fig. E.7a: it provides a close fit at all distances whereas the one-slope model shows its best fit for the range of distances corresponding to the bulk of observations. Fitting the one-slope model to $\mathcal{D}4_F$, where the

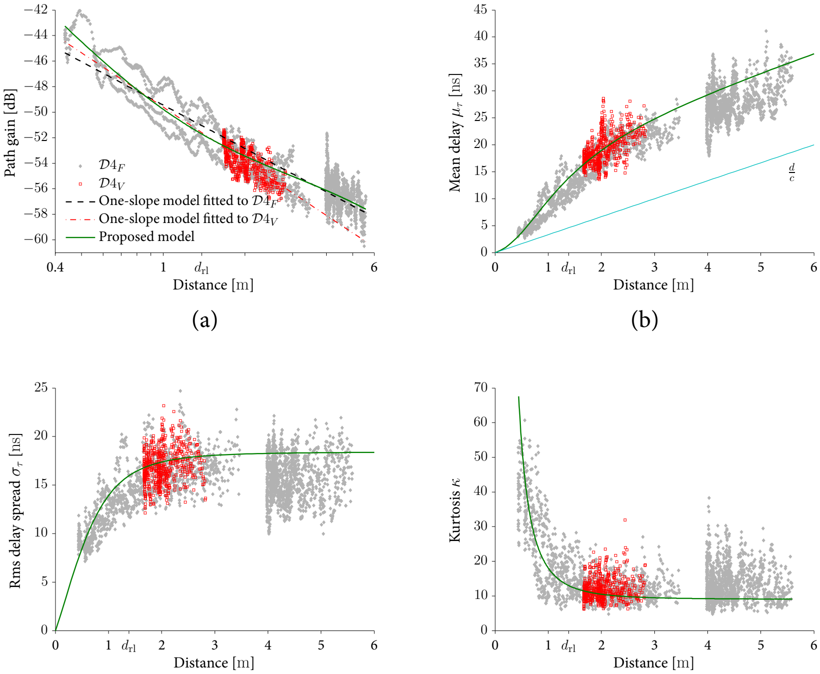

(a) (b)

(c) (d)

*Fig. E.7: Experimental results for $\mathcal{D}4_F$ and $\mathcal{D}4_V$ together with the model predictions (solid lines) using the reported parameters in Table E.3. The dashed and dashed dotted lines in (a) correspond to the standard path gain model. For reference we also plot the line corresponding to $\frac{d}{c}$ in (b).*

bulk of observations is at distances larger than 4 m leads to larger deviations at short distances. This is apparent by swapping the roles of the data sets $\mathcal{D}4_V$ and $\mathcal{D}4_F$: In this case, the one-slope model shows poor prediction for $d > 3$ m. A similar effect can be observed for room R3 in Fig. E.8a; however, the fit is worse at short distances as the bulk of samples covers larger distances ($d > 1.1$ m) in $\mathcal{D}3_V$.

The proposed model allows for the prediction of wideband parameters such as mean delay, rms delay spread and kurtosis. The prediction values are compared to estimates obtained from $\mathcal{D}4$ and $\mathcal{D}3$ in Fig. E.7 and Fig. E.8, respectively. We observe a good general agreement in trend between the predicted parameters and the estimates computed from both fitting and validation data sets for room R3 and R4. This agreement is remarkable considering that the model parameters are obtained from fitting the path gain model, but not the wideband parameters.

We quantify the agreement for $\mathcal{D}4$ by comparison of predictions obtained

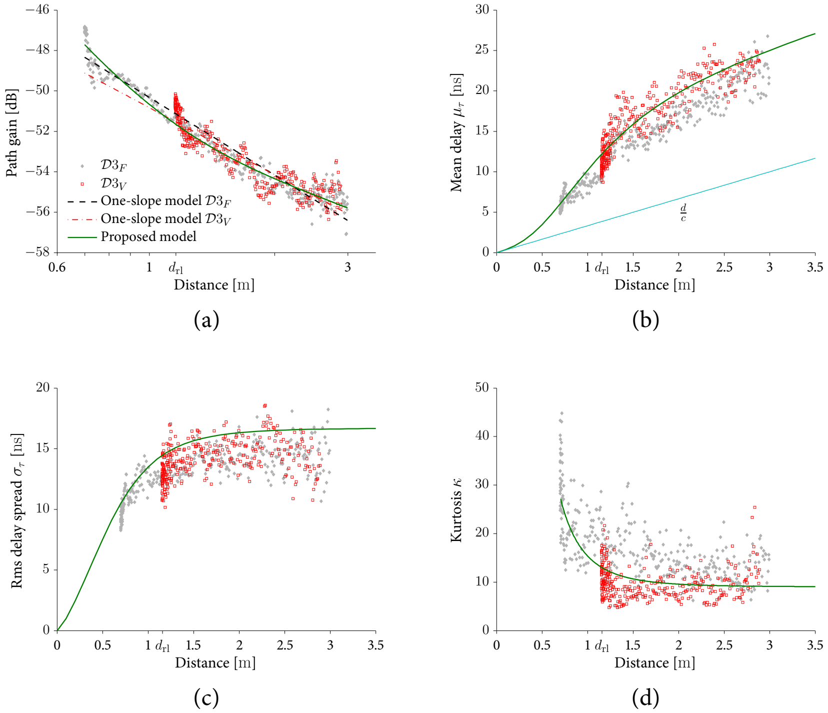

(a) (b)

(c) (d)

*Fig. E.8: Experimental results for $\mathcal{D}3_F$ and $\mathcal{D}3_V$ together with the model predictions (solid lines) using the reported parameters in Table E.3. The dashed and dashed dotted lines in (a) correspond to the one-slope path gain model. For reference we also plot the line corresponding to $\frac{d}{c}$ in (b).*

with the secondary models of the wideband parameters with spatial averages of the corresponding estimates. We compute the average of mean excess delay $\mu_\tau(d) - \frac{d}{c}$, rms delay spread and kurtosis evaluated at the same set of distances exceeding 2 m as used for the experimental data. The relative errors between the average values of estimates and the corresponding values predicted by the models for room R4 are 2.4 ns for mean excess delay, 1.9 ns for rms delay spread, and 3.4 for the kurtosis. Using the values from model prediction, the relative errors amount to 16%, 11% and 35%, respectively. The average values of estimates are observed to be close to the model predictions, especially when considering that $\widehat{T}$ varies by $\pm 1$ ns for different settings of $\tau_{\rm s}$ and/or $\tau_{\rm max}$. We remark that by using the procedure described in [17], which uses the rms delay spread to compute an estimate of $\widehat{T}$, we can obtain a better agreement of the rms delay spread and mean delay. However, with this “fine tuning” of the model one uses more data for the fitting procedure and thus discards the rms delay spread for prediction/validation purposes. In this contribution we focus on the model validation and therefore we use for model fitting the estimate $\widehat{T}$ obtained from the slope of the estimated delay power spectrum.

The variation of the estimates of mean delay, rms delay spread and kurtosis around their respective model prediction is occasionally large. This is caused by small and large scale fading, which is not entirely removed in the estimated delay power spectra used to compute the parameter estimates. Additionally, for some transmitter locations we observe strong peaks with a delay separation of approximately 35 $\mathrm{ns}$, e.g. indicated with arrows in Fig. E.6 and the lower panel of Fig. E.5. These peaks originate from propagation paths that are generated by multiple reflections between the metallic whiteboard and the windows. These multiple reflections were identified in [21] as Fabry-Pérot modes.

The truncation of the delay power spectrum in the post-processing may distort the estimated parameters. To evaluate the relevance of this effect, we modified the proposed model to include the truncation in the delay power spectrum. For the investigated environment and chosen $\theta$ this led to no significant changes of the predicted path gain and mean delay. However, in the considered scenario the truncation reduced the predicted rms delay spread by at most 0.5 $\mathrm{ns}$. We also noticed a reduction of the predicted $d_{\mathrm{ru}}$. This effect is, however, of no practical relevance, since the value is still much larger than the length of the diagonal of the room.

### E.4.1 Model Parameter Estimates

Estimates of the model parameters are listed in Table E.3. The estimates of the path loss exponent for both rooms ($\widehat{n} = 1.13$ and $\widehat{n} = 1.27$) reported for the one-slope model are slightly below published values obtained from in-room measurement data; see [7] and references therein. The path gain exponent estimate for room R4 computed from $\mathcal{D}4_V$ is $\widehat{n} = 1.41$ which is in the range of values reported in [7]. The measurements used to generate $\mathcal{D}3_V$ were taken within the reverberation region. This explains why the estimate of the path loss exponent is only $\widehat{n} = 1.1$. Path loss exponents below two are traditionally attributed to wave guiding effects. However, considering the room dimensions, a reverberation phenomenon seems to be a more plausible reason of the low values.

For room R4, the estimated path gain exponent $\widehat{n} = 2.2$ of the proposed model's primary component is close to the exponent of free-space propagation. The value $\widehat{R}_0 = 0.35$ indicates that at 1 $\mathrm{m}$ distance 35% of the total power is contained in the reverberant component and with increasing distance the reverberant component will gain importance. For room R3 we obtain $\widehat{R}_0 = 0.41$, which is even larger than for R4. Thus, the reverberant component in these two rooms significantly contributes to the total path gain.

The estimate of the reverberation time is within the range of values reported in [11, 12, 15, 37, 38]. The estimated reverberation distance $\widehat{d}_{\mathrm{rl}}$ is about one sixth of the maximum possible distance in rooms R3 and R4. This indicates that the reverberant component dominates over the primary component for a large portion of the room. This in turn leads to the low path loss exponents that we also observe. In addition, $\widehat{d}_{\max}$ is larger than the length of the room diagonal.

## E.5 Examples of Applications

In the following we give two example applications of the proposed delay power spectrum model. The first example is a distance dependent description of the Rice K-factor and the second is a model to generate discrete-time impulse responses.

### E.5.1 Example 1: Modeling the Rice Factor as a Function of Distance

In the literature the amplitude of the narrowband radio channel response is often modeled as a Rice distributed random variable. This random variable can be characterized by the Rice K-factor which was observed in [11, 13, 39] to vary with distance. In the following we utilize the model of the delay power spectrum to model the K-factor.

The narrowband channel response is obtained as:

$$h(d) = \int h(\tau, d)\,\mathrm{d}\tau = h_{\mathrm{pri}}(d) + h_{\mathrm{rev}}(d). \tag{E.37}$$

The primary component $h_{\mathrm{pri}}(d)$ consists of the contributions of the direct line of sight path and possible first order reflections, whereas the reverberant component $h_{\mathrm{rev}}(d)$ is the sum of many higher order reflections. For fixed $d$, we assume the two components to be independent and normal distributed random variables. More specifically,

$$h_{\mathrm{pri}}(d) \sim \mathcal{CN}\{\mu_{\mathrm{pri}}(d), G_{\mathrm{pri}}(d) - |\mu_{\mathrm{pri}}(d)|^2\}, \tag{E.38}$$

$$h_{\mathrm{rev}}(d) \sim \mathcal{CN}\{0, G_{\mathrm{rev}}(d)\}, \tag{E.39}$$

where $\mathcal{CN}\{\cdot,\cdot\}$ denotes a circular symmetric complex Normal distribution. Hence, $|h_{\mathrm{pri}}(d)|$ and $|h_{\mathrm{rev}}(d)|$ are respectively Rice and Rayleigh random variables. We assume the K-factor of the primary component to be independent of distance:

$$K_{\mathrm{p}} = \frac{|\mu_{\mathrm{pri}}(d)|^2}{G_{\mathrm{pri}}(d) - |\mu_{\mathrm{pri}}(d)|^2}. \tag{E.40}$$

Later in this section we will validate this assumption with experimental data. Consequently, $|h(d)| = |h_{\text{pri}}(d) + h_{\text{rev}}(d)|$ is Rice distributed with K-factor

$$K(d) = \frac{|\mu_{\text{pri}}(d)|^2}{G_{\text{pri}}(d) + G_{\text{rev}}(d) - |\mu_{\text{pri}}(d)|^2}. \tag{E.41}$$

Making use of (E.40) and (E.9) we obtain

$$K(d) = \frac{1 - R(d)}{\frac{1}{K_{\text{p}}} + R(d)}. \tag{E.42}$$

Fig. E.9a reports (E.42). Notice that the distance dependency in (E.42) stems solely from the distance dependent reverberation ratio. We observe that for the chosen parameter settings the graphs of $K(d)$ are close to that of its limit for $K_{\text{p}} \to \infty$

$$K_{\infty}(d) = \frac{1 - R(d)}{R(d)} \tag{E.43}$$

when $K_{\text{p}} > 20$. This special case corresponds to a non-fading primary component, for instance contributed by the sole propagation path via line of sight and no first order reflection. Further properties of $K(d)$ are stated in Appendix E.III.

The proposed model of the Rice factor can be related to similar models presented in [39] and [13]. The derivation of the model proposed in [39] relies on the following steps: i) assume $K_{\text{p}} = \infty$, ii) approximate $G_{\text{rev}}(d)$ with a distance independent term $G_{\text{rev}}$ and iii) use the definition of the reverberation distance to obtain $G_{\text{rev}} = G_{\text{pri}}(d_{\text{rl}})$. Inserting the latter term into (E.43) via (E.7) one obtains the model $K(d) = (d_{\text{rl}}/d)^n$ in [39]. Note that in [39] $n$ and $d_{\text{rl}}$ are observed to be frequency dependent. The approximation ii) may be sufficient when the reverberation time is large, such as in reverberation chambers. However, in-room environments found in office or residential buildings have typically much lower reverberation times and therefore the distance dependent onset of the reverberant component cannot be neglected. The model in [13] is similar to that in [39] except that i) it includes the directivity of the transmit antenna, ii) the expression for the effective radius (reverberation distance) obtained from reverberation theory is not inserted, and iii) $n = 2$ is used.

In Fig. E.9b and Fig. E.9c we compare estimates of $K$ to the model (E.42). These estimates are obtained from measurements made in room R3 and R4 as described in Appendix E.IV. We obtain an estimate of $K_{\text{p}}$, denoted by $\widehat{K}_{\text{p}}$, by fitting (E.42) to the estimates of $K$ using the parameters reported in Table E.3. The obtained values of $\widehat{K}_{\text{p}}$ are reported in Table E.4. The estimates of $K$ and the model (E.42) agree well in trend, except for a few outliers at approximately

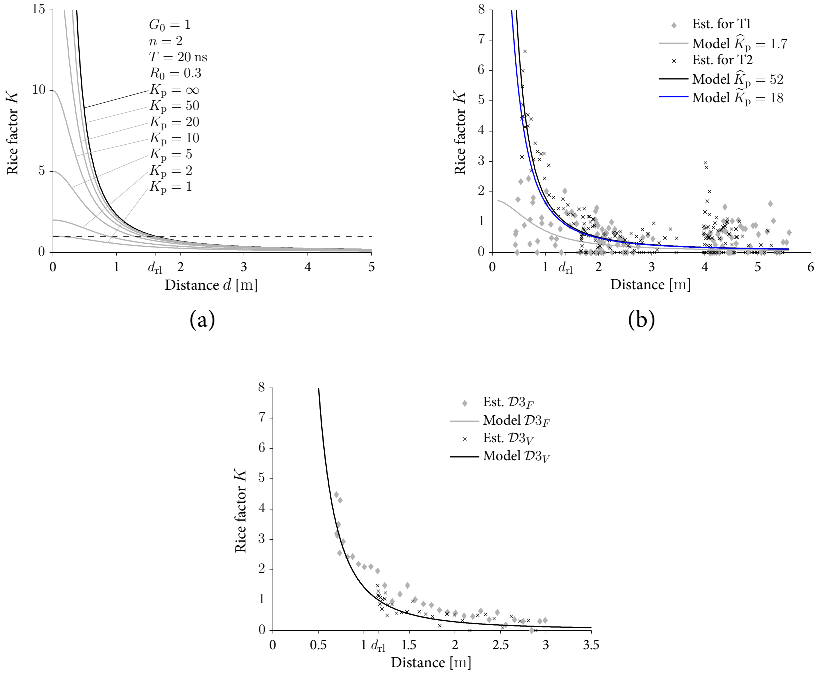

(a) (b)

(c)

*Fig. E.9: Graphs of the proposed Rice K-factor model* (E.42) *with* $K_\mathrm{p}$ *as a parameter are shown in (a). Estimated K-factors for measurement set* $\mathcal{D}4_F$ *in room R4 are shown individually for track T1 and T2 in (b). The graphs of* (E.42) *for these estimates are included too. The graphs of* (E.42) *for* $\widehat{K}_\mathrm{p} = 52$, $\widetilde{K}_\mathrm{p} = 18$, *and* $K_\mathrm{p} = \infty$ *are practically the same for the considered distance range. Estimated K-factors for the measurement sets* $\mathcal{D}3_F$ *and* $\mathcal{D}3_V$ *in room R3 are shown in (c). The graphs of* (E.42) *are also included. For the two sets the curves fall on top of each other and are practically identical to* $K_\mathrm{p} = \infty$.

*Table E.4: Estimates of* $K_\mathrm{p}$ *for room R3 and R4.*

| | R4 T1 | R4 T2 | R3 Rp6 | R3 Rp7 |
|---|---|---|---|---|
| $\widehat{K}_\mathrm{p}$ (fitting (E.42)) | 1.7 | 52 | $1.59 \times 10^5$ | $1.59 \times 10^5$ |
| $\widetilde{K}_\mathrm{p}$ (Appendix E.IV) | $0 \ldots 2$ | $10 \ldots 18$ | — | — |

4 m on track T2 in R4 where the concentration of estimates is high. Line-of-sight conditions are fulfilled at all times: However, we observe two distinct behaviors corresponding to either a large or small $\widehat{K}_\mathrm{p}$. A small value indicates that the primary component fades, which was not considered in [13, 39].

We investigate the observed differences in the values of $\widehat{K}_\mathrm{p}$ for track T1 and T2 in room R4. The analysis of the tail of the impulse responses confirms that $|h_{\mathrm{rev}}(d)|$ is Rayleigh distributed with almost identical parameters for tracks T1 and T2. We obtain estimates of $K_{\mathrm{p}}$ from $|h_{\mathrm{pri}}(d)|$ directly using a different estimation procedure detailed in Appendix E.IV. This estimator relies on the fact that the wideband data are available and returns the estimates $\widetilde{K}_{\mathrm{p}}$ for distances up to the reverberation distance. Values of $\widetilde{K}_{\mathrm{p}}$ are reported in Table E.4. In neither track, a distance dependence of $\widetilde{K}_{\mathrm{p}}$ is observed. Thus, the assumption made in (E.40) is appropriate for our measurements. The values of $\widetilde{K}_{\mathrm{p}}$ are close to $\widehat{K}_{\mathrm{p}}$ obtained from model fitting for track T1, see Table E.4. The difference between $\widetilde{K}_{\mathrm{p}}$ and $\widehat{K}_{\mathrm{p}}$ for track T2 may seem large, however, the graphs of $K(d)$ for $K_{\mathrm{p}}$ set equal to these estimates are close to each other in the used distance range as shown in Fig. E.9b. More importantly, we observe that the $\widetilde{K}_{\mathrm{p}}$ values for the two tracks diverge by one order of magnitude. This indicates that the distinct behavior of $K(d)$ for the two tracks is caused by differences in the primary components. We do not have enough data outside the reverberation region to estimate $K_{\mathrm{p}}$ for room R3.

The deviation between the estimates of $K_{\mathrm{p}}$ obtained for track T1 and T2 may be attributed to the dissimilarity of the near surroundings of the transmitter and the receiver. Track T1 runs closely along a metallic whiteboard leading to a strong first order reflection, resulting in fading of the primary component and thus in small $K_{\mathrm{p}}$ values. Track T2 runs along windows with metallic frames and metal coated glass. We expect the metal coated glass to have a lower reflection coefficient than the whiteboard, and thus $K_{\mathrm{p}}$ to be high. In room R3, the track and the receiver positions are in the center in the room. This leads at short transmitter-receiver distances to larger differences between the propagation lengths of the direct path and first order reflection paths, which in turn leads to a higher $K_{\mathrm{p}}$.

In conclusion, for modeling purposes the assumption $K_{\mathrm{p}} = \infty$ holds if the first order reflections are weak. Conversely, if strong first order reflections are present $K_{\mathrm{p}}$ should be chosen close to unity.

### E.5.2 Example 2: Model for the Discrete-time Channel Impulse Response

This example is inspired from [40], where the idea of a discrete-time model based on reverberation theory is outlined. We obtain the discrete-time model by use of (E.2)–(E.4) and (E.42). At distance $d$ the sampled impulse response of a bandlimited channel is modeled as a sequence $\{h[m]\}$ of independent random variables indexed by $m$. The sample times are chosen as $m\Delta_\tau + d/c$, thus the reference at $m = 0$ of the discrete-time grid is $d/c$. The random variables in $\{h[m]\}$ are defined as follows:

$$h[m] \sim \begin{cases} \mathcal{CN}(\mu[m], \sigma^2[m]), & m = 0, 1, 2, \dots \\ 0, \quad m < 0. \end{cases} \tag{E.44}$$

We impose the equality

$$\mathrm{E}[|h[m]|^2]\,\Delta_\tau = \int_{(m-\frac{1}{2})\,\Delta_\tau+\frac{d}{c}}^{(m+\frac{1}{2})\,\Delta_\tau+\frac{d}{c}} G(\tau,d)\,\mathrm{d}\tau\ . \tag{E.45}$$

We select $|\mu[m]|$ for $m = 0, 1, 2, \ldots$ such that the K-factor of $|\sum_m h[m]|$ equals $K(d)$ in (E.42). Similarly to (E.39), we assume $|\mu[m]| = 0$ for $m > 0$. Consequently by (E.45),

$$|\mu[0]|^2 = \frac{\frac{1}{\Delta_\tau} G(d)\,K(d)}{1+K(d)}. \tag{E.46}$$

Using (E.42) and (E.8) we obtain $|\mu[0]|$ in

$$\mu[0] = \sqrt{\frac{G_0 d_0^n}{\Delta_\tau d^n \left(1+\frac{1}{K_\mathrm{p}}\right)}}\,e^{-j\phi}, \tag{E.47}$$

where $j = \sqrt{-1}$ and the random phase $\phi$ is uniformly distributed on $[0, 2\pi)$. The variance of $h[m]$ has the form

$$\sigma^2[m] = \begin{cases} \frac{G_0}{\Delta_\tau}\left(\frac{\left(\frac{d_0}{d}\right)^n}{1+K_\mathrm{p}} + \frac{R_0}{1-R_0} e^{\frac{d_0-d}{c\,T}}\left(1-e^{-\frac{\Delta_\tau}{2\,T}}\right)\right), & \\ & m = 0 \\ \frac{2\,G_0}{\Delta_\tau}\frac{R_0}{1-R_0} e^{\frac{d_0-d}{c\,T}-\frac{m\Delta_\tau}{T}}\sinh\left(\frac{\Delta_\tau}{2\,T}\right), & m > 0. \end{cases} \tag{E.48}$$

The sampling interval $\Delta_\tau$ should be chosen such that the differences between the mean delay, rms delay spread and higher moments of the time-discrete model and (E.16), (E.20) and (E.55), respectively, are sufficiently small.

## *E.6 Conclusions*

The proposed model of the delay power spectrum of an in-room reverberant channel includes a primary component which follows an inverse distance power law ($d^{-n}$) and a reverberant component which decays exponentially versus delay and exhibits a distance dependent onset. The proposed model allows for the characterization of path gain, mean delay and rms delay spread, higher order centered moments and the kurtosis value versus distance. We obtained the moment generating function from the analytic expression of the delay power spectrum. The model was validated using measurement data. The prediction of mean delay, rms delay spread and kurtosis agrees with the respective estimates obtained from the measurement data. In the investigated environments the ratio of the reverberant component path gain to the total path gain at the reference distance of $1\ \mathrm{m}$ are 0.41 and 0.35 for room R3 and R4, respectively. Hence, the reverberant component is prominent in these environments. The observed reverberation distances are close to $1\ \mathrm{m}$ despite the line of sight condition. Thus for large portions of the room the power of the reverberant component exceeds the primary one. This surprising result may have implications on placing wireless access points in a room, radio localization using the received power, multi-link communication, interference alignment, etc.

The estimated path gain exponent of the primary component in the proposed model is close to the free-space path gain exponent for one data set. Due to its inability to separate the primary component from the reverberant component the one-slope path gain model yields path gain exponents close to 1.1. The one-slope path gain model merely provides a fit of the path gain that blends the contributions from the primary and reverberant component. As a consequence it gives different results for the same environment but different measurement locations.

We presented two applications of the proposed model. The first application is a model for the distance dependent Rice factor. The model is in good agreement with the experimental data. We observe two distinct behaviors, both of which are covered by the model: Either the magnitude of the primary component is practically deterministic, or it is Rayleigh fading. The second application is a discrete-time model which allows for the simulation of impulse responses that depend on distance.

## E.I Impulse Response Model Relations

In (E.1) we define the delay power spectrum as the expectation of the magnitude squared impulse response. We propose to split the delay power spectrum into a primary and reverberant component. In the following we show that under certain assumptions this can be directly mapped into splitting the impulse response into a primary and reverberant component.

$$\begin{aligned} G(\tau, d) &= \mathrm{E}[|h_{\mathrm{pri}}(\tau, d) + h_{\mathrm{rev}}(\tau, d)|^2], && \text{(E.49)} \\ &= \mathrm{E}[|h_{\mathrm{pri}}(\tau, d)|^2] + \mathrm{E}[|h_{\mathrm{rev}}(\tau, d)|^2] \\ &\quad + \mathrm{E}[h_{\mathrm{pri}}(\tau, d)\, h^*_{\mathrm{rev}}(\tau, d)] + \mathrm{E}[h^*_{\mathrm{pri}}(\tau, d)\, h_{\mathrm{rev}}(\tau, d)], && \text{(E.50)} \\ &= G_{\mathrm{pri}}(\tau, d) + G_{\mathrm{rev}}(\tau, d) && \text{(E.51)} \end{aligned}$$

The cross terms $\mathrm{E}[h_{\mathrm{pri}}(\tau, d)\, h^*_{\mathrm{rev}}(\tau, d)]$ and $\mathrm{E}[h^*_{\mathrm{pri}}(\tau, d)\, h_{\mathrm{rev}}(\tau, d)]$ are assumed to be zero.

## E.II Derivation of Normalized Centered Moment Generating Function and Kurtosis

The centered moment generating function for (E.2) reads

$$M(x,d) = \frac{1}{G(d)} \int e^{x(\tau-\mu_\tau(d))} G(\tau,d) \,\mathrm{d}\tau. \tag{E.52}$$

The $k$th order centered moment is obtained by taking the $k$th derivative of $M(x,d)$ and evaluating at $x = 0$. By Leibnitz's rule and evaluating the $k^{\text{th}}$ derivative at $x = 0$ we have

$$\begin{aligned}\tfrac{\mathrm{d}^k}{\mathrm{d}^k x} M(0,d) = \tfrac{G_0}{G(d)} \Big( \left(\tfrac{d}{c} - \mu_\tau(d)\right)^k \left(\tfrac{d_0}{d}\right)^n \\ + \tfrac{R_0}{1-R_0} e^{\frac{d_0-2d+\mu_\tau(d)}{c\,T}} T^k \Gamma\left(k+1, \tfrac{d-c\mu_\tau(d)}{c\,T}\right)\Big),\end{aligned} \tag{E.53}$$

where $\Gamma(s,x)$ is the upper incomplete gamma function for positive integers $s$ [27]:

$$\Gamma(s,x) = (s-1)!\, e^{-x} \sum_{k=0}^{s-1} \frac{x^k}{k!}. \tag{E.54}$$

Inserting for $\mu_\tau$ the normalized $k^{\text{th}}$ centered moment generating function reads

$$\begin{aligned}\mu_k(d) &= \tfrac{\mathrm{d}^k}{\mathrm{d}^k x} M(0,d) \\ &= R(d)\, T^k \Big[ (-1)^k \left(R^{k-1}(d) - R^k(d)\right) \\ &\qquad + e^{-R(d)} \Gamma(k+1, -R(d)) \Big].\end{aligned} \tag{E.55}$$

The kurtosis in (E.23) thus reads

$$\kappa(d) = R^{-1}(d) \frac{R^3(d) - R^4(d) + e^{-R(d)}\Gamma(5,-R(d))}{\left[R(d) - R^2(d) + e^{-R(d)}\Gamma(3,-R(d))\right]^2}. \tag{E.56}$$

## E.III Further Properties of $K(d)$

From the properties of $R(d)$ (see Section E.2.2) it follows that

$$\lim_{d\to 0} K(d) = K_{\mathrm{p}}, \qquad \lim_{d\to\infty} K(d) = K_{\mathrm{p}} \tag{E.57}$$

and

$$K(d) \geq \frac{1 - R(d_{\max})}{\frac{1}{K_{\mathrm{p}}} + R(d_{\max})} \geq 0. \tag{E.58}$$

The special case $K(d_{\max}) = K(d) = 0$ occurs only for $R(d_{\max}) = 1$. At the boundaries of the reverberation region, $R(d_{\mathrm{rl}}) = R(d_{\mathrm{ru}}) = \frac{1}{2}$, and thus

$$K(d_{\mathrm{rl}}) = K(d_{\mathrm{ru}}) = \frac{1}{1 + \frac{2}{K_{\mathrm{p}}}}. \tag{E.59}$$

## *E.IV Estimation of $K(d)$ and $K_{\mathrm{p}}$*

For the estimation of the Rice factor $K(d)$ we use the averaged measured frequency response $\widehat{H}_{m,r,p,q}[f]$, see Section E.3.2. We collect $|\widehat{H}_{m,r,p,q}[f]|$ for all receive antennas $m$ and ten consecutive transmitter positions $p$ on track $q$, for a specific receiver position $r$ into one data set. We apply the method of moments [41] on this data set to compute an estimate $\widehat{K}$ of the Rice factor. As in [41] we set $\widehat{K} = 0$ when the ratio of the first and second moment of the experimental data is below the theoretical value obtained for $K = 0$. Ten consecutive transmitter positions span approximately 1.6 wavelengths. Accordingly, the transmitter-receiver distance is measured from the center of the circular array to the mean of the ten positions.

The estimation of $K_{\mathrm{p}}$ is done differently: We consider all impulse responses obtained from the eight receive antennas for transmitter positions at a distance to the transmitter within an interval of length 0.15 $\mathrm{m}$. We select in each of these impulse responses the sample at the delay value closest to $d/c$. These samples are used to estimate $K_{\mathrm{p}}$. To check for distance dependency of $K_{\mathrm{p}}$ we limit the interval length to 0.15 $\mathrm{m}$. We slide the distance interval in 1 $\mathrm{cm}$ steps from the shortest available transmitter-receiver distance up to the reverberation distance $d_{\mathrm{rl}}$ to check for distance dependency of $K_{\mathrm{p}}$.

## *References*

[1] H. Liu, H. Darabi, P. Banerjee, and J. Liu, “Survey of Wireless Indoor Positioning Techniques and Systems,” *IEEE Trans. Syst., Man, Cybern. C*, vol. 37, no. 6, pp. 1067–1080, Nov. 2007.

[2] H. Hashemi, “The Indoor Radio Propagation Channel,” *Proc. IEEE*, vol. 81, no. 7, pp. 943–968, July 1993.

[3] J. Keenan and A. Motley, “Radio coverage in buildings,” in *Br. Telecom Technol. J.*, vol. 8, no. 1, Jan. 1990, pp. 19–24.

[4] E. Damosso, Ed., *Digital mobile radio towards future generation systems: Cost 231 Final Report*. Bruxelles, Belgium: European Commission, 1999.

[5] R. Vaughan and J. B. Andersen, *Channels, Propagation and Antennas for Mobile Communications*. Institution of Engineering and Technology, Feb. 2003.

[6] P. Nobles and F. Halsall, "Indoor Propagation at 17 GHz and 60 GHz – Measurements and Modelling," in *Antennas and Propagation, 1999. IEE National Conference on.*, Mar. 1999, pp. 93–96.

[7] D. Xu, J. Zhang, X. Gao, P. Zhang, and Y. Wu, "Indoor Office Propagation Measurements and Path Loss Models at 5.25 GHz," *Vehicular Technology Conference, 2007. VTC-2007 Fall. 2007 IEEE 66th*, pp. 844–848, 30 Sept. - 3 Oct. 2007.

[8] J. Kunthong and C. Bunting, "A Novel Hybrid Propagation Model," in *IEEE International Symposium Antennas and Propagation Society (AP-S)*, July 2008, pp. 1–4.

[9] C. Holloway, M. Cotton, and P. McKenna, "A model for predicting the power delay profile characteristics inside a room," *IEEE Trans. Veh. Technol.*, vol. 48, no. 4, pp. 1110–1120, 1999.

[10] R. Rudd, "Statistical prediciton of indoor radio channel impulse response," Ph.D. dissertation, University of Surrey, Sept. 2007.

[11] J. Andersen, J. Nielsen, G. Pedersen, G. Bauch, and J. Herdin, "Room electromagnetics," *IEEE Antennas Propag. Mag.*, vol. 49, no. 2, pp. 27–33, 2007.

[12] J. Nielsen, J. Andersen, G. Pedersen, and M. Pelosi, "On Polarization and Frequency Dependence of Diffuse Indoor Propagation," in *Vehicular Technology Conference, 2011 IEEE 74th*, Sept. 2011.

[13] D. A. Hill, *Electromagnetic Fields in Cavities: Deterministic and Statistical Theories*, ser. IEEE Press Series on Electromagnetic Wave Theory. Piscataway, NJ: Wiley/IEEE Press, 2009.

[14] H. Kuttruff, *Room Acoustics*, 4th ed. London: Taylor & Francis, 2000.

[15] J. Kunisch and J. Pamp, "Measurement Results and Modeling Aspects for the UWB Radio Channel," *Ultra Wideband Systems and Technologies, 2002. Digest of Papers. 2002 IEEE Conf. on*, pp. 19–23, 2002.

[16] V. Erceg, D. Michelson, S. Ghassemzadeh, L. Greenstein, J. Rustako, A.J., P. Guerlain, M. Dennison, R. Roman, D. Barnickel, S. Wang, and R. Miller, "A Model for the Multipath Delay Profile of Fixed Wireless Channels," *IEEE J. Sel. Areas Commun.*, vol. 17, no. 3, pp. 399–410, Mar. 1999.

[17] G. Steinböck, T. Pedersen, B. Fleury, W. Wang, T. Jost, and R. Raulefs, "Model for the Path Loss of In-room Reverberant Channels," in *Vehicular Technology Conference, 2011 IEEE 73rd*, May 2011, pp. 1–5.

[18] R. Bultitude, P. Melancon, H. Zaghloul, G. Morrison, and M. Prokki, "The Dependence of Indoor Radio Channel Multipath Characteristics on Transmit/Receiver Ranges," *IEEE J. Sel. Areas Commun.*, vol. 11, no. 7, pp. 979–990, Sept. 1993.

[19] J. McDonnell, T. Spiller, and T. Wilkinson, "Characterization of the Spatial Distribution of RMS Delay Spread in Indoor LOS Wireless Environments at 5.2 GHz," in *IEEE International Symposium on Personal, Indoor and Mobile Radio Communications (PIMRC)*, vol. 2, Sept. 1998, pp. 621–624.

[20] ITU-R, "Recommendation ITU-R P.1407-4 (10/2009): Multipath propagation and parameterization of its characteristics," Nov. 2009.

[21] R. E. Richardson, "Reverberant Microwave Propagation," Naval Surface Warfare Center, Dahlgreen Division, Tech. Rep. NSWCDD/TR-08/127, Oct. 2008.

[22] J. Khodjaev, Y. Park, and A. Saeed Malik, "Survey of NLOS identification and error mitigation problems in UWB-based positioning algorithms for dense environments," *Annals of Telecommunications*, vol. 65, pp. 301–311, 2010.

[23] L. Mucchi and P. Marcocci, "A new UWB indoor channel identification method," in *Cognitive Radio Oriented Wireless Networks and Communications, 2007. CrownCom 2007. 2nd International Conference on*, Aug. 2007, pp. 58–62.

[24] F. Montorsi, F. Pancaldi, and G. M. Vitetta, "Statistical Characterization and Mitigation of NLOS Bias in UWB Localization Systems," in *NEWCOM++ / COST 2100 Joint Workshop on Wireless Communications*, Paris, France, 1-2 Mar. 2011.

[25] S. Maranò, W. Gifford, H. Wymeersch, and M. Win, "NLOS Identification and Mitigation for Localization Based on UWB Experimental Data," *IEEE J. Sel. Areas Commun.*, vol. 28, no. 7, pp. 1026–1035, Sept. 2010.

[26] Z. Xiao, Y. Hei, Q. Yu, and K. Yi, "A survey on impulse-radio uwb localization," *SCIENCE CHINA Information Sciences*, vol. 53, pp. 1322–1335, 2010.

[27] M. Abramowitz and I. Stegun, *Handbook of mathematical functions: with formulas, graphs, and mathematical tables*. Dover Publications, 1965.

[28] R. M. Corless, G. H. Gonnet, D. E. G. Hare, D. J. Jeffrey, and D. Knuth, "On the Lambert W function," *Advances in Computational Mathematics*, vol. 5, no. Apr., pp. 329–359, 1996.

[29] K. Siwiak, H. Bertoni, and S. Yano, "Relation between multipath and wave propagation attenuation," *IET Electron. Lett.*, vol. 39, no. 1, pp. 142–143, Jan. 2003.

[30] N. Alsindi, B. Alavi, and K. Pahlavan, "Measurement and Modeling of Ultrawideband TOA-Based Ranging in Indoor Multipath Environments," *IEEE Trans. Veh. Commun.*, vol. 58, no. 3, pp. 1046–1058, Mar. 2009.

[31] C. Holloway, D. Hill, J. Ladbury, and G. Koepke, "Requirements for an Effective Reverberation Chamber: Unloaded or Loaded," *IEEE Trans. Electromagn. Compat.*, vol. 48, no. 1, pp. 187–194, Feb. 2006.

[32] M. Awad, K. Wong, and Z. bin Li, "An Integrated Overview of the Open Literature's Empirical Data on the Indoor Radiowave Channel's Delay Properties," *IEEE Trans. Antennas Propag.*, vol. 56, no. 5, pp. 1451–1468, May 2008.

[33] G. Steinböck, T. Pedersen, and W. Wang, "AAU-DLR 2010 Indoor Measurement Campaign – Measurements for Validation of Models for Reverberant and Cooperative Channels," AAU and DLR," Report, 2011.

[34] J. Stephan, Y. Lostanlen, J. Keignart, W. Wang, D. Slock, and F. Kaltenberger, "Measurements of location-dependent channel features," ICT- 217033 WHERE, Deliverable 4.1, Oct. 2008, http://www.ict-where.eu/.

[35] Huber+Suhner, "Datasheet for Sencity Antenna For In-Carriage Wireless Communication, Type: SOA 5600/360/3/20/V_1," Document No. 01.02.1358, May 2007.

[36] Mathworks, "Matlab Curve Fitting Toolbox, Version 1.2.2 (r2008b)," 2008.

[37] A. Bamba, W. Joseph, D. Plets, E. Tanghe, G. Vermeeren, L. Martens, J. Andersen, and J. Nielsen, "Assessment of reverberation time by two measurement systems for room electromagnetics analysis," in *IEEE International Symposium on Antennas and Propagation (APSURSI)*, July 2011, pp. 3113–3116.

[38] J. Kunisch and J. Pamp, "An Ultra-Wideband Space-Variant Multipath Indoor Radio Channel Model," *Proc. IEEE 2006 Int. Conf. on Ultra-Wideband*, pp. 290–294, 16-19 Nov. 2003.

[39] Y. Lustmann and D. Porrat, "Indoor Channel Spectral Statistics, K-Factor and Reverberation Distance," *IEEE Trans. Antennas Propag.*, vol. 58, no. 11, pp. 3685–3692, Nov. 2010.

[40] J. B. Andersen, J. O. Nielsen, G. Bauch, and M. Herdin, "The large office environment - measurement and modeling of the wideband radio channel," in *Proc. IEEE 17th Int. Symposium on Personal, Indoor and Mobile Radio Commun. PIMRC 2006*, 2006, pp. 1–5.

[41] K. K. Talukdar and W. D. Lawing, "Estimation of the parameters of the Rice distribution," *J. Acoust. Soc. Am.*, vol. 89, no. 3, pp. 1193–1197, Mar. 1991.

Paper **F**

# Channel Measurements and Characteristics for Cooperative Positioning Applications

Wei Wang, Gerhard Steinböck, Thomas Jost, Troels Pedersen, Ronald Raulefs, and Bernard H. Fleury

*IEEE International Conference on Localization and GNSS, 2012*

© 2012 IEEE

*The layout has been revised.*

## *Abstract*

We have conducted an indoor channel measurement campaign to characterize the propagation channel for the development of cooperative positioning algorithms. The campaign focused particularly on the characteristics of multi-link channels with applications to positioning. In this contribution we present the measurement campaign and preliminary results on correlation characteristics of the received power. It is observed that the link-pair log power is uncorrelated. Moreover, the received log power can be modeled by realizations of independent Gaussian distributions for each link, based on the measured results.

## *F.1 Introduction*

Cooperative positioning for indoor scenarios has gained much interest in past years. Such techniques rely on measuring and exchanging ranging and related information between terminals in cooperative communication networks [1] [2] [3]. In a cooperative network, anchor terminals at known positions are used to identify unknown positions of the mobile terminals given observations of ranges of a set of links as shown in Fig. F.1. The estimated positions of mobile terminals are used to help and improve the position estimation of other mobile terminals. For each link, range observations can be obtained from different distance related channel features, e.g., the received signal strength indicator (RSSI) of the radio channel [4]. Thus knowledge of the relationship between range and radio channel features is a prerequisite for cooperative positioning in communication networks.

According to the survey [5], several works on channel characterization for cooperative communication scenarios have recently appeared. Models of the received power reported in [6, 7] consider large scale fading in cooperative networks. They may be used to study positioning methods relying on RSSI observations. However, these investigations of cooperative channels for communications focus on aspects where the relation to link ranges is less relevant. Consequently, many of these contributions lack the accuracy in the description of the link geometry necessary for indoor positioning purposes.

In the present contribution we characterize the received power for cooperative positioning. The characterization is obtained based on an indoor channel measurement campaign conducted at the German Aerospace Center (DLR) facilities. The measurements were performed with a purpose-built measurement platform allowing for accurate transceiver position information during the quasi-static measurement.

We introduce a multi-link signal model for the log power in Section F.2 and present the measurement campaign in Section F.3. Post processing the measurements as outlined in Section F.4 provides the results in Section F.5.

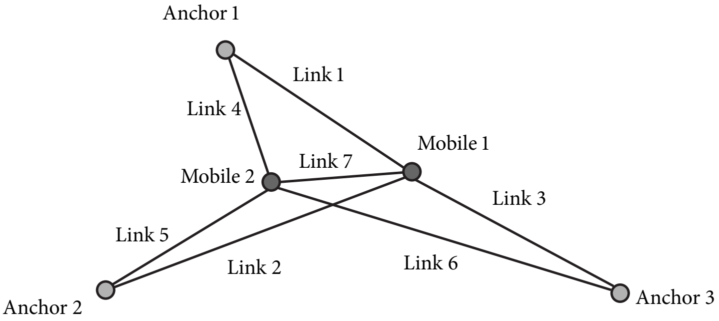

*Fig. F.1: The considered cooperative scenario with anchors and mobiles at known and unknown positions respectively. The position of each mobile is estimated based on range dependent radio channel observations of its links in the network.*

The results indicate that the log power values are Gaussian with low correlation between links. Based on these observations we propose to model the log power of the links as independent Gaussian random variables with the mean following a path loss model such as [4, 8].

## F.2 Multi-link Model for Positioning

We consider the scenario in Fig. F.1 with several anchor terminals and mobile terminals. Both anchor-to-mobile and mobile-to-mobile links are considered. Let $P_\ell$ denote the received log power of link $\ell$ after averaging out the fast fading due to multi-path propagation.[1] We consider $P_\ell$ as a random variable with mean $\mu_\ell$. We rewrite $P_\ell = \mu_\ell + R_\ell$ where the residual $R_\ell$ is a zero mean random variable. The observations from all $L$ links can be expressed in vector form as

$$\mathbf{P} = \boldsymbol{\mu} + \mathbf{R}, \tag{F.1}$$

with $\mathbf{P} = [P_1, \ldots, P_\ell, \ldots, P_L]^T$ and vectors $\boldsymbol{\mu}$ and $\mathbf{R}$ defined similarly. The mean power $\boldsymbol{\mu}$ can be expressed via an appropriate path loss model [4, 8]. However, in this work we do not consider a specific path loss model. The residual may include deviations from the mean power due to the environment and the locations of the anchors and mobile nodes in the environment. In practical settings, $\mathbf{R}$ also includes estimation errors of an RSSI estimator. In this contribution we do not consider the mean power but focus on the second order characterization of $\mathbf{R}$ jointly for all links. The covariance matrix of $\mathbf{R}$ and thus of $\mathbf{P}$ is denoted as

$$\boldsymbol{\Sigma} = \mathrm{cov}(\mathbf{R}) = E\{\mathbf{R}\mathbf{R}^T\}, \tag{F.2}$$

---

[1] This averaging can be done in practical implementations in the spatial and/or frequency domain.

*Table F.1: Channel sounder settings.*

| Parameter | Value |
|---|---|
| RF centre frequency | 5.2 GHz |
| Bandwidth | 120 MHz |
| Number of sub-carriers | 1537 |
| Sub-carrier spacing $\Delta f$ | 78.125 kHz |
| Transmit power | 1 mW |
| Signal period | 12.8 $\mu$s |
| Number of snapshots per block | 20 |
| Block repetition rate | 131.072 ms |
| Transmitter antenna | Omni-directional (V-polarized) |
| Receiver antenna | 8-element UCA (V-polarized) |
| Train speed | $0.074 \pm 0.01$ m/s |

where $E\{\cdot\}$ is the expectation operator. The correlation coefficient matrix obtained by normalizing $\boldsymbol{\Sigma}$ as

$$\boldsymbol{\rho} = \boldsymbol{D}_{\boldsymbol{\Sigma}}^{-1/2}\,\boldsymbol{\Sigma}\,\boldsymbol{D}_{\boldsymbol{\Sigma}}^{-1/2}, \tag{F.3}$$

where $\boldsymbol{D}_{\boldsymbol{\Sigma}}$ is a diagonal matrix with the same diagonal entries as $\boldsymbol{\Sigma}$. It is worth to note that $\boldsymbol{\Sigma}$ can be recovered if $\boldsymbol{D}_{\boldsymbol{\Sigma}}$ and $\boldsymbol{\rho}$ are known.

## F.3 Channel Measurement Campaign

The measurements were conducted with a MEDAV RUSK broadband channel sounder at the premises of the German Aerospace Center (DLR). The parameter setup of the channel sounder is summarized in Table F.1. A wideband signal, more specifically a multitone, was sent by the transmitter. The single transmit antenna depicted on the left side of Fig. F.2 was mounted on the top of a railway model which was running along a track, see Fig. F.3. The receiver was equipped with an 8-element uniform circular array (UCA) as visualized on the right side of Fig. F.2. Both the transmit and receive antennas were vertically polarized. In a snapshot all eight channel frequency responses are sequentially measured. The sounder was operating in "block" mode. In each block 20 consecutive snapshots are performed. The block period is 131.072 ms. The transmitting antenna mounted on the model train shown on the left side of Fig. F.2 moved with a speed of about 0.074 m/s. Thus from block to block the transmitter moved approximately 7.8 mm or 0.14 wavelengths. From snapshot to snapshot within a block the transmitter moved approximately $2 \times 10^{-4}$ wavelengths.

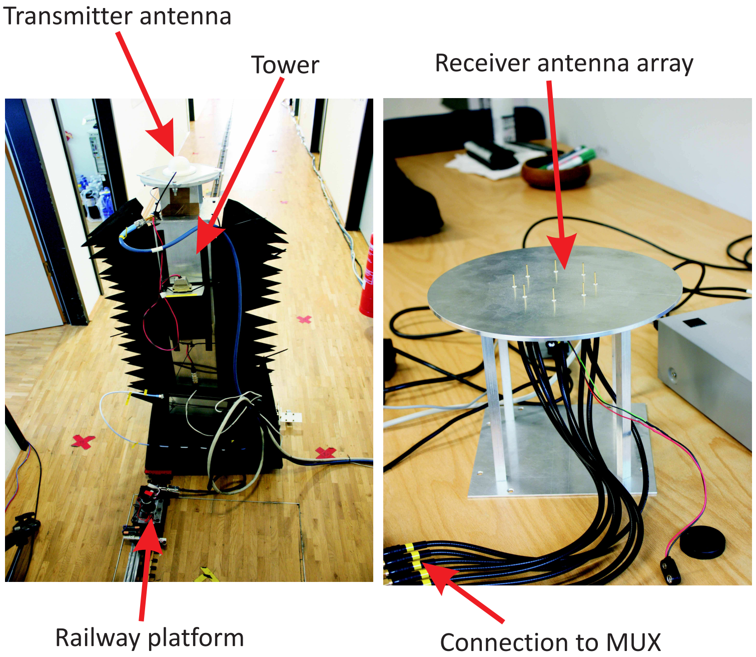

*Fig. F.2: Measurement setup with the used antennas.*

The center position of the receiver array was precisely determined using a tachymeter giving a nominal accuracy in the sub-cm domain. To get a similar accuracy for the transmitter antenna, we run the model train by a cogwheel. The motor of the train is equipped with a rotary encoder which generates 500 impulses per motor turn. This results in a precise measurement of the traveled distance along the track for each captured channel transfer function. More details of the hardware setup can be found in [9].

The experimentally investigated indoor environment is depicted in Fig. F.3 and described in [10]. The receiver array was placed at positions labeled from Rp1 to Rp9. The receivers at those locations may act as anchor nodes and/or mobile nodes while the transmitter was running on tracks T1, T2 and T3. Moreover, the receiver array was also located at 5 positions on track T1 and T2 while the transmitter was running on track T2 and T1 respectively. The corresponding locations are labeled from T1Rp1 to T1Rp5 and T2Rp1 to T2Rp5. In this contribution we only focus on the measurements with the transmitter moving on track T1 and the receivers located in room R4.

As the hardware setup allows only single link measurements, we alternatively measure the links sequentially, one by one. By using the high positioning accuracy of the measurement platform, we are able to associate and group the measured channel transfer functions to link-pairs. This data association

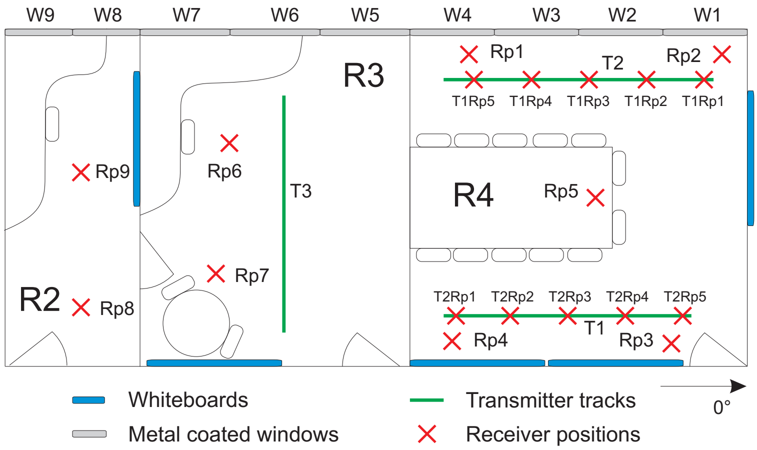
W9
W8
W7
W6
W5
W4
W3
W2
W1
R3
Rp1
T2
Rp2
T1Rp5
T1Rp4
T1Rp3
T1Rp2
T1Rp1
Rp9
Rp6
T3
R4
Rp5
Rp7
R2
Rp8
T2Rp1
T2Rp2
T2Rp3
T2Rp4
T2Rp5
T1
Rp4
Rp3
Whiteboards
Metal coated windows
Transmitter tracks
Receiver positions
0°

*Fig. F.3: Overview of the measured indoor environment.*

is addressed in Section F.4 in more details. During the measurement time, no persons were inside the room and the door was closed to keep the environment as stable as possible.

## F.4 Data Processing

The channel transfer function can be assumed as constant within each block due to the high measurement rate. This allows to reduce the noise floor by averaging the measured transfer functions within a block. The average channel transfer function recorded from link $\ell$ with receive antenna $m$ at subcarrier $f$ within block $b$ is denoted by $H_{\ell,m}(b, f)$, where $f = 0, \ldots, N-1$.

### F.4.1 Data Association

The experimental data was obtained by sequentially measuring the links one by one in a quasi-static environment. Thus, to emulate a multi-link scenario for a particular transmitter position we would consider the single link data obtained at that position. This, however, can be done only approximately, because the measurements were taken with a fixed time grid and a varying train velocity. In this work we consider the displacement along the track of the transmitter. Fig. F.4 visualizes the transmitter displacement as a function of the block time index. We only consider the measurement data collected when the train was moving and discard the measurement data collected in the beginning and end of the track when the train was stationary. We observe different slopes of the lines, indicating a difference in the train velocity

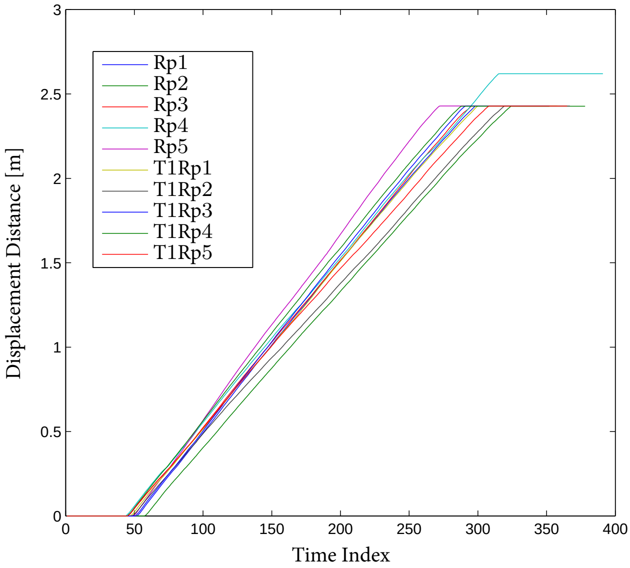

*Fig. F.4: Displacement along track T1 for the measurements.*

for each measured link. The displacement along track T1 for adjacent time indices is approximately 1 cm.

For each link $\ell$ we measured $B_\ell$ blocks of channel transfer functions at the corresponding displacement distances $d_{1,\ell}, \dots, d_{B_\ell,\ell}$ . We choose as the displacement reference for a given track the displacement of link $\widehat{\ell}$ where the train was moving the fastest on this track. This fastest run results in a minimum number of measured blocks. For block $i \in \{1, \dots, B_{\widehat{\ell}}\}$ with the reference displacement $d_{i,\widehat{\ell}}$ we seek the block with index $b_\ell(i)$ which is recorded closest to the reference displacement; ie.

$$b_\ell(i) = \arg\min_j ||d_{i,\widehat{\ell}} - d_{j,\ell}||, \qquad \ell = 1, \dots, L. \tag{F.4}$$

For block index $i$ we assign the average displacement $d_i$ calculated as

$$d_i = \frac{1}{L} \sum_{\ell=1}^{L} d_{b_\ell(i),\ell}. \tag{F.5}$$

The displacement $d_i$ corresponds to the average of matched displacement distances of the links between a transmitter position and all $L$ receiver antenna array positions. The cumulative distribution of the displacement errors $(d_i - d_{b_\ell(i),\ell})$ are shown in Fig. F.5. The error is almost uniformly distributed over $\pm 5$ mm.

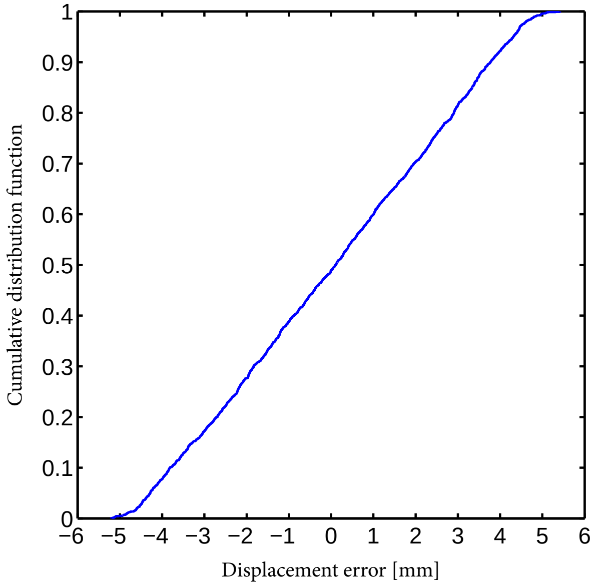

*Fig. F.5: Cumulative distribution function of displacement errors.*

### *F.4.2 Estimation of Power, Residual and Correlation Coefficients*

The log of the averaged received power at the $\ell$-th link and position $d$ is obtained by averaging in the frequency domain and spatial domain (8-elements of the receiver array) as

$$\widehat{P}_\ell(d) = 10\log_{10}\left(\frac{1}{8\,N}\sum_{m=1}^{8}\sum_{f=0}^{N-1}|H_{\ell,m}(d,f)|^2\right) \quad [\mathrm{dB}]\,. \tag{F.6}$$

In this contribution the estimate of the mean power $\widehat{\mu}_\ell(d)$ at $d$ is obtained by averaging the corresponding $\widehat{P}_\ell(d)$ within a sliding window size of approximately 42 cm. This window size corresponds to estimates of 41 blocks, centered at position $d$. We collect the estimates $\widehat{P}_\ell(d)$ and $\widehat{\mu}_\ell(d)$ for all links and positions in matrices $\widehat{\mathbf{P}} \in \mathbb{R}^{L\times B_{\widehat{\ell}}}$ and $\widehat{\boldsymbol{\mu}} \in \mathbb{R}^{L\times B_{\widehat{\ell}}}$ respectively. The estimated residual reads

$$\widehat{\mathbf{R}} = \widehat{\mathbf{P}} - \widehat{\boldsymbol{\mu}}. \tag{F.7}$$

The covariance matrix is estimated from $\widehat{\mathbf{R}}$ by averaging over all positions $d$ as

$$\widehat{\boldsymbol{\Sigma}} = \frac{1}{B_{\widehat{\ell}}}\widehat{\mathbf{R}}\widehat{\mathbf{R}}^T. \tag{F.8}$$

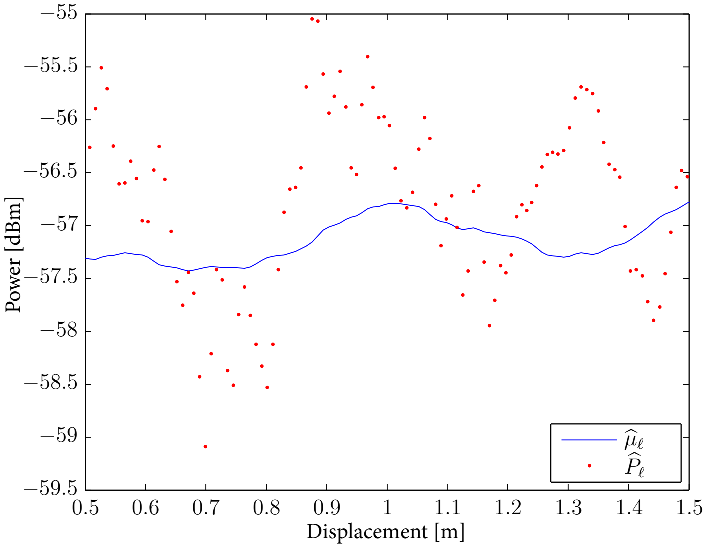

*Fig. F.6: Measured power at Rp2 versus displacement. The mean power computed using the sliding window of length 42* cm *is also reported.*

By insertion of $\widehat{\boldsymbol{\Sigma}}$ in Eq. (F.3) we obtain the estimate of $\widehat{\boldsymbol{\rho}}$.

## F.5 Results

We make the assumption that the displacement errors after the data association do not effect the evaluation of $\widehat{\boldsymbol{\Sigma}}$. To validate this, we evaluate the correlation coefficient of the residual from adjacent blocks which are approximately 1 cm spaced. The calculation is performed similar as Eq. (F.8) except that the correlation coefficients are computed for adjacent blocks instead of different links. The estimates of the adjacent block correlation coefficients range from 0.7 to 0.9 for the different links and the average is 0.82. Fig. F.6 shows an example of the power measured at Rp2 versus the displacement. The appearance of this plot once more confirms the assumption of highly correlated neighboring samples.

The correlation coefficients of the experimental residual log power values of any two links are reported in Fig. F.7. The magnitude of the correlation coefficients ranges from 0.0 to 0.4 with an average of 0.14. This result confirms the weak correlation of large scale fading observed in a cooperative communication setting in [7]. The standard deviations of the log power residuals for the different links obtained as the square root of the diagonal entries (listed in Fig. F.7) of $\widehat{\boldsymbol{\Sigma}}$ range from 0.65 to 0.85. Further investigation of the

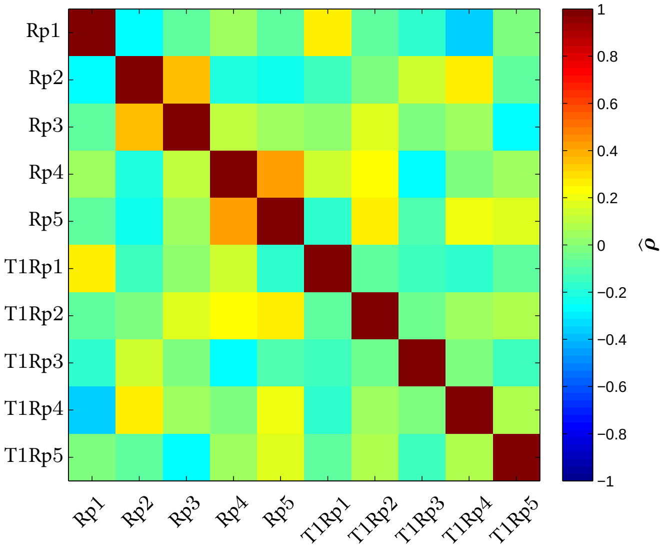

*Fig. F.7: Link-pair correlation coefficient* $\widehat{\boldsymbol{\rho}}$. *The values along the main diagonal of* $\widehat{\boldsymbol{\Sigma}}$ *are* 0.67, 0.72, 0.43, 0.72, 0.69, 0.67, 0.52, 0.53, 0.54, *and* 0.43.

correlation coefficients can be performed with scatter plots of the residuals from different links as shown in Fig. F.9. The figure shows only the results of link-pairs among T1Rp1 to T1Rp5. The other link-pairs have similar scatter plots. These scatter plots confirm that there is no strong link-level correlation. We remark that the adjacent spacing of points from T1Rp1 to T1Rp5 is 0.5 m. Even those rather closely spaced receivers show no correlation of the power residual.

The Quantile-Quantile plot of the power residual $\widehat{\mathbf{R}}$ versus a Gaussian probability density function with mean of $-0.01$ and standard deviation of 0.77 estimated from $\widehat{\mathbf{R}}$ is presented in Fig. F.8. The good fit in Fig. F.8 suggests to model the residuals as Gaussian random variables.

The scatter plot of residuals versus the true range is shown in Fig. F.10. We observe no range dependency of the residuals variance obtained along track T1. However, the residuals variance obtained along track T2, not shown here, indicates a distance dependency for ranges below 1.5 m but similarly as in track T1 no range dependency above 1.5 m.

Based on our signal model we propose an interim model for the received log power as

$$\mathbf{P} \sim \mathcal{N}(\boldsymbol{\mu}, \boldsymbol{\Sigma}), \tag{F.9}$$

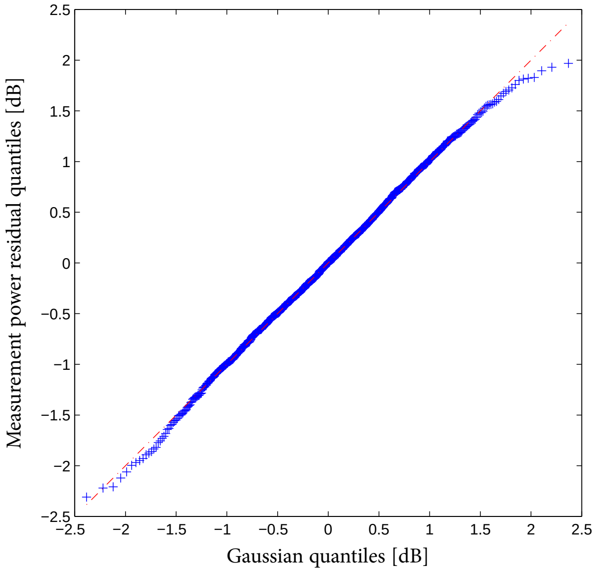

*Fig. F.8: Quantile-Quantile plot of the measured residual samples versus the Gaussian quantiles.*

where $\boldsymbol{\mu}$ can be obtained from a path loss model [4, 8] and the covariance matrix $\mathbf{\Sigma}$ is diagonal:

$$\mathbf{\Sigma} = \begin{bmatrix} \sigma_1^2 & & 0 \\ & \ddots & \\ 0 & & \sigma_L^2 \end{bmatrix}. \tag{F.10}$$

Due to the small observed variations in $\widehat{\mathbf{\Sigma}}$ for $\sigma_1^2$ to $\sigma_L^2$ we propose the approximation $\mathbf{\Sigma} \approx \sigma^2 \, \mathbf{I}$, where $\mathbf{I}$ is the identity matrix and $\sigma$ is the sample mean of $\sigma_1^2$ to $\sigma_L^2$ of $\widehat{\mathbf{\Sigma}}$. Thus $R_1, \ldots, R_L$ are approximated as i.i.d. Gaussian random variables.

## F.6 Conclusion and Outlook

The proposed data association method allows to convert the single link measurements into virtual multi-link measurements. We show that for the used measurement platform, the conversion approach is accurate enough to characterize the received powers of multi-link channels.

The presented results obtained from measurements collected in an in-room environment show only insignificant correlation between the log power

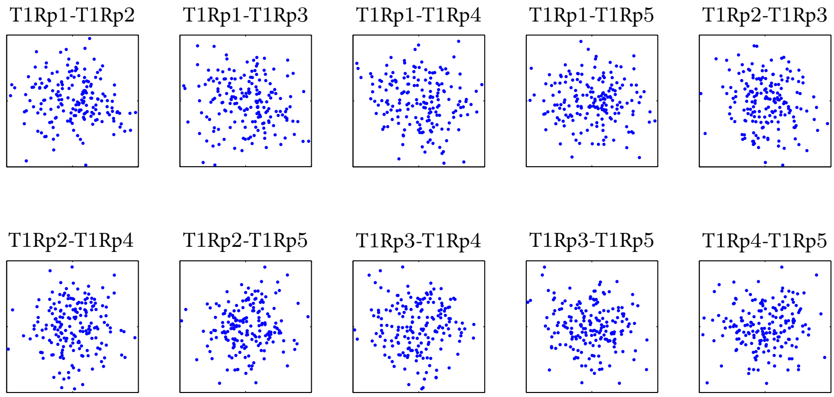

*Fig. F.9: Scatter plot of link-pair power residuals. The horizontal (vertical) component of any point represents the residual of the first (second) link given by the title and measured at the same displacement. The considered range is* $[-2, 2]$ *dB.*

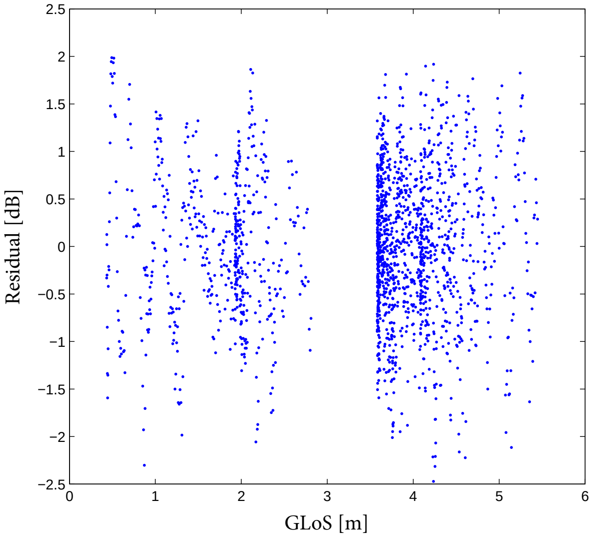

*Fig. F.10: Scatter plot of power residuals versus the geometric line of sight (GLoS).*

values of different links. This is in accordance with the observations in [7]. We observe the log power values to be Gaussian distributed with a range dependent mean. The behavior of the mean versus range can be described according to a path loss model. In the presented results the variance of the log power values appeared to be constant with range. However, preliminary results of another measurement, exhibited an increasing variance with range up to 1.5 m and appeared to be constant above. Further investigations are needed to provide a deeper insight into this phenomenon and to characterize the typical behavior of the variance.

## Acknowledgment

This work was founded by the European Community's project Wireless Hybrid Enhanced Mobile Radio Estimators 2 (WHERE2). It was also conducted within the frame work of COST IC1004. The authors would like to thank Siwei Zhang for his support during the measurement campaign.

## References

[1] S. Zhang and R. Raulefs, "Improved Particle Filtering by Exploring Nodamic Movements," in *5th International Symposium on Communications, Control, and Signal Processing*, Rome, Italy, May 2012.

[2] H. Wymeersch, J. Lien, and M. Win, "Cooperative Localization in Wireless Networks," *Proceedings of the IEEE*, vol. 97, no. 2, pp. 427–450, Feb. 2009.

[3] Patwari, N. and Ash, J.N. and Kyperountas, S. and Hero, A.O., III and Moses, R.L. and Correal, N.S., "Locating the Nodes: Cooperative Localization in Wireless Sensor Networks," *IEEE Signal Processing Magazine*, vol. 22, no. 4, pp. 54–69, July 2005.

[4] ICT-WHERE Deliverable, "Estimation of Location-dependent Channel Information (Final Report)," 2010.

[5] C. Oestges, "Multi-link propagation modeling for beyond next generation wireless," in *Antennas and Propagation Conference (LAPC), 2011 Loughborough*, Nov. 2011.

[6] K. Butterworth, K. Sowerby, and A. Williamson, "Base station placement for in-building mobile communication systems to yield high capacity and efficiency," *IEEE Transactions on Communications*, vol. 48, no. 4, pp. 658–669, April 2000.

[7] N. Jalden, P. Zetterberg, B. Ottersten, A. Hong, and R. Thomä, "Correlation Properties of Large Scale Fading Based on Indoor Measurements," in *Wireless Communications and Networking Conference (WCNC)*, March 2007.

[8] G. Steinboeck, T. Pedersen, B. Fleury, W. Wang, T. Jost, and R. Raulefs, "Model for the path loss of in-room reverberant channels," in *Proceedings of the IEEE 73rd Vehicular Technology Conference (VTC-Spring)*, Budapest, Hungary, May 2011.

[9] W. Wang and T. Jost, "A Low-Cost Platform for Time-Variant Wireless Channel Measurements with Applications to Positioning," *IEEE Transactions on Instrumentation and Measurement*, to appear in 2012.

[10] G. Steinboeck, T. Pedersen, and W. Wang, "AAU-DLR 2010 Indoor Measurement Campaign : Measurements for Validation of Models for Reverberant and Cooperative Channels," 2011.

Paper G

# Wireless Indoor Positioning Relying on Observations of Received Power and Mean Delay

Stjepan Begušić, Daniel Nygaard Urup, Jasmina Kolonić, Henrik
Holbæk Pedersen, Wei Wang, Ronald Raulefs, Morten Lomholt
Jakobsen, Gerhard Steinböck, and Troels Pedersen

*IEEE International Conference on Communications, 2013*

© 2013 IEEE

*The layout has been revised.*

## *Abstract*

This contribution introduces position estimation methods relying on observations of the received power and mean delay obtained in a wideband multi-link scenario. In particular, one- and two-step methods are introduced based on statistical models of the observed link parameters. The proposed methods are tested on data from a wideband measurement campaign. The results show that including observations of mean delay of the wideband links can notably improve positioning accuracy as compared to relying on observations of received power alone.

## *G.1 Introduction*

Indoor positioning techniques rely on observations of channel-related parameters obtained from a number of radio-links. These techniques fall in two categories [1]: The first category is the so-called fingerprinting techniques where position estimates are obtained by matching observed channel parameters (called fingerprints) to a prerecorded database. The second category are the model-based techniques where observations of link-parameters are related to geometrical parameters (e.g. distances, directions, position, etc) via models of the radio channel. In this contribution we consider the model-based approaches. Popular link parameters for model-based indoor positioning include the received power and the time-of-arrival (ToA) [2–4]. The received power can be obtained via the Received Signal Strength Indicator (RSSI) available in most communication systems. However, due to fading of the received power, the derived position estimates are endowed with large errors [2]. In contrast, to obtain ToA estimates accurate enough for indoor positioning very large signal bandwidth is needed; typically, this is only possible in ultra wideband (UWB) systems [2–4]. Therefore, it remains important to identify link parameters useful for indoor positioning and yet obtainable in communication systems with limited bandwidth.

For a link-parameter to be useful in practical indoor positioning systems, it must be easy to obtain and carry useful information about the position. Examples of such parameters related to link-distance which can be computed in wideband[1] systems include the received power and the first- and second moments of the squared magnitude impulse response, i.e. the mean delay and rms delay. In [5] a distance-dependent model is derived for the delay power spectrum of an in-room channel taking into account effects due to reverberation. From this model, secondary models for other link parameters, such as the average path gain and the mean delay of a radio link, are also

---

[1] We consider here the bandwidth of “wideband systems” to be less than that of UWB systems.

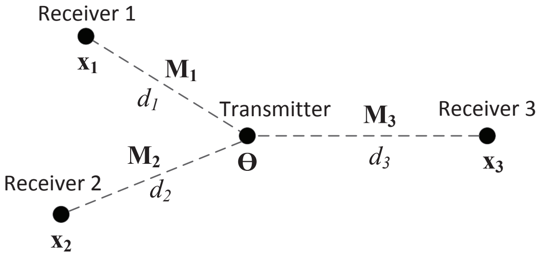

*Fig. G.1: A positioning scenario with three receivers in known positions ($\mathbf{x}_1, \mathbf{x}_2, \mathbf{x}_3$) and a transmitter in an unknown position $\theta$. The vector $\mathbf{M}_i$ of distance dependent parameters is obtained from link $i$.*

derived. From the path gain (which is the inverse of the path loss) the received power can be computed for known transmitted power. It is evident from these secondary models that both mean delay and received power are distance dependent. The mean delay is an attractive link parameter to consider in a positioning context since it can be obtained using both UWB or wideband systems.

In this contribution we consider positioning algorithms relying on measurements of the mean delay and the received power of each link. The methods are derived using the secondary models from [5] modified to include random fluctuations due to multipath propagation. In line with the observations of [6] we model the fluctuations of different links as independent random variables. Moreover, as a first simplifying approximation, we consider fluctuations in the parameters of each single link to be independent. Our modeling is used to propose one-step and two-step positioning algorithms. The derived methods are tested via simulation and by applying them to in-room wideband measurement data. These tests show that including observations of the mean delay yields high accuracy, even in the case of wideband systems.

## G.2 Signal Model

An indoor positioning scenario is considered, with $K$ receivers in known positions $\mathbf{x}_1, \mathbf{x}_2, \ldots, \mathbf{x}_K$ and a transmitter in an unknown position $\theta$, as shown in Fig. G.1. The transmitter is communicating with the receivers via $K$ radio links. Its position is estimated using distance dependent link parameters. The observations can be described as random variables, where the mean is predicted by the models. We denote the vector of observed link parameters by $\mathbf{M} = [\mathbf{M}_1, \mathbf{M}_2, \ldots, \mathbf{M}_K]$ where $\mathbf{M}_i$ denotes the observations obtained for link $i$. Each link allows for observations of received power $G_i$, observed mean delay $\mu_i$ or both. This corresponds to the cases, $\mathbf{M}_i = G_i$, $\mathbf{M}_i = \mu_i$, or $\mathbf{M}_i = [G_i, \mu_i]$, respectively. We model the received power (in dB) for link

$i$ as:

$$10 \log G_i = 10 \log G(d_i) + \varepsilon_{G,i} \tag{G.1}$$

where $G(d_i)$ is the average power, predicted by a path loss model and $d_i$ is the distance of link $i$, i.e. the distance between the transmitter and receiver $i$. The observation noise $\varepsilon_{G,i}$ is a zero-mean random variable with the same standard deviation $\sigma_G$ for all links. Similarly, the model for the observed mean delay for link $i$ reads

$$\mu_i = \mu_\tau(d_i) + \varepsilon_{\mu,i}, \tag{G.2}$$

where $\mu_\tau(d_i)$ is predicted by a mean delay model and the observation noise $\varepsilon_{\mu,i}$ is a zero-mean random variable with the same standard deviation $\sigma_\mu$ for all links.

### G.2.1 Mean Models for Link Parameters

We apply the models for the received power and mean delay proposed in [5]. These models are both derived from a model of the delay power spectrum of an in-room wideband channel, which is a superposition of a primary component and a component due to reverberation. The secondary models have the same superposition structure. The average power is thus a sum of a primary component and a reverberant component:

$$G(d) = G_0 \left( \frac{d_0}{d} \right)^n + G_0 \frac{R_0}{1 - R_0} e^{\frac{d_0 - d}{cT}}, \tag{G.3}$$

where $G(d)$ is the average power at distance $d$. The parameters of the model are: $d_0$ (reference distance), $G_0$ (average power at $d_0$), $R_0$ (reverberation ratio at $d_0$), $n$ (path loss exponent) and $T$ (reverberation time). The constant $c$ is the speed of light. The the first term in (G.3) is due to the primary component, i.e. it accounts for the directly propagating signal and possibly first order reflections with small excess delays. The second term is due to an exponentially decaying diffuse tail of the delay-power spectrum with onset at delay $d/c$. As a consequence of the distance dependent onset, the second term in (G.3) decays exponentially with distance. The reverberant component in (G.3) vanishes when $R_0 = 0$ and the expression becomes equivalent to the well-known one-slope path loss model [7]. The model for mean delay reads

$$\mu_\tau(d) = \frac{d}{c} + TR(d). \tag{G.4}$$

with reverberation ratio

$$R(d) = \frac{1}{1 + \frac{1-R_0}{R_0} \left( \frac{d_0}{d} \right)^n e^{\frac{d-d_0}{cT}}}. \tag{G.5}$$

This model accounts for the shift in mean delay due to an exponential tail of the delay-power spectrum.

### G.2.2 Statistical Models for Link Parameters

We analyze the received power residuals and observed mean delay residuals in order to formulate a statistical model for the observations in (G.1) and (G.2). As found in [8], received power can be assumed independent for different links. Moreover, it appears from further analysis of the same measurement data that the correlation of observed mean delay residuals between links is small. Received power is typically modeled as log-normal (i.e. Gaussian if taken in dB) [7], which was also confirmed in [8]. Furthermore, the analysis of the observed mean delay residual suggests that mean delay can be modeled as a Gaussian random variable. Therefore, as a first approximation we consider the observations in **M** to be independent random variables with joint pdf

$$f_{\mathbf{M}}(\mathbf{M};\mathbf{d}) = \prod_{i=1}^{K} f_{\mathbf{M}_i}(\mathbf{M}_i; d_i), \tag{G.6}$$

where $\mathbf{d} = [d_1, d_2, ..., d_K]$ and the $i$th factor is of the form

$$f_{\mathbf{M}_i}(\mathbf{M}_i; d_i) = \begin{cases} f_G(G_i; d_i), & M_i = G_i \\ f_\mu(\mu_i; d_i), & M_i = \mu_i \\ f_G(G_i; d_i) \cdot f_\mu(\mu_i; d_i), & M_i = [G_i, \mu_i] \end{cases} \tag{G.7}$$

where $f_G$ is the log-normal pdf

$$f_G(G_i; d_i) = \frac{1}{\ln 10 G_i \sigma_G \sqrt{2\pi}} \times \\ \exp\left( - \frac{(10 \log G_i - 10 \log G(d_i))^2}{2\sigma_G^2} \right), \quad G_i > 0 \tag{G.8}$$

while $f_\mu$ is a Gaussian pdf

$$f_\mu(\mu_i; d_i) = \frac{1}{\sigma_\mu \sqrt{2\pi}} \exp\left( - \frac{(\mu_i - \mu(d_i))^2}{2\sigma_\mu^2} \right), \tag{G.9}$$

with mean $\mu(d_i)$ given by (G.4) and variance $\sigma_\mu^2$.

## G.3 Position Estimation

Position estimation can be performed following one of the two approaches: one-step or two-step. In a one-step approach the position $\boldsymbol{\theta}$ is estimated directly from the observations **M**. In a two-step approach, the distances in the vector d are first extracted from the observations **M** and then used to infer on

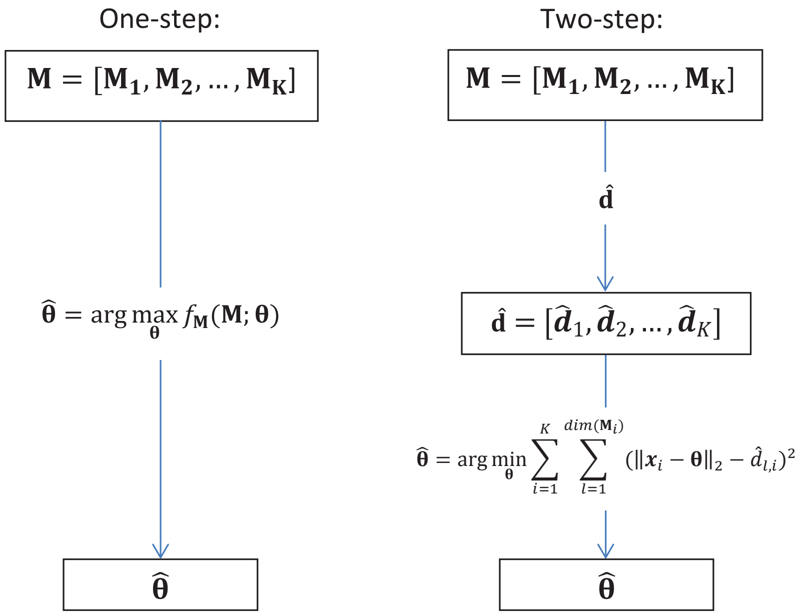
One-step:
Two-step:
$\mathbf{M} = [\mathbf{M}_1, \mathbf{M}_2, \ldots, \mathbf{M}_K]$
$\mathbf{M} = [\mathbf{M}_1, \mathbf{M}_2, \ldots, \mathbf{M}_K]$
$\hat{\boldsymbol{\theta}} = \arg\max_{\boldsymbol{\theta}} f_{\mathbf{M}}(\mathbf{M}; \boldsymbol{\theta})$
$\hat{\mathbf{d}}$
$\hat{\mathbf{d}} = [\hat{\boldsymbol{d}}_1, \hat{\boldsymbol{d}}_2, \ldots, \hat{\boldsymbol{d}}_K]$
$\hat{\boldsymbol{\theta}} = \arg\min_{\boldsymbol{\theta}} \sum_{i=1}^{K} \sum_{l=1}^{dim(\mathbf{M}_i)} (\|\boldsymbol{x}_i - \boldsymbol{\theta}\|_2 - \hat{d}_{l,i})^2$
$\hat{\boldsymbol{\theta}}$
$\hat{\boldsymbol{\theta}}$

*Fig. G.2: Overview of the considered one-step (left) and two-step (right) positioning methods.*

the position $\theta$. Although two-step methods are typically less accurate, their complexity is lower in comparison to one-step methods. We describe first a one-step maximum likelihood method and then a heuristic two step method. Fig. G.2 gives an overview of the algorithms.

First we consider a one-step method where the position $\theta$ is directly estimated from the observations $\mathbf{M}$ via the maximum likelihood principle. Writing the distance $d_i$ as a function of the unknown position $\theta$, $d_i(\theta) = ||\mathbf{x}_i - \theta||_2$, and defining $f_{\mathbf{M}}(\mathbf{M}; \theta) = f_{\mathbf{M}}(\mathbf{M}; \mathbf{d}(\theta))$ with $\mathbf{d}(\theta) = [d_1(\theta), \ldots, d_K(\theta)]$, the maximum likelihood estimator for $\theta$ reads

$$\hat{\theta} = \arg\max_{\theta} f_{\mathbf{M}}(\mathbf{M}; \theta). \tag{G.10}$$

The complex structure of the likelihood function prohibits an analytical solution to this maximization. Therefore, we resort to numerical optimization techniques. Due to the complexity of the likelihood function and the presence of local maxima, we applied a modified version of the simulated annealing algorithm [9]. This is an iterative method which requires initialization. For this purpose we used the position estimate obtained by the two-step method described in the following.

In the two-step method we first estimate the link distances $\mathbf{d}$ from the observed link parameters $\mathbf{M}$. The distance $d_i$ can be estimated from the

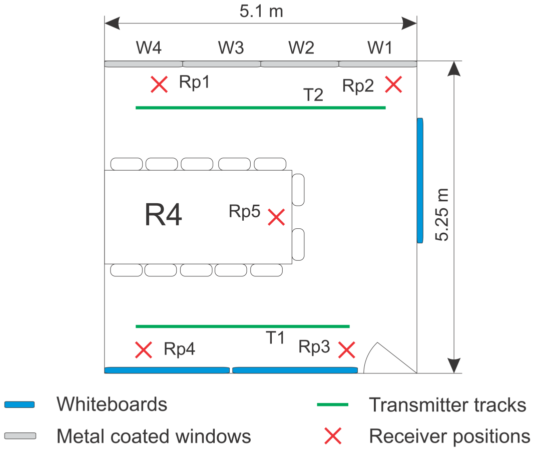

*Fig. G.3: Schematic of the room where the experiment took place.*

observed power as $G^{-1}(G_i)$ where $G^{-1}$ is the inverse of $G(d)$ in (G.3) which can be obtained numerically using a root-finding algorithm. In a similar way a distance estimate can be obtained as $\mu_\tau^{-1}(\mu_i)$ by inversion of (G.4). Thus for links with observations of both received power and mean delay, we obtain two distance estimates denoted by $\hat{d}_{1,i}$ and $\hat{d}_{2,i}$, respectively. The estimated link distances are then used for position estimation by solving a heuristically posed least squares problem:

$$\hat{\boldsymbol{\theta}} = \arg\min_{\boldsymbol{\theta}} \sum_{i=1}^{K} \sum_{\ell=1}^{\dim(\mathbf{M}_i)} (d_i(\boldsymbol{\theta}) - \hat{d}_{\ell,i})^2, \qquad \text{(G.11)}$$

where $\dim(\cdot)$ denotes the dimension of the vector given as argument. A solution to the nonlinear least squares problem (G.11) can be approximated by a Gauss-Newton algorithm [10].

## G.4 Measurement Data

The proposed methods are evaluated using measurement data obtained from an indoor experiment, conducted at the premises of the German Aerospace Center (DLR) [5], [8]. The measurements were taken in a room, depicted in Fig. G.3.

The receiver was placed at fixed positions (Rp1 to Rp5), and the transmitter was moving along two tracks (T1 and T2). The positions of the receivers and transmitters were measured with an accuracy of about 1 cm. The environment was static and nobody was in the room during the measurements gathering. The measurements for different receiver positions were collected sequentially.

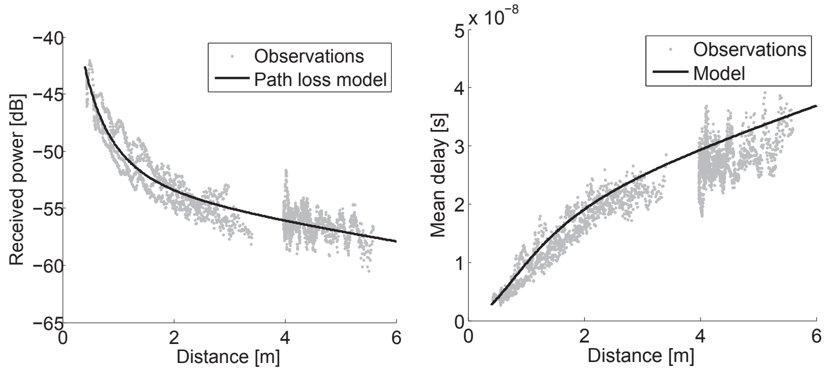

*Fig. G.4: Observed power (left), mean delay (right). Parameter values of fitted mean models.* $G_0 = 6.85 \cdot 10^{-6}$, $n = 2.2$, $R_0 = 0.35$, $T = 18.4$ ns. *Estimated standard deviations:* $\hat{\sigma}_G = 0.93$ *[dB], and* $\hat{\sigma}_\mu = 2.57$ *[ns], respectively.*

They are combined according to the respective transmitter positions to obtain a set of multi-link measurements for the positioning application.

The used transmit antenna was omni-directional. At the receiver a uniform circular array with 8 monopoles was used. The transmitter and receiver antenna heights were 1.26 m and 1.1 m, respectively. The transmitter and the receiver were synchronized via cables to a common clock. The channel transfer function for a bandwidth of 120 MHz and a carrier frequency of 5.2 GHz was measured [8].

Similar to [5], the magnitude squared samples of the channel transfer function are averaged over the entire frequency band and the 8 receiver antennas to obtain an estimate of the received power. After filtering the channel transfer function with a Hann window we apply the inverse discrete Fourier transform to obtain estimates of the channel impulse responses. We take the average of the magnitude squared channel impulse responses for the 8 receiver antennas to obtain an estimate of the delay power spectrum. From the estimated delay power spectrum we estimate the mean delay in [5]. The models (G.3) and (G.4) were fitted to the measurement data using non-linear least-squares techniques. The obtained results are reported in Fig. G.4.

## G.5 Results

The proposed one- and two-step positioning methods were tested by applying them to measurement and simulation data. The resulting positioning errors are computed as the Euclidean distance between the estimated and the true position of the transmitter. In the simulations, the observations of received power and mean delay are generated for the scenario with receiver

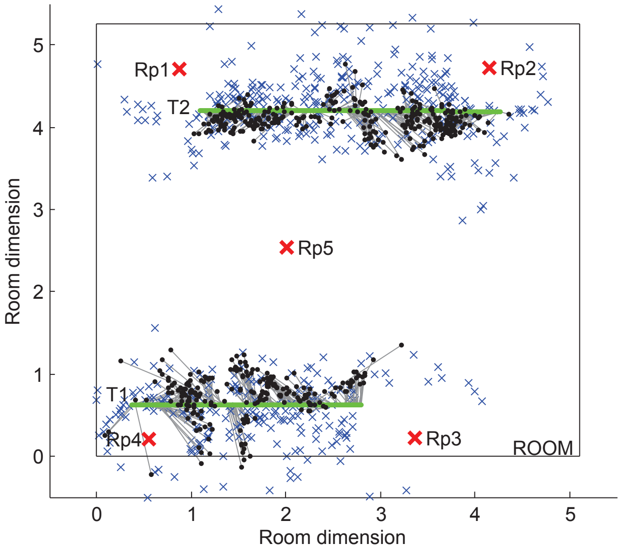

*Fig. G.5: Position estimates of the one-step algorithm in a simulated scenario for two cases of observed link parameters $\mathbf{M}_i$: Blues crosses: received power, i.e., $\mathbf{M}_i = G_i$. Black dots: mean delay observations, i.e., $\mathbf{M}_i = \mu_i$. Grey lines: errors for the $\mathbf{M}_i = \mu_i$ case.*

and transmitter positions as in Fig. G.3 by the statistical models defined in Subsection G.2.2. The results are reported in the empirical cdfs of the position error for the proposed methods, for measured data in Fig. G.8 and for the simulations in Fig. G.7. The results are summarized in terms of the root mean squared error (RMSE) in Table G.1.

The simulation results in Fig. G.5 and Fig. G.7 demonstrate that both one- and two-step methods work for the considered statistical model. Moreover, as expected, some performance loss in terms of accuracy results from using the two-step method. For both one- and two-step methods, it is apparent that between the two considered types of link parameters, the power observation is least and mean delay is the most informative. It also appears from Fig. G.7 that the gain in accuracy by including both types of observations in the estimator, is modest compared to positioning relying on mean delay only.

The results in Fig. G.6 and Fig. G.8 obtained for the measurement data are very similar to the simulation results. However, the improvement that hybrid methods (i.e. with observation of both received power and mean delay) have compared to methods using only mean delay is less pronounced than in the simulation data. The effect is also visible in the RMSE values in Table G.1. The RMSE obtained by the one-step method for mean delay observations alone is 0.34 m which is only reduced by mere 1 cm by taking received power into account in addition. It seems plausible to attribute a part of this effect

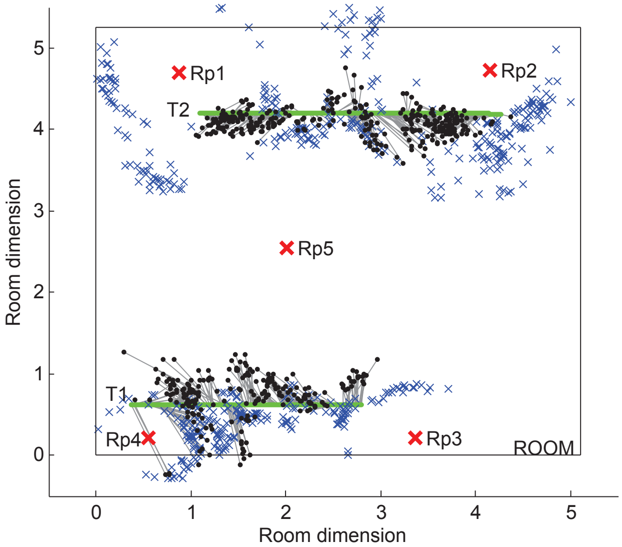

*Fig. G.6: Position estimates of the one-step algorithm for measurement data for two cases of observed link parameters $\mathbf{M}_i$: Blues crosses: received power, i.e., $\mathbf{M}_i = G_i$. Black dots: mean delay observations, i.e., $\mathbf{M}_i = \mu_i$. Grey lines: errors for the $\mathbf{M}_i = \mu_i$ case.*

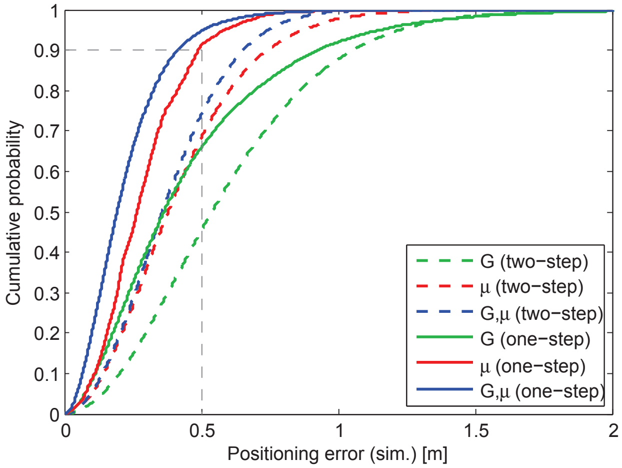

*Fig. G.7: Empirical cdfs of the positioning errors from simulation data.*

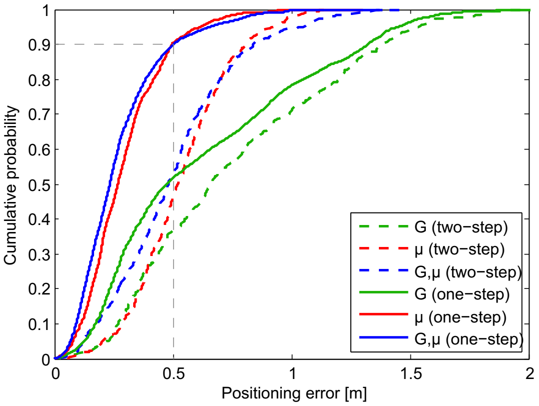

*Fig. G.8: Empirical cdfs of the positioning errors from measurement data.*

to the approximation of statistically independent observations of mean delay and power. Moreover, it seems that considering only observed power, that the estimators return larger errors as compared to the simulations. This may indicate that the model for the received power could be refined, i.e. a better suited model than the log-normal fading should be considered.

The obtained RMSE is remarkably low for indoor positioning when considering the 120 MHz bandwidth of the sounding signal. At this bandwidth, first order reflections interfere with the direct signal which leads to poor performance of ToA estimators [3]. This effect is less severe for mean delay estimation. This observation demonstrates the value of mean delay observation for positioning algorithms using data from wideband systems. The performance of the mean delay estimator and its impact on the positioning accuracy should be further investigated to conclude on how much the performance degrades if the signal bandwidth is reduced.

To provide a rough comparison of the relative computational demand of each of the methods, runtimes for Matlab implementations of each of the methods are given in G.1. The reported runtimes are averages of ten runs on a standard PC. One run includes position estimation of all points on both tracks using measurement data.

## G.6 Conclusion

In this contribution we considered in-room positioning utilizing observations of received power and mean delay. This work relies on the delay power spectrum model and the secondary models of path gain and mean delay [5]. These models predict the mean of the link parameters and were extended to include observation noise due to multipath propagation. As a starting point,

Table G.1: Root Mean Squared Errors of Position Estimates and Algorithm Runtimes

| Method | $\mathbf{M}_i$ | RMSE [m] | | Runtime [s] |
|---|---|---|---|---|
| | | meas. | sim. | |
| Two-step | $G$ | 0.87 | 0.68 | 0.63 |
| Two-step | $\mu$ | 0.57 | 0.49 | 0.44 |
| Two-step | $G$,$\mu$ | 0.57 | 0.43 | 1.44 |
| One-step | $G$ | 0.77 | 0.58 | 4.20 |
| One-step | $\mu$ | 0.34 | 0.33 | 2.24 |
| One-step | $G$,$\mu$ | 0.33 | 0.28 | 4.50 |

we modeled the observations of path gain and mean delay to be statistically independent. This assumption was made for reasons of simplicity. Based on this model we investigated two different methods for positioning: A one-step method where the position is directly obtained from the measurements via a maximum-likelihood estimator, and a two-step method where the position is obtained from distances estimated from each link.

The proposed methods were tested on data from a wideband measurement campaign. The experiment was carried out using a signal bandwidth of 120 MHz. The results show that the mean delay parameter improves the positioning accuracy in comparison to methods relying on observations of received power only. In the considered set-up, relying on power only the one-step method could achieve a root mean squared error of 0.77 m; for mean delay the corresponding number is 0.34 m. Using observations of both power and mean delay lowers the RMSE to 0.33 m, i.e. by only 1 cm. It thus seems that the mean delay data is very informative for estimation of position. This conclusion is remarkable, in particular when compared to the long pulse duration for the sounding signal used in the measurement. Further work is needed in order to yield insight into how the bandwidth affects the positioning accuracy when relying on the mean delay.

## Acknowledgment

This work was co-funded by the European Union via the project ICT- 248894 Wireless Hybrid Enhanced Mobile Radio Estimators 2 (WHERE2).

## References

[1] E. Falletti and M. Luise, “Review of satellite, terrestrial outdoor, and terrestrial indoor positioning techniques,” Newcom++, Tech. Rep., 2008.

[2] H. Liu, H. Darabi, and P. Banerjee, "Survey of wireless indoor positioning techniques and systems," *IEEE Trans. Syst. Man and Cybernetics*, vol. 37, no. 6, pp. 1067–1080, 2007.

[3] N. Alsindi, B. Alavi, and K. Pahlavan, "Measurement and modeling of ultrawideband TOA-based ranging in indoor multipath environments," *IEEE Trans. Vehicular Techn.*, vol. 58, no. 3, pp. 1046–1058, Mar. 2009.

[4] A. Conti, M. Guerra, D. Dardari, N. Decarli, and M. Z. Win, "Network experimentation for cooperative localization," *IEEE J. on Selected Areas in Commun.*, vol. 30, no. 2, pp. 467–475, Feb. 2012.

[5] G. Steinböck, T. Pedersen, B. H. Fleury, W. Wang, and R. Raulefs, "Distance dependent model for the delay power spectrum of in-room reverberant channels," 2012.

[6] W. Wang, G. Steinböck, T. Jost, T. Pedersen, R. Raulefs, and B. Fleury, "Channel Measurements and Characteristics for Cooperative Positioning Applications," in *International Conference on Localization and GNSS (ICL-GNSS)*. IEEE, 2012, pp. 1–5.

[7] T. S. Rappaport, *Wireless Communications Principles and Practice.* Prentice Hall, 2002.

[8] G. Steinböck, T. Pedersen, and W. Wang, "AAU-DLR 2010 indoor measurement campaign: Measurements for validation of models for reverberant and cooperative channels," Aalborg University, Tech. Rep., 2011.

[9] M. Fleischer, "Simulated annealing: Past, present, and future," in *Proc. of the 1995 Winter Simulation Conference*, 1995.

[10] Å. Björck, *Numerical methods for least squares problems.* Siam, 1996.